2016

Two-dimensional materials and hierarchical nanostructured composites for sodium / lithium battery anodes

Tengfei Zhou
University of Wollongong

UNIVERSITY
OF WOLLONGONG
AUSTRALIA

Two-dimensional Materials and Hierarchical Nanostructured Composites for Sodium / Lithium Battery Anodes

This thesis is presented as part of the requirements for the Award of the Degree of

Doctor of Philosophy

from the

University of Wollongong

by

TENGFEI ZHOU
B. Eng., M. Sc.

School of Mechanical, Materials and Mechatronic Engineering

Faculty of Engineering and Information Sciences

August 2016

CERTIFICATION

I, Tengfei Zhou, declare that this thesis, submitted in fulfilment of the requirements for the award of Doctor of Philosophy, in the Institute for Superconducting and Electronic Materials, School of Mechanical, Materials and Mechatronic Engineering, Faculty of Engineering and Information Sciences, University of Wollongong, is wholly my own work unless otherwise referenced or acknowledged. This document has not been submitted for qualifications at any other academic institution.

Tengfei Zhou

28/08/ 2016

DEDICATION

To my sweetheart Yuzhou, and my family who stand by me all the time.

ACKNOWLEDGEMENTS

My thesis was undertaken with the support of everyone in the Institute for Superconducting and Electronic Materials (ISEM), Australian Institute for Innovative Materials (AIIM), School of Mechanical, Materials and Mechatronic Engineering, Faculty of Engineering (MMM) and Information Sciences at the University of Wollongong in Australia, as well as at the Hefei National Laboratory for Physical Sciences at the Microscale, University of Science & Technology of China (USTC).

Over time and with age, four years of PhD study will be end and a new starting-point is in front of us, but at this moment, the word ‗gratitude' stays at the forefront in my mind throughout the day. First, I owe my deepest gratitude to my respected supervisor Prof. Zaiping Guo. Without her enthusiasm, encouragement, continuous support, and optimism throughout my whole PhD study, this thesis would hardly have been completed. In every step of my progress, I received much enthusiastic help from my supervisor. Thinking back, these past several years have not been an easy ride, either academically or personally. I truly thank Prof. Zaiping Guo for sticking by my side, even when I was irritable and depressed. Prof. Zaiping Guo was the reason why I decided to go on to pursue a career in research. Her profound knowledge, acute insights, modesty, rigorous scholarship, enthusiasm, and love for teaching are contagious. She showed and motivated me in different ways to approach each research problem and inculcated the need to be persistent to accomplish any

goal. Here, I pay my highest respects and express my gratitude to my respected supervisor Prof. Zaiping Guo.

I am deeply grateful to Prof. Yi Xie for her support and guidance in my research when I was a visiting student at the Hefei National Laboratory for Physical Sciences at the Microscale in China. I also wish to thank Dr. Chong Xiao for his guidance when I was a visiting student in the University of Science & Technology of China.

Furthermore, I wish to express my appreciation to Prof. Hua Kun Liu, for her suggestions and guidance during group meetings. My deep gratitude goes to my co-workers, Prof. Chaofeng Zhang (HeFei University of Technology), Prof. Jianping Yang (Donghua University), Mr. Yang Zheng, Dr. Wei Kong Pang, Mr. Youwen Liu (University of Science & Technology of China), Dr. Chaoji Chen (Huazhong University of Science and Technology), Prof. Lifang Jiao (Nankai University), and Dr. Shudi Min (East China University of Science and Technology), who have all been very helpful, sharing their experience and knowledge. I would also like to thank Dr. Tania Silver for her critical reading of my manuscripts and thesis.

Moreover, many thanks to Dr. Li Li, Dr. Dan Li, Dr. Kuok Hua Seng, Dr. Qing Meng, Dr. Sha Li, Dr. Jianfeng Mao, Mr. Hongqiang Wang, Mr. Sujith Kalluri, Dr. Jincheng Zhuang, Dr. Yunxiao Wang, Dr. Feixiang Xiang, Ms. Hong Gao, Ms. Yajie Liu, Ms. Qing Zhang, Mr. Wenchao Zhang, Dr. Qinghong Wang, Dr. Yuanzhen Chen, Dr. Peng Zhang, Ms. Jing Cuan, Dr. Guanglin Xia, Mr. Jian Hong, Mr. Kan Huang, Mr. Ruixiang Yu, Mr. Gregoire Dubrulle, Dr. Tao Huang, Ms. Yunwei Wang, Mr. Renjie Wei, Mr. Xianlong Zhou, Ms. Li Zhao, Ms. Meng Zhang, Ms. Yu Zhang, Mr. Zhou Li, Mr. Kun Li, Mr. Pengcheng Huang, Mr. Wei Bai, Ms. Xuemin Hua,

Ms. Jing Chen, Dr. Shan Gao, Ms. Liang Liang, Ms. Shuang Li, and other students and staff for their kind help and valuable advices.

With the completion of this thesis, I would also like to thank the staff members and technicians at ISEM for their kind help and assistance, including Dr. Germanas Peleckis (XRD), Dr. Xun Xu (XRD and tube furnace), Dr. Gilberto Casillas (TEM), Dr. Kosta Konstantinov (BET, TGA/DTA), Dr. Dongqi Shi (XPS), Mr. Tony Romeo (SEM, EDS), Mrs. Narelle Badger, Mrs. Crystal Login, Mrs. Joanne George (OH&S), Mrs. Candace Gabelish, Mr. Robert Morgan, and Mr. Mathew Davis. I am grateful to Prof. Sean Li from the University of New South Wales for his powerful help in electron paramagnetic resonance (EPR) measurements. Many thanks to Dr. Justin Kimpton, Dr. Neeraj Sharma and Dr. Qinfen Gu for their kind help. Part of this thesis was undertaken on the Powder Diffraction beamline at the Australian Synchrotron, Victoria, Australia.

I would never have gotten into the position of being able to do PhD study without my parents, my wife and sweetheart Yuzhou, and my sister, who always encouraged me to achieve to my full potential and provided generous care and moral support in every possible way throughout my education. The warmth of family has been and will always be the strong backing behind my life. It is difficult to pay them back with words alone. Without them, I would not have remained as motivated as I was throughout various stages of the work, and I dedicate this thesis to them.

Finally, I would like to express my gratitude to all those who have cared, welcomed, and helped me throughout my whole study. This thesis would not have been possible without the inspiration and support of a number of wonderful individuals - my thanks and appreciation to all of them for being part of this journey.

ABSTRACT

More and more sodium/lithium-ion battery anode materials are being developed with the aims of high energy density, high cycling stability, and excellent rate capability, in which two-dimensional (2D) and hierarchical nanostructured materials are showing promise due to their shortened paths for sodium ion transportation and their larger surface areas for sodium ion absorption. Moreover, 2D materials (e.g. graphene) have been proved to be excellent supporting and conducting agents in anodes due to their high electrical conductivity and structural stability. Synergetic effects between the graphene and the active materials are generally observed. This doctoral work is focused on the recent progress in the use of 2D active materials and of composites consisting of both 2D supports and active materials as anodes. Based on the manner of energy storage, their electrochemical performance for energy storage is discussed in terms of four subprojects, including (1) enhanced sodium-ion battery performance by a structural phase transition from 2D hexagonal-SnS_2 to orthorhombic-SnS; (2) enhanced charge transfer in SnS/SnO_2 heterostructures: towards high rate capability for sodium ion batteries; (3) a surface engineering and design strategy for surface‐amorphized hierarchical nanostructured TiO_2@graphene hybrids for high power Li‐ion battery electrodes; and (4) highly ordered dual porosity mesoporous hierarchical nanostructured cobalt oxide for sodium‐ion batteries. The main challenges and perspectives on 2D energy storage materials are also discussed.

TABLE OF CONTENTS

LIST OF FIGURES

LIST OF TABLES

NOMENCLATURE

List of Abbreviations

Abbreviation	Full name
a.u.	Arbitrary unit
1D	One-dimensional
2D	Two-dimensional
3D	Three-dimensional
BET	Brunauer-Emmett-Teller
CMC	Carboxymethyl cellulose
CNTs	Carbon nanotube
CV	Cyclic voltammogram
DEC	Diethyl carbonate
DEGDME	Diethylene glycol dimethyl ether
EC	Ethylene carbonate
EDS	Energy dispersive X-ray spectroscopy
EES	Electrical energy storage
EIS	Electrochemical impedance spectroscopy
EV	Electric vehicle
FEC	Fluoroethylene carbonate
FESEM	Field-emission scanning electron microscopy
HEVs	Hybrid electric vehicles
HRTEM	High-resolution transmission electron microscopy
JCPDS	Joint Committee on Powder Diffraction Standards
LIBs	Lithium ion batteries
SIB	Sodium ion batteries
MWCNTs	Multi-walled carbon nanotubes
NMP	1-methyl-2-pyrrolidinone
OCV	Open circuit voltage

PAA	Polyacrylic acid
PC	Propylene carbonate
PVDF	Polyvinylidene fluoride
GO	Graphene oxide
RGO	Reduced graphene oxide
SAED	Selected area electron diffraction
SEI	Solid electrolyte interphase
SEM	Scanning electron microscopy
SHE	Standard hydrogen electrode
STEM	Scanning transmission electron microscopy
HAADF	High-angle annular dark-field
TEM	Transmission electron microscopy
TGA	Thermogravimetric analysis
XAS	X-ray absorption spectroscopy
XPS	X-ray photoelectron
XRD	X-ray diffraction
PD	Powder diffraction
EPR	Electron paramagnetic resonance
ESR	Electron spin resonance

List of Symbols

Symbol	**Name**	**Unit**
2θ	Peak position of XRD	°
C	Charge or discharge rate	C
d	Lattice spacing	nm
I	Current	mA
m	Active material weight	g
N	Avogadro's number = 6.022×10^{-23}	mol^{-1}
P/P_0	Relative pressure	
PD	Power density	$W\ L^{-1}$
Q	Specific capacity	$mAh\ g^{-1}$
R	Resistance	Ω
$SBET$	Specific BET surface area	$m^2\ g^{-1}$
SE	Specific energy	$Wh\ kg^{-1}$
SP	Specific power	$W\ kg^{-1}$
t	Time	s
T	Temperature	K or °C
t_{Na}	Sodium transference number	
V	Voltage	volt
η	Coulombic efficiency	%
λ	X-ray wavelength	Å

CHAPTER 1 INTRODUCTION

1.1 General background

Electrochemical secondary battery technology is one of the most promising means of storing electricity, in applications ranging from portable electronic devices to vehicles and then to large-scale electric energy storage systems for stationary applications. Lithium ion batteries (LIBs) have dominated most of the first two applications. The last application, however, calls for the next generation of energy storage alternatives with low cost and good sustainability. Therefore, Na-ion batteries (SIBs) are a highly promising alternative to meet the demands of grid-level storage due to the practically infinite nature of sodium resources and their low cost. More importantly, the energy storage mechanisms of both types of batteries are similar, which makes knowledge attained by developing LIBs valuable for the design of SIB electrodes. Therefore, rapid progress has been made on SIB cathode materials, where layered metal oxides and polyanionic compounds have exhibited encouraging results. Pure graphite, however, as the standard anode for LIBs can only provide very small capacity in SIBs under normal conditions. Therefore, the development of anode materials with high capacity and long cycle life is critical for the success of SIBs. During the past several years, various SIB anode materials have been developed with the aims of high energy density, high cycling stability, and excellent rate capability, in which two-dimensional (2D) materials are showing promise due to the shortened paths for sodium ion transportation and larger surface areas for sodium ion absorption. The integration of 2D materials and their composites into SIB anodes

offers opportunities to address the challenges to the design of better SIB materials intended for stationary applications in a timely way. This doctoral work summarizes various types of hybrid 2D materials by classifying them according to the mechanism of their sodium storage and discusses the remaining issues that need to be addressed so that LIBs/SIBs can reach their full potential.

This doctoral work aims to realize higher sodium/lithium-storage performance via surface engineering of nanostructured electrode materials and optimizing other battery components. Specifically, the emphases of this doctoral work are outlined as follows: (1) Incorporation of electrochemically active materials into a 2D carbon matrix as electrode materials for sodium/lithium ion batteries. These 2D composites feature enhanced surface area, improved charge diffusion, and greater electronic and ionic conductivity, which will increase the overall electrochemical performance. (2) Optimization of the charge transfer pathways by using 2D inorganic electrode materials for the sodium ion battery. This involves enhancing the charge transfer in electrodes via induced electric field within the interacting hetero-nanosheets. (3) Engineering nanocrystals with core@amorphous shell structure for high power sodium ion batteries. (4) Fabrication of sodium ion batteries together with specifically chosen electrolytes to support charge storage processes on the electrode/electrolyte interface. The nano-engineered composites will be applied in these sodium/lithium ion battery systems. (5) Study of the charge transfer mechanism in the electrode materials of the battery systems. (6) Study of the transformations in composition and physical structure as functions of the electrochemical processes by in-situ and ex-situ X-ray diffraction (XRD), powder diffraction (PD), and X-ray photoelectron spectroscopy (XPS) in order to optimize the active materials and

electrolytes, and to further improve the energy storage performance. (7) Fabrication, testing, and evaluation of the sodium ion batteries with selected promising anode materials. (8) Establishing an evaluation model through electrochemical testing and measurements to guide the battery design.

1.2 Chapter overview

Chapter 2 contains some basic background knowledge about energy storage systems. Various topics are briefly introduced in Chapter 2, including the background of sodium ion batteries, 2D materials used as anode, and an overview of the other battery components, such as the electrode materials, binders, additives, and electrolyte.

Chapter 3 presents the experimental and characterization methods used in this thesis, including the details of chemicals, synthesis procedures, physical characterization techniques, and electrochemical characterization methods.

In **Chapter 4**, we introduce the structural phase transitions, which can be used to alter the properties of a material without adding any additional elements and are therefore of significant technological value. We provide the first report on a SnS@graphene architecture for application as a sodium-ion battery anode, which is built from 2D SnS and graphene nanosheets as complementary building blocks. The formation mechanism of SnS@graphene and the synergistic Na-storage reactions of SnS in the anode are discussed in detail. The lesser structural changes in SnS during the conversion are expected to lead to good structural stability and excellent cycling stability in its sodium-ion battery performance.

Ultrafine SnS/SnO_2 heterostructures were fabricated and applied as anode for sodium-ion batteries in **Chapter 5**. The as-prepared material shows excellent performance and outstanding cycling stability at high rates, which can be ascribed to the charge-transfer driving force, good structural stability, and excellent electrical conductivity.

Chapter 6 presents a novel strategy that is utilized to improve the rate performance of TiO_2 in lithium-ion batteries. Surface amorphization provides unprecedented opportunities for altering and tuning material properties. Surface-amorphized TiO_2@graphene synthesized using a specially designed low temperature phase transformation technique exhibits significantly improved rate capability compared to well-crystallized TiO_2@graphene and bare TiO_2 electrodes. Those improvements facilitate lithium-ion transport in both insertion and extraction process, and enhance electrolyte absorption capability.

Chapter 7 is a study of the electrochemical properties of highly ordered mesoporous cobalt oxide (m-Co_3O_4), which is applied as an electroactive material in sodium-ion battery anodes. The most notable feature of our dual porosity mesoporous Co_3O_4 is that the highly ordered structure can provide much better transport pathways than the reference bulk Co_3O_4 derived nanostructure, because it can facilitate the mass transport of electrolyte in the larger pores and sodium ion diffusion in the smaller pores, while also providing a large electrode–electrolyte interface for electrolyte adsorption due to the surface disorder of the Co_3O_4.

CHAPTER 2 LITERATURE REVIEW

Sodium-ion batteries (SIBs) have attracted great attention recently due to the abundance of sodium resources, particularly for large scale electric energy storage applications for renewable energy and smart grids. More and more sodium-ion battery anode materials have been developed with the aims of high energy density, high cycling stability, and excellent rate capability, in which two-dimensional (2D) materials are showing promise due to their shortened paths for sodium ion transportation and larger surface areas for sodium ion absorption. Moreover, 2D materials (e.g. graphene) have been proved to be excellent supporting and conducting agents in SIB anodes due to their high electrical conductivity and structural stability. Synergetic effects between the graphene and the active materials are generally observed.

This review is devoted to the recent progress in the use of 2D active materials and in composites consisting of both 2D supports and active materials as anodes. Based on the manner of sodium storage, their electrochemical performance for sodium storage is discussed in terms of four classifications, including carbonaceous materials (graphene and carbon nanosheet), alloy based materials (Sn, Sb, and P), conversion materials (oxides/sulphides), and intercalation materials (Ti-based compounds). Finally, the main challenges and perspectives on 2D sodium storage materials are discussed.

2.1 General background

Batteries are continually being developed to power an increasingly diverse range of applications, from microchips to vehicles and then stationary energy storage devices.[1] For application in large-scale energy storage, the cycle life and cost are regarded as more essential factors than the energy density. Thus, Li-ion batteries (LIBs) are only expected to contribute in part to large-scale energy storage, which is needed to support the widespread use of renewable energy, due to their high cost and low stability.[2,3] These requirements call for the next generation of energy storage alternatives to have low cost and good sustainability. Sodium-ion batteries (SIBs) have again attracted increasing attention for large-scale energy storage of renewable energy and smart grid applications in the past few years (**Figure 2.1a**), because of the high abundance and low cost of sodium resources, and their decent energy densities.[4-6] More importantly, sodium has similar chemical properties to lithium, which makes knowledge acquired from developing LIBs valuable for the design of SIB electrodes. Challenges still remain, however, since the ionic radius of Na^+ is larger than that of Li^+ (0.98 Å vs. 0.69 Å). The larger Na^+ ions will lead to slower ion transport, more sluggish reaction kinetics, and larger volume changes upon Na^+/Na insertion/extraction, which usually result in limited rate capability and Na storage reversibility. For example, graphite, as the most commonly used anode material in LIBs, can only provide very small capacity in SIBs under normal conditions. Therefore, the development of high-capacity and long-cycle life anode materials is critical for the success of SIBs.

In the past several years, research on SIBs has been accelerated, and significant improvements have been made in developing SIBs anode materials with the aim of

increase the cycling stability, rate capability, and energy density.[6] Compared to bulk structures, nanostructures normally provide much better performance. Two-dimensional (2D) materials in particular show unique advantages regarding transport kinetics and mechanical properties. With atomic or molecular thickness and infinite planar lengths, 2D materials have different atomic structures from their bulk counterparts, including differences in atomic arrangement, chemical valence, coordination number, and bond length. Moreover, their more exposed interior atoms would inevitably induce the formation of vacancies/pits/defects, which would have a non-negligible effect on their chemical and physical properties. Actually, 2D materials have already displayed fascinating properties in the energy storage field, including shorter ion diffusion lengths and a large exposed surface for electrochemical processes. Furthermore, 2D nanomaterials, such as graphene, are well-known for acting as functional substrates for incorporating active materials into SIBs, which increases their structural robustness, improves the electrical conductivity of the electrodes, and hence, enhances their overall performance (**Figure 2.1b**).

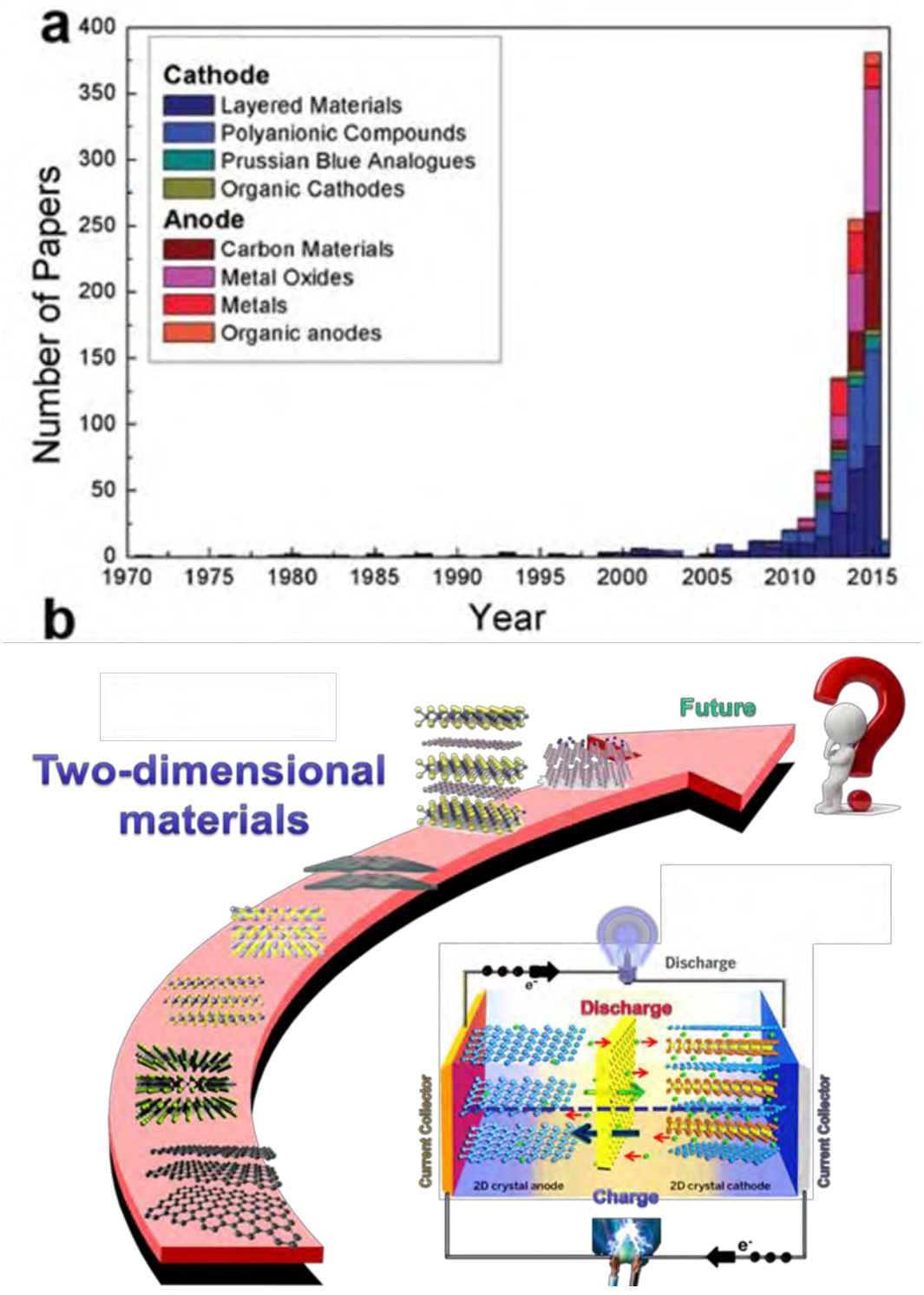

Figure 2.1 (a) Number of publications related to sodium for energy storage devices, from 1970 to 2015. (b) Schematic illustration of 2D-based battery electrodes.

In the present review, we provide an overview of the current state of SIB anode materials from a structural design perspective. The notion of 2D favored structure will be discussed in terms of both 2D active materials and 2D composites. Its topics include carbonaceous materials, sodium alloy/compounds, oxides/sulphides, and titanium based materials. The unprecedented functionalities and promising applications of these materials are described first, and then the difficulties and challenges for these materials are discussed. Subsequently, we summarize the latest efforts toward addressing these limitations in order to uncover the structural features of the 2D architectures. Finally, we also outline future prospects for the major challenges and opportunities facing the 2D materials. The advances discussed here will lead to a broader understanding of SIB anode materials and can illuminate the material innovations in other energy conversion and storage realms.

2.2 Two-dimensional carbonaceous anodes

Carbonaceous anodes are extensively applied in batteries due to their wide availability. Graphite, the bulk form of graphene, is the dominant commercial anode material in LIBs, but it only provides a very small capacity in SIBs under normal conditions.[7-10] A reasonable capacity was only obtained in modified graphite via enlarging the interlayer distance or through co-intercalation with ether-based electrolytes.[11-13] Thus, interest has been attracted to other carbonaceous materials with low graphitization, where the Na storage is realized by combining Na intercalation and Na filling of pores or defects. Hard carbon is widely recognized as a potential anode material for the sodium ion battery due to the large interlayer d-spacing and rather high capacity (~300 mAh g^{-1}).[14-19] Nevertheless, these materials are limited by their poor rate capability and cyclability because of their intrinsically

low graphitization. In addition, their low charging potential may induce electrode instability and safety issues. For carbonaceous anodes, it is widely accepted that the sodium insertion mechanism strongly depends on the particle size, the degree of graphitization, the structure or textural disorder, and the porosity.[20] Therefore, controlling the morphology is an effective strategy to improve the dynamic performance of carbonaceous materials. Two-dimensional materials, especially those having structures with large surface area, have excellent electronic conductivity and chemical stability, because this kind of structure can bring the materials into adequate contact with the electrolyte, promote the transport of ions, and facilitate strain relaxation during the charge-discharge process.[21,22]

Graphene, a unique 2D carbon material, with large surface area, excellent chemical stability, and outstanding electronic conductivity, exhibits extraordinary advantages in energy storage systems.[23,24] In addition to its use as a functional supporting matrix, graphene itself can serve as an active material in the electrochemical reaction.[25,26] The use of rGO as an anode material in SIBs has been found to deliver a high capacity of 141 mA h g^{-1} at 0.2 C, with a long cycle life of over 1000 cycles and a reversible capacity of 95.6 mA h g^{-1} at the high current rate of 5 C.[25] Such performance is attributed to the unique structure of rGO, in which the interconnected graphene nanosheets are able to greatly reduce the diffusion length of sodium ions. Moreover, Datta et al.[27] discovered that Na could be absorbed into defective graphene, which is not the case for pristine graphene. The capacities of Na^+ batteries reached 1450 mA h g^{-1} when the divacancy defect density reached its limit. In addition, the introduction of aliovalent elements such as boron, sulfur, and phosphorus into graphene helps to generate abundant defect sites to absorb the

sodium ions and improves the surface hydrophilicity of the graphene, which facilitates electrode-electrolyte interactions and hence leads to higher Na-storage capacity.[28-33] For example, Zhang et al. utilized polydopamine, a conformal and uniform coating material, as the nitrogen source to modify graphene oxide by a pyrolysis method to synthesize N-doped graphene sheets, which showed quite stable cycling performance, with no capacity decay after 600 cycles.[30] Chen et al.[33] synthesized sulfur-doped graphene, with phenyl disulfide as the sulfur source, as an anode material for sodium storage. The sulfur atoms covalently bonded to the graphene sheets led to changes in the electronic structure of the graphene sheets. The obtained material exhibited long cycling stability and superior rate capability.

On the other hand, the construction of hierarchically porous structure is effective for improving the dynamic performance of the carbon because the electrolyte can enter the holes and the diffusion distance of the Na-ions can be decreased.[34-36] Therefore, the combination of a porous structure and 2D morphology should be an excellent strategy to improve the electrochemical performance of materials. Xu et al. prepared well-defined three-dimensional (3D) mesoporous nitrogen-doped graphene foams, which not only possessed a superior 3D mesoporous graphene structure, but also induced defects by N-doping (**Figure 2.2a**).[37] All these factors were combined to make contributions to the significant improvement of the electrochemical performance. As a result, the material showed 852.6 mAh g-1 initial reversible capacity (at the current density of 500 mA g^{-1}) and 594 mA h g^{-1} after 150 cycles, corresponding to capacity retention of 69.7% (**Figure 2.2b**).

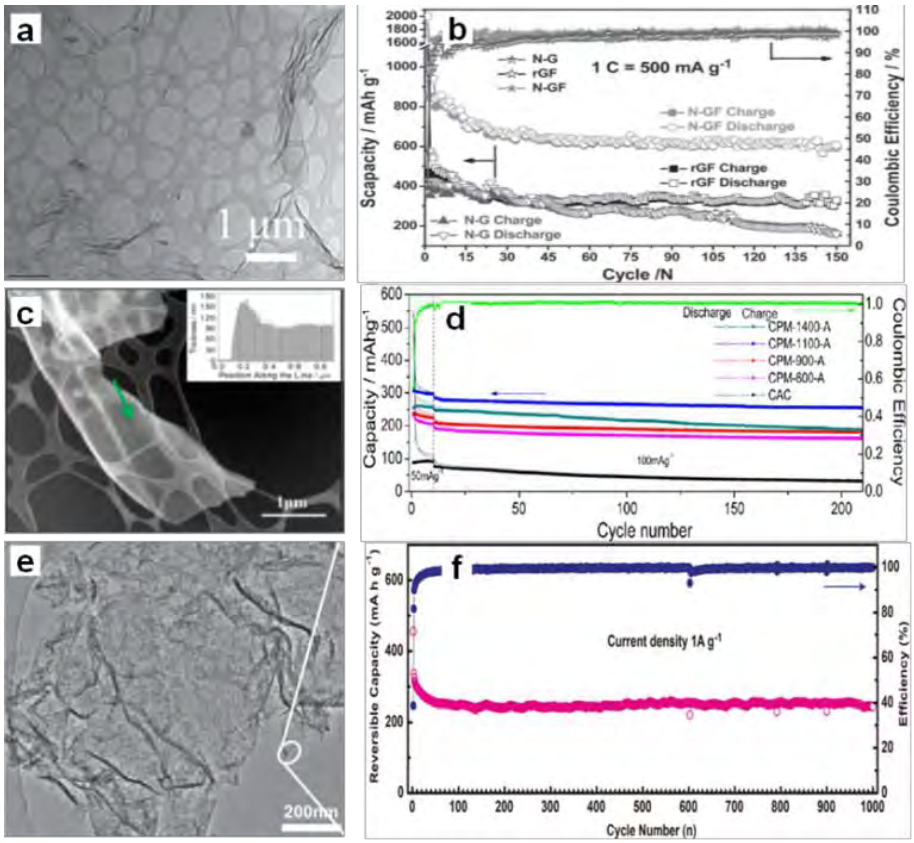

Figure 2.2 (a) STEM images of the nitrogen–graphene foam (N-GF), (b) cycling performance of the nitrogen doped graphene (N-G), reduced graphene foam (rGF), and N-GF at 1 C in the voltage range of 0.02–3.0 V (assumed 1 C = 500 mA g^{-1}; Scapacity = specific capacity). (c) high-angle annular dark field–transmission electron microscope (HAADF TEM) micrograph and electron energy loss spectroscopy (EELS) thickness profile (inset) of the carbon strand marked by the arrow in CPM-1100-A, (d) Extended cycling performance of the CPM-A and CAC electrodes, with the Coulombic efficiency of the CPM-1100-A electrode. (e) TEM image of the graphene–hierarchically porous carbon (G@HPC) composite; and (f) cycling performance under 1 A g^{-1}.

Ding et al. reported (**Figure 2.2c**) [38] carbon nanosheets with a much larger intergraphene spacing (0.388 nm) than graphite (c/2 = 0.3354 nm). Due to the 3D

macroporous interconnected networks and the dilated graphene interlayer spacing, the carbon nanosheets allowed for fast sodium intercalation and extraction (**Figure 2.2d**). Furthermore, Yan et al. designed a sandwich-like hierarchically porous carbon/graphene nanocomposite by a facile ionothermal process, which overcomes the low graphitization problem of the hard carbon materials. The graphene, sandwiched by hierarchically porous carbon on both sides, facilitates electron transport (**Figure 2.2e**).[39] The nanocomposite exhibited capacity of 250 mAh g^{-1} at the current density of 1 A g^{-1}, even after 1000 cycles (**Figure 2.2f**), in which the hierarchical porous carbon facilitates Na^+ insertion and the graphene guarantees high electronic conductivity for the supply of electrons.

2.3 Alloy based anodes

Alloys are anticipated to be promising anode materials in SIBs due to their high volumetric and gravimetric capacities. A number of elements, such as Sn, Sb, Bi, Pb, Ge, and P, can form binary alloys with Na. They can principally be used as anodes for sodium ion batteries.[40-51] Only Sn, Sb, and P were intensively investigated, however, owing to their relatively higher specific capacity and excellent electrochemical performance. Hence, the review of the alloy anodes is mainly focused on these three elements and their related compounds with 2D architectures.

2.3.1 Tin and antimony based alloy anodes

Tin (Sn) can deliver a theoretically capacity of 847 mA h g^{-1} according to the formation of $Na_{15}Sn_4$.[40,46,47] Electrochemical sodiation/desodiation for the Na-Sn system occurs in a series of steps: Sn, $NaSn_5$, NaSn, Na_9Sn_4, and $Na_{15}Sn_4$.[40,46,47,42] In contrast, antimony (Sb) can deliver a theoretical capacity of 660 mAh g^{-1}

according to the formation of Na_3Sb.[48,49,53] During sodiation, crystalline Sb is first electrochemically reduced to an amorphous phase, NaxSb. Then, the amorphous Na_xSb is reduced to crystalline Na_3Sb with a hexagonal lattice through the formation of cubic Na_3Sb as a metastable intermediate phase. Upon desodiation, the crystalline Na_3Sb is oxidized into amorphous Sb.[48] It is believed that the formation of the intermediate amorphous phase may act as a buffer to relieve strain and hence improve the cycling performance. Thus, unlike the bulk Sn, the bulk Sb particles showed good electrochemical performance, although nanosized Sb (10-20 nm) particles exhibited enhanced rate capability and higher cycling stability.[53] The volume expansion of pure Sn upon alloying to $Na_{15}Sn_4$ and upon the alloying of Sb to Na_3Sb is 420 and 293 %, respectively, which is extremely high. This enormous volume expansion will lead to continuous and cumulative pulverization, leading to the loss of electrical contact and resulting in capacity decay during cycling.

One strategy to deal with the volume expansion is to introduce a secondary matrix. Such a matrix can act as a buffer to suppress the volume changes and particle aggregation of the metal during the sodiation/desodiation cycling, and hence, allow a much higher number of cycles. 2D carbon materials such as graphene and carbon nanosheets are excellent matrix materials due to their high surface area and highly electrically conductive properties.[54-62] For example, a hierarchical tin@carbon composite composed of a graphene carbonaceous matrix and well-confined tin nanoparticles (NPs) with a typical size of ~15 nm was investigated as anode material for Na-ion storage (**Figure 2.3a**).[57] The matrix with its two-dimensional graphene backbone not only acts as a confinement layer preventing the tin nanoparticles from aggregating during the material preparation, but also functions as a physical barrier

to buffer the volume change effect during charge/discharge cycling. As a consequence, the composite demonstrates excellent rate performance and cycling stability for Na-ion storage, and a reversible Na-ion storage capacity of 413 mA h g^{-1} with negligible fading was achieved (**Figure 2.3b**). Antimony/carbon nanosheets (**Figure 2.3c**) [61] displayed high reversible capacity, good rate performance, and long cycling stability for Na-ion batteries, largely due to rich N-doping defects and the uniform dispersion of Sb NPs. At high charge–discharge rate of 2 A g^{-1}, a large specific capacity of 220 mA h g^{-1} was still achieved (**Figure 2.3d**). Ideally, the Sn or Sb nanoparticles are embedded or partially encapsulated in the matrix, thus better accommodating the stress and strain without being pulverized, shortening the ionic and electronic transport pathways and preventing loss of electrical contact.

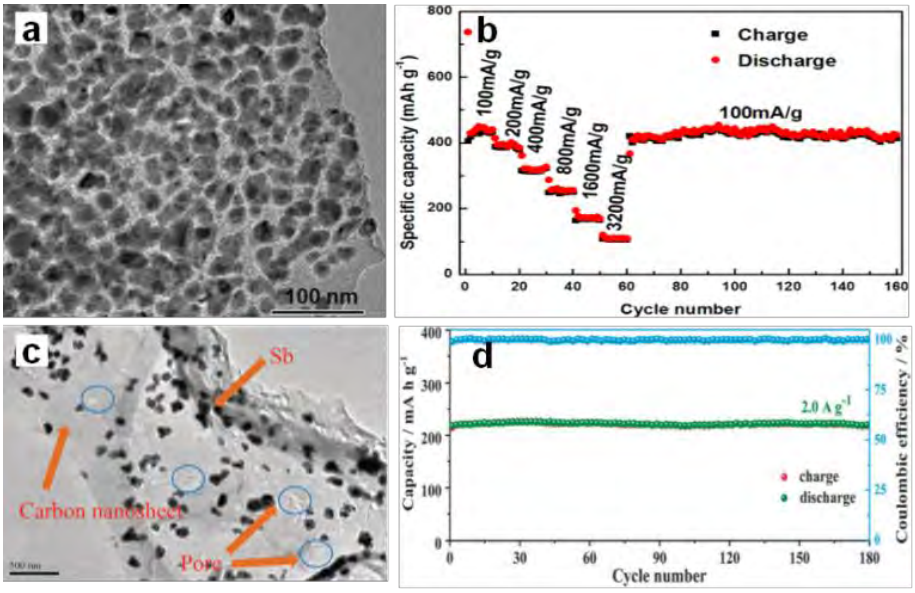

Figure 2.3 (a) TEM image of the foam like graphene backboned carbonaceous matrix and well-confined tin nanoparticles (F-G/Sn@C); (b) Rate capability and cycling performance of the F-G/Sn@C electrodes in the voltage range of 10 mV to

2.0 V for Na ion storage. (c) TEM image of the Sb N-rich C (Sb–N/C) composite, (d) prolonged cycling performance of the Sb–N/C electrode at 2.0 A g^{-1} with the coulombic efficiency.

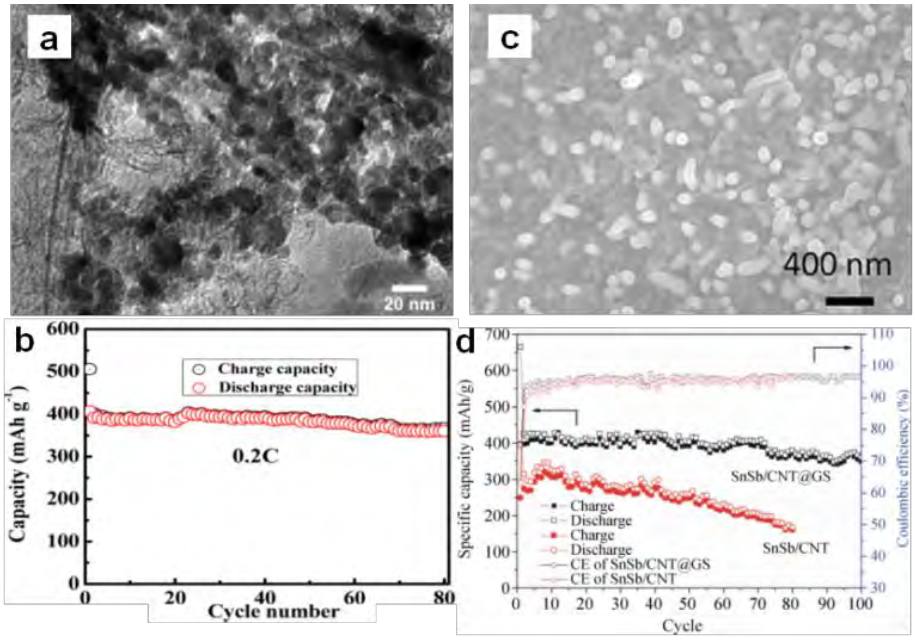

Figure 2.4 (a) TEM image of RGO-SnSb nanocomposites; (b) Cycling performance of RGO-SnSb electrodes in the voltage window of 0.001−2.5 V at a cycling rate of 0.2 C. (c) FE-SEM images of the SnSb/CNT@GS, (d) Cycling performance and corresponding Coulombic efficiency at the current density of 100 mA g-1 of SnSb/CNT@graphene and SnSb/CNT between 0.005–1.5 V in 1 M $NaClO_4$ with PC + 5% FEC.

The secondary matrix can also either be composed of an electrochemically inactive element, such as Cu, Ni, Zn, Mo, and Fe,[63-68] or an active element, such as Sn, Sb, Bi, and P.[69-80] Various Sn and Sb based binary alloy materials, such as Cu_6Sn_5,[63] Ni_3Sn_2,[64] Zn_4Sb_3,[65] Mo_3Sb_7,[66] Cu_2Sb,[67] $FeSb_2$,[68] SnSb,[69-73] and Sn-P (Sn_4P_3, SnP_3)[74-79] and Bi–Sb alloys80 have been investigated as SIB anodes. The

most studied binary alloys are SnSb[69-73] and Sn_4P_3,[74-78] where all the elements are electrochemically active upon sodiation. Thus, in these systems, the two different active metal phases can work as mutual buffers for each other to alleviate the volume changes. During sodiation and desodiation, the mechanism consists of both conversion and alloying reactions. Sn_4P_3 will be discussed in the following section on phosphorus. SnSb was first sodiated to form amorphous Na_3Sb and Sn, followed by the sodiation of Sn into $Na_{15}Sn_4$.[69] The coexisting Sb- and Sn-rich phases generated during the sequential reactions can self-support one another. As a result, the SnSb electrode can maintain stability and good electrical contact during the sodiation/desodiation processes. Therefore, high initial capacity (544 mA h g^{-1}) and good cyclability were achieved.[69] The performance of SnSb can be further improved by dispersing the SnSb nanoparticles on various substrates such as graphene, which further increases the structural robustness and ion/electron diffusion. For example, Ji et al. synthesized reduced graphene oxide/tin−antimony alloy (RGO-SnSb) nanocomposites through a hydrothermal reaction and the subsequent thermal reduction treatments, where SnSb nanoparticles with an average size of about 20−30 nm are uniformly dispersed on the RGO surfaces (**Figure 2.4a**).[72] When they were used as anodes for SIBs, these as-synthesized RGO-SnSb nanocomposite anodes delivered a high initial reversible capacity of 407 mA h g^{-1}, stable cyclic retention for more than 80 cycles and excellent cycle stability at ultrahigh charge/discharge rates up to 30 C (**Figure 2.4b**). The significantly improved performance can be attributed to the synergetic effects of RGO−based flexible framework and the nanoscale dimension of the SnSb alloy particles. The SnSb core/carbon-shell nanocables composed of carbon nanotubes (CNTs), which were anchored on graphene sheets (**Figure 2.4c**).[73] The carbon coating and the encapsulation of SnSb

is effective for alleviating the volume-change problem in SIBs. The optimized coaxial SnSb/carbon nanocable/GS nanostructure can retain a capacity of 360 $mAhg^{-1}$ for up to 100 cycles, which is 71% of the theoretical capacity (**Figure 2.4d**).

2.3.2 Phosphorus based anodes

Phosphorus (P) has the highest theoretical capacity of 2596 mA h g^{-1} according to the formation of Na_3P.[50,51] Meanwhile, its redox potential of about 0.4 V vs. Na^+/Na is appropriate for an anode in SIBs. The volume change between P and Na_3P is huge (490 %), however. P has three main allotropes: white, red, and black, but only Red P (RP) and Black P (BP) are suitable as electrode materials for battery application. RP is amorphous and commercially available, although RP has low electronic conductivity (~1×10^{-14} S cm^{-1}). Thus, a secondary matrix with high conductivity is necessary to achieve high performance and stable cyclability.[81-87] Graphene nanosheets[85-87] were utilized as the conducting matrix to improve the electrical conductivity of red phosphorus and alleviate the volume changes during the sodiation/desodiation process. For example, Song et al. fabricated a novel phosphorus/graphene nanosheet hybrid through ball milling (**Figure 2.5a**).[85] The graphene stacks are exfoliated to form nanosheets that chemically bond with the surfaces of phosphorus particles. As anode for SIBs, the phosphorus/graphene nanosheet hybrid delivers a high reversible capacity of 2077 mA h g^{-1} with excellent cycling stability (1700 mA h g^{-1} after 60 cycles) and high Coulombic efficiency (> 98%) (**Figure 2.5b**). Moreover, P-G composites with a well-designed structure of nanosized phosphorus particles encapsulated in graphene scrolls were fabricated in Chen‘s group (**Figure 2.5c**).[86] The graphene scrolls in P-G can not only offer an interconnected conductive network, but also buffer the large volume changes and

maintain the integrity of the electrode. As SIB anode, the P-G composite with phosphorus content of 52.2% showed the best performance, delivering a high reversible capacity of 2355 mAh g^{-1} and good capacity retention of 92.3% after 150 cycles (**Figure 2.5d**). More recently, a flexible paper made of nitrogen-doped graphene and amorphous phosphorus was developed (**Figure 2.5e**). The restructured anode exhibits ultra-stable cycling performance and excellent rate capability (809 mAh g^{-1} at 1500 mA g^{-1}).[87]

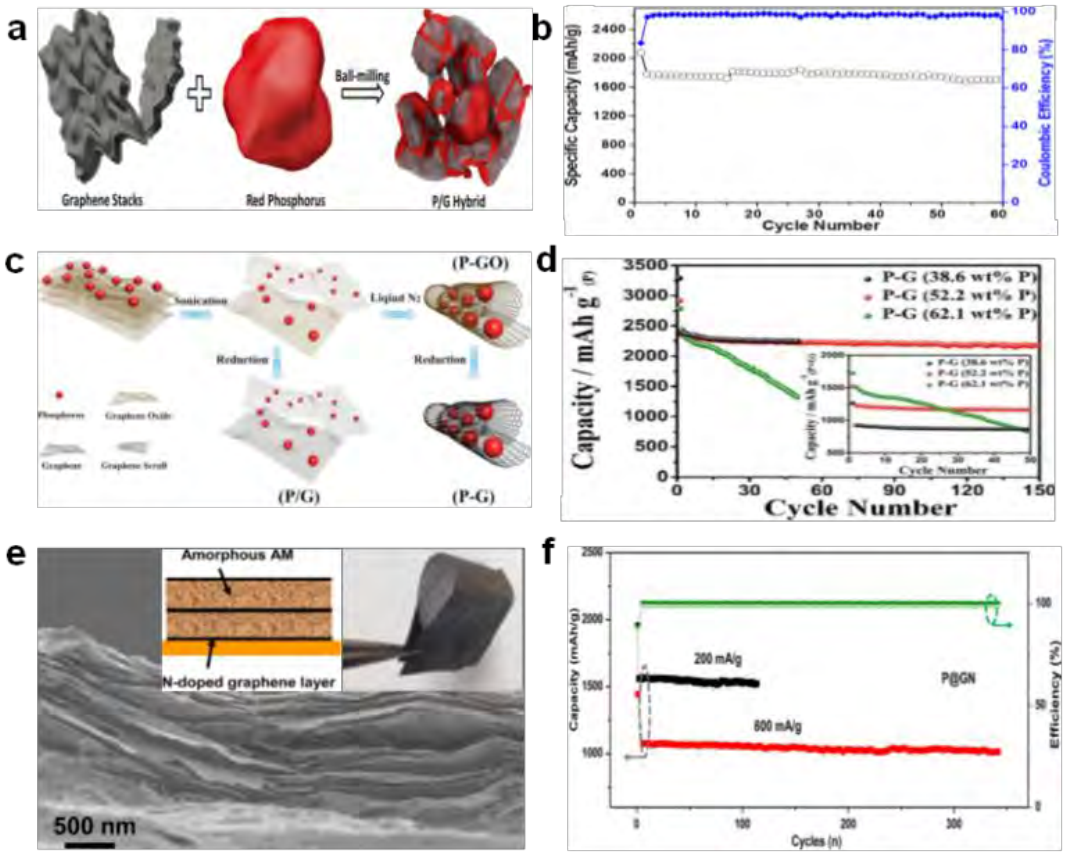

Figure 2.5 (a) Schematic illustration of the synthesis of a phosphorus/graphene nanosheet (P/G) hybrid; (b) cycling stability and Coulombic efficiency of the P/G hybrid anode at a current density of 260 mA g-1. (c) schematic illustration of the synthesis of P-G composite; (d) cycling performance of the three P-G composites at a current density of 250 mA g-1 (inset: cycling performance of the P-G composites

based on the total mass of the composite). (e) cross-sectional SEM image of P@GN paper, with the inset showing the designed novel ―bread and butter"-like anode structure, consisting of amorphous P layers sandwiched with N-doped graphene frameworks; (f) cycling performance and Coulombic efficiency of P@GN at 200 mA g-1 and 800 mA g-1, respectively.

Orthorhombic black phosphorous (BP, layered crystal structure in **Figure 2.6a**) is thermodynamically the most stable allotrope, and it is nonflammable and insoluble in most solvents. BP is very similar to graphite in terms of appearance, structure, and properties. Indeed, single layer 2D BP, called ―phosphorene", can be exfoliated just like graphene from graphite.[88] The BP/C nanocomposite synthesized by a particular ball milling unit has been investigated as SIB anode.[89] It was found that the composite can display impressive initial capacity at the level of approximately 1300 mA h g^{-1} (per total weight of the composite). Nevertheless, the capacity gradually deteriorates when the cycling is performed within the potential window of 2.0–0.01 V vs. Na/Na^{+}. In contrast, attractive stable cycling performances at the level of 350–400 mA h g^{-1} can be observed if the potential window is restricted to 2.0–0.33 V vs. Na/Na^{+}. The post-cycling SEM studies reveal that electrodes gradually disintegrate and delaminate from their current collectors when the electrochemical testing is conducted within wider potential windows. Such an effect is absent for the restricted potential windows, leading to stable cycling performances in these potential windows.

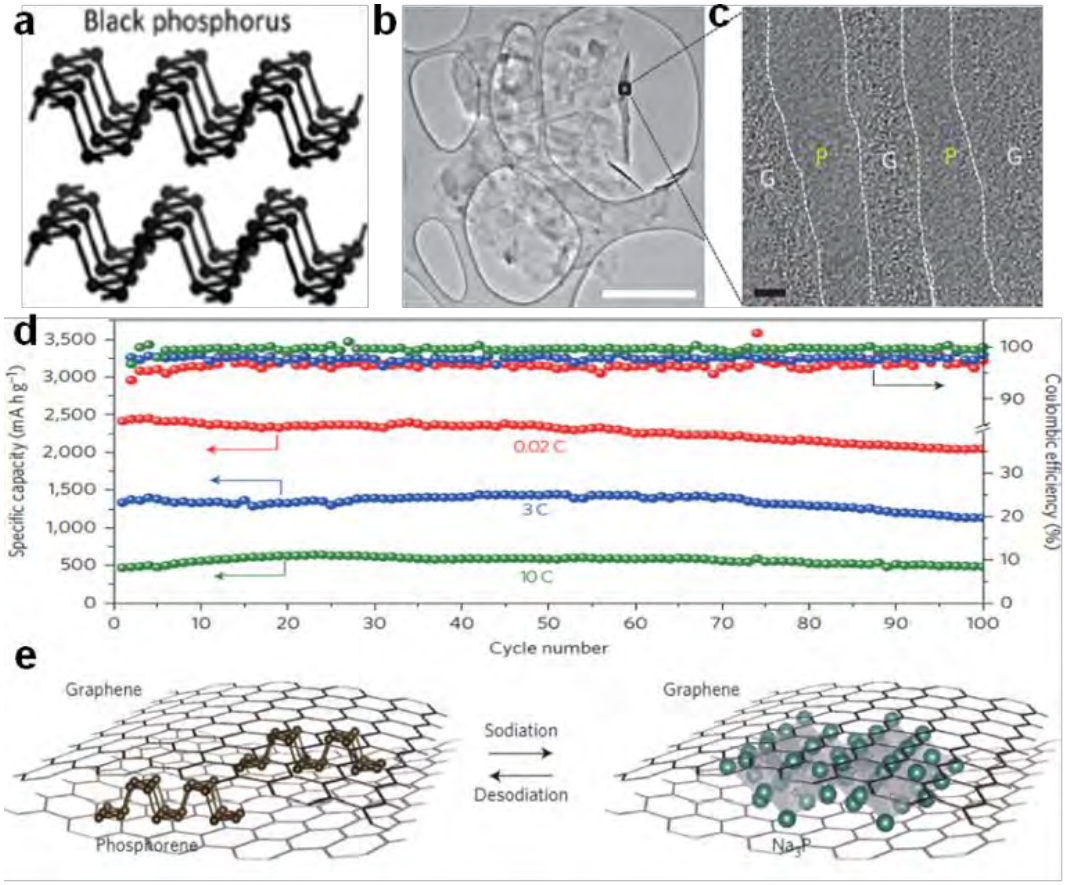

Figure 2.6 (a). Structure of black phosphorus. (b) TEM image of the phosphorene–graphene hybrid. Scale bar, 2 μm. (c) Cross-sectional HRTEM image of the phosphorene–graphene hybrid (the turned-up right edge in (b). Scale bar, 2 nm. (d). Reversible desodiation capacity and Coulombic efficiency for the first 100 galvanostatic cycles of the phosphorene/graphene (48.3 wt% P) anode tested at different current densities. (e). Structural evolution of the sandwiched phosphorene–graphene structure during sodiation.

Most recently, Cui et al. demonstrated a BP/graphene nanostructured composite, fabricated as a sandwich-structure comprising a few phosphorene layers alternating with several graphene layers (**Figure 2.6b,c**).[90] This phosphorene/graphene structure delivers an extremely high capacity of 2440 mA h g^{-1} at 50 mA g^{-1} and features 83% capacity retention for 100 cycles (**Figure 2.6d**). They discovered that

the graphene layers not only function as an electrical conductor but also serve as an elastic buffer for accommodating the volume expansion during cycling (**Figure 2.6e**).

Moreover, other alternatives are P based binary alloy compounds such as NiP_3,[91] FeP,[92] CoP,[93] and Sn-P (Sn_4P_3, SnP_3).[74-79] It was demonstrated that the full sodiation of M-P (M = Ni, Co, Fe) electrode leads to the formation of Na_3P electrode embedded with inactive M nanoparticles. Fast capacity fading was observed for these three samples, however, which was attributed to the agglomeration of active elements and the continuous pulverization of alloy anodes during the repeated sodiation/desodiation cycles because of the volume changes. If these elements can reform the starting compounds after Na extraction, the pulverization can be partially repaired, and the accumulation of pulverization can be terminated. An excellent example is a layered structure material, Sn_4P_3,[74-78] which exhibited a high reversible capacity of 718 mA h g^{-1}, with negligible capacity fading over 100 cycles.[74] Mechanism studies showed that Sn_4P_3 was first converted into Na_3P and Sn during sodiation through the conversion reaction, and the Sn was further sodiated to form $Na_{15}Sn_4$ after full sodiation through the alloy reaction. After desodiation, the Sn_4P_3 was recovered through the reversible conversion reaction (Sn_4P_3 + 9Na ↔ $3Na_3P$ + 4Sn). The excellent electrochemical performance of Sn_4P3 was attributed to synergistic reactions of the Sn and P components. On the other hand, the reversible reaction is critical for enhanced performance, because it repairs the cracks, damage, and aggregation of Sn particles that occur in the alloying process, 4Sn + 15Na ↔ $Na_{15}Sn_4$ during cycling, and hence terminates the pulverization.[77] Therefore, a so-called "self-healing" mechanism is demonstrated.[77] More recently, a new "self-healing" tin phosphide alloy, SnP_3, which exhibits much higher theoretical mass

capacity (1616 mA h g^{-1}) than the previously reported Sn_4P_3 (1133 mA h g^{-1}), has now been reported.[79] It provides a high capacity of ~810 mA h g^{-1} (~2820 mAh cm^{-3} for the composite including carbon) at 150 mA g^{-1}, maintains the same capacity for 150 cycles, and can retain 400 mA h g^{-1} even at 2560 mA g^{-1}.[79]

2.4 Conversion materials

In addition to carbon-based and alloy anode materials, conversion-type materials have also been studied as candidates for SIB anodes due to their high theoretical specific capacities. The conversion materials, usually including metal oxides and sulphides, can store Na^+ ions through a conversion reaction, or by a combined conversion reaction and Na-alloy reaction. In this section, we mainly focus on the typical application of two-dimensional (2D) active nanosheets and graphene-supported active materials as anodes in sodium storage.

2.4.1 Metal oxides

Bare oxide anodes usually suffer from bad rate capability and poor cyclability because of their extremely large volume changes during the sodium insertion-extraction process. One remedy is to use 2D nanosheets, since the nanosheets could provide short paths for ion transport. For example, ultrathin NiO nanosheets (4-5 nm in thickness) were synthesized via a facile solvothermal process followed by annealing in air (**Figure 2.7a**).[94] For sodium storage, the NiO nanosheets deliver a high reversible specific capacity of 299 mA h g^{-1} at a current density of 1 A g^{-1}, and the capacity still remains as high as 266 mA h g^{-1} after the 100th cycle (**Figure 2.7b**). Another strategy is to combine the oxide with graphene, which could enhance the electrical conductivity with its highly conductive network and accommodate the

volume changes to maintain the structural integrity. Various oxides, including Fe_2O_3,[95-97] Fe_3O_4,[98,99] Co_3O_4,[100] NiO,[101] CuO,[102] MoO_3,[103] Mn_3O_4,[104] and SnO_2,[105-111] have been combined with graphene to act as SIB anodes. Among them, SnO_2 is attracting special attention owing to its high theoretical reversible capacity (~782 mA h g^{-1}), moderate operating voltage, good performance, and low cost. For example, Wang et al. reported SnO_2 nanoparticles (5 nm) anchored on 2D rGO frameworks via a simple hydrothermal method, and the composite electrode delivered a stable capacity of 302 mA h g^{-1} over 100 cycles at a current density of 160 mA g^{-1}.[107] More recently, Chen et al. demonstrated that 3D SnO_2@G (SnO_2@3DG) showed better sodium storage performance than its 2D equivalent (SnO_2@2DG), which was attributed to the high surface area and 3D porous architecture.[110] They designed and achieved ultra-small SnO2 nanoparticles embedded in 3D graphene (SnO2@3DG) as anode for SIBs via assembling ice-templated 3DG with a tin source in a hydrothermal process (**Figure 2.7c**). Compared to the SnO_2@2DG anode, the SnO_2@3DG anode showed a higher reversible capacity of 432 mA h g^{-1} after 200 cycles at 100 mA g^{-1} (**Figure 2.7d**).[110]

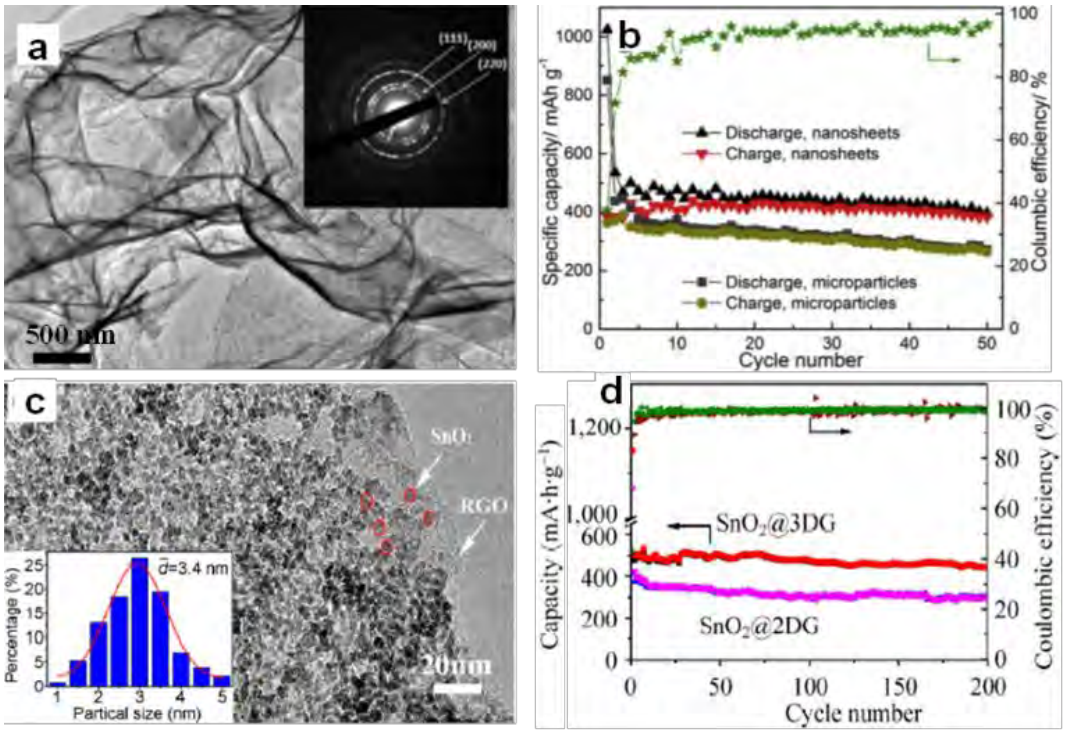

Figure 2.7 (a) High-resolution TEM (HRTEM) image of NiO nanosheets, with the inset the selected-area electron diffraction (SAED) pattern, (b) cycling performances of SIBs with NiO nanosheet electrode at 0.1 A g^{-1} and NiO microparticle electrode at 0.2 A g^{-1}. (c) TEM image of SnO_2@3DG. Inset: The corresponding particle size distribution calculated from 100 particles, (d) cycling performances of SnO_2@3DG and SnO_2@2DG at the current density of 100 mA g^{-1}.

2.4.2 Metal sulphides

Compared to the metal oxide anodes, metal sulphide anodes have several potential advantages: (1) greater gravimetric energy density due to the lower weight of the S atoms; (2) better structural stability due to the smaller volume changes; (3) higher initial cycling efficiency resulting from the better reversibility of Na_2S formed during sodiation than its counterpart oxide (Na_2O). Various metal sulphides, such as FeS_2,[112,113] FeS,[114] Ni_3S_2,[115] CoS,[116] MnS,[117] ZnS,[118] and Bi_2S_3,[119] have

shown attractive electrochemical performance in sodium batteries. Moreover, the discovery of the amazing properties of graphene has stimulated exploration of single- and few-layer structures of layered inorganic materials. Layered metal sulfides (MoS_2,[120-132] SnS_2,[134–140] SnS,[141–145] Sb_2S_3,[146-148] and WS_2[149,150]) have been extensively investigated as anode materials for sodium ion batteries. These layered metal sulfides typically have a unique layered structure with a large interlayer spacing, which makes them suitable for the intercalation of Na ions and allows compensation of the alloying/de-alloying volume changes. Nevertheless, the bulk materials still suffer from sluggish reaction kinetics and severe volume changes during the sodiation/desodiation process. Several strategies have been investigated to overcome these problems, including increasing the interlayer spacing, obtaining few-layer nanosheets, and making hybrids with graphene flakes.

One way to accommodate Li/Na ions is to increase the interlayer spacing to facilitate ion transport by creating a lower energy barrier to ion movement through the interlayer space.[120-123] For example, Hu et al. synthesized graphene-like MoS_2 nanoflowers with expanded interlayers, which showed high performance as anode material for SIBs.[120] The expanded and gradually exfoliated interlayers contribute to a lowering of the Na^+ insertion and extraction barrier, thus reducing the charge transfer resistance and providing more active sites for Na^+ storage (**Figure 2.8a,b**). Li et al. expanded the interlayer spacing of MoS_2 with insertion of an ionic conductor, polymer poly(ethylene oxide) (PEO), (**Figure 2.8c**).[121] The expanded interlayer PEO–MoS_2 nanocomposites exhibited improvements in capacity, rate performance, and diffusivity as Na-ion battery anode materials (**Figure 2.8d**).

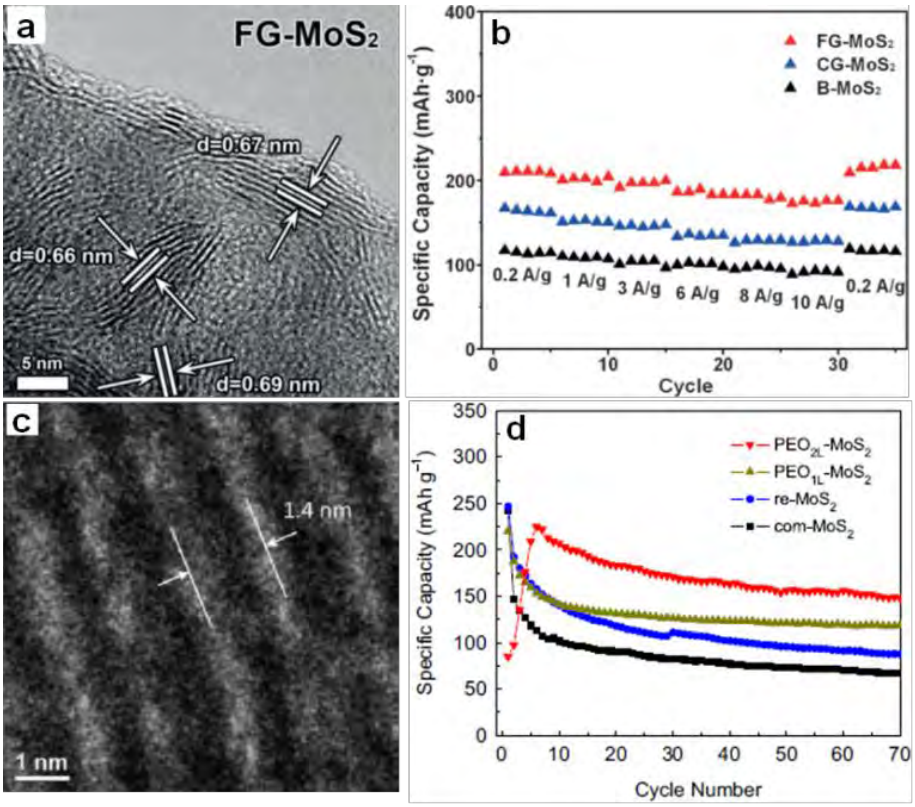

Figure 2.8 (a) HRTEM image of FG-MoS_2, (b) rate performance of the as-prepared graphene-like MoS_2 nanoflowers (FG-MoS_2), well-crystallized MoS_2 (labeled as CG-MoS_2), and bulk MoS_2 (B-MoS_2). (c) HRTEM image shows a cross-sectional view of the interlayer spacing in PEO2L–MoS_2 sample, (d) typical cycling behavior of com-MoS_2, re-MoS_2, PEO1L–MoS_2 and PEO2L–MoS_2 at 50 mA g^{-1}.

Another method is to obtain few-layer nanosheets, which facilitates the high-rate transportation of sodium ions due to the short diffusion paths provided by the ultrathin thickness. For example, ultrathin few-layer MoS_2 nanosheets (~10 nm in thickness) have been prepared through a simple and scalable exfoliation technique (**Figure 2.9a**).[123] When applied as anode material in SIBs, the MoS_2 nanosheet electrode demonstrated a high reversible specific capacity of 530 mA h g^{-1}, good cyclability, and high-rate performance (**Figure 2.9b**). 2D SnS_2 nanosheets (3-4 nm in thickness) were synthesized via a facile refluxing process and evaluated as an anode

material for SIBs (**Figure 2.9c**).[133] The SnS2 nanosheets delivered a high reversible specific capacity of 733 mA h g^{-1} at 0.1 A g^{-1}, and still exhibited high capacity retention of 647 mA h g^{-1} during the 50th cycle at 0.1 A g^{-1} (**Figure 2.9d**). The excellent electrochemical properties observed on the few layer nanosheets could be ascribed to the ultrathin nanosheet architecture, which is beneficial for achieving fast sodiation/desodiation reaction kinetics and accommodating electrode volume changes.

Furthermore, nanocomposites of few-layer sulfide and graphene or reduced graphene oxide (rGO) flakes for use as SIB anodes have been developed. Normally, the excellent performance of a 2D sulphide/graphene hybrid can be attributed to the 2D conductive channels provided by the graphene, the small lateral size and ultrathin nature of layered sulfide, the unique hybrid structure with enhanced electrolyte penetration, and the rapid Na-ion transport across the thin SEI layer. For example, Zhang et al. fabricated a unique plate-on-sheet structured SnS_2/rGO nanohybrid consisting of ultrafine (< 10 nm), few-layered (⩽ 7 layers) SnS_2 and few-layered rGO (< 6 layers) (**Figure 2.10a**).[134] The charge capacity at 100 mA g^{-1} increased from 178 mA h g^{-1} for bare SnS_2 to 649 mA h g^{-1} for SnS_2/rGO due to the dispersive and conductive effects of rGO. Moreover, the hybrid could yield high charge capacities of 524, 501, and 452 mA h g^{-1}, respectively, at high current densities of 1.6, 3.2, and 6.4 A g^{-1} (**Figure 2.10b**). Our recent results showed that the hexagonal-SnS_2 phase can also be transformed into the orthorhombic-SnS phase after an annealing step in argon atmosphere, and the thus transformed SnS shows sodium-ion storage performance that is enhanced over that of the original SnS_2.[142] As shown in **Figure 2.10c,d**, the SnS@graphene hybrid nanostructured composite, built from

two-dimensional SnS and graphene nanosheets as complementary building blocks, delivers an excellent specific capacity of 940 mA h g^{-1} and impressive rate capability of 492 and 308 mA h g^{-1} after 250 cycles at the current densities of 810 and 7290 mA g^{-1}, respectively, which is much better than the performance of the SnS_2@graphene hybrid.

More recently, our group successfully designed ultrafine SnS/SnO_2 heterostructures, where an interfacial amorphous carbon layer anchored SnS/SnO_2 heterostructures directly to graphene nanosheets.[145] When evaluated as an anode material for sodium-ion batteries, the C@SnS/SnO_2@Gr sample (where Gr is graphene), featured excellent performance and outstanding cycling stability at high rates, so that it had much superior performance compared to C@SnO_2@Gr, C@SnS@Gr, or a mechanical mixture of them. The boosted charge transfer in SnS/SnO_2 heterostructures is attributed to the heterostructure interface effect, which induces an electric field within the nanocrystals, giving them much lower ion-diffusion resistance and facilitating interfacial electron transport.

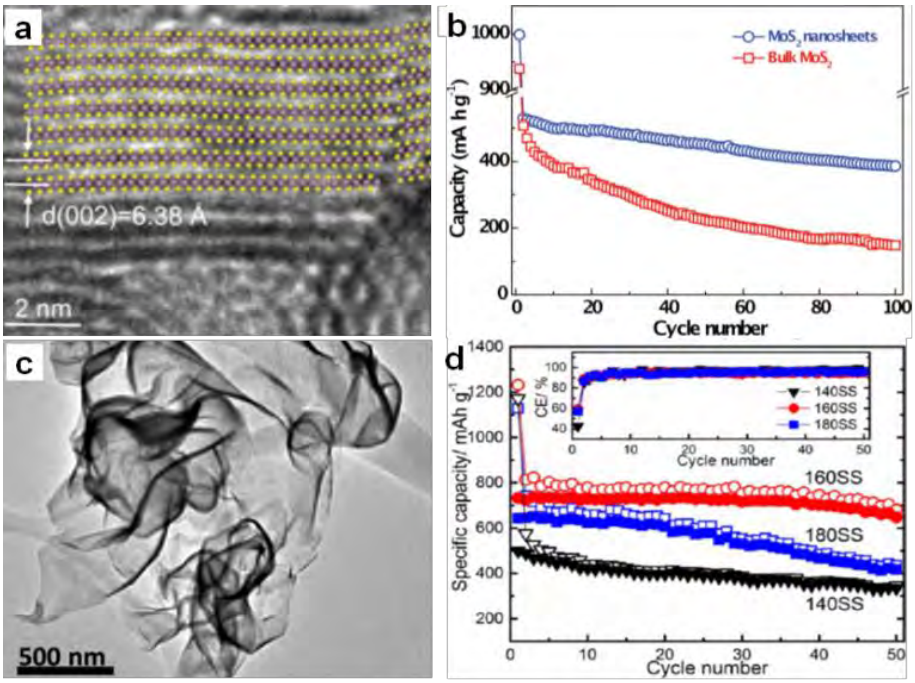

Figure 2.9 (a) Lattice resolved HRTEM image of MoS_2 nanosheet; (b) comparison of cycling performances of bulk and exfoliated MoS_2 nanosheet electrodes at 40 mA g-1 current density. Inset of (a) is the crystal structure of MoS_2 viewed along the b–axis. (c) HRTEM image of SnS_2 synthesized at 160 ℃, (d) Cycling performances of the cells with samples synthesized at 140 ℃ (140SS), 160 ℃ (160SS), and 180 ℃ (180SS), respectivelyu, at 0.1 A g^{-1}. Inset of (d) is the Coulombic efficiency (CE) of the three cells.

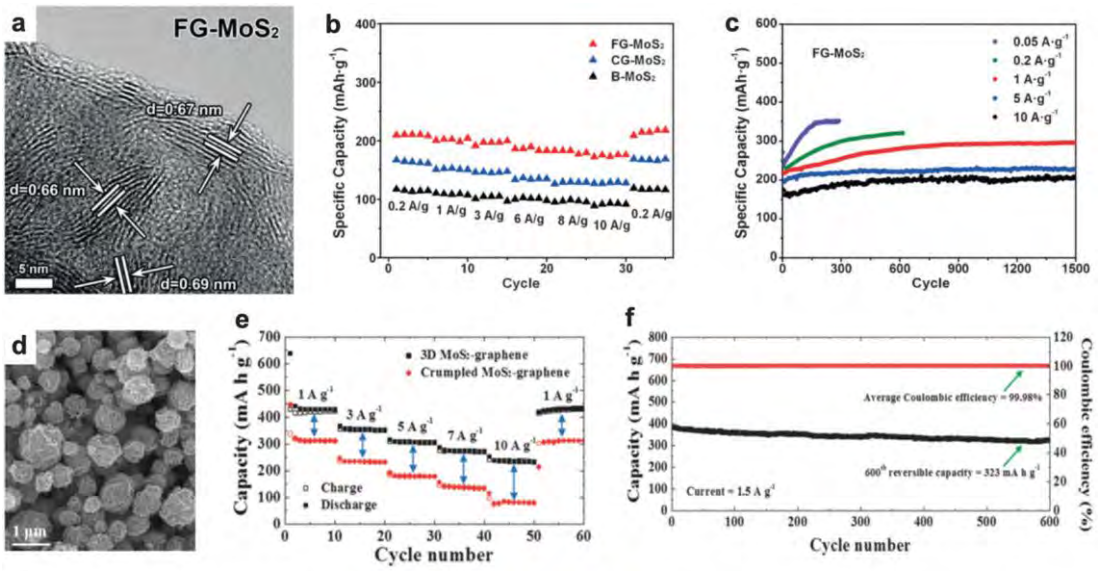

Figure 2.10 MoS_2–graphene composites for Na ion battery applications. (a) HRTEM image of graphene-like MoS_2 (FG-MoS_2) prepared by a hydrothermal method and having expanded interlayer distances. (b) SIB rate performance of FG-MoS_2, well-crystallized MoS_2 (CG-MoS_2) and bulk MoS_2 (B-MoS_2). (c) Cycling properties of the FG-MoS_2 material at different current densities. (d) SEM image of the 3D MoS_2–graphene microspheres prepared via ultrasonic spray pyrolysis. Rate capability (e) and cycling properties and Coulombic efficiencies (f) of the 3D MoS_2–graphene composite at 1.5 A g^{-1}.

2.5 Ti-based anode materials

With higher potentials for sodium insertion than those of carbon based materials, sodium plating can be avoided in Ti-based materials, which makes them also promising candidates for safe anodes in Li/Na-ion batteries. In the following sections, recent research achievements on titanium based anode materials are reviewed, with the focus on 2D architectures.

2.5.1 Conventional Ti-based materials

Various TiO_2 polymorphs, including amorphous TiO_2,[151] anatase,[152–157] rutile,[158,159] and TiO_2(B),[160-162] have been introduced as efficient anode materials for Na ion storage. For example, Xiong et al.[151] investigated amorphous TiO_2 grown on a 2D Ti substrate. Interestingly, capacity increased gradually with charge–discharge cycling, presumably owing to the amorphous structure. A recent study, however, showed that anatase TiO_2 presented better capacity than mixed anatase/rutile TiO_2 or amorphous TiO_2@C.[156] It was revealed that the anatase TiO_2 crystal structure supplies 2D diffusion paths for Na-ion intercalation and more accommodation sites. The TiO_2(B) has an open-channel structure and has been regarded as the most promising polymorph of TiO_2 for LIBs due to its outstanding Li-ion mobility and superior electrochemical performance.[162] The reported electrochemical performance of TiO_2(B) in SIBs is not as good as in LIBs, however, which is possibly due to the poor electrical and ionic conductivity of TiO_2.[160-162] Enhancing the electrical conductivity of TiO_2(B) will most likely lead to improved electrochemical performance in SIBs. More recently, Chen et.al reported Na^+ intercalation pseudocapacitance in TiO^2 (consisting of 76.9% TiO^2(B) and 23.1% anatase TiO^2)/graphene nanocomposite, which enabled high-rate capability and long cycle life in a sodium-ion battery. In their study, the hybridization of graphene with TiO_2 nanocrystals provided a more feasible channel at the graphene–TiO_2 interface for sodium intercalation/de-intercalation with a much lower energy barrier, thus leading to fast charge storage and long-term cyclability (**Figure** 11a-f).[163]

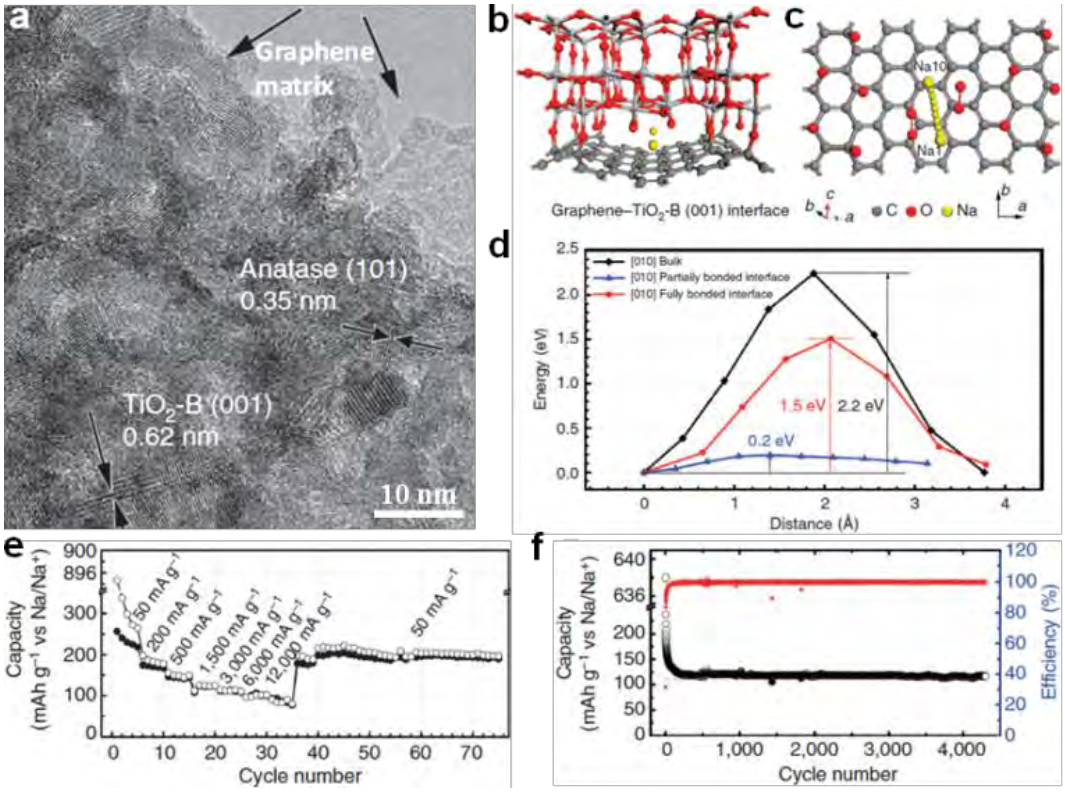

Figure 2.11 (a) High-resolution TEM image of TiO_2/graphene composite, clear lattices with spacings of 0.62 and 0.35nm are assigned to the (001) plane of TiO_2-B and (101) plane of anatase, respectively. (b) Illustration of the partially bonded graphene-TiO_2-B (001) interface. (c) Top-view of a, illustrating the Na diffusion path along the [010] direction from Na1 to Na10 sites. (d) Migration activation energy of the Na^+ ion diffusing along the [010] direction in bulk TiO_2-B, fully bonded and partially bonded graphene-TiO_2-B (001) interface calculated with DFT. (e) Rate performance at various current densities from 50 to 12,000 mA g^{-1}. (f) Long-term cycling performance at a current density of 500 mA g^{-1} (~2 C).

Spinel-type $Li_4Ti_5O_{12}$ (LTO) is well known as a „zero-strain" anode material for long-life stationary lithium-ion batteries [164]. Recently, the suitability of $Li_4Ti_5O_{12}$ as an anode for Na-ion batteries has been revealed.[165-170] The intercalation mechanism has been proposed to involve three-phase separation, which is very different from

that observed in LIBs.[165] It was also reported that the sodium storage properties of LTO in SIBs are size- dependent, demonstrating that nanostructuring could lead to a significant increase in the specific capacity.[166] Recently, LTO nanosheets were fabricated via a simple hydrothermal reaction and found to deliver a reversible capacity of up to 145 mA h g^{-1} at 1 C, with 91% capacity retention after 400 cycles.[168] Based on a scan rate-dependent cyclic voltammetry test, a pseudocapacitive charge storage mechanism has been proposed for Na-ion storage in pristine LTO electrode, which contributes to the excellent rate capacity and high cycling stability of LTO electrodes for SIBs. More recently, ultra-small MoS_2 quantum dots (QDs) were exploited as surface sensitizers to boost the electrochemical properties of 2D LTO nanosheets.[170] The LTO/MoS_2 composite was prepared by anchoring ultra-small MoS_2 QDs on 2D LTO nanosheets by using a simple and effective assembly technique (**Figure 2.12a**). Impressively, such zero-dimensional (0D)/2D heterostructure composites possess enhanced surface-controlled Na storage behavior. During sodiation, a high capacity of 91 mAh g^{-1} at the rate of 5 C and superior capacity retention, with 101 mAh g^{-1} after 200 cycles at the rate of 2 C, were achieved (**Figure 2.12b,c**).

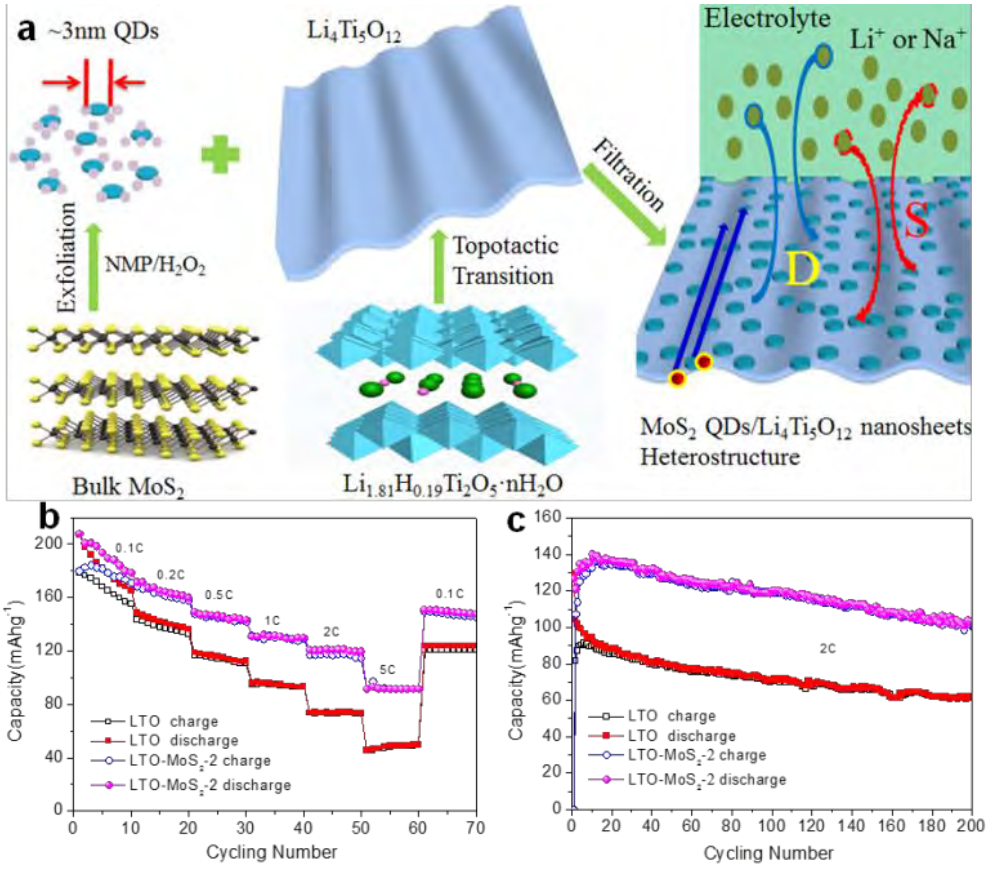

Figure 2.12 (a) Schematic showing the synthesis of the heterostructure composite composed of ultrasmall MoS2 QDs and ultrathin LTO nanosheets. (b) Corresponding rate capabilities at different current rates from 0.1 C to 5 C for the LTO-MoS2-2 composite and LTO nanosheets electrodes. (c) Long cycling performance of the LTO-MoS2-2 composite and LTO nanosheets as NIBs electrode at a rate of 2 C.

Sodium titanate ($Na_2Ti_3O_7$), with a lower discharge plateau and abundant raw material resources, is another promising titanium-based anode material for SIBs.[171-175] The $Na_2Ti_3O_7$ structure consists of zigzag layers of titanium and oxygen octahedra, in which up to 3.5 Na ions per formula unit can be intercalated into the interlayer space and easily exchanged, leading to a capacity of 310 mA h g^{-1}. Pan et al.[174] found that layered $Na_2Ti_3O_7$ shows a reversible capacity of 85 mAh g^{-1} (0.5 C) after 100 cycles. At the same time, the $Na_2Ti_3O_7$ also suffers from structural

distortion, which may account for the low Coulombic efficiency and continuous capacity fading of $Na_2Ti_3O_7$ electrodes.[173,174] One strategy is to engineer $Na_2Ti_3O_7$ nanostructures to improve the conductivity and stability issues. It was reported that surface engineered $Na_2Ti_3O_7$ nanotube arrays directly grown on Ti substrates showed enhanced performance.[175] The fabrication of the nanotube arrays involves the hydrothermal growth of $Na_2Ti_3O_7$ nanotubes, surface deposition of a thin layer of TiO_2, and subsequent sulfidation (**Figure 2.13a,b**). The resulting nanoarrays deliver high reversible capacities of 221 mAh g^{-1} at 0.2 C (with 1 C equal to 2 Na insertions into $Na_2Ti_3O_7$ in 1 h, i.e., 177 mA g^{-1}) and exhibit superior cycling efficiency and rate capability, retaining 101 mAh g^{-1} at 5 C (885 mA g^{-1}) over 1000 continuous cycles (**Figure 2.13c**). The improved performance is associated with the lower charge transfer resistance and the better interfacial kinetics enabled by the surface modification.

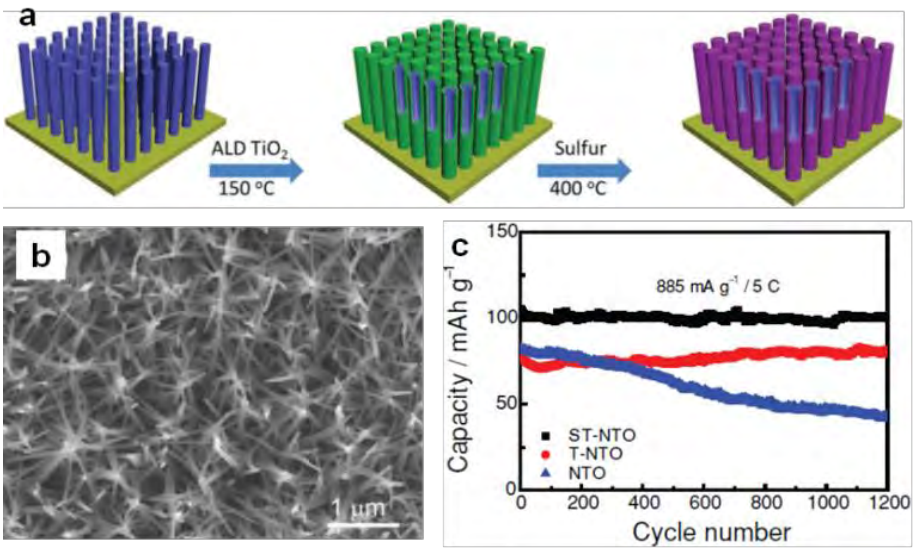

Figure 2.13 (a) Schematic illustration of the fabrication of surface engineered $Na_2Ti_3O_7$ nanotube arrays grown on Ti foil. (b) SEM images of ST-NTO. (c) Comparison of cycling stability at a rate of 5 C.

Transition metal phosphates, such as $NaTi_2(PO_4)_3$ (NTP),[176-181] have also been studied so far. NTP has an open three-dimensional sodium superionic conductor (NASICON)-type framework structure and high Na^+ conductivity, which are decisive advantages for electrochemical storage kinetics. Its low electronic conductivity has hindered practical applications by low capacity release and poor cycling stability. An effective conductive network created by combining NTP with electrically conductive materials will improve its performance, however. A novel architecture consisting of nanosized porous NTP particles embedded in a microsized 3D graphene network has been designed by Wu et al. (**Figure 2.14a-d**).[178] Such architecture synergistically combines the advantages of a 3D graphene network and of 0D porous nanoparticles. It greatly increases the electron/ion transport kinetics and endows the electrode with structural integrity, leading to attractive electrochemical performance, as reflected by its high rate-capability (112 mAh g^{-1} at 1 C, 105 mAh g^{-1} at 5 C, 96 mAh g^{-1} at 10 C, 67 mAh g^{-1} at 50 C) and long cycle-life (capacity retention of 80% after 1000 cycles at 10 C) (**Figure 2.14e**). It also should be noted that NTP has a relatively high voltage plateau at ~ 2.1 V vs. Na^+/Na, which sacrifices energy density to some extent when compared to other anodes (e.g., hard carbon). This redox reaction takes place, however, at potentials that are much more positive than the H2 evolution potential of water in the Na2SO4 electrolyte (< -1.2 V vs. Ag/AgCl). Thus this disadvantage has turned into a benefit in neutral aqueous solutions, excluding the decomposition of water.[179-181]

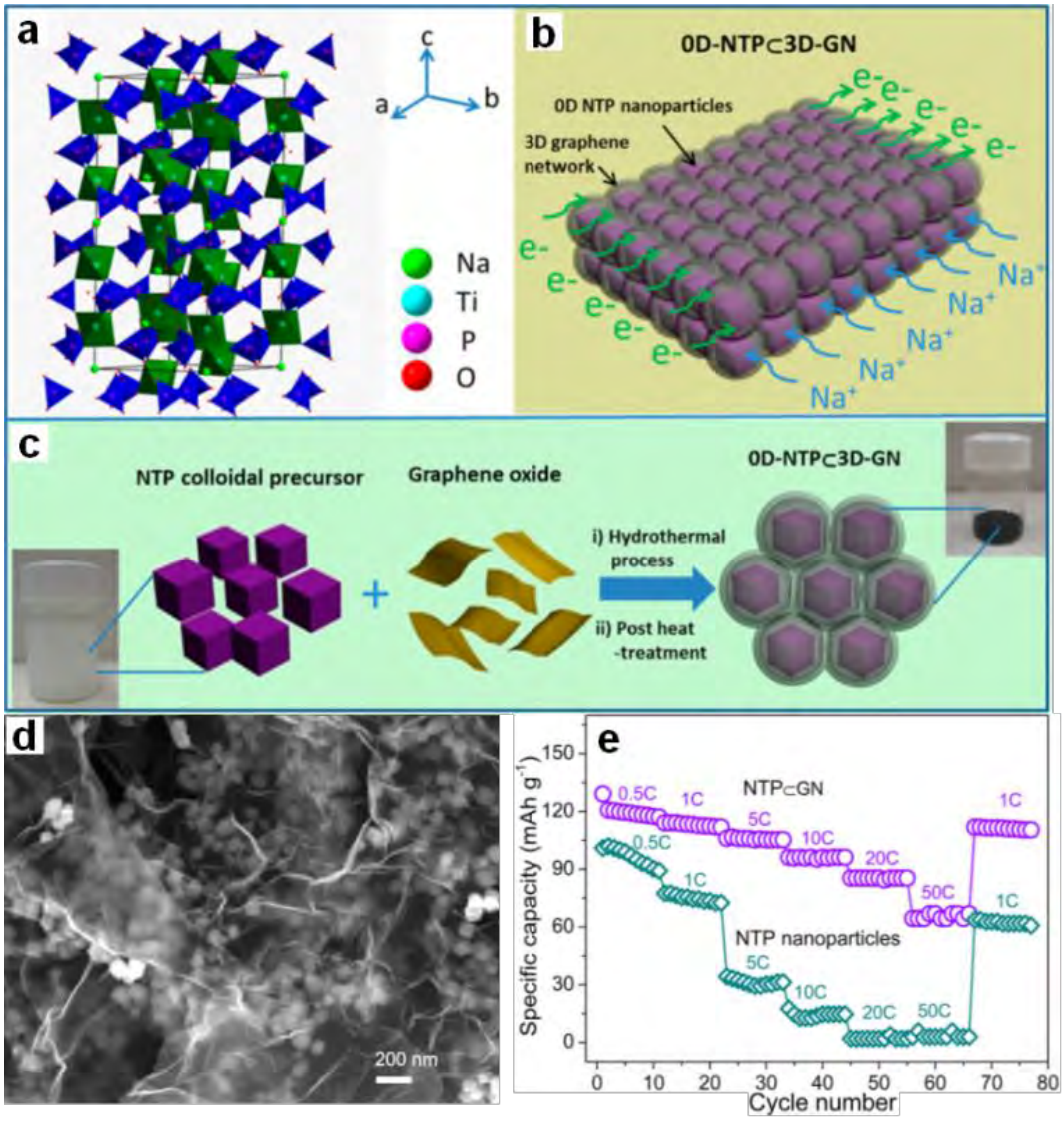

Figure 2.14 (a) Crystal structure of the NTP phase. (b) Schematic illustration of 0D-NTP⊂3D-GN, showing that 0D porous NTP nanoparticles are embedded in 3D graphene network. (c) Schematic synthesis of 0D-NTP⊂3D-GN, including the two steps of hydrothermal process and post heat treatment. (d) SEM images of NTP⊂GN, (e) Rate performance and capacity retention ability of the NTP⊂GN and NTP particle electrodes.

2.5.2 New Ti-based materials: MXene nanosheets

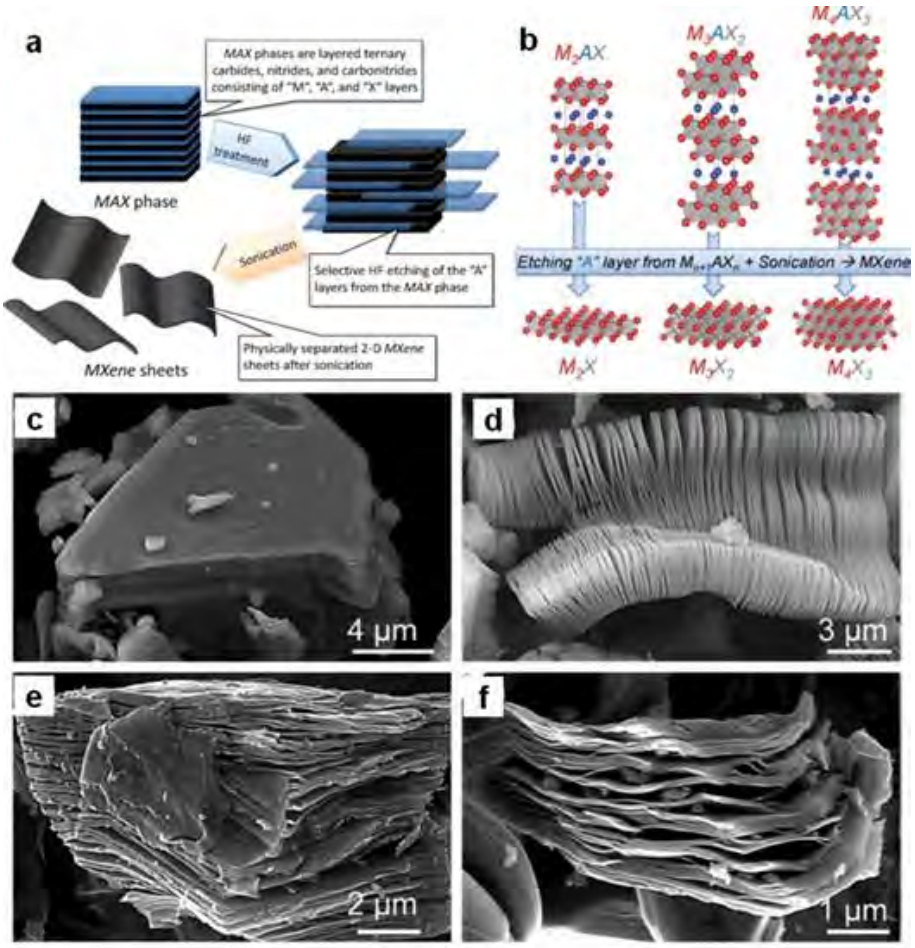

Figure 2.15 (a) Schematic describing the synthesis process of MXenes from MAX phases. (b) Structure of MAX phases and the corresponding MXenes. Secondary electron SEM micrographs for (c) Ti_3AlC_2 particle before treatment, which is typical of unreacted MAX phases, (d) Ti_3AlC_2 after HF treatment, (e) Ti_2AlC after HF treatment, (f) Ta_4AlC_3 after HF treatment.

Recently, a new group of 2D materials called MXenes ($M_{n+1}X_nT_x$: M = Ti, V, Nb, etc.; X = C, N; n = 1−3; Tx is the functional termination group) has been discovered, and their potential applications have been demonstrated in rechargeable batteries,

including sodium ion batteries.[182-187] MXenes are produced by selective etching of the A element from the MAX phases (**Figure 2.15 a,b**). The latter are so-called because of their composition: namely, $M_{n+1}AX_n$, where M is an early transition metal, A is mainly a group IIIA or IVA (i.e., groups 13 or 14) element, X is C and/or N, and n = 1, 2, or 3. The MAX phase structure can be described as 2D layers of early transition metal carbides and/or nitrides –glued" together with an A element (**Figure 2.15b**). As example, the SEM image of Ti_2AlC after the HF treatment (**Figure 2.15d**) confirms successful exfoliation of individual particles, which is similar to that of exfoliated Ti_3AlC_2 (**Figure 2.15e**) or Ta_4AlC_3 (**Figure 2.15f**), where the layers are clearly separated from each other compared to the unreacted powder (**Figure 2.15c**). Sonication of the treated powders resulted in the separation of 2D sheets.

These MXene nanosheets have rich surface chemistries and high electronic conductivities and exhibit prominent performances in many applications that range from sensors and electronic device materials to catalysts in the chemical industry, and electrochemical energy storage materials.[182] In particular, the family of MXene nanosheets is an emerging electrode material capable of the electrochemical reaction with various ions including sodium.[184-187] The screened MXene materials can provide a theoretical capacity of 190–288 mA h g^{-1} by accommodating two alkali ions per formula unit. They also exhibit an activation barrier of 0.1–0.2 eV for ionic motion, suggesting that this kind of material is promising for high-power applications. [184-185] In particular, the MXene $Ti_3C_2T_x$ has been demonstrated as an anode material for sodium-ion batteries and found to show good capacity retention over 1000 cycles as well as excellent rate capability (**Figure 2.16a-f**).[186,187] Detailed

analyses demonstrate that $Ti_3C_2T_x$ undergoes expansion of the interlayer distance during the first sodiation, whereby desolvated Na^+ is intercalated/deintercalated reversibly. Meanwhile, the Na^+ intercalation/deintercalation during the electrochemical reaction is not accompanied by any substantial structural change (**Figure 2.16g**).[187] Thus MXene $Ti_3C_2T_x$ is very promising as SIB anode due to its structural stability and excellent performance.

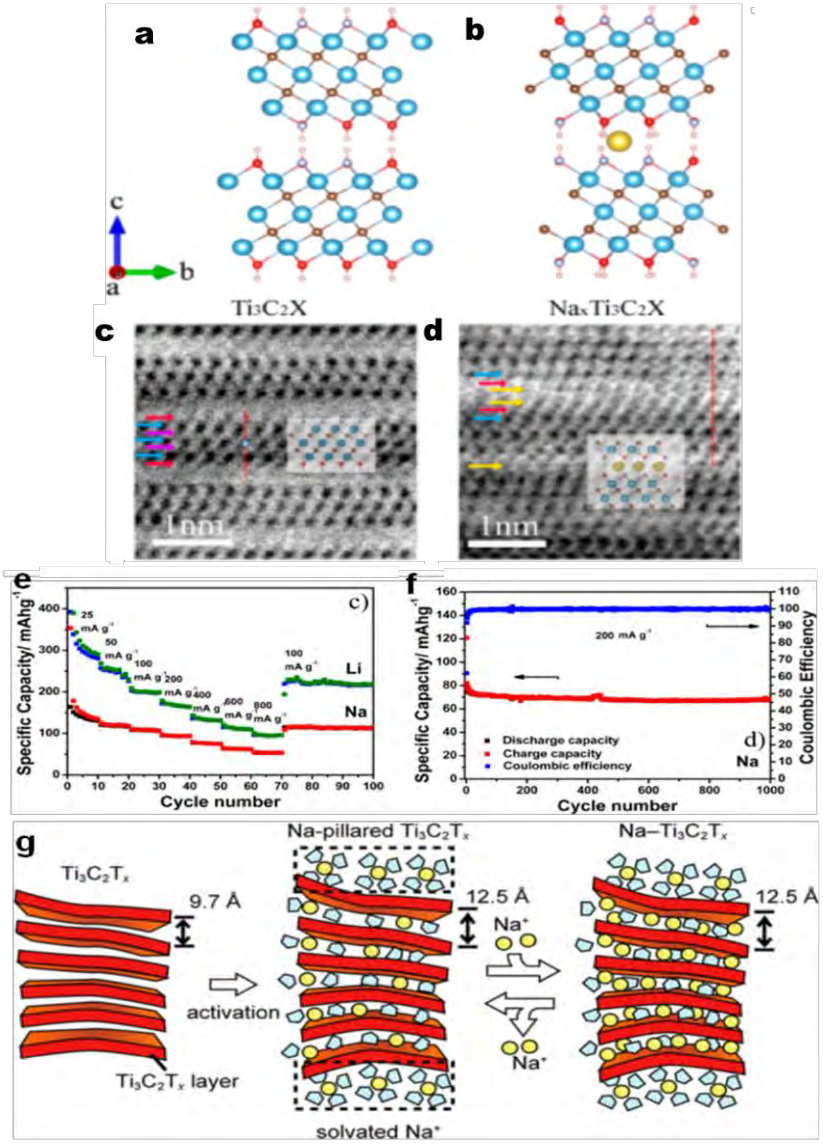

Figure 2.16 Optimized geometries of Ti_3C_2X (a) and $Na_xTi_3C_2X$ (b) from side view. (c) ABF image of Ti_3C_2X observed along the a/b axis, two C atomic layers (labeled

with purple arrows) interleave into three Ti-atomic layers (labeled with blue arrows) with a sequence of Ti(s)−C−Ti(c)−C−Ti(s), forming an edge-shared TiC_6 octahedral stacking. (d) ABF images of Ti_3C_2X electrodes upon Na intercalation with cutoff potential of 0.0 V. The Ti_3C_2X nanosheets exhibit excellent rate performance (e) and long-term cycling stability (f). Schematic illustration for the proposed mechanism of Na^+ insertion into Ti_3C_2X (g).

2.6 Electrolytes

The electrolyte is a key component for battery, since it is directly associated with the formation of solid electrolyte interphase (SEI) films and electron transfer during the energy storage process.

Firstly, the electrolyte should be intrinsically safe, have as low toxicity as possible and meet cost requirements for the targeted applications. All these features are intrinsically dependent on the nature of the salts, the solvent(s) and the potential use of additives. As compiled for electrolytes, a good electrolyte should exhibit: (1) good ionic conductivity, (2) a large electrochemical window, (3) no reactivity towards the cell components, and (4) a large thermal stability window.

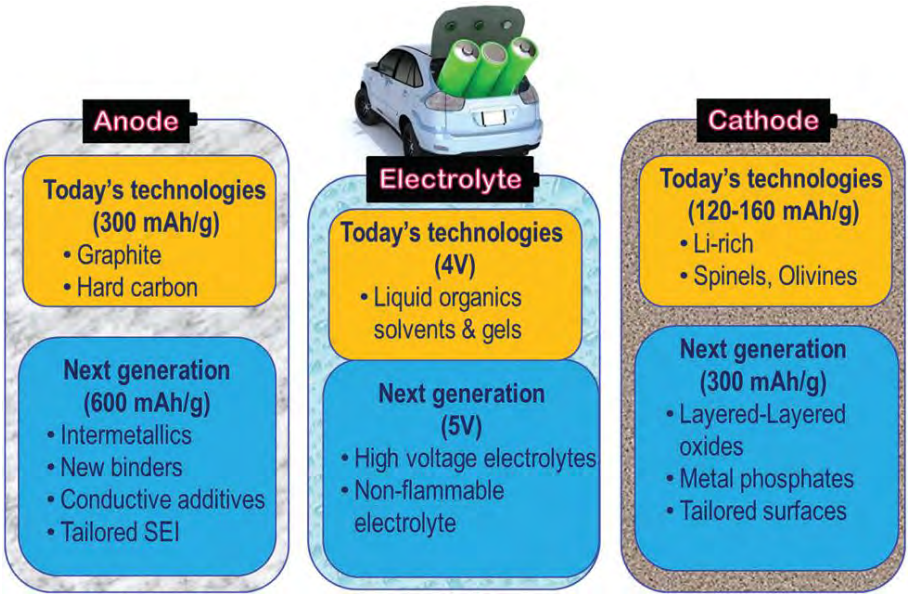

Figure 2.17 Schematic diagram showing the current and future technologies for batteries based on the main components.

2.6.1 Solvents

The solvents used in the electrolyte also need to comply with most of the prerequisites set for the salts.

In addition, the presence of polar groups to dissolve sufficient amounts of salt is a compulsory feature. The families of organic solvents investigated are much the same as those used for LIBs. The electron acceptor/donor capability of a solvent is important as it will influence the electrochemical stability window.

2.6.2 Additives

The limited amount of additives that are needed originates from the preferred reactions taking place at the electrolyte/electrode interfaces. Typical interface/surface actions of an additive are modifying the SEI, increasing the wetting of the surface,

and protecting against overcharging events by redox shuttles that can accommodate the overcharge.

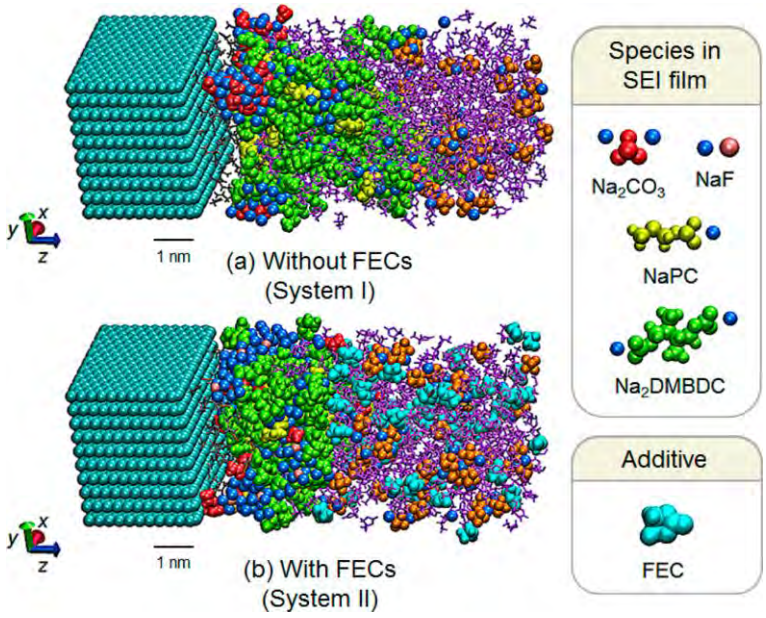

Figure 2.18 Schematic illustration of the SEI films and $NaPF_6$–PC electrolyte visualized from the carbon anode surface: (a) without and (b) with FEC molecules.

Fluoroethylene carbonate (FEC) can be an efficient electrolyte additive to improve the SEI film formation in the battery system (**Figure 2.18**). To investigate the mechanism, atomistic reaction simulations in propylene carbonate (PC)-based electrolyte with and without FEC additives were performed, and they successfully reproduced experimental observations such as the smaller irreversible capacity and the smoother SEI film in FEC-added electrolyte.[188] The study showed that intact FEC molecules can improve SEI film formation so as to enhance the network formation of organic species, owing to the large electronegativity of their fluorine atoms.

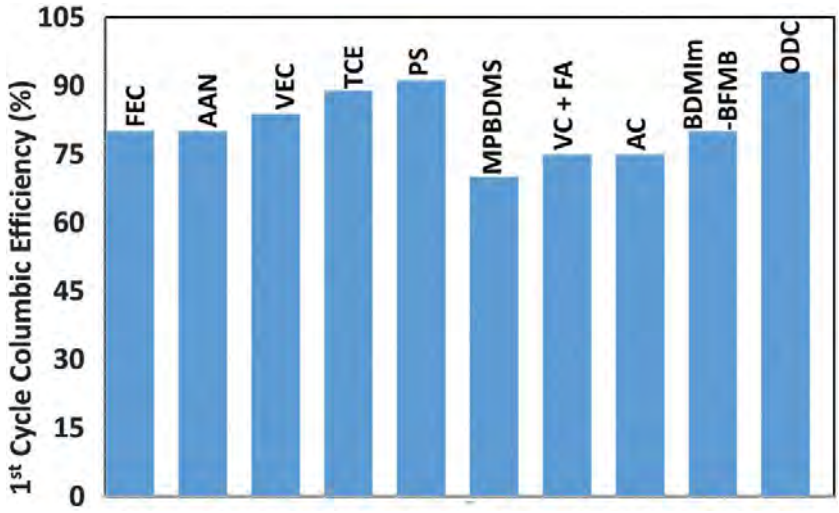

Figure 2.19 First cycle coulombic efficiency of selected additives, used for PC based electrolytes, on carbon electrodes.[fluoroethylene carbonate (FEC), acrylic acid nitrile (AAN), vinyl ethylene carbonate (VEC), Tetrachloroethylene (TCE), 1,3-propane sultone (PS), Methyl phenyl bis-methoxydiethoxysilane (MPBMDS), vinylene carbonate (VC), Fluoroalkyl (FA), allyl cyanide (AC), 1-butyl-2,3-dimethylimidazolium bis(fluoromalonato)-borate (BDMIm BFMB), (4R,5R)-dimethyl 2-oxo-1,3-dioxolane-4,5-dicarboxylate (ODC)]. [189]

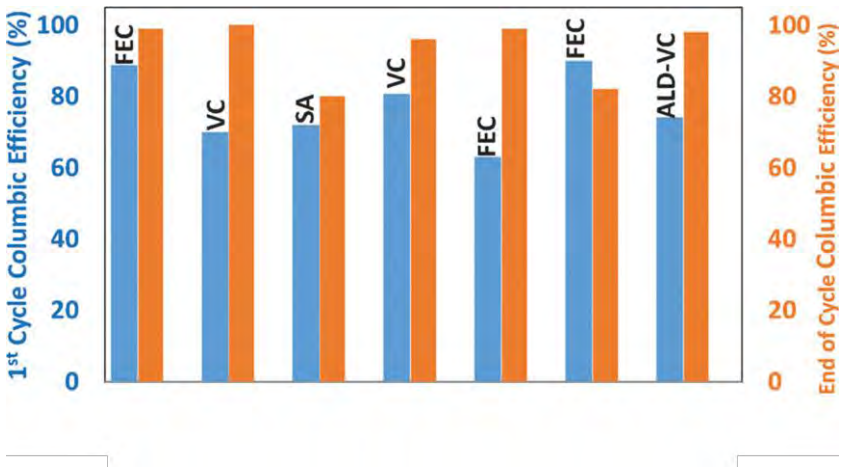

Figure 2.20 First cycle and afterwards cycle coulombic efficiency of selected additives used for the silicon electrode.

In addition to the film forming additives, there are other additives that protect the electrode under abuse conditions such as overcharging. In addition to overcharge, other safety issues include mechanical abuse, such as crushing and penetration, and thermal abuse, such as heat generation, combustion, and flame attack.[189]

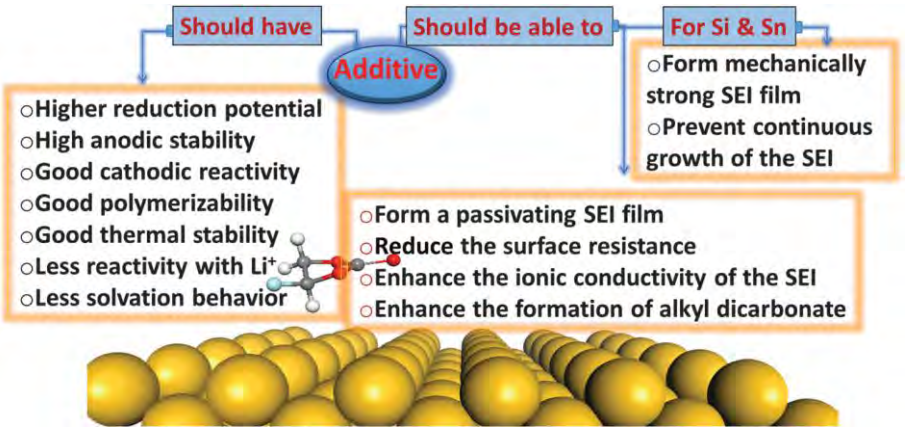

Figure 2.21 Summary of the properties of additives for anode materials.

2.7 Summary and future prospects

Undoubtedly, the most difficult issue facing the demonstration of Na-ion batteries is how to achieve high capacity and good cycle life. With the ability to prepare various 2D nanosized materials, combined with advanced nanofabrication techniques, current research on the preparation of SIB anode materials depends on not only the choice of functional active material components, crystal phase, and structure, but also on the spatial organization/assembly, surface exposure, interaction between the individual components, and geometric properties of the composites. By using 2D nanomaterials with unique properties, planar hybrids, porous hierarchical architectures, and vertically stacked heterostructures have been prepared, which have shown impressive properties, enhanced functions, and improved performance. Even

so, there are still many tough challenges to overcome before high energy storage systems based on SIBs can be achieved in the future.

Firstly, it should be admitted that the study of 2D-based functional composite anodes for the sodium-ion battery is still in its infant stage. The underlying mechanisms of Na storage in 2D materials are still unclear, so more understanding with respect to the surface functionalities/defects, the hierarchical electrode structures, and kinetic transport at the electrode/electrolyte interface is needed to achieve better electrochemical performance. For example, the high surface area of graphene and its composites may lead to large irreversible capacity loss in the first cycle, and porous graphene-based composites exhibit small tap densities and consequently, an unfavorably low volumetric capacity. Secondly, the compatibility of each of the components in the 2D materials needs to be further improved, and heterostructure interface problems still exist due to the weak interaction forces in the hybrid structure, although not in heterostructures with crystalline bonding. Meanwhile, comparisons between amorphous and crystalline materials might prove to be an interesting area. The charge storage mechanism of such amorphous materials is still vague, and explanations are leaning more towards pseudocapacitive behavior instead. Thirdly, some special conditions are often needed to obtain novel 2D structures, which often lead to a high-cost synthesis. Thus, controlled low-cost and large-scale synthesis methods for novel 2D nanostructures need to be developed by integrating various advanced technologies, since the high cost of electrode materials significantly restricts scalable production and application. Fourthly, design of new and old high theoretical capacity electrode materials (e.g. alloy materials) in2D form is likely to be the next performance growth point for SIB anode materials. Since the

discovery of graphene, many other 2D materials have been coming into the spotlight. They form a very large family that includes hexagonal boron nitride, transition metal dichalcogenides, metal oxides, common clays, and the recently discovered transition metal carbides, as well as silicene, germanene, phosphorene, and stanene. All of them have great promise and will inevitably cause a new peak in SIB research. On the other hand, most of the materials used for hybridization with 2D anode materials are inorganic nanomaterials, such as alloy metals, metal oxides, and carbonaceous nanomaterials. One of the future directions lies in the combination of 2D anode materials with polymers to create 2D-based polymer composites for a wide range of applications. Finally, in addition to the materials, further studies are needed on electrolytes, additives, and binders, which can greatly influence the electrode performance. With continuous endeavors by all parties concerned, it is expected that the high performance 2D materials and composites can be applied in commercialized high-performance SIBs in the near future.

2.8 References

[1] M. Armand and J.-M. Tarascon, Nature, 2008, 451, 652.

[2] Z. G. Yang, J. L. Zhang, M. C. W. Kintner-Meyer, X. C. Lu, D. W. Choi, J. P. Lemmon and J. Liu, Chem. Rev., 2011, 111, 3577.

[3] J. Liu, J. G. Zhang, Z. G. Yang, J. P. Lemmon, C. Imhoff, G. L. Graff. L. Y. Li, J. Z. Hu, C. M. Wang, J. Xiao, G. Xia, V. V. Viswanathan, S. Baskaran, V. Sprenkle, X. L. Li, Y. Y. Shao and B. Schwenzer, Adv. Funct. Mater., 2013, 23, 929.

[4] S. W. Kim, D. H. Seo, X. H. Ma, G. Cede and K. Kang, Adv. Energy Mater., 2012, 2, 710.

[5] H. L. Pan, Y. S. Hu and L. Q. Chen, Energy Environ. Sci., 2013, 6, 2338.

[6] N. Yabuuchi, K. Kubota, M. Dahbi and S. Komaba, Chem. Rev., 2014, 114, 11636.

[7] R. C. Asher, J. Inorg. Nucl. Chem., 1959, 10, 238.

[8] P. Ge and M. Fouletier, Solid State Ionics, 1988, 28-30, 1172.

[9] M. M. Doeff, Y. Ma, S. J. Visco and L. C. De Jonghe, J. Electrochem. Soc., 1993, 140, L169.

[10] I. A. Udod, H. B. Orman and V. K. Genchel, Carbon, 1994, 32, 101.

[11] B. Jache and P. Adelhelm, Angew. Chem., Int. Ed., 2014, 53, 10169.

[12] H. Kim, J. Hong, Y. U. Park, J. Kim, I. Hwang and K. Kang, Adv. Funct. Mater., 2014, 25, 534.

[13] Y. Wen, K. He, Y. J. Zhu, F. D. Han, Y. H. Xu, I. Matsuda, Y. Ishii, J. Cumings and C. S. Wang, Nat. Commun., 2014, 5, 4033.

[14] D. A. Stevens and J. R. Dahn, J. Electrochem. Soc., 2000, 147, 1271.

[15] D. A. Stevens and J. R. Dahn, J. Electrochem. Soc., 2001, 148, A803.

[16] R. Alcántara, J. M. Jiménez-Mateos, P. Lavela and J. L. Tirado, Electrochem. Commun., 2001, 3, 639.

[17] S. Komaba, W. Murata, T. Ishikawa, N. Yabuuchi, T. Ozeki, T. Nakayama, A. Ogata, K. Gotoh and K. Fujiwara, Adv. Funct. Mater., 2011, 21, 3859.

[18] K. L. Hong, L. Qie, R. Zeng, Z. Q. Yi, W. Zhang, D. Wang, W. Yin, C. Wu, Q. J. Fan, W. X. Zhang and Y. H. Huang, J. Mater. Chem. A, 2014, 2, 12733.

[19] Y. L. Cao, L. F. Xiao, M. L. Sushko, W. Wang, B. Schwenzer, J. Xiao, Z. M. Nie, L. V. Saraf, Z. G. Yang and J. Liu, Nano Lett., 2012, 12, 3783.

[20] X. F. Luo, C. H. Yang, Y. Y. Peng, N. W. Pu, M. D. Ger, C. T. Hsieh and J. K. Chang, J. Mater. Chem. A, 2015, 3, 10320.

[21] J. Liu and X. W. Liu, Adv. Mater., 2012, 24, 4097.

[22] L. L. Peng, Y. Zhu, D. H. Chen, R. S. Ruoff and G. H. Yu, Adv. Energy Mater., 2016, 10.1002/aenm.201600025.

[23] X. Huang, X. Qi, F. Boey and H. Zhang, Chem. Soc. Rev., 2012, 41, 666.

[24] R. Raccichini, A. Varzi, S. Passerini and B. Scrosati, Nat. Mater., 2015, 14, 271.

[25] Y. X. Wang, S. L. Chou, H. K. Liu and S. X. Dou, Carbon, 2013, 57, 202.

[26] X. S. Zhou, X. S. Zhu, X. Liu, Y. Xu, Y. X. Liu, Z. H. Dai and J. C. Bao, J. Phys. Chem. C, 2014, 118, 22426.

[27] D. Datta, J. W. Li and V. B. Shenoy, ACS Appl. Mater. Interfaces, 2014, 6, 1788.

[28] J. P. Paraknowitsch and A. Thomas, Energy Environ. Sci., 2013, 6, 2839.

[29] H. G. Wang, Z. Wu, F. L. Meng, D. L. Ma, X. L. Huang, L. M. Wang and X. B. Zhang, ChemSusChem, 2013, 6, 56.

[30] T. Z. Yang, T. Qian, M. F. Wang, X. W. Shen, N. Xu, Z. Z. Sun and C. L. Yan, Adv. Mater., 2016, 28, 539.

[31] H. W. Song, N. Li, H. Cui and C. X. Wang, Nano Energy, 2014, 4, 81.

[32] F. H. Yang, Z. A. Zhang, K. Du, X. X. Zhao, W. Chen, Y. Q. Lai and J. Li, Carbon, 2015, 91, 88.

[33] X. L. Wang, G. Li, F. M. Hassan, J. D. Li, X. Y. Fan, R. Batmaz, X. C. Xiao, Z. W. Chen, Nano Energy, 2015, 15, 746.

[34] K. Tang, L. Fu, R. J. White, L. Yu, M. M. Titirici, M. Antonietti and J. Maier, Adv. Energy Mater., 2012, 2, 873.

[35] S. Wenzel, T. Hara, J. Janek and P. Adelhelm, Energy Environ. Sci., 2011, 4, 3342.

[36] Z. Guan, H. Liu, B. Xu, X. Hao, Z. X. Wang and L. Q. Chen, J. Mater. Chem. A, 2015, 3, 7849.

[37] J. T. Xu, M. Wang, N. P. Wickramaratne, M. Jaroniec, S. X. Dou, and L. M. Dai, Adv. Mater., 2015, 27, 2042.

[38] J. Ding, H. L. Wang, Z. Li, A. Kohandehghan, K. Cui, Z. W. Xu, B. Zahiri, X. H. Tan, E. M. Lotfabad, B. C. Olsen and D. Mitlin, ACS Nano, 2013, 7, 11004.

[39] Y. Yan, Y. X. Yin, Y. G. Guo and L. J. Wan, Adv. Energy Mater., 2014, 4, 1301584.

[40] V. L. Chevrier and G. Ceder, J. Electrochem. Soc., 2011, 158, A1011.

[41] L. D. Ellis, B. N.Wilkes, T. D. Hatchard and M. N. Obrovac, J. Electrochem. Soc., 2014, 161, A416.

[42] Y. L. Xu, E. Swaans, S. Basak, H. W. Zandbergen, D. M. Borsa and F. M. Mulder, Adv. Energy Mater., 2016, 6, doi: 10.1002/aenm.201501436

[43] D. W. Su, S. X. Dou and G. X. Wang, Nano Energy, 2015, 12, 88.

[44] L. Baggetto, J. K. Keum, J. F. Browning and G. M. Veith, Electrochem. Commun., 2013, 34, 41.

[45] A. Kohandehghan, K. Cui, M. Kupsta, J. Ding, E. M. Lotfabad, W. P. Kalisvaart and D. Mitlin, Nano Lett., 2014, 14, 5873.

[46] L. D. Ellis, T. D. Hatchard and M. N. Obrovac, J. Electrochem. Soc., 2012, 159, A1801.

[47] J. W. Wang, X. H. Liu, S. X. Mao and J. Y. Huang, Nano Lett., 2012, 12, 5897.

[48] A. Darwiche, C. Marino, M. T. Sougrati, B. Fraisse, L. Stievano, and L. Monconduit, J. Am. Chem. Soc., 2012, 134, 20805.

[49] J. F. Qian, Y. Chen, L. Wu, Y. L. Cao, X. P. Ai and H. X. Yang, Chem. Commun., 2012, 48, 7070.

[50] J. F. Qian, X. Y. Wu, Y. L. Cao, X. P. Ai, and H. X. Yang, Angew. Chem., Int. Ed., 2013, 52, 4633.

[51] Y. J. Kim, Y. Park, A. Choi, N. S. Choi, J. S. Kim, J. S. Lee, J. H. Ryu, S. M. Oh, and K. T. Lee, Adv. Mater., 2013, 25, 3045.

[52] L. Baggetto, P. Ganesh, R. P. Meisner, R. R. Unocic, J.-C. Jumas, C. A. Bridges and G. M. Veith, J. Power Sources, 2013, 234, 48.

[53] M. He, K. Kravchyk, M. Walter and M. V. Kovalenko, Nano Lett., 2014, 14, 1255.

[54] H. L. Zhu, Z. Jia, Y. C. Chen, N. Weadock, J. Y. Wan, O. Vaaland, X. G. Han, T. Li and L. B. Hu, Nano Lett., 2013, 13, 3093.

[55] Y. H. Liu, Y. H. Xu, Y. J. Zhu, J. N. Culver, C. A. Lundgren, K. Xu and C. S. Wang, ACS Nano, 2013, 7, 3627.

[56] X. Q. Xie, K. Kretschmer, J. Q. Zhang, B. Sun, D. W. Su and G. X. Wang, Nano Energy, 2015, 13, 208.

[57] B. Luo, T. F. Qiu, D. L. Ye, L. Z. Wang and L. J. Zhi, Nano Energy, 2016, 22, 232.

[58] H. S. Hou, M. J. Jing, Y. C. Yang, Y. Zhang, W. X. Song, X. M. Yang, J. Chen, Q. Y. Chen and X. B. Ji, J. Power Sources, 2015, 284, 227.

[59] K. F. Li, D. W. Su, H. Liu and G. X. Wang, Electrochimica Acta, 2015, 177, 304.

[60] C. Nithya and S. Gopukumar, J. Mater. Chem. A, 2014, 2, 10516.

[61] X. L. Zhou, Y. R. Zhong, M. Yang, M. Hu, J. P. Wei and Z. Zhou, Chem. Commun., 2014, 50, 12888.

[62] L. Y. Hu, X. S. Zhu, Yichen Du, Y. F. Li, X. S. Zhou and J. C. Bao, Chem. Mater., 2015, 27, 8138.

[63] J. S. Thorne, R. A. Dunlap and M. N. Obrovaa, Electrochimica Acta, 2013, 112, 133.

[64] J. Liu, Y. R. Wen, P. A. van Aken, J. Maier and Y. Yu, Nano Lett., 2014, 14, 6387.

[65] E. D. Jackson, S. Green, and A. L. Prieto, ACS Appl. Mater. Interfaces, 2015, 7, 7447.

[66] L. Baggetto, E. Allcorn, R. R. Unocic, A. Manthiram and G. M. Veith, J. Mater. Chem. A, 2013, 1, 11163.

[67] L. Baggetto, K. J. Carroll, H. Y. Hah, C. E. Johnson, D. R. Mullins, R. R. Unocic, J. A. Johnson, Y. S. Meng, and G. M. Veith, J. Phys. Chem. C, 2014, 118, 7856.

[68] L. Baggetto, H. Y. Hah, C. E. Johnson, C. A. Bridges, J. A. Johnson and G. M. Veith, Phys. Chem. Chem. Phys., 2014, 16, 9538.

[69] L. F. Xiao, Y. L. Cao, J. Xiao, W. Wang, L. Kovarik, Z. M. Nie and J. Liu, Chem. Commun., 2012, 48, 3321.

[70] I. T. Kim, S. O. Kim and A. Manthiram, J. Power Sources, 2014, 269, 848.

[71] L. W. Ji, M. Gu, Y. Y. Shao, X. L. Li, M. H. Engelhard, B. W. Arey, W. Wang, Z. M. Nie, J. Xiao, C. M. Wang, J. G. Zhang and J. Liu, Adv. Mater., 2014, 26, 2901.

[72] L. W. Ji, W. D. Zhou, V. Chabot, A. P. Yu, and X. C. Xiao, ACS Appl. Mater. Interfaces, 2015, 7, 24895.

[73] L. Li, K. H. Seng, D. Li, Y. Y. Xia, H. K. Liu and Z. P. Guo, Nano Research, 2014, 7, 1466.

[74] J. F. Qian, Y. Xiong, Y. L. Cao, X. P. Ai and H. X. Yang, Nano Lett., 2014, 14, 1865.

[75] Y. Kim, Y. Kim, A. Choi, S. Woo, D. Mok, N. S. Choi, Y. S. Jung, J. H. Ryu, S. M. Oh and K. T. Lee, Adv. Mater., 2014, 26, 4139.

[76] W. J. Li , S. L. Chou, J. Z. Wang, J. H. Kim, H. K. Liu and S. X. Dou, Adv. Mater., 2014, 26, 4037.

[77] J. F. Mao, X. L. Fan, C. Luo, and C. S. Wang, ACS Appl. Mater. Interfaces, 2016, 8, 7147.

[78] J. Liu, P. Kopol, C. Wu, P. A. van Aken, J. Maier and Y. Yu, Energy Environ. Sci., 2015, 8, 3531.

[79] X. L. Fan, J. F. Mao, Y. J. Zhu, C. Luo, L. M. Suo, T. Gao, F. D. Han, S. C. Liou and C. S. Wang, Adv. Energy Mater., 2015, 5, 1500174.

[80] Y. B. Zhao and A. Manthiram, Chem. Mater., 2015, 27, 3096.

[81] N. Yabuuchi, Y. Matsuura, T. Ishikawa, S. Kuze, J. Y. Son, Y. T. Cui, H. Oji and S. Komaba, ChemElectroChem, 2014, 1, 580.

[82] W. J. Li, S. L. Chou, J. Z. Wang, H. K. Liu and S. X. Dou, Nano Lett., 2013, 13, 5480.

[83] Y. J. Zhu, Y. Wen, X. L. Fan, T. Gao, F. D. Han, C. Luo, S. C. Liou and C. S. Wang, ACS Nano, 2015, 9, 3254.

[84] B. Y. Ruan, J. Wang, D. Q. Shi, Y. F. Xu, S. L. Chou, H. K. Liu and J. Z. Wang, J. Mater. Chem. A, 2015, 3, 19011.

[85] J. X. Song, Z. X. Yu, M. L. Gordin, S. Hu, R. Yi, D. H. Tang, T. Walter, M. Regula, D. Choi, X. L. Li, A. Manivannan and D. H. Wang, Nano Lett., 2014, 14, 6329.

[86] L. K. Pei, Q. Zhao, C. C. Chen, J. Liang and J. Chen, ChemElectroChem, 2015, 2, 1652.

[87] C. Zhang, X. Wang, Q. F. Liang, X. Z. Liu, Q. H. Weng, J. W. Liu, Y. J. Yang, Z. H. Dai, K. J. Ding, Y. Bando, J. Tang and D. Golberg, Nano Lett., 2016, 16, 2054.

[88] L. Z. Kou, C. F. Chen and S. C. Smith, J. Phys. Chem. Lett., 2015, 6, 2794.

[89] T. Ramireddy, T. Xing, M. M. Rahman, Y. Chen, Q. Dutercq, D. Gunzelmann and A. M. Glushenkov, J. Mater. Chem. A, 2015, 3, 5572.

[90] J. Sun, H. W. Lee, M. Pasta, H. T. Yuan, G. Y. Zheng, Y. M. Sun, Y. Z. Li and Y. Cui, Nat. Nanotechnology, 2015, 10, 980.

[91] J. Fullenwarth, A. Darwiche, A. Soares, B. Donnadieu and L. Monconduit, J. Mater. Chem. A, 2014, 2, 2050.

[92] W. J. Li, S. L. Chou, J. Z. Wang, H. K. Liu and S. X. Dou, Chem. Commun., 2015, 51, 3682.

[93] W. J. Li, Q. R. Yang, S. L. Chou, J. Z. Wang and H. K. Liu, J. Power Sources, 2015, 294, 627.

[94] W. P. Sun, X. H. Rui, J. X. Zhu, L. H. Yu, Y. Zhang, Z. C. Xu, S. Madhavi and Q. Y. Yan, J. Power Sources, 2015, 274, 755.

[95] Z. L. Jian, B. Zhao, P. Liu, F. J. Li, M. B. Zheng, M. W. Chen, Y. Shi and H. S. Zhou, Chem. Commun., 2014, 50,1215.

[96] X. J. Liu, T. Q. Chen, H. P. Chu, L. Y. Niu, Z. Sun, L. K. Pan and C. Q. Sun, Electrochimica Acta, 2015, 166, 12.

[97] Z. J. Zhang, Y. X. Wang, S. L. Chou, H. J. Li, H. K. Liu and J. Z. Wang, J. Power Sources, 2015, 280, 107.

[98] Y. Q. Fu, Q. L. Wei, X. Y. Wang, G. X. Zhang, H. B. Shu, X. K. Yang, A. C. Tavares and S. H. Sun, RSC Adv., 2016, 6, 16624.

[99] S. h. Zhang, W. J. Li, B. Tan, S. L. Chou, Z. Li and S. X. Dou, J. Mater. Chem. A, 2015, 3, 4793.

[100] Y. G. Liu, Z. Y. Cheng, H. Y. Sun, H. Arandiyan, J. P. Li and M. Ahmad, J. Power Sources, 2015, 273, 878.

[101] F. Zou, Y. M. Chen, K. W. Liu, Z. T. Yu, W. F. Liang, S. M. Bhaway, M. Gao and Y. Zhu, ACS Nano, 2016, 10, 377.

[102] X. J. Li, A. L. Hector and J. R. Owen, J. Phys. Chem. C, 2014, 11, 29568.

[103] J. F. Huang, Z. W. Xu, L. Y. Cao, Q. L. Zhang, H. B. Ouyang and J. Y. Li, Energy Technology, 2015, 3, 1108.

[104] Y. Z. Jiang, M. J. Hu, D. Zhang, T. Z. Yuan, W. P. Sun, B. Xu and M. Yan, Nano Energy, 2014, 5, 60.

[105] D. W. Su, H. J. Ahn and G. X. Wang, Chem. Commun., 2013, 49, 3131.

[106] S. Li, Y. Z. Wang, J. X. Qiu, M. Ling, H. H. Wang, W. Martens, S.Q. Zhang, RSC Adv., 2014, 4, 50148.

[107] Y. X. Wang, Y. G. Lim, M. S. Park, S. L. Chou, J. H. Kim, H. K. Liu, S. X. Dou and Y. J. Kim, J. Mater. Chem. A, 2014, 2, 529.

[108] Y. D. Zhang, J. Xie, S. C. Zhang, P. Y. Zhu, G. S. Cao and X. B. Zhao, Electrochimica Acta, 2015, 151, 8.

[109] X. Q. Xie, D. W. Su, J. Q. Zhang, S. Q. Chen, A. K. Mondal and G. X. Wang, Nanoscale, 2015, 7, 3164.

[110] L. K. Pei, Q. Jin, Z. Q. Zhu, Q. Zhao, J. Liang and J. Chen, Nano Research, 2015, 8, 184.

[111] X. Q. Xie, S. Q. Chen, B. Sun, C. Y. Wang, G. X. Wang, ChemSusChem, 2015, 8, 2948.

[112] Z. Hu, Z. Q. Zhu, F. Y. Cheng, K. Zhang, J. B. Wang, C. C. Chen and J. Chen, Energy Environ. Sci., 2015, 8, 1309.

[113] Y. J. Zhu, X. L. Fan, L. M. Suo, C. Luo, T. Gao, and C. S. Wang, ACS Nano, 2016, 10, 1529.

[114] Y. X. Wang, J. P. Yang, S. L. Chou, H. K. Liu, W. X. Zhang, D. Y. Zhao and S. X. Dou, Nat. Commun., 2015, 6, 8689.

[115] 115 T. S. Wang, P. Hu, C. J. Zhang, H. P. Du, Z. H. Zhang, X. G. Wang, S. G. Chen, J. W. Xiong and G. L. Cui, ACS Appl. Mater. Interfaces, 2016, 8, 7811.

[116] S. J. Peng, X. P. Han, L. L. Li, Z. Q. Zhu, F. Y. Cheng, M. Srinivansan, S. Adams and S. Ramakrishna, Small, 2016, 12, 1359.

[117] X. J. Xu, S. M. Ji, M. Z. Gu and J. Liu, ACS Appl. Mater. Interfaces, 2015, 7, 20957.

[118] W. Qin, D. S. Li, X. J. Zhang, D. Yan, B. W. Hu and L. K. Pan, Electrochimica Acta, 2016, 191, 435.

[119] W. P. Sun, X. H. Rui, D. Zhang, Y. Z. Jiang, Z. Q. Sun, H. K. Liu and S. X. Dou, J. Power Sources, 2016, 309, 135.

[120] Z. Hu, L. X. Wang, K. Zhang, J. B. Wang, F. Y. Cheng, Z. L. Tao and J. Chen, Angew. Chem., Int. Ed., 2014, 53, 12794.

[121] Y. F. Li, Y. L. Liang, F. C. R. Hernandez, H. D. Yoo, Q. Y. An and Y. Yao, Nano Energy, 2015, 15, 453.

[122] S. Zhang, X. B. Yu, H. L. Yu, Y. J. Chen, P. Gao, C. Y. Li and C. L. Zhu, ACS Appl. Mater. Interfaces, 2014, 6, 21880.

[123] D. W. Su, S. X. Dou and G. X. Wang, Adv. Energy Mater., 2015, 5, 1401205.

[124] G. S. Bang, K. W. Nam, J. Y. Kim, J. Shin, J. W. Choi and S. Y. Choi, ACS Appl. Mater. Interfaces, 2014, 6, 7084.

[125] 125 M. W. Xu, F. L. Yi, Y. B. Niu, J. L. Xie, J. K. Hou, S. G. Liu, W. H. Hu, Y. T. Li and C. M. Li, J. Mater. Chem. A, 2015, 3, 9932.

[126] T. S. Sahu and S. Mitra, Sci. Rep., 2015, 5, 12571.

[127] L. David, R. Bhandavat and G. Singh, ACS Nano, 2014, 8, 1759.

[128] X. Q. Xie, T. Makaryan, M. Q. Zhao, K. L. Van Aken, Y. Gogotsi and G. X. Wang, Adv. Energy Mater., 2016, 6, 1502161.

[129] S. H. Choi, Y. N. Ko, J. K. Lee, Y. C. Kang, Adv. Funct. Mater., 2015, 25, 1780.

[130] Y. X. Wang, S. L. Chou, D. Wexler, H. K. Liu and S. X. Dou, Chem. Eur. J., 2014, 20, 9607.

[131] X. Q. Xie, Z. M. Ao, D. W. Su, J. Q. Zhang and G. X. Wang, Adv. Funct. Mater., 2015, 25, 1393.

[132] C. B. Zhu, X. K. Mu, P. A. van Aken, Y. Yu and J. Maier, Angew. Chem., Int. Ed., 2014, 53, 2152.

[133] W. P. Sun, X. H. Rui, D. Yang, Z. Q. Sun, B. Li, W. Y. Zhang, Y. Zong, S. Madhavi, S. X. Dou and Q. Y. Yan, ACS Nano, 2015, 9, 11371.

[134] Y. D. Zhang, P. Y. Zhu, L. L. Huang, J. Xie, S. C. Zhang, G. S. Cao and X. B. Zhao, Adv. Funct. Mater., 2015, 25, 481.

[135] C. Liu, H. Y. Kang, L. F. Jiao, C. C. Chen, K. Z. Cao, Y. J. Wang and H. T. Yuan, Nanoscale, 2015, 7, 1325.

[136] B. H. Qu, C. Z. Ma, G. Ji, C. H. Xu, J. Xu, Y. S. Meng, T. H. Wang and J. Y. Lee, Adv. Mater., 2014, 26. 3854.

[137] P. V. Prikhodchenko, D. Y. W. Yu, S. K. Batabyal, V. Uvarov, J. Gun, S. Sladkevich, A. A. Mikhaylov, A. G. Medvedev and O. Lev, J. Mater. Chem. A, 2014, 2, 8431.

[138] Y. Jiang, M. Wei, J. K. Feng, Y. C. Ma and S. L. Xiong, Energy Environ. Sci., 2016, 9, 1430.

[139] X. Q. Xie, D. W. Su, S. Q. Chen, J. Q. Zhang, S. X. Dou and G.X. Wang, Chem. Asian J., 2014, 9, 1611.

[140] J. J. Wang, C. Luo, J. F. Mao, Y. J. Zhu, X. L. Fan, T. Gao, A. C. Mignerey and C. S. Wang, ACS Appl. Mater. Interfaces, 2015, 7, 11476.

[141] L. Wu, H. Y. Lu, L. F. Xiao, J. F. Qian, X. P. Ai, H. X. Yang and Y. L. Cao, J. Mater. Chem. A, 2014, 2, 16424.

[142] T. F. Zhou, W. K. Pang, C. F. Zhang, J. P. Yang, Z. X. Chen, H. K. Liu and Z. P. Guo, ACS Nano, 2014, 8, 8323.

[143] P. K. Dutta, U. K. Sen and S. Mitra, RSC Adv., 2014, 4, 43155.

[144] S. H. Choi and Y. C. Kang, Nano Research, 2015, 8, 1595.

[145] Y. Zheng, T. F. Zhou, C. F. Zhang, J. F. Mao, H. K. Liu and Z. P. Guo, Angew. Chem., Int. Ed., 2016, 55, 3408.

[146] D. Y. W. Yu, P. V. Prikhodchenko, C. W. Mason, S. K. Batabyal, J. Gun, S. Sladkevich, A. G. Medvedev and O. Lev, Nat. Commun., 2013, 4, 2922.

[147] Y. B. Zhao and A. Manthiram, Chem. Commun., 2015, 51, 13205.

[148] H. S. Hou, M. J. Jing, Z. D. Huang, Y. C. Yang, Y. Zhang, J. Chen, Z. B. Wu and X. B. Ji, ACS Appl. Mater. Interfaces, 2015, 7, 19362.

[149] S. H. Choi and Y. C. Kang, Nanoscale, 2015, 7, 3965.

[150] D. W. Su, S. X. Dou and G. X. Wang, Chem. Commun., 2014, 50, 4192.

[151] H. Xiong, M. D. Slater, M. Balasubramanian, C. S. Johnson and T. Rajh, J. Phys. Chem. Lett., 2011, 2, 2560.

[152] L. M. Wu, D. Buchholz, D. Bresser, L.G. Chagas and S. Passerini, J. Power Sources, 2014, 251, 379.

[153] K. T. Kim, G. Ali, K. Y. Chung, C. S. Yoon, H. Yashiro, Y. K. Sun, J. Lu, K. Amine and S. T. Myung, Nano Lett., 2014, 14, 416.

[154] Y. Xu, E. M. Lotfabad, H. L. Wang, B. Farbod, Z. W. Xu, A. Kohandehghan and D. Mitlin, Chem. Commun., 2013, 49, 8973.

[155] S. M. Oh, J. Y. Hwang, C. S. Yoon, J. Lu, K. Amine, I. Belharouak and Y. K. Sun, ACS Appl. Mater. Interfaces, 2014, 6, 11295.

[156] D. W. Su, S. X. Dou and G. X. Wang, Chem. Mater., 2015, 27, 6022.

[157] L. M. Wu, D. Bresser, D. Buchholz, G. A. Giffin, C. R. Castro, A. Ochel, S. Passerini, Adv. Energy Mater., 2015, 5, 1401142.

[158] Y. Zhang, X. L. Pu, Y. C. Yang, Y. R. Zhu, H. S. Hou, M. J. Jing, X. M. Yang, J. Chen and X. B. Ji, Phys. Chem. Chem. Phys., 2015, 17, 15764.

[159] H. Usui, S. Yoshioka, K. Wasada, M. Shimizu and H. Sakaguchi, ACS Appl. Mater. Interfaces, 2015, 7, 6567.

[160] L. M. Wu, D. Bresser, D. Buchholz and S. Passerini, J. Electrochem. Soc., 2015, 16, A3052.

[161] J. P. Huang, D. D. Yuan, H. Z. Zhang, Y. L. Cao, G. R. Li, H. X. Yang and X. P. Gao, RSC Advances, 2013, 3, 12539.

[162] M. Fehse and E. Ventosa, ChemPlusChem, 2015, 80, 785.

[163] C. Chen, Y. Wen, X. Hu, X. Ji, M. Yan, L. Mai, P. Hu, B. Shan and Y. H. Huang, Nat. Commun., 2015, 6, 6929.

[164] T. F. Yi, S. Y. Yang and Y. Xie, J. Mater. Chem. A, 2015, 3, 5750.

[165] Y. Sun, L. Zhao, H. Pan, X. Lu, L. Gu, Y.-S. Hu, H. Li, M. Armand, Y. Ikuhara, L. Chen and X. Huang, Nat. Commun., 2013, 4, 1870.

[166] X. Q. Yu, H. L. Pan, W. Wan, C. Ma, J. M. Bai, Q. P. Meng, S. N. Ehrlich, Y. S. Hu and X. Q. Yang, Nano Lett., 2013, 13, 4721.

[167] G. Hasegawa, K. Kanamori, T. Kiyomura, H. Kurata, K. Nakanishi and T. Abe, Adv. Energy Mater., 2015, 5, 1400730.

[168] L. Y. Yang, H. Z. Li, J. Liu, S. S. Tang, Y. K. Lu, S. T. Li, J. Min, N. Yan and M. Lei, J. Mater. Chem. A, 2015, 3, 24446.

[169] J. Q. Wang, W. H. Li, Z. Z. Yang, L. Gu and Y. Yu, RSC Adv., 2014, 4, 25220.

[170] G. B. Xu, L. W. Yang, X. L. Wei, J. W. Ding, J. X. Zhong and P. K. Chu, Adv. Funct. Mater., 2016, doi: 10.1002/adfm.201505435

[171] P. Senguttuvan, G. Rousse, V. Seznec, J.-M. Tarascon and M. R. Palacín, Chem. Mater., 2011, 23, 4109.

[172] W. Wang, C. J. Yu, Y. J. Liu, J. G. Hou, H. M. Zhu and S. Q. Jiao, RSC Adv., 2013, 3, 1041.

[173] A. Rudola, K. Saravanan, C. W. Mason and P. Balaya, J. Mater. Chem. A, 2013, 1, 2653.

[174] H. L. Pan, X. Lu, X. Q. Yu, Y. S. Hu, H. Li, X. Q. Yang and L. Q. Chen, Adv. Energy Mater., 2013, 3, 1186.

[175] J. F. Ni, S. D. Fu, C. Wu, Y. Zhao, J. Maier, Y. Yu and L. Li, Adv. Energy Mater., 2016, doi: 10.1002/aenm.201502568.

[176] P. Senguttuvan, G. Rousse, M. E. A. Y. de Dompablo, H. Vezin, J. M. Tarascon and M. R. Palacin, J. Am. Chem. Soc., 2013, 135, 3897.

[177] W. Wu, J. Yan, A. Wise, A. Rutt and J. F. Whitacre, J. Electrochem. Soc., 2014, 161, A561.

[178] C. Wu, P. Kopold, Y. L. Ding, P. A. van Aken, J. Maier and Y. Yu, ACS Nano, 2015, 9, 6610–661.

[179] S. I. Park, I. Gocheva, S. Okada and J.-i. Yamaki, J. Electrochem. Soc., 2011, 158, A1067.

[180] X. Y. Wu, Y. L. Cao, X. P. Ai, J. F. Qian and H. X. Yang, Electrochem. Commun., 2013, 31, 145.

[181] X. N. Li, X. B. Zhu, J. W. Liang, Z. G. Hou, Y. Wang, N. Lin, Y. C. Zhu and Y. T. Qian, J. Electrochem. Soc., 2014, 161, A1181.

[182] M. Naguib, V. N. Mochalin, M. W. Barsoum and Y. Gogotsi, Adv. Mater., 2014, 26, 992.

[183] O. Mashtalir, M. Naguib, V. N. Mochalin, Y. Dall'Agnese, M. Heon, M. W. Barsoum and Y. Gogotsi, Nat. Commun., 2013, 4, 1716.

[184] M. Naguib, O. Mashtalir, J. Carle, V. Presser, J. Lu, L. Hultman, Y. Gogotsi and M. W. Barsoum, ACS Nano, 2012, 6, 1322.

[185] A. N. Enyashin and A. L. Ivanovskii, Theor. Chem., 2012, 989, 27.

[186] X. F. Wang, X. Shen, Y. R. Gao, Z. X. Wang, R. C. Yu, and L. Q. Chen, J. Am. Chem. Soc., 2015, 137, 2715.

[187] S. Kajiyama, L. Szabova, K. Sodeyama, H. Iinuma, R. Morita, K. Gotoh, Y. Tateyama, M. Okubo and A. Yamada, ACS Nano, 2016, 10, 3334..

[188] T. Norio, S. Hirofumi, S. Yuichi, U. Purushotham, N. Masataka, J. Phys. Chem. C 2015, 119, 18046.

[189] A. Haregewoin, A. Wotangoa, B. Hwang, Energy Environ. Sci., 2016, 9, 1955.

CHAPTER 3 EXPERIMENTAL METHODS

3.1 Experimental procedures

In this project, a series of the single-component layered materials and heterostructures based on two-dimensional layered materials with adjustable nanostructures will be designed to investigate their potential and feasibility for sustainable energy resources. An extensive research will be undertaken to enhance the charge transfer performance and environmental friendliness of the designed materials, followed by detailed reaction mechanism and calculations study. The research work in this thesis follows the procedures described in **Figure 3.1**. Various active anode materials were synthesized. Furthermore, different physical characterization techniques were carried out to confirm and observe the properties of the as-prepared samples.

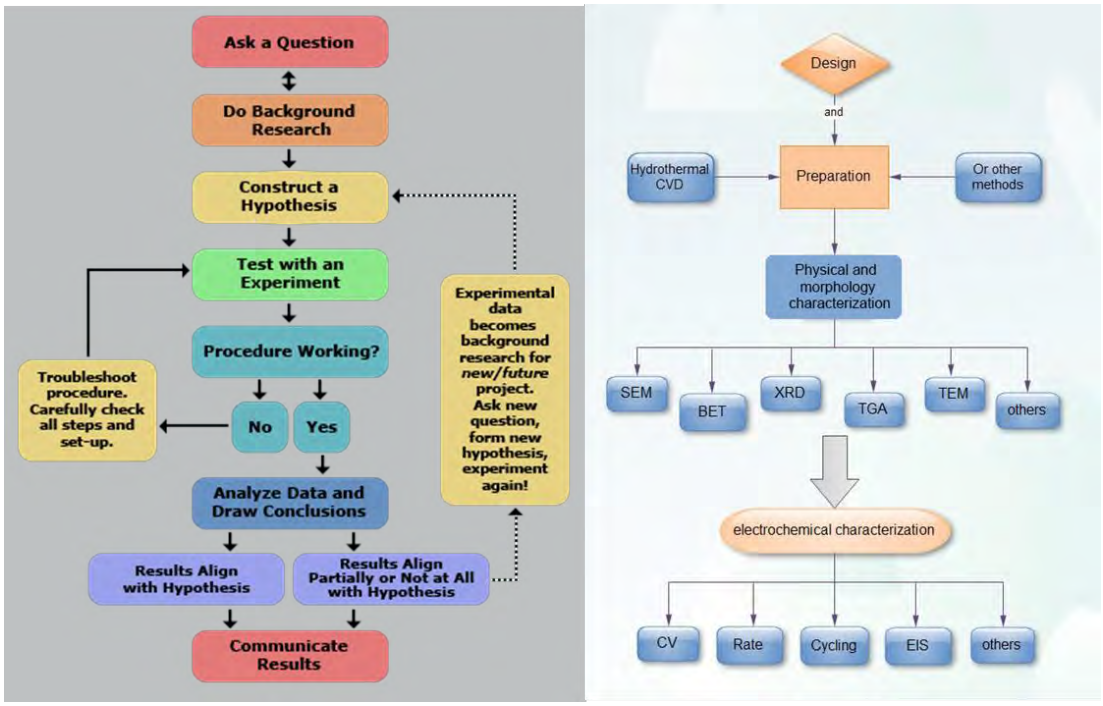

Figure 3.1 Outline of experimental procedures and techniques conducted in this thesis.

3.2 Chemicals

The chemicals used in this thesis are summarized in details in **Table 3.1**.

Table 3.1 List of chemicals used in this thesis

Chemicals	**Formula**	**Purity (%)**	**Supplier**
Carbon black	C	Super P	Timcal, Belgium
Acetone	$(CH_3)_2CO$	99	Ajax Finechem
Aluminium foil	Al	N/A	Vanlead Tech
Copper foil	Cu	N/A	Vanlead Tech
CR2032 coin cells	N/A	N/A	China ChemsT
Diethyl carbonate (DEC)	$C_5H_{10}O_3$	99+	Sigma Aldrich, Australia
Ethanol	C_2H_5OH	Reagent	Q-store, Australia
Ethylene carbonate (EC)	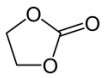	99	Sigma Aldrich, Australia
Fluoroethylene carbonate	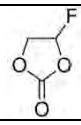	N/A	Sigma Aldrich, Australia
Graphite	C	N/A	Sigma Aldrich, Australia
Hydrogen peroxide	H_2O_2	30	Sigma Aldrich, Australia
Single-wall carbon nanotubes (SWCNTs)	C	98	NanoAmor
Multi-wall carbon nanotubes (MWCNTs)	C	95	NanoAmor
N-methyl-2-pyrrolidone	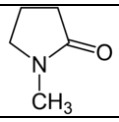	99.5	Sigma Aldrich, Australia
Poly (acrylic acid) (MW=130,000)	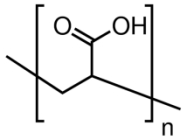	N/A	Sigma Aldrich, Australia

Polyvinylidene difluoride (MW=543,000)	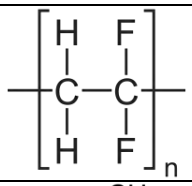	N/A	Sigma Aldrich, Australia
Propylene carbonate	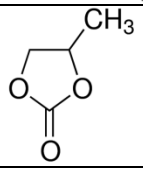	99.7	Sigma Aldrich, Australia
Sodium carbonate	Na_2CO_3	99	Sigma Aldrich, Australia
Sodium carboxymethyl cellulose (MW = 90,000)	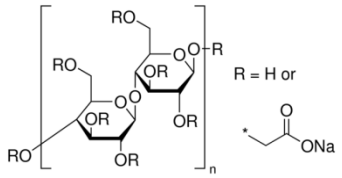	N/A	Sigma Aldrich, Australia
Sodium cubes (stored in mineral oil)	Na	99.9	Sigma Aldrich, Australia
Sodium ingot	Na	99.95	Sigma Aldrich, Australia
Sodium perchlorate	$NaClO_4$	98	Sigma Aldrich, Australia
Polyvinylidene difluoride (PVDF)	$(CH_2CF_2)n$	N/A	Sigma Aldrich, Australia
DI Milli-Q Water	H_2O	5 ppb (TOC)	Millipore, USA
Ethanol	C_2H_5OH	Reagent	Q-store, Australia
High pure ethanol	C_2H_5OH	99.95% absolute	Sigma Aldrich, Australia
Polypropylene separator	$(C_3H_6)n$	Celgard 2500	Hoechst Celanese Corporation, USA
Lithium foil	Li	99.9	Sigma Aldrich, Australia
Tin chloride dihydrate	$SnCl_2 \cdot 2H_2O$	99	Sigma Aldrich, Australia
Potassium permanganate	$KMnO_4$	99+	Sigma Aldrich, Australia

Ammonium heptamolybdate tetrahydrate	$(NH_4)_6Mo_7O_{24}\cdot 4H_2O$,	99.98	Sigma Aldrich, Australia
Nitric acid	HNO_3	69	Sigma Aldrich, Australia
Tin (II) chloride dihydrate	$SnCl_2\cdot 2H_2O$	96	Fluka, Australia
Potassium Hydroxide	KOH	98	Sigma Aldrich, Australia
Urea	NH_2CONH_2	Bioreagent	Sigma Aldrich
Potassium stannate trihydrate	$K_2SnO_3\cdot 3H_2O$	99.9	Sigma Aldrich
Sulfur	S	99.5+	Sigma Aldrich
Acetic acid	CH_3COOH	99.7+	Sigma Aldrich, Australia
Ethylene carbonate	$C_3H_4O_3$	99	Sigma Aldrich, Australia
Diethyl carbonate (DEC)	$C_5H_{10}O_3$	99+	Sigma Aldrich, Australia
Lithium hexafluorophosphate	$LiPF_6$	99.99	Sigma Aldrich, Australia
Dimethyl carbonate	$C_3H_6O_3$	99+	Sigma Australia
Glucose	$C_{12}H_{22}O_{11}$	99	Sigma Aldrich, Australia
Hydrochloric acid	HCl	36.5	Sigma Aldrich
Sulfuric acid	H_2SO_4	98	Sigma Aldrich, Australia

3.3 Methodology and theory of experiments

3.3.1 Liquid exfoliation layering the bulk materials (Top-down approach)

Liquid exfoliation is a process of exfoliating layered materials into mono- or few-layers by chemical reaction or intercalation (**Figure 3.2**). Such a technique involves introducing guest species in-between the gaps of the host layered materials then separating them. Specifically, graphene oxides were prepared by a modified Hummers‘ method. In addition, ultra-sonication is an important procedure for realizing better exfoliation and guaranteeing homogeneous dispersion. Meanwhile, centrifuging is a key step to remove un-exfoliated impurity. The development of layered materials is driven by fundamental interest and their potential applications. Layered materials provide a wide range of basic building blocks with unique electrical, optical, and thermal properties which do not exist in their bulk counterparts. These brand-new materials can bridge the microscopic superior electronic and magnetic features with the macroscopic ultrathinness and flexibility, thus definitely achieving a maximum functionality with a minimized size. In particular, along with the discovery of graphene, layered crystals have increasingly attracted fundamental research interest owing to their unique open morphologies and high electric conductivity and fast potassium diffusivity will significantly reduce the change transfer resistance, lower the polarization effect and thus achieve high electrochemical performance. Using layered materials as electrodes have been believed one of ideal strategies in maximize the interface and maintain the structure stability of electrode during charge transfer process.

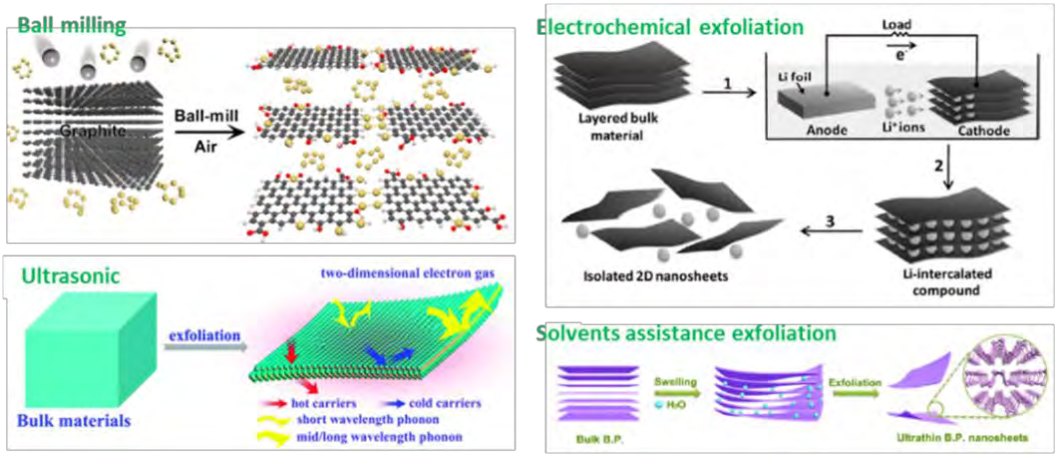

Figure 3.2 Schematic illustration of exfoliation processes and synthetic methods for layered material production.

3.3.2 Hydrothermal method

The hydrothermal method is a process to crystallize substances from high-temperature aqueous solutions at high vapour pressures. This method is efficient for crystal growth and nanomaterials synthesis. As shown in **Figure 3.3**, the device consists of a vessel and a stainless steel protector. The composition, morphology, and crystal structure of the products is associated with several factors. The volume of the solvent is related to the pressure of the autoclave. The concentration of the precursors is responsible for the size and morphology of the final products. The temperature for hydrothermal synthesis is a key parameter as well, directly deciding the final resultant. Thus, the relevant parameters should be considered in order to fabricate target materials.

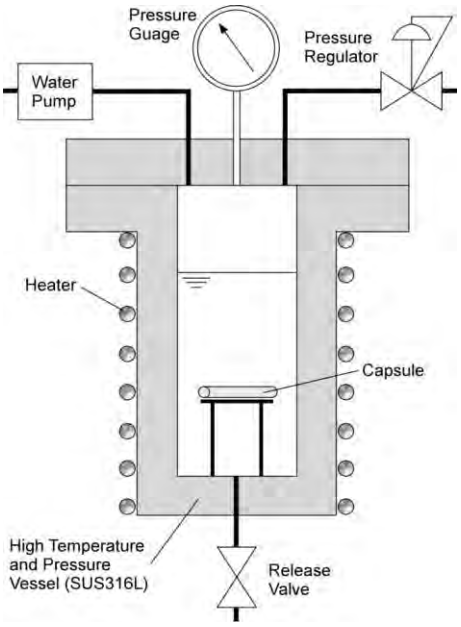

Figure 3.3 Schematic diagram of stainless steel autoclave.

3.3.3 CVD

Chemical vapour deposition (CVD) is a chemical process used to produce high-purity, high-performance solid materials (**Figure 3.4**). In a typical CVD process, the substrate is exposed to one or more volatile precursors, which react and/or decompose on the substrate surface to produce the desired deposit or react with substrate. Frequently, volatile by-products are also produced, which are removed by gas flow through the reaction chamber. The advantages of CVD include a high

deposition rate and high degree of control. Tuning the process is simply a matter of manipulating the vapour flows in the coating zone, and the coating layer can be very uniform.

Figure 3.4 Schematic diagram of CVD apparatus.

3.3.4 Nanocasting

Nanocasting (**Figure 3.5**) is a powerful method for creating materials that are more difficult to synthesize by conventional processes. Structure replication on the nanometer length scale allows materials' properties to be manipulated in a controlled manner, such as tunable composition, controllable structure and morphology, and specific functionality. The nanocasting pathway with hard templates opens the door to the design of highly porous solids with multifunctional properties and interesting application perspectives.

Figure 3.5 Nanocasting of mesoporous materials.

3.4 Characterization and measurement methods

3.4.1 X-ray diffraction

X-ray crystallography is a tool used for identifying the atomic and molecular structure of a crystal, in which the crystalline atoms cause a beam of incident X-rays to diffract into many specific directions. By measuring the angles and intensities of these diffracted beams, a crystallographer can produce a three-dimensional picture of the density of electrons within the crystal. From this electron density, the mean positions of the atoms in the crystal can be determined, as well as their chemical bonds, their disorder and various other information. [1]

In this thesis, powder samples are loaded onto a quartz holder, which is put on one axis of the diffractometer and tilted by an angle θ, while a detector rotates around it on an arm at a 2θ angle. The XRD devices used in this thesis were a GBC MMA diffractometer in ISEM, UOW. All the XRD devices use Cu Kα radiation, λ = 1.54056 Å.

3.4.2 Scanning electron microscopy

The scanning electron microscope (SEM) is a type of electron microscope to scan a sample surface with a high-energy beam of electrons. The electrons interact with atoms in the sample, producing various signals that can be detected and that contain information about the sample's surface topography and composition. The electron beam is generally scanned in a raster scan pattern, and the beam's position is combined with the detected signal to produce an image. SEM can achieve resolution better than 1 nanometer. The morphology and structure of samples in this thesis were characterized with a field-emission scanning electron microscope (FESEM; JEOL 7500 in EMC, UOW).

3.4.3 Transmission electron microscopy

Transmission electron microscopy (TEM) is a microscopy technique in which a beam of electrons is transmitted through an ultra-thin specimen, interacting with the specimen as it passes through it. An image is formed from the interaction of the electrons transmitted through the specimen; the image is magnified and focused onto an imaging device, such as a fluorescent screen, on a layer of photographic film, or to be detected by a sensor such as a charge-coupled device. It is a technique to observe sample‘s morphology, lattice spacing, crystal orientation and electronic structure. TEM is capable of significantly higher resolution imaging than light microscopes. Selected area electron diffraction (SAED) is a crystallographic experimental technique, which is often complementary to TEM. TEM specimen stage designs include airlocks to allow for insertion of the specimen holder into the vacuum with minimal increase in pressure in other areas of the microscope. [1]

Annular dark-field imaging is a method of mapping samples in a scanning

transmission electron microscope (STEM). These images are formed by collecting scattered electrons with an annular dark-field detector. An annular dark field detector collects electrons from an annulus around the beam, sampling far more scattered electrons than can pass through an objective aperture. An annular dark field image formed only by very high angle, incoherently scattered electrons - as opposed to Bragg scattered electrons — is highly sensitive to variations in the atomic number of atoms in the sample (Z-contrast images). This technique is also known as high-angle annular dark-field imaging (HAADF). [1]

The sample is placed on the inner meshed area, having a diameter of approximately 2.5 mm. The grid is placed on the sample holder, which is paired with the specimen stage. The samples for TEM in this work were dispersed in ethanol and then loaded onto a holey carbon support film on a copper grid. The TEM used in this thesis were TEM, JEOL 2011 and JEOL JEM-ARM200F. Elemental mapping was performed on the X-ray spectrometer attached to the TEM instrument.

3.4.4 Energy-dispersive X-ray spectroscopy

Energy-dispersive X-ray spectroscopy (EDS, EDX, or XEDS), sometimes called energy dispersive X-ray analysis (EDXA) or energy dispersive X-ray microanalysis (EDXMA), is an analytical technique used for the elemental analysis or chemical characterization of a sample. To stimulate the emission of characteristic X-rays from a specimen, a high-energy beam of electrons, X-rays or protons is focused onto the sample being studied. In this doctoral work, point and mapping analysis EDS spectroscopy was generally used in both SEM and TEM studies of the materials. [1]

3.4.5 Thermogravimetric analysis

Thermogravimetric analysis or thermal gravimetric analysis (TGA) is a method of thermal analysis in which changes in physical and chemical properties of materials are measured as a function of increasing temperature (with constant heating rate), or as a function of time (with constant temperature and/or constant mass loss). TGA can provide information about physical phenomena, such as second-order phase transitions, including vaporization, sublimation, absorption, adsorption, and desorption. Commonly, it is used to determine selected characteristics of materials that exhibit mass loss or increase because of decomposition, oxidation, or loss of volatiles. In this work, TGA was used to determine the carbon contents in the carbon composite materials. TGA was carried out in air atmosphere using a SETARAM Thermogravimetric Analyzer (France) in ISEM, UOW or a PerkinElmer TG/DTA 6300 in KETI.

3.4.6 Brunauer-Emmett-Teller

Brunauer-Emmett-Teller (BET) method is an important analysis technique to explain the physical adsorption of gas molecules on a solid surface and measure the specific surface area of a material. BET analysis is conducted at liquid nitrogen temperature (77 K) over different relative pressures. Surface area of samples can be calculated using experimental points at a relative pressure of P/P_0 = 0.05-0.25. Pore size distribution can be calculated by the Barrett-Joyner-Halenda (BJH) method, using the amount of nitrogen adsorbed at a relative pressure of P/P_0 = 0.99. In this work, nitrogen sorption was measured by a Quanta Chrome Nova 1000 in ISEM, UOW.

3.4.7 Raman spectroscopy

Raman spectroscopy is a spectroscopic technique for analysis of the vibrations of chemical bonds and symmetry of molecules, which is commonly used in chemistry to identify materials. In a Raman spectrometer, a laser light interacts with molecular vibrations, phonons, or other excitations of the sample, resulting in characteristic shifts in laser photons. The Raman spectra in this work were collected on a JOBIN Yvon Horiba Raman Spectrometer model HR800, employing a 10 mW helium/neon laser at 632.8 nm in ISEM, UOW. [1]

3.4.8 X-ray photoelectron spectroscopy

X-ray photoelectron spectroscopy (XPS) is a surface-sensitive quantitative spectroscopic technique to measure the elemental composition, empirical formula, chemical state and electronic state of the elements within a material. The valence states of elements can be identified and the ratio of each valence state can be estimated from the spectra. In this work, XPS was carried out on a VG Scientific ESCALAB 2201XL instrument in ISEM, UOW, and a Thermo Scientific Sigma Probe instrument in KETI using Al Kα X-ray radiation and fixed analyser transmission mode. [1]

3.4.9 Electron paramagnetic resonance

Electron paramagnetic resonance (EPR) or electron spin resonance (ESR) spectroscopy is a method for studying materials with unpaired electrons. The basic concepts of EPR are analogous to those of nuclear magnetic resonance (NMR), but it is electron spins that are excited instead of the spins of atomic nuclei. EPR spectroscopy is particularly useful for studying metal complexes or organic radicals.

Continuous-wave electron paramagnetic resonance (EPR) experiments were carried out using a Bruker ELEXSYS E580 spectrometer operating in the X-band (9.4 GHz) mode and equipped with an Oxford CF935 helium flow cryostat with an ITC-5025 temperature controller. The g tensors were calibrated for homogeneity and accuracy by comparison to a coal standard, g = 2.00285 ± 0.00005. The receiver gain and number of scans were adjusted to every spectrum of a particular sample to enable comparisons at a reasonable signal-to-noise ratio.

3.4.10 Diffuse reflectance spectra

Diffuse reflection (**Figure 3.6**) is the reflection of light from a surface such that an incident ray is reflected at many angles rather than at just one angle as in the case of specular reflection. An illuminated ideal diffuse reflecting surface will have equal luminance from all directions which lie in the half-space adjacent to the surface (Lambertian reflectance).

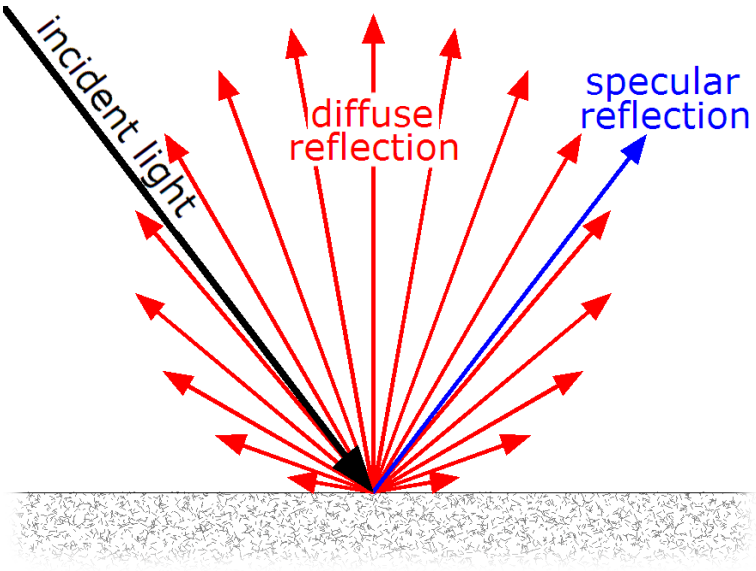

Figure 3.6 Diffuse and specular reflection.

A surface built from a non-absorbing powder such as plaster, or from fibers such

as paper, or from a polycrystalline material such as $BaSO_4$, reflects light diffusely with great efficiency. Many common materials exhibit a mixture of specular and diffuse reflection.

3.5 Electrode fabrication and cell assembly

3.5.1 Electrode preparation

Mixtures were prepared by mixing the active materials, conductive reagents, and binder in specific ratios. After thoroughly mixed, an appropriate solvent was added into the mixtures. Homogenous slurry could be obtained after mixing. The slurry was then uniformly pasted onto current collectors by a doctor blade. The prepared working electrodes were dried in a vacuum. The dried electrodes were punched into discs after a press procedure. The discs were then ready to be assembled into a testing cell in an argon filled glove box. [1]

3.5.2 Coin cell assembly

Cell assembly was carried out in an Ar-filled glove box using 2032-type coin cells. In the order of assembly shown in **Figure 3.7**, the cut Na/Li foil was first placed at the positive cap followed by dripping 2-3 drops of electrolyte; the separator was then evenly immersed in the electrolyte, and an extra 1-2 drops of electrolyte were added. The electrode disc was placed onto the separator followed by stainless steel spacer, spring, and positive cap subsequently. After tight sealing of the coin cell, the batteries were rested for overnight (>12 H) before electrochemical testing, in order to assure the full penetration of electrolyte into the electrodes and separator components.

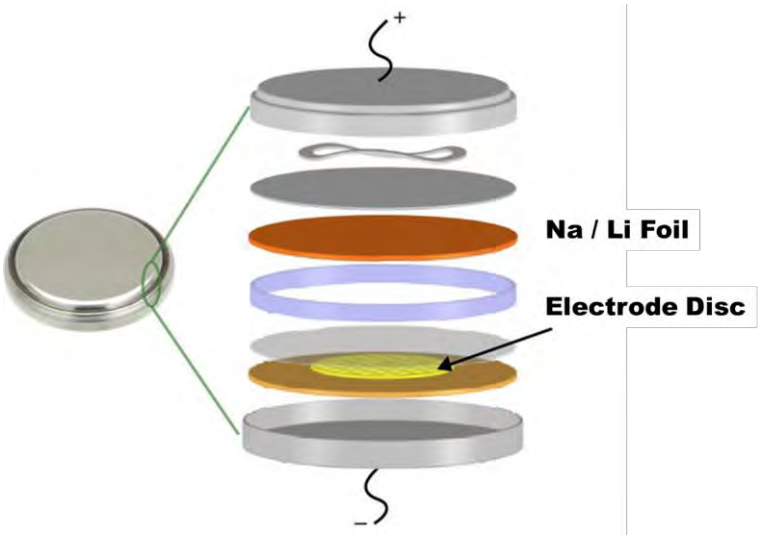

Figure 3.7 Schematic diagram and order assembly of 2032-type coin cells.

3.6 Electrochemical measurements

3.6.1 Cyclic voltammetry

Cyclic voltammetry (CV) is an electrochemical technique to investigate the electrochemical reactions in a cell. CV is conducted by cycling the potential of a working electrode at a specified scan rate, and the response current is recorded. CV testing for coin cells is based on the two-electrode model, in which Na/Li foil act as both reference electrode and counter electrode. A peak would be observed in both anodic and cathodic curves when a redox reaction occurs. The CV data were acquired on a Biologic VMP-3 electrochemical workstation.

3.6.2 Galvanostatic electrochemical testing

The electrochemical performance of a cell can be estimated by galvanostatic testing, in which the cell is charged and discharged during a certain cut-off voltage at a constant current mode. The charge and discharge capacity can be calculated based on the applied current and the total accumulated time for the full charge and

discharge process. This testing technique can also be used to evaluate rate capability by applying various current densities over a number of cycles. The instrument used here to obtain the data was a Land battery tester.

3.6.3 Electrochemical Impedance Spectroscopy

Electrochemical Impedance Spectroscopy (EIS) is a common method to investigate the inner resistance of a cell. The impedance spectrum for active materials usually includes a high-frequency semicircle and a low-frequency linear tail. The semicircle is related to the kinetic processes reflecting the charge transfer resistance and the double layer capacitance. The linear tail reflects the solid-state diffusion of Na ions into the bulk of the active materials. In this thesis, EIS data were collected on a Biologic VMP-3 electrochemical workstation.

3.6.4 Synchrotron in-situ X-ray powder diffraction

Batteries are used worldwide to power portable electronic devices. The technology has many benefits and considerable research is underway to further improve the electrochemical performance, particularly at the electrodes. In-situ X-ray powder diffraction (**Figure 3.8**) provides an opportunity to examine the reactions at the electrodes and gain a greater understanding of the mechanisms involved during the charge and discharge cycles. [1]

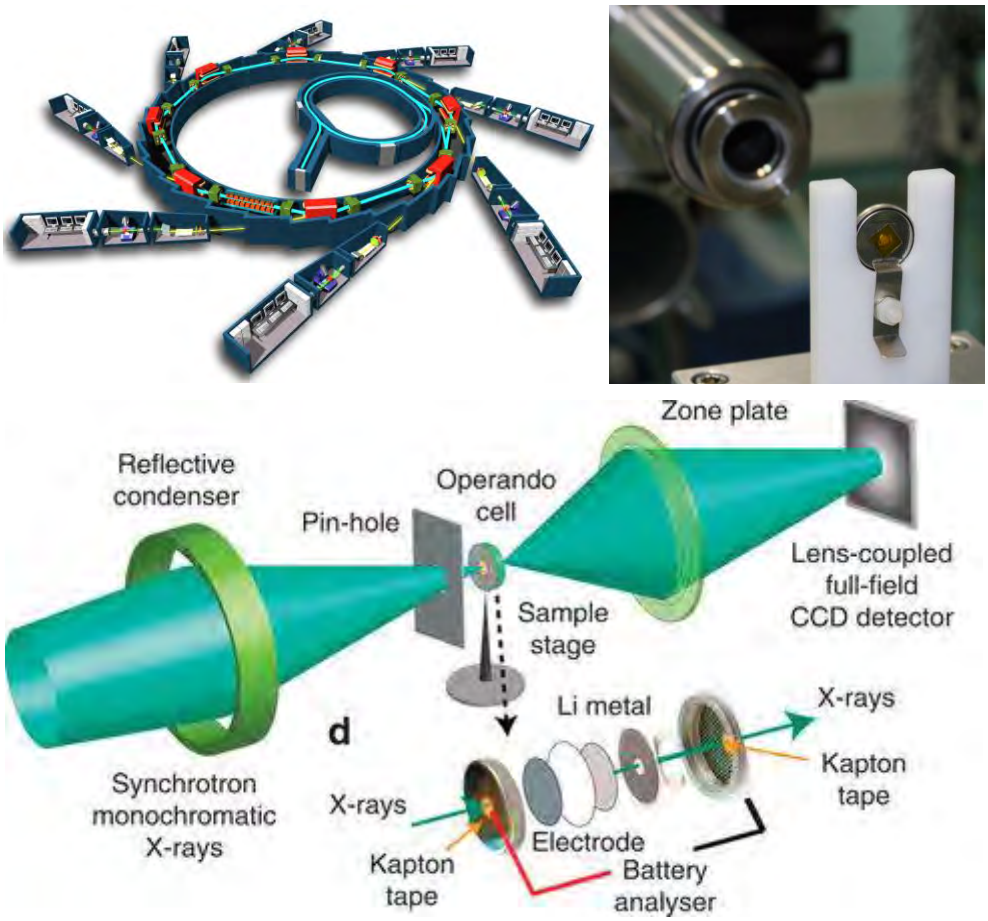

`

Figure 3.8 The coin cell sample stage with a sample mounted. The hole, sealed using polyimide film, permits the diffracted X-rays to leave the cell.

3.7 References

[1] https://en.wikipedia.org/wiki/Main_Page

CHAPTER 4 ENHANCED SODIUM-ION BATTERY PERFORMANCE BY STRUCTURAL PHASE TRANSITION FROM TWO-DIMENSIONAL HEXAGONAL SNS2 TO ORTHORHOMBIC SNS

Structural phase transitions can be used to alter the properties of a material without adding any additional elements and are therefore of significant technological value. It was found that the hexagonal-SnS_2 phase can be transformed into orthorhombic-SnS phase after an annealing step in an argon atmosphere, and the thus transformed SnS shows enhanced sodium ion storage performance over that of the SnS_2, which is attributed to its structural advantages. Here, we provide the first report on an SnS@graphene architecture for application as sodium ion battery anode, which is built from two-dimensional (2D) SnS and graphene nanosheets as complementary building blocks. The as-prepared SnS@graphene hybrid nanostructured composite delivers excellent specific capacity of 940 mAh g^{-1} and impressive rate capability of 492 and 308 mAh g^{-1} after 250 cycles at the current densities of 810 and 7290 mA g^{-1}, respectively. The performance was found to be much better than those of most reported anode materials for Na ion batteries. Based on combined ex-situ Fourier transform infrared spectroscopy, X-ray photoelectron spectroscopy, and ex-situ X-ray diffraction, the formation mechanism of SnS@graphene and the synergistic Na-storage reactions of SnS in the anode are discussed in detail. The SnS experienced a two-structural-phase transformation mechanism (orthorhombic-SnS to cubic-Sn to orthorhombic-$Na_{3.75}Sn$), while the SnS_2 experienced a three-structural-phase transformation mechanism (hexagonal-SnS_2 to tetragonal-Sn to orthorhombic-$Na_{3.75}Sn$) during the sodiation process. The lesser structural changes of SnS during the conversion are expected to lead to good structural stability and excellent cycling

stability in its sodium ion battery performance. These results demonstrate that the SnS@graphene architecture offers unique characteristics suitable for high-performance energy storage application.

4.1 Introduction

Bestowed by its similar chemical nature to Li, the Na-ion battery has recently again attracted increasing attention for large-scale energy storage in renewable energy and smart grid applications, because of both the low cost associated with its high natural abundance and the decent energy densities. [1-5] Many electrode materials for the Li-ion chemistry have been investigated as drop-in replacements for Na-ion batteries. [6] Most such efforts have been ineffective, however, as evidenced by low capacity utilization, inferior rate capability, poor cycling stability, or even complete electrochemical inactivity, for which the larger size of the Na-ion relative to the Li-ion is generally believed to be responsible.[7]

Among the limited number of Na-ion battery anode materials, tin (Sn) is a promising high theoretical capacity material with theoretical capacity of 847 mA h g^{-1} ($Na_{15}Sn_4$).[8] The large volume expansion (~ 420 %) of Sn during sodiation, however, essentially prevents access to this capacity.[9, 10] To circumvent these issues, studies on the preparation of composites containing carbon based materials and other metals as well as tin were carried out. For example, Xiao et al. developed nanosized SnSb/C to dilute the opportunities for Sn aggregation, which achieved an unprecedented capacity of 435 mA h g^{-1}.[11] Xu et al. have produced porous carbon in a composite with tin, and they have tested it as anode for both sodium and lithium ion batteries. [9] Recently, metal sulfides have been intensively studied as alternative candidates for commercial anode materials because of their higher capacities.[12-18] And it was found that the electrochemical properties of layered sulfides (SnS_2, MoS_2, WS_2) can be further improved by integration with graphene [18-23]. Among the various

metal sulfide anodes, orthorhombic-SnS has a unique layered structure with a large interlayer spacing (c = 0.4330 nm, space group Pnma), so that this crystallographic feature makes it suitable for the intercalation of Na ions and compensation of the alloying/de-alloying volume changes.[24, 25] In addition, the arrangement of Sn atoms in SnS were much similar to that of cubic-Sn, which is the phase after sodiation, expecting a good structural stability and excellent cycling stability for the performance on the sodium ion battery. Moreover, the layered structure of SnS should also be viable for reversible Na^+ storage. Exfoliation of these materials into layer sheets largely preserves their properties and also leads to additional characteristics due to confinement effects.[26-30] The intralayer Sn–S bonds are predominantly covalent in nature, whereas the layers are coupled by weak van der Waals forces, thus allowing the crystal to readily cleave along the layer surface.[31] Studies have shown that the analogous single layers are stabilized by the development of a ripple structure, as in the case of graphene.[32, 33] Furthermore, graphene sheets can easily self-assemble into conductive networks, not only offering a large number of accessible open pores to Na^+ in the electrolyte, but also allowing for the growth and anchoring of functional inorganic nanomaterials at high loading.[9, 34, 35] In addition to the composition and arrangement of atoms in materials, dimensionality also plays a crucial role in determining their fundamental properties.[36] This has been most strikingly highlighted over the past few years with two-dimensional (2D) graphene.[15-17, 37-39] For electrode materials, to completely utilize the 2D nature of graphene, an ideal second phase should be 2D as well, because the diffusion time ($t = L^2/D$) of ions in electrode materials is proportional to the square of the diffusion length, L and inversely proportional to the diffusion coefficient, D, so that a filmy 2D structure with shorter diffusion length will

significantly improve the diffusion efficiency of alkali metal ions and thus enhance the rate performance of sodium/lithium ion batteries.[1, 35, 37, 40]

Herein, we demonstrate a simple hydrothermal and annealing approach to construct hybrid architectures by employing 2D nanosheets of SnS and graphene as complementary building blocks via their controllable assembly properties. The resulting SnS@graphene architecture offers unique characteristics needed for high-performance electrodes. For electrical conductivity, such a structure enables locally intimate contact between the SnS and the graphene, which ensures excellent network conductivity throughout the whole electrode. For ion transport, the porous structure provides numerous channels that allow access to the electrolyte, while the active framework made from filmy 2D SnS nanosheets provides a shortened ion-diffusion length. For electrode stability, during the charge/discharge process, the SnS experienced a two-structural-phase transformation while the SnS_2 experienced a three-structural-phase transformation mechanism. That could be largely improving the structural stability and excellent cycling stability of SnS for their performance in the sodium ion battery. And the graphene component, the SnS layer structure, and the porous structure help to buffer the volume changes and stress that are generated during charge and discharge, and thus maintain the structural stability of the whole electrode. As a consequence, the optimal SnS@graphene hybrid architecture exhibits a very high reversible capacity of 940 mAh g^{-1} and excellent high-rate capability for Na ion storage. After 250 cycles, the specific capacities are still 492 and 308 mAh g^{-1}, as the current densities are increased to 810 and 7290 mA g^{-1}, respectively.

4.2 Experimental methods

4.2.1 Sample preparation

Natural graphite powder was oxidized to graphite oxide by the modified Hummers‘ method. The SnS@graphene hybrid architecture was prepared by a hydrothermal route. In a typical batch, hexadecyltrimethyl ammonium bromide (CTAB, 0.218 g, 0.6 mmol) was dissolved in deionized (DI) water, and the as-prepared graphene oxide (GO, 4.0 mg mL-1, 10 mL, 40 mg) was added into the solution. The mixture was stirred for another 2 h to allow CTA^+ adsorption on the GO surface by electrostatic interaction. After that, L-cysteine (0.500 g, 4.0 mmol) and $K_2SnO_3•3H_2O$ (0.300 g, 1.0 mmol) were dissolved into the mixture, and DI water was added to adjust the volume of the mixture to 40 ml. After ultrasonication and stirring for 20 min, the mixed suspension was transferred into a 50 mL Teflon-lined stainless steel autoclave, sealed tightly, and heated to 200 ℃ for 24 h. After cooling naturally, the black solid product was collected by centrifugation, washed several times with DI water and ethanol, and dried in a vacuum oven at 60 ℃ for 24 h. The as-prepared product was then annealed in a tube furnace at 600 ℃ for 2 h in flowing argon. For the control experiment, SnS_2 was also prepared by the above procedure without the presence of GO nanosheets.

4.2.2 Characterization

The crystalline structure of the as-prepared materials and ex-situ XRD were characterized by X-ray diffraction (XRD, MMA GBC). The morphologies and particle sizes of the samples were observed by field emission scanning electron microscopy (FESEM; JEOL-7500). The details of the crystal structure were further characterized by transmission electron microscopy (TEM), which was conducted on

a JEOL-2010 transmission electron microscope operating at 200 kV. Selected area electron diffraction (SAED) patterns were recorded using a Gatan charge coupled device (CCD) camera in a digital format. X-ray photoelectron spectroscopy (XPS) was conducted on a VG Multilab 2000. All of the binding energies were referenced to the C 1s peak at 284.8 eV of the surface adventitious carbon. Thermogravimetric analysis (TGA) was conducted on a TA 2000 Thermo-analyzer.

4.2.3 Electrochemical measurements

The electrochemical tests were carried out via CR2032 coin type cells. The working electrodes were prepared by mixing the as-prepared materials, Super P, sodium carboxymethyl cellulose / polyacrylic acid (1:1) at a weight ratio of 70:20:10. The resultant slurry was pasted on Cu foil and dried in a vacuum oven at 150 °C for 3 h, followed by pressing at 300 kg cm^{-2}. The weight of the materials on individual electrodes was 1.0 ± 0.2 mg cm^{-2}. Electrochemical measurements were carried out using two-electrode coin cells with Na metal as counter and reference electrode and glass microfiber (Whatman) as the separator. The electrolyte consisted of a solution of 1 M NaClO4 in ethylene carbonate (EC) / propylene carbonate (PC) (1/1; v/v) with 5 wt% fluoroethylene carbonate (FEC). Electrochemical impedance spectroscopy (EIS) and cyclic voltammetry (CV) were conducted on a VMP-3 electrochemical workstation at a scan rate of 0.1 mV s^{-1}. The cells were galvanostatically charged and discharged over a voltage range of 0.01-3 V versus Na/Na^{+} at different constant current densities, based on the weight of the samples, on a Land CT2001A battery tester. At least five parallel cells were tested for each electrochemical measurement, in order to make sure that the results were reliable and represented the typical behavior of the samples.

4.3 Results and Discussion

The overall synthetic procedure for the hybrid SnS architecture involves two steps: (1) the preparation of the SnS_2@graphene precursor under hydrothermal conditions (as shown in **Figure 4.1)**; and (2) the subsequent structural phase transition process in argon in order to obtain the SnS@graphene hybrid architecture (as shown in **Figure 4.3)**.

To understand the synthetic procedures, *ex-situ* Fourier transform infrared (FTIR) spectroscopy was conducted. Two peaks are found at 2914 and 2838 cm^{-1} in the FTIR spectrum of the SnS_2@graphene nanocomposite [**Figure 4.2(a)**], which can be assigned to the C-H stretching vibrations of $-CH_3$ and $-CH_2$ in CTA^+, respectively, indicating that the CTA^+ has adsorbed on the GO surface. The adsorption of CTA^+ on GO is due to the electrostatic interaction between the cationic surfactant and the negatively charged GO,[35] which imparts a positive charge to the GO to overcome the innate charge incompatibility between GO and SnO_3^{2-}. Consequently, SnO_3^{2-} could be attached to the CTA^+-GO surface to form a SnO_3^{2-}-CTA^+-GO complex. After that, L-cysteine is added into the suspension. L-cysteine is of particular interest to researchers due to its multifunctional groups (-SH, $-NH_2$, and $–COO^-$), which can be used for the conjugation of metallic ions or other functional groups.[17, 41] The intensity of the characteristic N-H deformation and C=O stretching vibration of the amide bond observed at 1535 cm^{-1} and 1657 cm^{-1}, respectively, for pure *L*-cysteine is weakened in the products, while the doublet peaks at 3350 and 3250 cm^{-1} from the symmetric vibration of peptide groups in *L*-cysteine merge into a broad band in the range of 3420-3200 cm^{-1}, suggesting that the nitrogen atom of the amide bond is possibly coordinated to the SnO_3^{2-} ion.[16]

$$HSCH_2CHNH_2COOH + H_2O \rightarrow CH_3COOH + NH_3 + H_2S \quad (1)$$

$$SnO_3^{2-} + 2H_2S + 2CH_3COOH \rightarrow SnS_2 + 3H_2O + 2CH_3COO^- \quad (2)$$

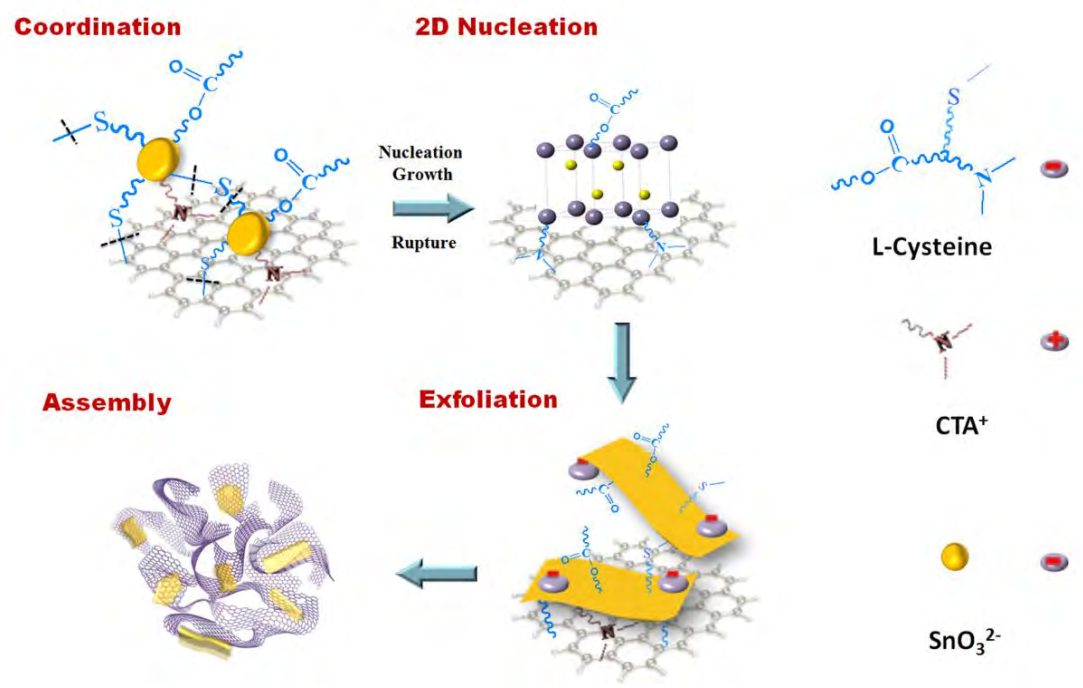

Figure 4.1 Schematic diagram illustrating the hydrothermal preparation of the hybrid tin sulfide and graphene architecture. Coordination: CTA^+ adsorbed on the GO due to the electrostatic interaction between the cationic surfactant and the negatively charged GO, then, SnO_3^{2-} could be attached to the CTA^+-GO surface to form a SnO_3^{2-}--CTA^+-GO complex. 2D Nucleation: In the presence of GO and L-cysteine, the crystal nucleated with the typical 2D nucleation-layer growth (atom color code: purple, Tin; yellow, Sulphur). Exfoliation: The excess L-cysteine can be negatively charged under alkaline solution and make the L-cysteine-capped SnS_2 particles repel each other and promote the exfoliation. Assembly: Hybrid architecture formed by the self-assembly of flexible graphene and layered SnS_2 nanosheets.

In our synthetic procedures, *L*-cysteine not only plays the role of a reducing agent and sulfur donor, but also acts as a stabilizing agent during the whole hydrothermal process, in which the *L*-cysteine releases H_2S as a sulfide source as well as a reducing agent [Equation (1)], resulting in the SnO_3^{2-} precursor to SnS_2 and the reduction of GO to graphene [Equation (2)]. The excess *L*-cysteine that remains in the solution as a stabilizing agent is a key factor that promotes the exfoliation of the hybrid precursor and enhances the stability of the colloidal dispersion. From the FTIR spectrum of SnS_2@graphene precursor after 1h hydrothermal reaction [**Figure 4.2(a)**], the peaks at 3124 and 3026 cm^{-1} for L-cysteine assigned to the N-H stretching vibration of the zwitterion ($^-OOC\text{-}C\text{-}NH_3^+$) and the peak at 1713 cm^{-1} assigned to the stretching vibration of the -COOH group of glycine residue, respectively, also disappear in the products, indicating that both the amino and the carboxyl groups of *L*-cysteine have been deprotonated, and the alkaline solution is generally believed to be responsible for this.[42] This is because the *L*-cysteine can be negatively charged under alkaline solution and make the *L*-cysteine-capped SnS_2 particles repel each other.[43]

The intensities of the characteristic N-H deformation and C=O stretching vibration of the amide bond at 1535 cm^{-1} and 1657 cm^{-1}, respectively, in pure *L*-cysteine were weakened in the products, while the doublet peaks at 3350 and 3250 cm^{-1} from the symmetric vibration of peptide groups in *L*-cysteine merged into a broad band in the range of 3420-3200 cm^{-1}, suggesting that the nitrogen atom of the amide bond was possibly coordinated to the SnO_3^{2-} ion. Two peaks were found at 2914 and 2838 cm^{-1}, which are assigned to the C-H stretching vibrations of $-CH_3$ and $-CH_2$ in CTA^+, respectively. All of these peaks from CTA^+ and *L*-cysteine disappeared completely after heat treatment as a result of the carbonization. The peaks at 2330 and 2353 cm^{-1}

were caused by CO_2 absorbed in the samples. The IR results indicated that the CTAB and *L*-cysteine would play important roles in the hydrothermal synthesis.

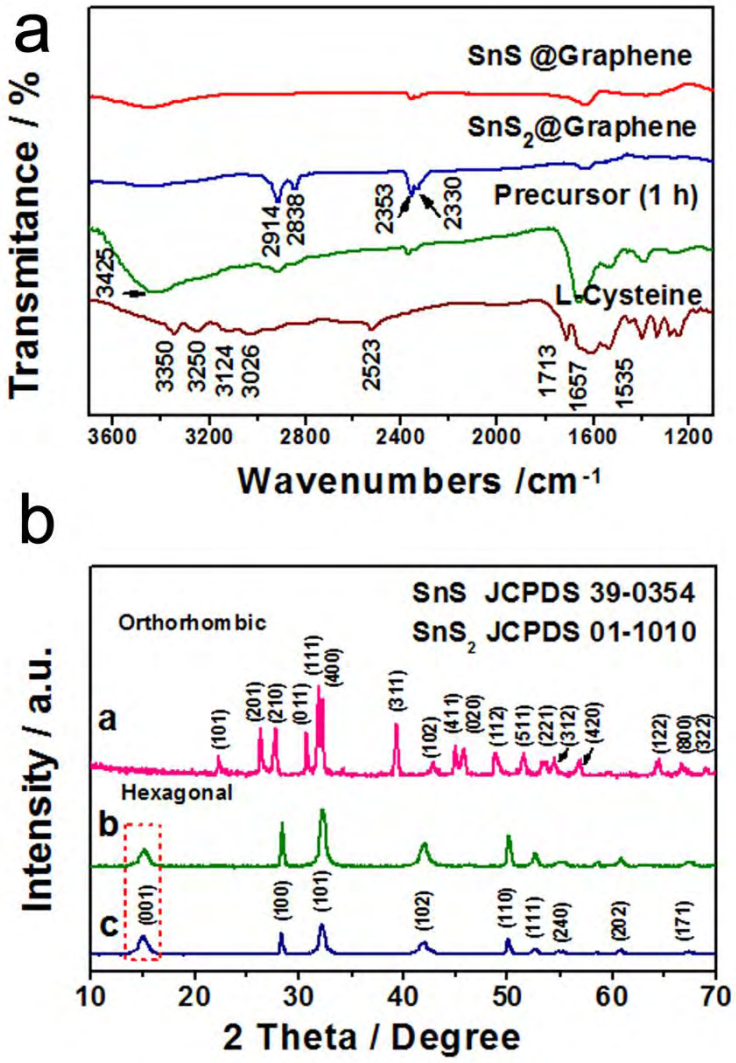

Figure 4.2 (a) FTIR spectra of SnS@graphene, SnS_2@graphene, SnS_2@graphene precursor after 1h hydrothermal reaction, and *L*-cysteine. (b) XRD patterns of a) SnS@graphene [orthorhombic SnS (JCPDS No. 39-0354)] and b) SnS_2@graphene architectures, and c) pristine SnS_2. The XRD pattern of the SnS_2@graphene composite is similar to that of pristine SnS_2 [hexagonal SnS_2 (JCPDS No. 01-1010)], the intensity of (001) plane is much lower than in the case of pristine SnS_2, indicating that growth of the SnS_2 was inhibited in the hybrid due to the intervention of

graphene and that a layered/sheet-like structure of SnS_2 was formed in the hybrid architecture.

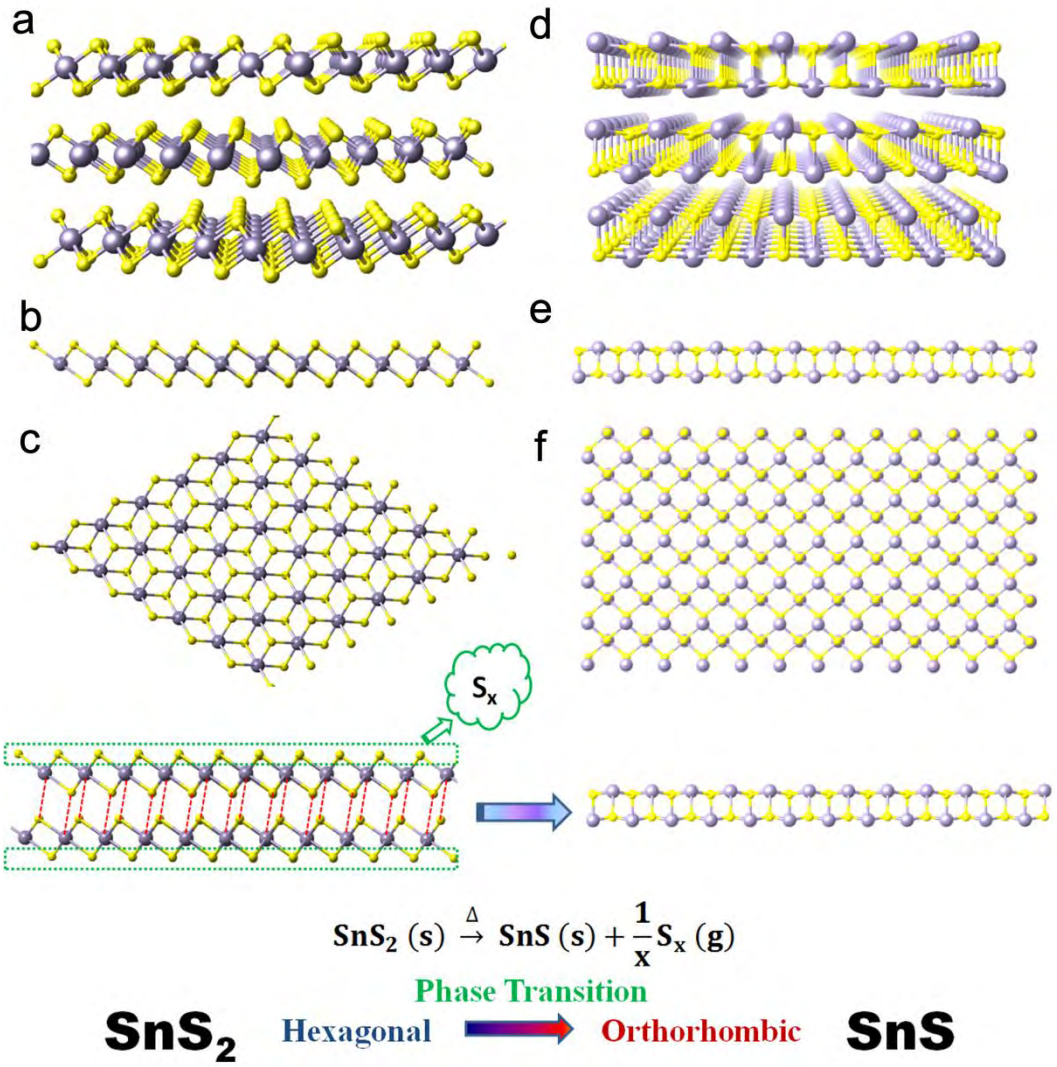

Figure 4.3 Schematic diagram (bottom) illustrating the phase transition process between SnS_2 and SnS. The crystal structures of hexagonal SnS_2 (a, b, c) and orthorhombic SnS (d, e, f) as shown in different sectional views (atom color code: purple, Tin; yellow, Sulphur). The formation of orthorhombic SnS phase may rely on the S_x depletion in a later stage of the phase transformation process. After annealing, the SnS_2 dissociation occurs, S depletion and high temperatures promote dissociation processes. This route is based on the incongruent sublimation of the SnS_2 and

proposes the direct formation of the SnS from SnS_2 through the proposed reaction in the scheme.

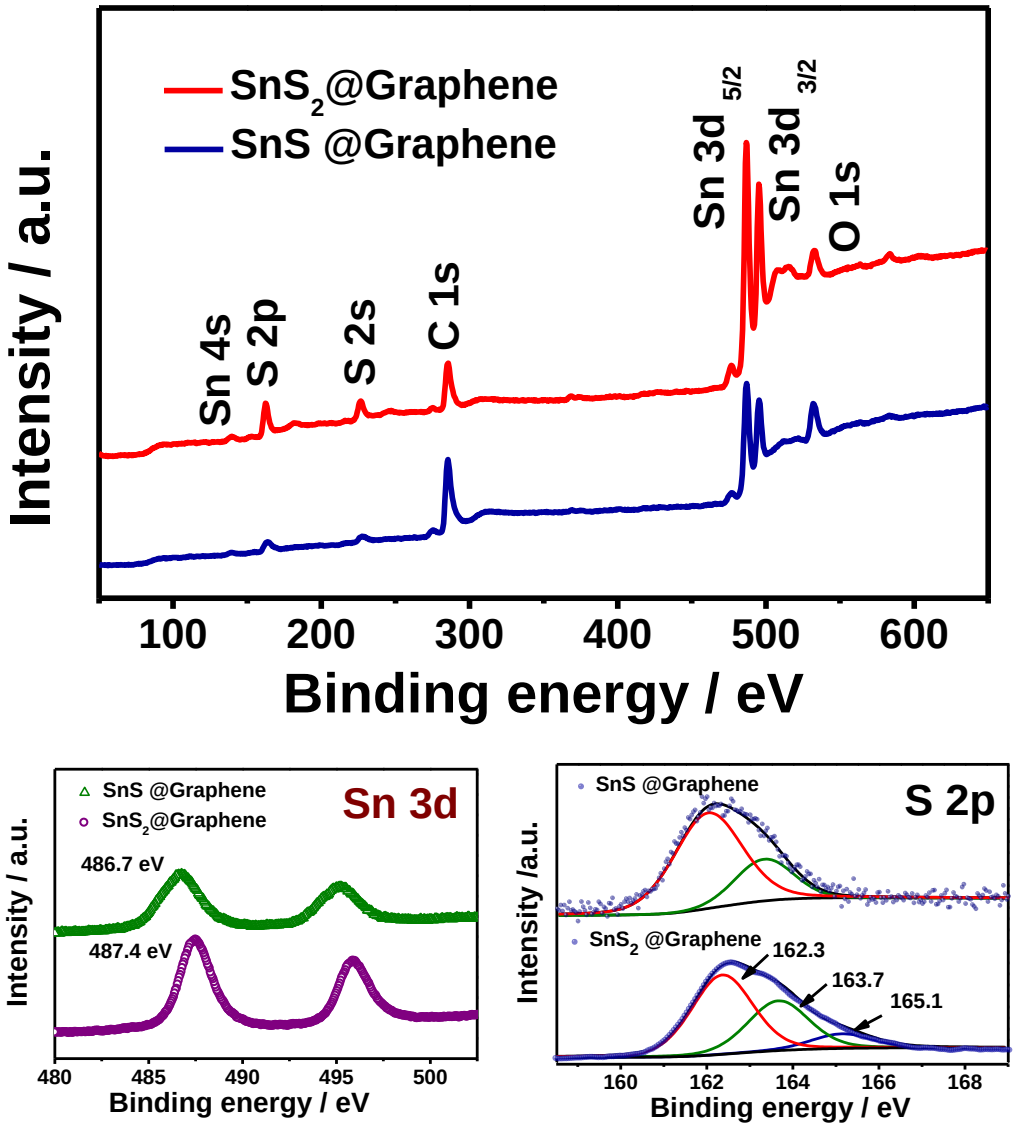

Figure 4.4 Typical a) survey XPS spectra of the SnS@Graphene and SnS_2@Graphene architectures. b) Sn 3d region XPS spectra, and c) S 2p region XPS spectra.

The subsequent structural phase transition process in argon would finalize the synthesis of the SnS@graphene architecture. The possible dissociation reaction at high temperature is proposed in the equation shown in **Figure 4.3**.[15, 44] **Figure 4.2(b)**

shows a representative X-ray diffraction (XRD) pattern of pristine SnS_2. All of the diffraction peaks can be indexed to hexagonal SnS_2 (JCPDS No. 01-1010) [**Figure 4.3 a,b and c**], indicating that pure, single-phase, and well crystallized SnS_2 has been obtained. The XRD pattern of the SnS_2@graphene composite is similar to that of pristine SnS_2, except for the (001) plane of the SnS_2 [**Figure 4.2b (b, c)**], the intensity of which is much lower than in the case of pristine SnS_2, indicating that growth of the SnS_2 (001) plane was inhibited in the hybrid due to the intervention of graphene and that a layered/sheet-like structure of SnS_2 was formed in the hybrid architecture. [14] As shown in Figure 1(b), after annealing, an entirely new and well crystallized phase of orthorhombic SnS (space group Pbnm (62), JCPDS No. 39-0354) can be observed from the XRD pattern [**Figure 4.3 d, e and f**]. The formation of this phase may rely on the S depletion in a later stage of the phase transformation process. Two intermediate processes could be involved in the synthesis of SnS [**Figure 4.3**]. Initially, in the high S availability regime, the SnS_2 dissociation occurs. After that, S depletion and high temperatures promote dissociation processes. The chalcogen depletion occurs mainly by localized film segregation and by condensation in other parts of the furnace and exhaust system.[45] This route is based on the incongruent sublimation of the SnS_2 and proposes the direct formation of the SnS from SnS_2 through the following reaction:[46]

$$SnS_2\,(s) \xrightarrow{\Delta} SnS\,(s) + \frac{1}{x}S_x\,(g) \qquad (3)$$

where $x = 2 - 8$, which represent the various S species that can be formed during this process. In order to measure the content of graphene in the as-synthesized SnS@graphene composite, thermogravimetric analysis (TGA) was carried out from

50 to 800 ° C in air (**Figure 4.5**). From the TGA curve, the major weight loss from 450 to 600 ° C was due to the removal of graphene by the oxidation process, and it can be calculated that the SnS@graphene composite contains 13.8% graphene.

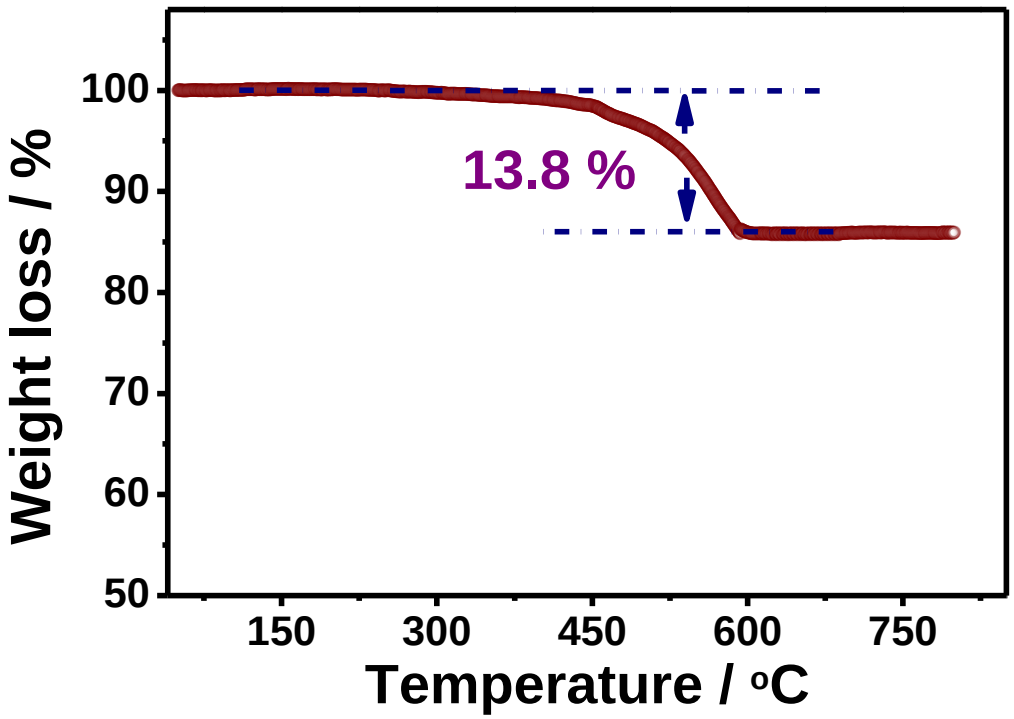

Figure 4.5 TGA curve of as prepared SnS@Graphene from 50 to 800 ° C in air. From the TGA curve, the major weight loss from 450 to 600 ° C was due to the removal of graphene by the oxidation process, and it can be calculated that the SnS@graphene composite contains 13.8% graphene.

XPS analysis was also conducted to investigate the surface electronic states and the chemical composition of the as-synthesized sample (**Figure 4.4**). Compared with the spectra of SnS_2@Graphene, the Sn 3d peaks of SnS@Graphene are shifted toward lower binding energy by 0.7 eV ($3d_{5/2}$) without any obvious change in the spectral

shape. This phenomenon results from the large difference in electronegativity between coordinating groups, which confirms that the evolution of the process goes through a transformation from the SnS_2-ligand complexes to SnS. From Figure S1(c), it can be seen that the asymmetrical S 2p spectrum for the SnS_2@Graphene, can be divided into three peaks, indicating that there are three chemical environments. The peaks at 162.3 eV and 163.7 eV could be attributed to the binding energies of S $2p_{3/2}$ and S $2p_{1/2}$ [34]. The other peak at 165.1 eV could be assigned to the binding energy of sulfur in the thiol group, which is in agreement with the above FTIR analysis [41].

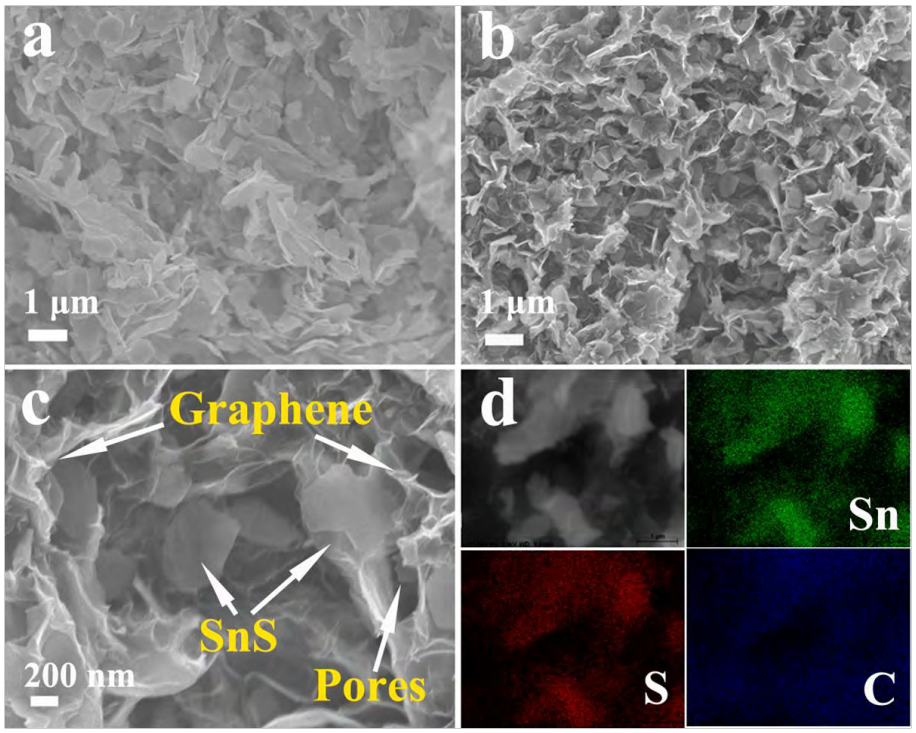

Figure 4.6 SEM image of hybird SnS_2@graphene (a); (b, c) typical SEM images of SnS@graphene architecture at different magnifications, which reveal the porous structure and thin walls containing both SnS and graphene nanosheets. (d) Element mapping images of the SnS@graphene with corresponding SEM image.

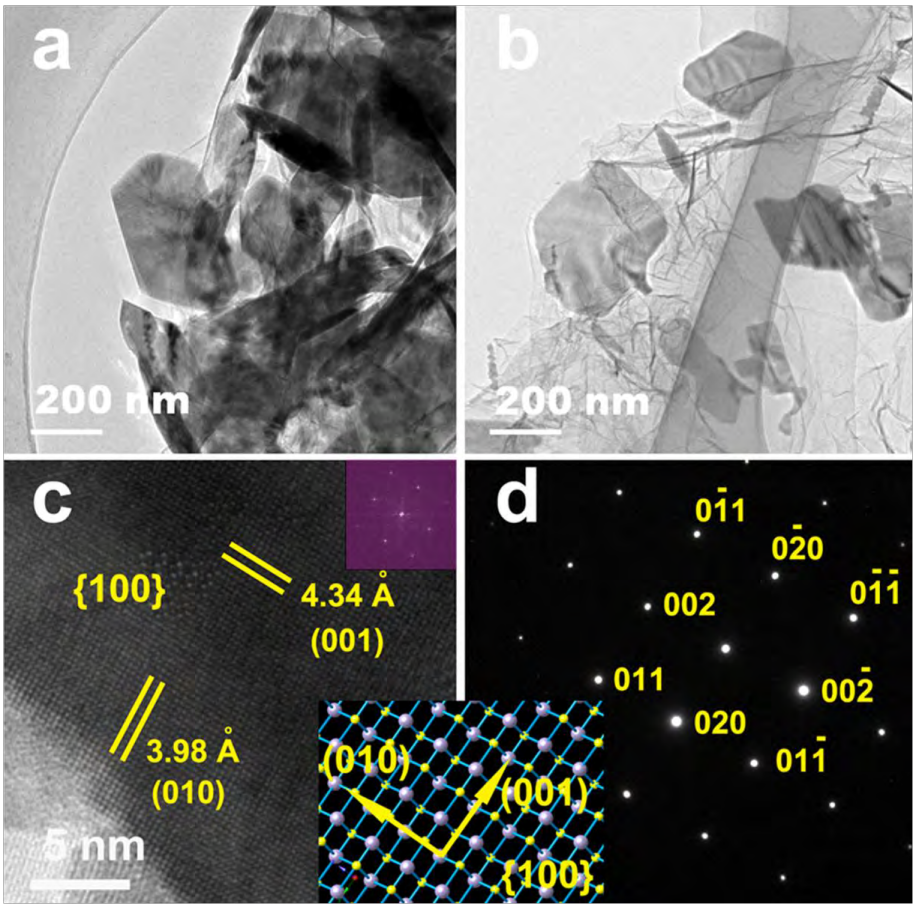

Figure 4.7 Representative TEM images of (a) SnS_2@graphene and (b) SnS@graphene. (c) HRTEM image of SnS with the resulting FFT pattern (inset), and (d) the corresponding SAED pattern, which can be indexed to SnS (100). The inset between (c) and (d) shows the atomistic model of the SnS (100) surface.

The morphology and microstructure of the as-prepared SnS_2@graphene and SnS@graphene composites were investigated *via* field emission scanning electron microscopy (SEM) and transmission electron microscopy (TEM). The GO sheets serve as the substrate for the nucleation and growth of SnS_2 into a layered structure, due to the interaction between the GO with functional groups and the SnO_3^{2-} precursor. On the other hand, GO in the composite also could restrain the stacking of SnS_2 in the *c*-direction to promote the formation of SnS_2 sheet-like structures.[14, 47, 48] With no GO in the synthetic process, the pristine SnS_2 materials mainly consist of irregular nanoparticles with a small quantity of sheet-like structures (**Figure 4.8**). Abundant SnS_2 nanosheets are clearly obtained after GO is included in the synthetic process [**Figure 4.2(a)** and **Figure 4.3(a)**]. From SEM observations, we found that the SnS nanosheets [**Figure 4.6 (c)**] are more rigid than the graphene nanosheets.[38] As shown in the SEM [**Figure 4.6 (b, c)**] and TEM [**Figure 4.7 (b)**] images, the as-prepared SnS@graphene architecture possesses a hybrid structure with interconnected pores, ranging from several nanometers to several micrometers in size. Moreover, the thin and rigid SnS nanosheets can be clearly observed and are homogeneously confined in the framework, which efficiently hampers their aggregation and restacking, as we expected. The partial overlapping or coalescing of flexible nanosheets is likely to have originated from the cross-linking of the functional groups in the graphene sheets, and thus, the SnS nanosheets are much easier to efficiently combine with graphene. Importantly, only 2D nanosheets were observed in this sample, indicating a nearly complete 2D morphological yield. Wide area energy dispersive spectroscopy (EDS) analysis indicated a nearly 1:1 atomic ratio of Sn to S (52 % Sn, 48 % S) for SnS and 1:2 for SnS_2 (35 % Sn, 65 % S),

confirming the SnS and SnS_2 stoichiometry (**Figure 4.9**). Analysis of an individual sheet by selected area electron diffraction (SAED) [**Figure 4.7 (d)**] indicated that it is single-crystalline and can be indexed to the (100) plane of SnS.[31] The high resolution TEM (HRTEM) image of the nanosheets [**Figure 4.7 (c)**] confirms their single-crystalline nature. Measurements of the reciprocal space distances between the fast Fourier transform (FFT) diffraction spots [inset image in **Figure 4.7 (c)**] were quantitatively consistent with those of the SAED pattern. The interatomic distances were determined to be 3.98 and 4.34 *Å*, respectively, corresponding to the (010) and (001) planes, and they match well with the *b* and *c* lattice constants of orthorhombic GeS-type SnS [inset image between **Figure 4.7 (c) and 4.7 (d)**] (b = 3.98 *Å*, c = 4.33 *Å*). Element mapping of the SnS@graphene composite demonstrates that the carbon, tin, and sulphur are homogeneously distributed in the sample and that the 2D SnS nanosheets have been very effectively combined with the graphene nanosheets [**Figure 4.7 (d)**].

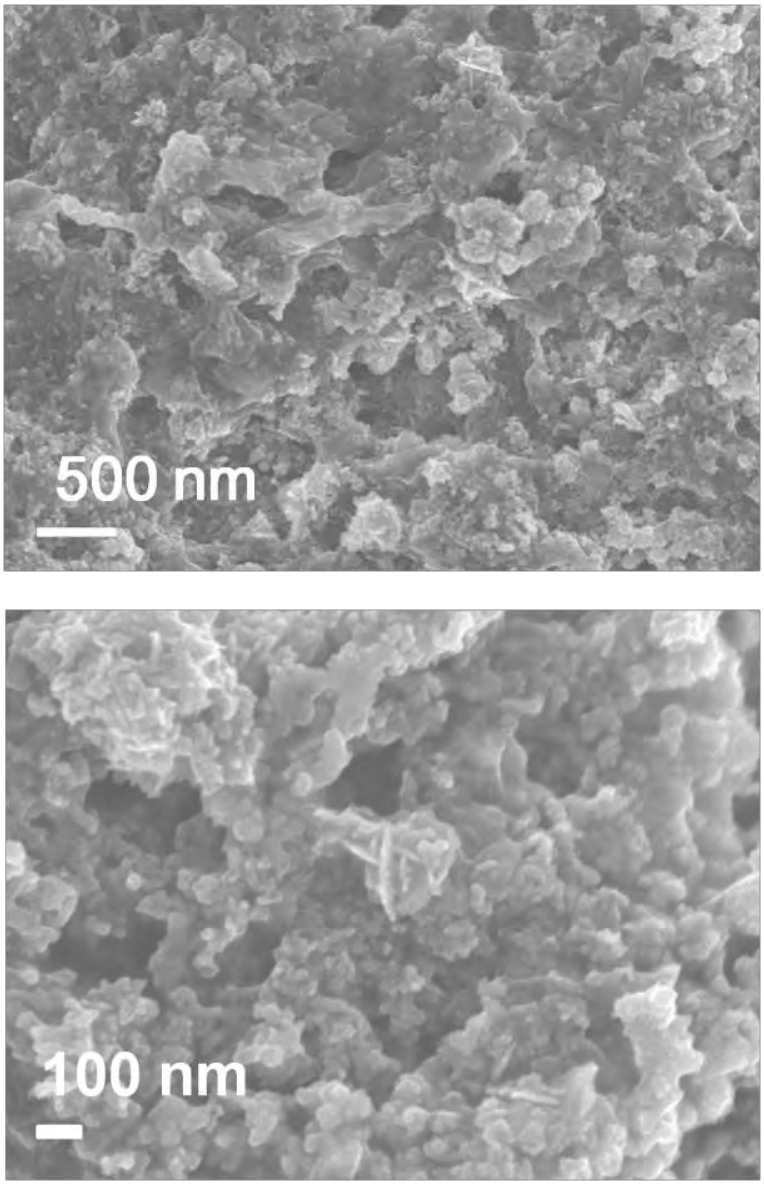

Figure 4.8 SEM images of SnS_2 prepared without GO by the hydrothermal method. With no GO in the synthetic process, the pristine SnS_2 materials mainly consist of irregular nanoparticles with a small quantity of sheet-like structures.

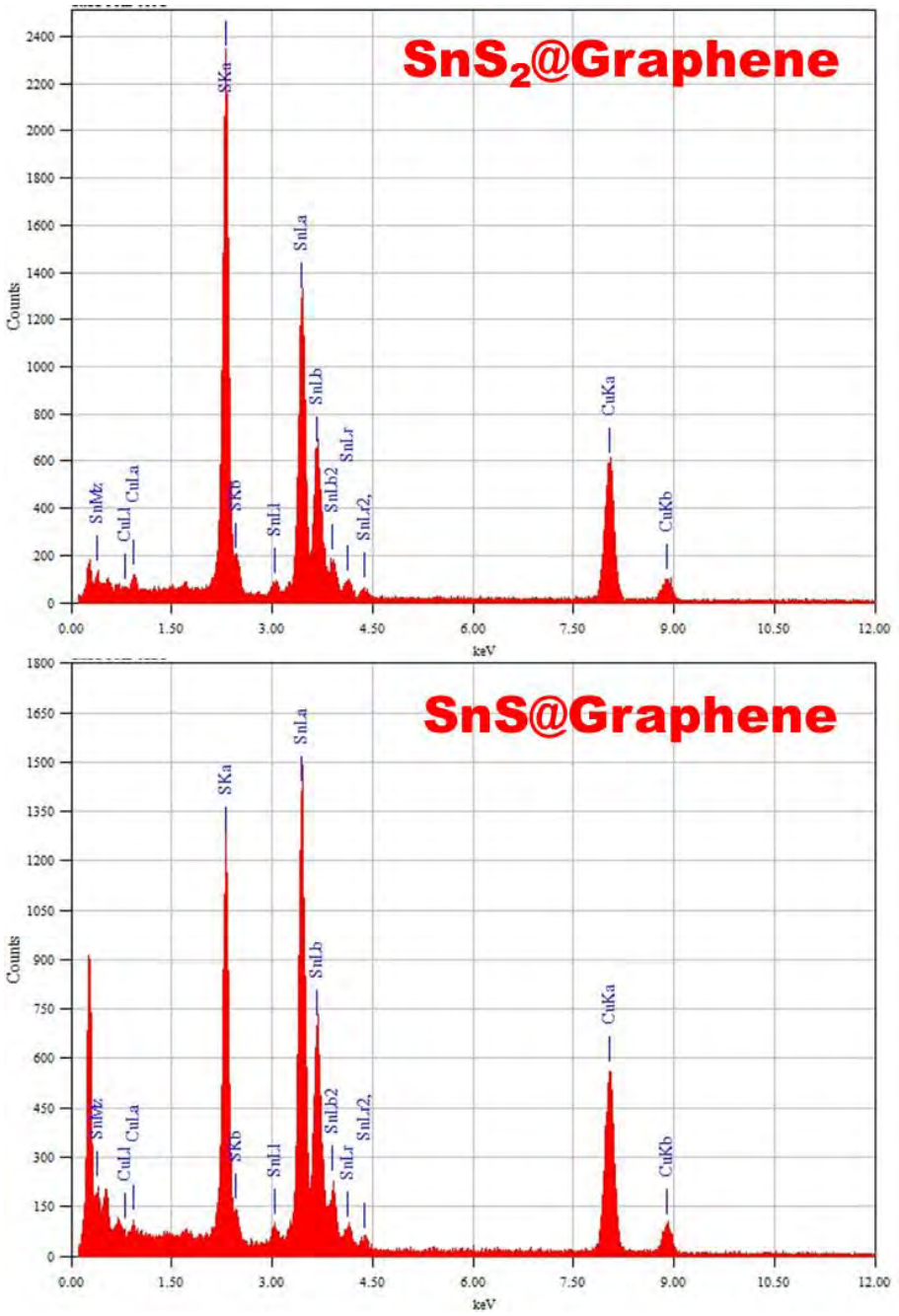

Figure 4.9 EDS spectra of SnS_2@Graphene (top) and SnS@Graphene (bottom). Wide area EDS analysis indicated a nearly 1:2 atomic ratio of Sn to S SnS_2 (35 % Sn, 65 % S) and 1:1 for (52 % Sn, 48 % S) for SnS, confirming the SnS and SnS_2 stoichiometry.

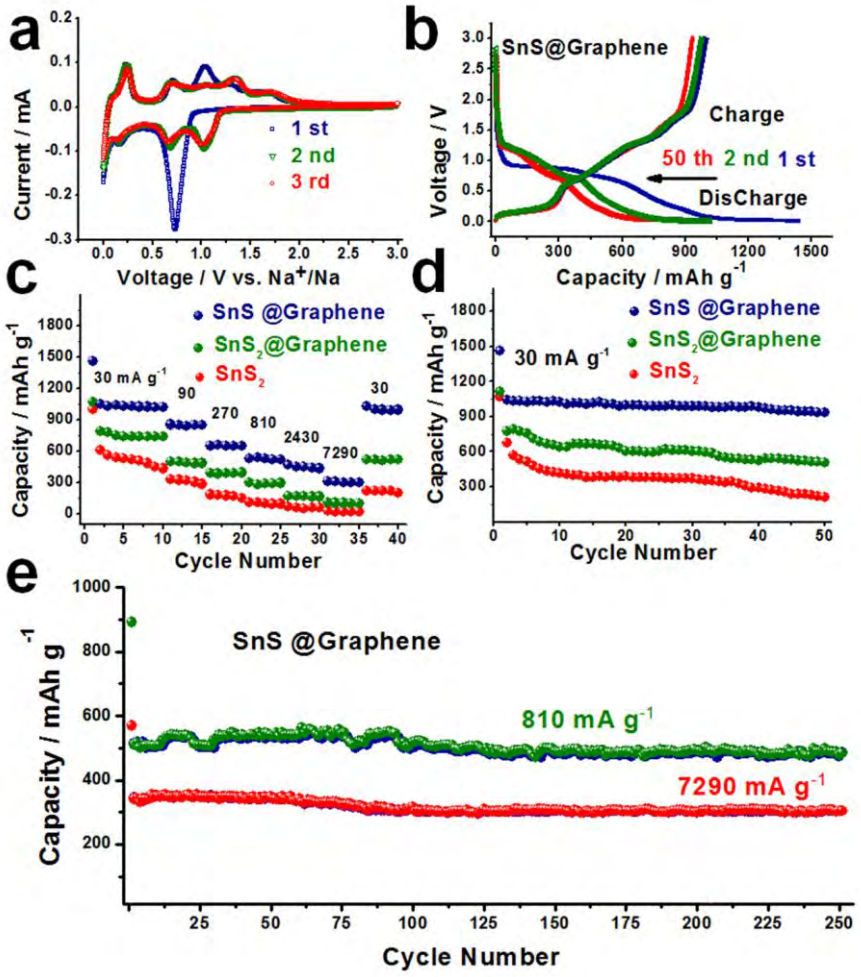

Figure 4.10 Electrochemical performance of SnS@graphene hybrid architecture for high-performance sodium storage. (a) Cyclic voltammograms for the first 3 cycles of SnS@graphene electrode at a scanning rate of 0.1 mV s^{-1}. (b) Galvanostatic discharge–charge profiles for selected cycles of SnS@graphene electrode at a current density of 30 mA g^{-1}. Comparisons of (c) rate capabilities and (d) cycling performances of SnS@graphene, SnS_2@graphene, and SnS_2 electrodes, and (e) long cycling performances of SnS@graphene electrode at different current densities.

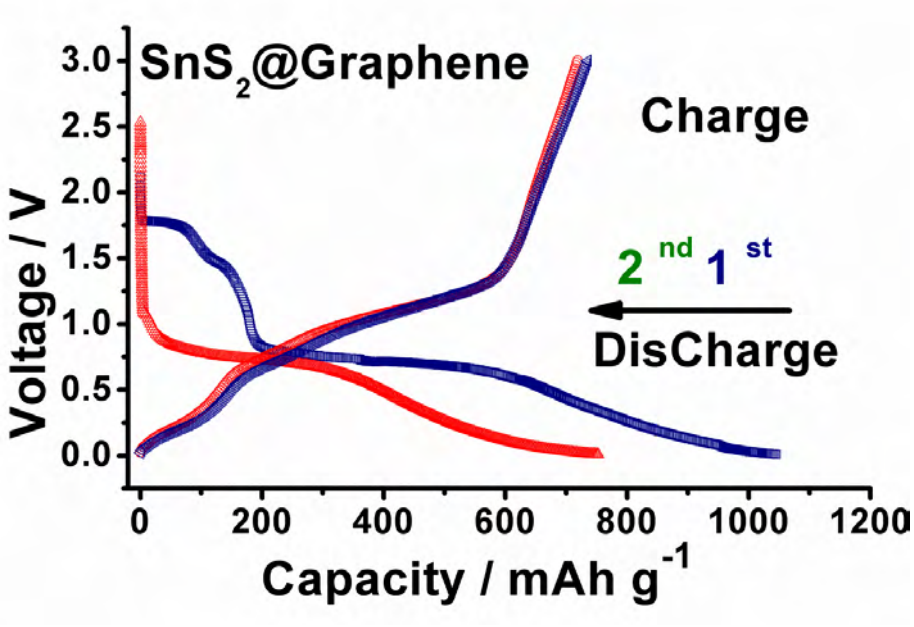

Figure 4.11 Galvanostatic discharge–charge profiles for selected cycles of SnS_2@graphene electrode at a current density of 30 mA g^{-1}.

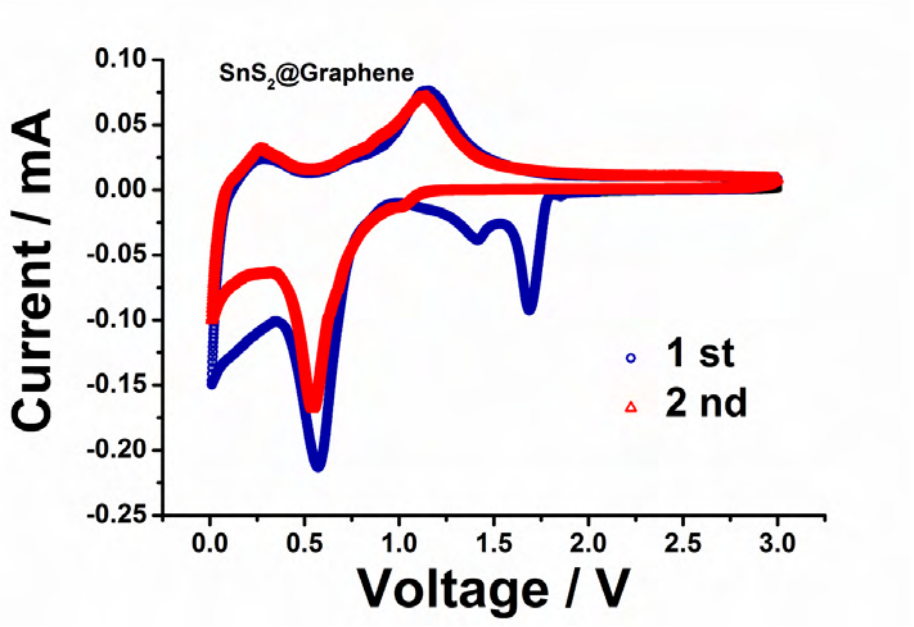

Figure 4.12 Cyclic voltammograms for the first 2 cycles of SnS_2@graphene electrode at a scanning rate of 0.1 mV s^{-1}.

The sodium ion storage behaviour of the composites was first characterized by cyclic voltammetry (CV) [**Figure 4.10 (a)**]. During the first negative scan, a strong reduction peak appeared at ~0.74 V and disappeared at the second negative scan, corresponding to the decomposition of electrolyte to form the solid-electrolyte interphase (SEI) film. Thus, after the first cycle, three pairs of oxidation/reduction peaks at 0.08 V/ 0 V, 0.24 V/ 0.15 V, and 0.70 V/ 0.66 V clearly emerged and then remained steady, representing the Na alloying/de-alloying reactions.[49] The peaks at 1.32 V/ 1.15 V in the CV curves can be attributed to the conversion reaction with sulphur atoms in the material, and the obvious platform represented by the charge-discharge plateaus also could confirm that the reaction between SnS and Sn is reversible. There is no obvious loss of area in the successive cycles, proving the good cycling stability of the composite. In the CV curves, it is worth noting that all the redox peaks of SnS@graphene composite are well matched to the charge-discharge plateaus [**Figure 4.10 (b)**]. And the SnS_2@graphene were much different from that of SnS@graphene, there is no plateau around 1.32 V/ 1.15 V in the curves of SnS_2@graphene, suggest that the reaction between SnS_2 and Sn is irreversible [**Figure 4.11 and 4.12**]. The basic reversible reactions of the composite are elucidated by Equations (4) and (5).

$$SnS + 2\,Na^+ + 2\,e^- \leftrightarrow Na_2S + Sn \quad (4)$$

$$4\,Sn + 15\,Na^+ + 15\,e^- \leftrightarrow Na_{15}Sn_4 \quad (5)$$

The electrochemical performance of the hybird SnS@graphene architecture was systematically evaluated by galvanostatic discharge-charge measurements. Remarkably, a very high capacity of 1437 mAh g^{-1} is achieved in the initial cycle at a

current density of 30 mA g^{-1}, in the case of the SnS@graphene architecture [**Figure 4.10 (c, d)**]. Even after 50 cycles, both the discharge and the charge capacities of this architecture are stable at about 940 mAh g^{-1}, delivering 92.4% of the 2nd cycle capacity (1037 mAh g^{-1}) [**Figure 4.10 (d)**]. It should be noted that a large capacity of nearly 1400 mA h g^{-1} is obtained for the SnS@Graphene electrode during the first discharge and charge processes. This may be partly attributed to both the presence of defects in the graphene and the disorder of the unique 2D structure of SnS. Moreover, the reversible formation/decomposition of the polymeric gel-like film on the surface of the active materials also contributed to the extra capacity, as reported elsewhere. [37, 39, 48] And in addition to the capacity comes from the alloying process of Sn, the reversible reaction between SnS and Sn also contributed to the capacity. (It is an interesting point as well for future studies to understand the reasons why extra sodium ions could be inserted into this hybrid material, and the relevant work is in progress.) These results are in stark contrast to the pure SnS_2 and the SnS_2@graphene architecture, which show continuous and progressive capacity decay as cycling progresses. More importantly, the as-prepared SnS@graphene architecture exhibits good high-rate performance. On increasing the current density to 810 and 7290 mA g^{-1} [**Figure 4.10 (e)**], the specific capacities at these current densities are still 492, and 308 mAh g^{-1} after 250 cycles, respectively. It is instructive to compare the performance of the SnS@graphene electrodes with the best systems reported in scientific literature. **Table 4.1** compares our results with the state-of the art in previously published research on Carbon, Sn, SnO_2, SnS_2, $Sn_4P_3$and MoS_2-based sodium ion battery anode materials. The performance of our prepared SnS@graphene architecture was found to be much better than those of most reported anode materials for Na ion batteries.

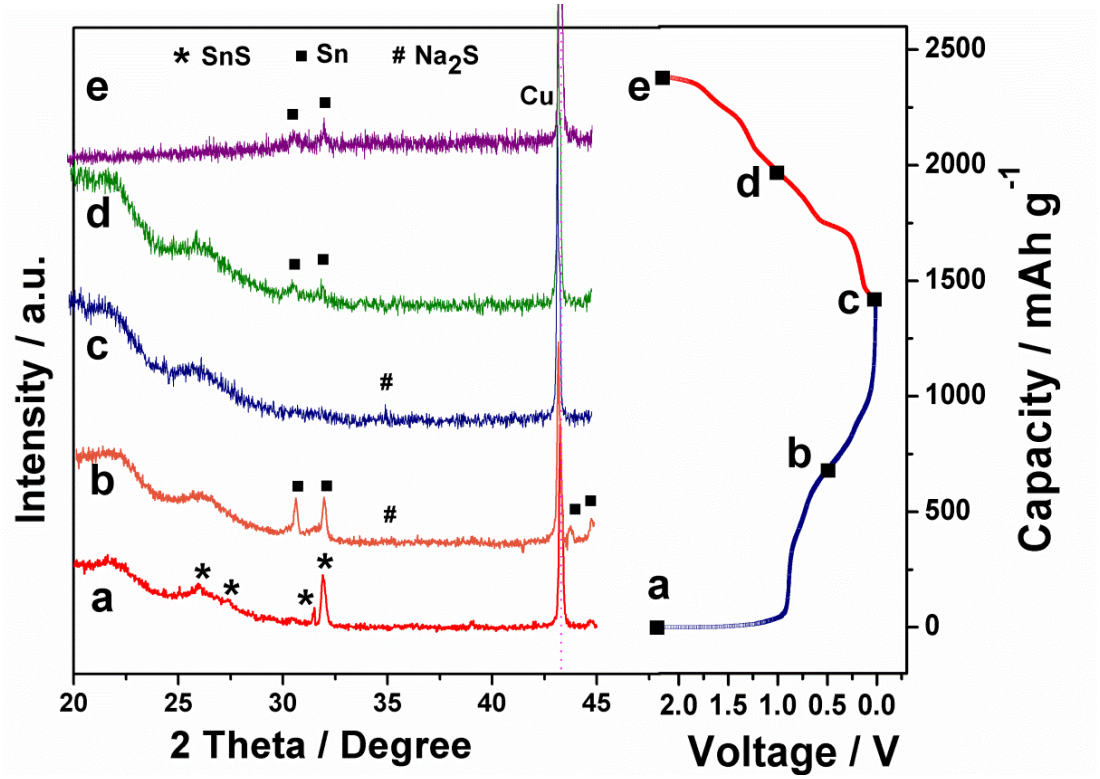

Figure 4.13 *Ex-situ* XRD patterns of the SnS@graphene electrode collected at various points as indicated in the corresponding voltage profile: (a) fresh electrode, (b) after 1st discharge to 0.5 V, (c) after 1st discharge to 0.01 V, (d) after 1st charge to 1.0 V, and (e) after 1st charge to 2.2 V.

In order to further clarify the structural changes upon sodiation/desodiation, *ex situ* XRD analysis of the SnS@graphene was performed, and it revealed that the reversible sodiation/desodiation of SnS proceeded in a two-phase reaction, as shown in **Figure 4.13**. The uncharged anode showed a clear XRD pattern of the SnS lattice [**Figure 4.13 (a)**]. Upon sodiation to 0.5 V, the intensity of the XRD peaks corresponding to SnS decreased [**Figure 4.13 (b)**], while the main reflections of Sn were observed, implying that the SnS lattice had transformed to metallic Sn and Na_2S phases at an initial stage of the Na insertion reaction, although no obvious Na_2S peaks were observed, which indicates that an amorphous Na_2S phase was formed

during sodiation, while nanocrystalline Na_xSn was not detectable by XRD owing to its very small crystallite size. When completely charged to a terminal potential of 0.01 V [**Figure 4.13 (c)**], the Na_2S signal became stronger, and the Sn signal disappeared, indicating that all of the Sn can participate in the Na-alloying reaction by the end of charge process. On desodiation, the intensity of the XRD peaks corresponding to Sn gradually increased [**Figure 4.13 (d, e)**], indicating that the conversion reaction of Sn to Na_2S and Na_xSn was reversible.

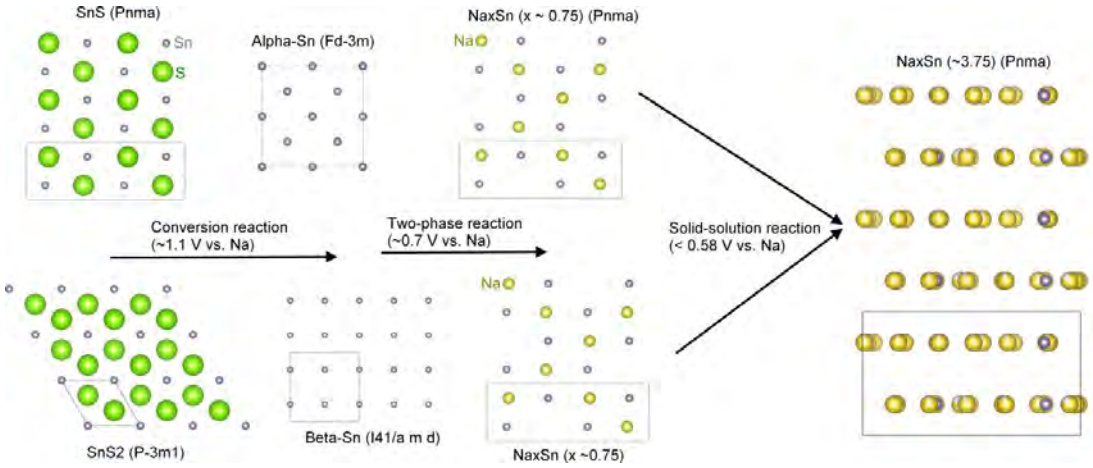

Figure 4.14 Schematic illustration of the structure evolution of orthorhombic-SnS and hexagonal-SnS_2 during the sodiation.

By combining the charge-discharge profiles [**Figure 4.10 (a, b, d)** and **Figures S5 and 4.12**] and the *ex-situ* X-ray diffraction study (**Figure 4.13**), we here propose a mechanism to illustrate the discharge process of SnS, which differs from that reported for SnS_2.[19] During discharging, the SnS anode is first reduced by Na ions through a conversion process, as described in Equation (4), resulting a flat plateau at 1.1 V (vs. Na). Alongside the S removal, the orthorhombic structure turns into a face-centered symmetry and forms alpha-Sn. [50] On further discharging to 0.7 V (vs.

Na), sodium ions intercalate into the Sn structure through a two-phase reaction and occupy the 4*c* site, which was the original site for S, forming an orthorhombic structure of Na_xSn alloy, which is isostructural to the original SnS, and the two-phase reaction results in a short plateau at around 0.7 V (*vs.* Na). As discharging continues down to 0.01 V (*vs.* Na), sodium ions occupy the other 4c sites via a solid-solution reaction, forming a sloping plateau-like feature.[8] The Na intercalation induces internal atomic rearrangement to minimize the strain and gradually form a huge orthorhombic structure, as recorded in ICSD#105168. On the other hand, hexagonal-SnS_2 transforms into beta-Sn with tetragonal structure and is followed by another two-phase reaction,[50] changing into orthorhombic $Na_{3.75}Sn$, so that it experiences a large lattice volume change (324% relative to SnS_2). The major difference between the discharging of SnS and that of SnS_2 is the formation of Sn after the conversion reaction. XRD patterns were obtained for SnS and SnS_2 electrodes after discharge/charge cycles (**Figure 4.15**). The stronger peak at $2\theta = 43°$ is attributed to the Cu foil electrode. The SnS_2 shows peaks at 30.47° and 31.90° corresponding to the (200) and (101) planes of beta-Sn. The alpha-Sn becomes the dominant phase for the SnS, as shown in the XRD pattern of the cell after matching to the (111) and (220) planes of alpha-Sn (JCPDS No. 87-0794; $a = 6.489$ *Å*). It can retain its crystallinity over repeated cycles, contributing to the excellent cycling performance. The total energy (E_{tot}, total energy of the most stable configuration of reaction products) difference between beta-Sn andorthorhombic-$Na_{3.75}Sn$ is 7.66 eV, higher than that of alpha-Sn (7.125 eV) (**Figure 4.18**).[50, 51] This is particularly important, as the alloying of Na with cubic-Sn (alpha) to form orthorhombic Na_xSn is easier than for tetragonal-Sn (beta), allowing higher intercalation capacity [**Figure 4.10 (d)**] as well as better rate capability [**Figure 4.10 (c)**]. The whole discharging process involves

lattice volume change [242% relative to SnS, smaller than that of Sn (420%)]; the structural change during conversion is two-phase, and the solid-solution reactions are smooth, leading us to expect good structural stability and excellent cycling stability, which agrees well with **Figure 4.10 (d)**. Compared to the Sn based anode materials, the potential advantages of SnS over Sn for Na insertion are: higher theoretical capacity than Sn because of the lower mass of the S atoms, as well as an expected improvement in mechanical stability due to smaller volume change during charge and discharge from the sulphides.[52] Moreover, sulphide formation is typically more reversible than oxide formation, resulting in a higher first cycle efficiency than for oxide materials. [51] From the perspective of structural stability during cycling, there is no doubt that SnS performs better than SnS_2 and Sn as an anode in the sodium ion battery.

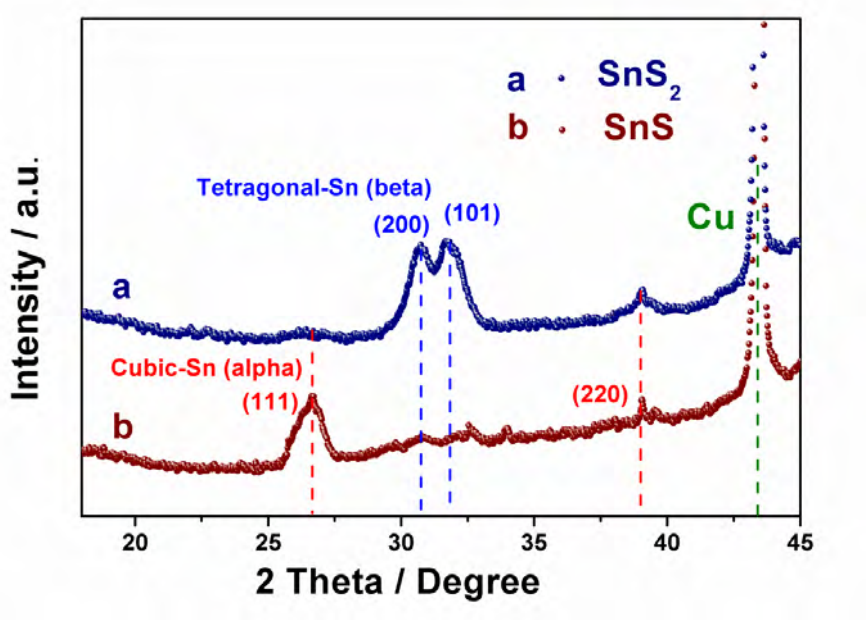

Figure 4.15 XRD patterns of the (a) SnS_2 and (b) SnS electrodes collected at after the 50th charge to 2.0 V.

Meanwhile, stable cycling of an electrode has strict requirements in terms of structural stability at the particle level, because even small changes in particle morphology could accumulate across the thickness of the electrode and cause electrode-level cracking and failure. After 20 deep cycles at the current density of 270 mA g^{-1}, the morphology of the SnS@graphene was examined with SEM. As the SEM micrographs in **Figure 4.16** demonstrate, intact graphene sheets with SnS inside are clearly visible. There are two interdependent characteristics of the two-layered compound design that enable superior battery performance. The first is the internally accommodated volume expansion and the structural compatibility within the two-layered hybrid SnS@graphene architecture, which retains the structural integrity of the secondary particles. The second characteristic is the porous SnS@graphene structure, which can effectively absorb the stress that is generated during charge and discharge. The reduced charge-transfer resistance compared to that of the SnS_2@graphene and bare SnS_2 electrodes is another factor, proving the high reactivity of the SnS@graphene electrode [**Figure 4.17(a)**]. This mechanism not only significantly stabilizes the mechanical, electrical, and electrochemical properties of the anode material, but also enables the inner void space to be retained.

Investigation of isolated active materials is no longer sufficient to solve all the different kinds of challenges for the development of large-scale energy storage. [53] In this work, we have optimized the composite electrode by using high tensile-strength binders, polyacrylic acid (PAA) and sodium carboxymethyl cellulose (CMC), both of which were used to improve the cycling performance of the Li-ion battery electrode materials with large volume expansion.[54, 55] Compared to the electrode using PAA-CMC as binder, the electrode prepared with polyvinylidene difluoride (PVdF)

exhibited severe capacity fading, which gave it much poorer performance than the cycling performance obtained with PAA-CMC binder [**Figure 4.17(b)**]. Additives such as fluoroethylene carbonate (FEC), which is known for stabilizing the SEI film in Na ion batteries, [56] were also introduced into the electrolyte [**Figure 4.17 7(c)**] in order to further improve its electrochemical performance.

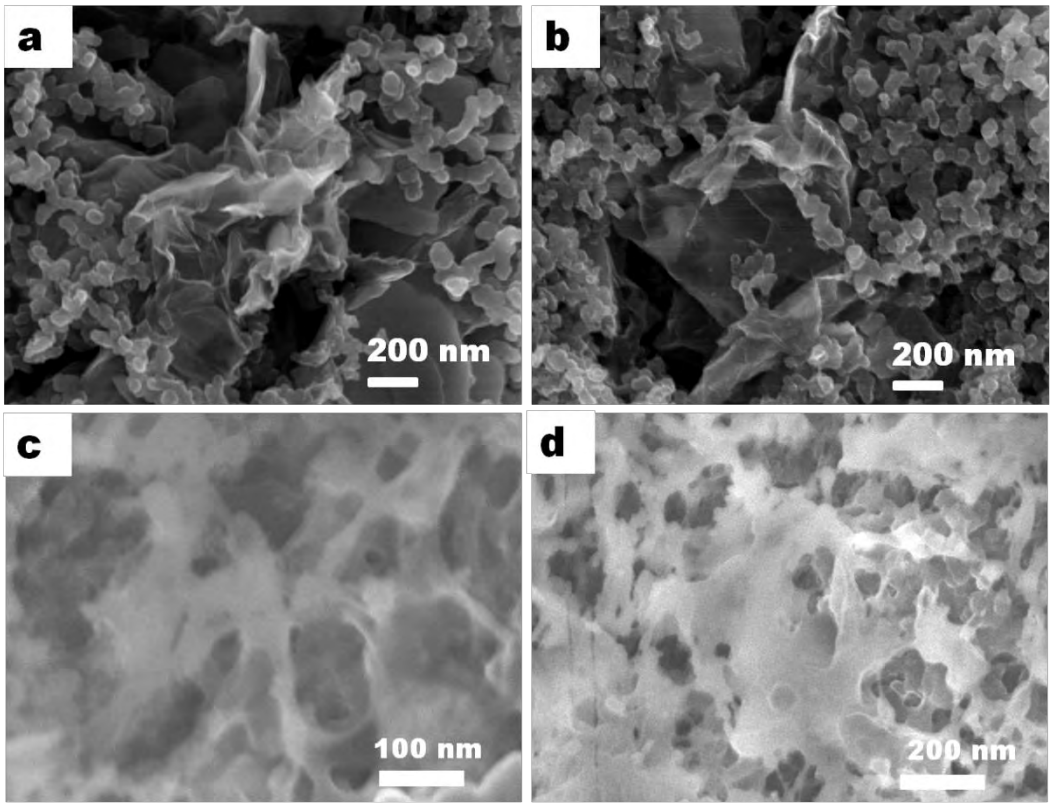

Figure 4.16 Typical SEM images of SnS@graphene electrode before (a) and after (b, c, d) 20 cycles at the current density of 270 mA g^{-1}.

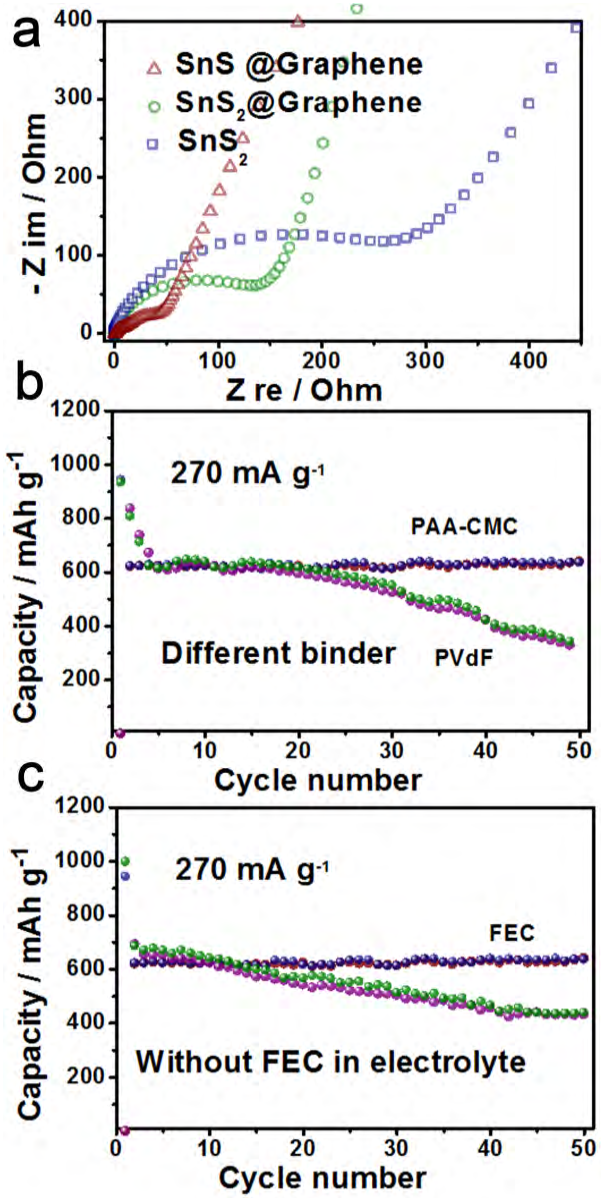

Figure 4.17 (a) Nyquist plots of electrodes containing hybrid SnS@graphene and SnS_2@graphene architectures, as well as bare SnS_2, obtained by applying a sine wave with an amplitude of 5.0 mV over the frequency range of 100 kHz–0.01 Hz. Representative cycling performances of electrodes with hybrid SnS@graphene architecture (b) with different binders and (c) with or without FEC in the electrolyte.

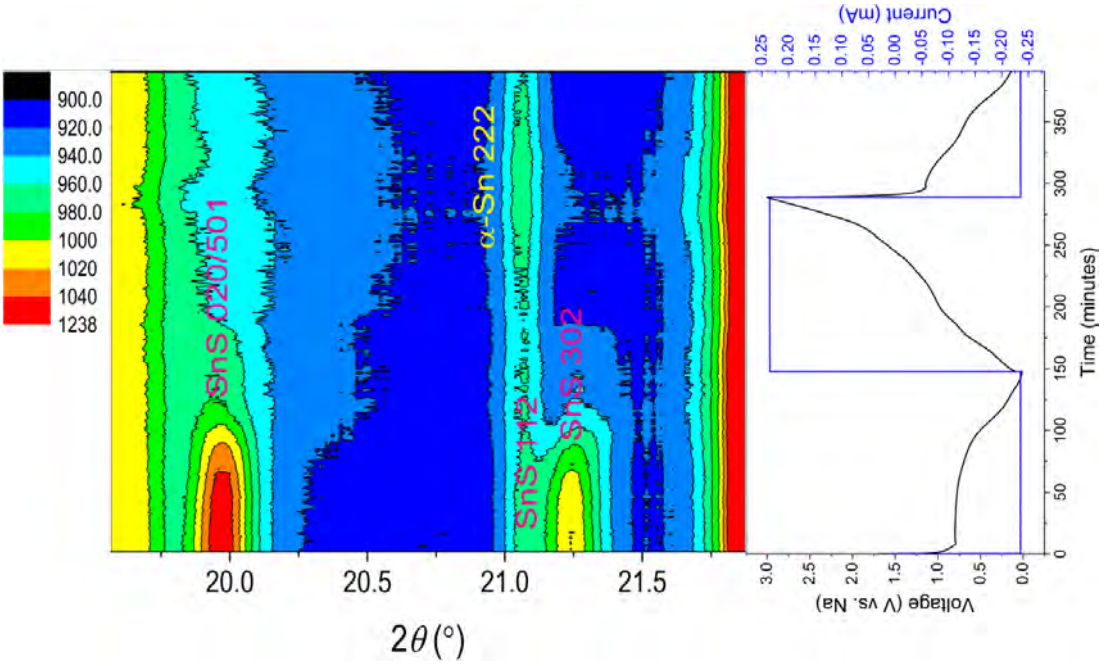

Figure 4.18 Contour plots of the operando synchrotron data of the SnS in sodium ion battery.

Table 4.1 Comparison of our best-performing materials with previously published Sn, SnO_2, SnS_2 and MoS_2-based sodium ion battery anodes, as well as some carbon nanostructures, in terms of capacity and rate capability.

Electrodes	**Cycling Capacity mAh g^{-1} (current density, mAg^{-1})**			**Rate Capability mAh g^{-1} (current density, mAg^{-1})**	
	Cycle number				
	1st	10 th	50 th		
SnS@Graphene (**This work**)	**1037** *30*	**1003** *30*	**940** *30*	**492** *810* *After 250 cycles*	**308** *7290* *After 250 cycles*
Hollow Carbon Nanowires[57]	251 50	~250 50	~240 50	149 500^1	n/a

Carbon Nanofibers[58]	~200 200	~180 200	175 200	~80 500	~60 2000
Graphene Oxide[59]	270 40	~212 40	~207 40	171 200	~100 1000
Mesoporous C/Sn Composite[60]	~300 20	~250 20	n/a	~70 800	~60 1000
Tin-Coated Viral Nanoforests [61]	~770 50	~580 50	~470 50	n/a	n/a
Sn @ Wood Fibers[62]	~350 84	~220 84	~250 84	~75 840	n/a
Sn/C Nanocomposite[63]	470 50	270 50	n/a	n/a	n/a
Sn-C Composite[64]	~240 100	~280 100	~220 100	~150 800	n/a
SnO_2@MWCNT Nanocomposite [65]	~500 (n/a) 0.1C	~450 (n/a) 0.1C	~380 (n/a) 0.1C	~310 (n/a) 0.5C	n/a
SnO_2–RGO Nanocomposite [66]	407 100	~500 100	~400 100	~200 500	~120 1000
SnO_2@graphene[67]	741 20	~720 20	~700 20	302 160	143 640
Sn_4P_3[68]	718 100	~700 100	700~ 100	n/a	n/a
$Sn_{4+x}P_3$	543	~540	~550	423.3	165

@Amorphous Sn-P[69]	100	100	100	500	5000
Sn_4P_3/C composite[70]	722 100	~600 100	~433 100	435 500	349 1000
SnS_2@Graphene[71]	750 20	~700 20	670 20	369 80	152 640
SnS_2@Graphene Oxide[72]	645 200	654 200	628 200	500 1000	~475 2000
Sn-SnS-C Composite[73]	~430 100	~425 100	~450 100	~350 800	n/a
MoS_2[74]	190 85	~120 85	~100 85	n/a	n/a
$MoS_{2@}$Graphene[75]	250 25	~240 25	n/a	180 150	150 200
MoS_2 Nanosheets[75]	165 20	161 20	161 20	140 400	120 800

After systematic design and optimization of the active materials, buffer layer, binder, conductive additive, and electrolyte, the capacity and high-rate performance of the SnS@graphene architecture are much better than for most reported anode materials for Na ion batteries. Such extraordinary performance and excellent capacity retention at high charge-discharge rates suggest that the hybrid SnS@graphene architecture has great potential for the anode material in Na-ion batteries. The unprecedented excellent electrochemical performance of SnS@graphene can be

attributed to the following reasons: (1) the structural compatibility within the two-layered hybrid SnS@graphene architecture and the excellent conductive electronic properties of the graphene network lead to very stable composites; (2) the porous structure of the composite electrode provides numerous channels to give access to the electrolyte, and the active framework made from filmy 2D SnS nanosheets provides a shortened ion diffusion path length; (3) the porous SnS@graphene structure can effectively absorb the stress which is generated during charge and discharge, while the structural stability of SnS layer structure should also be viable for reversible Na^+ storage, since in comparison to tin and other tin-based materials, it provides more buffering for the volume changes in Na-Sn reactions, so that acting together, they can perfectly maintain the structural stability of the whole electrode.

4.4 Conclusions

In summary, a hybrid SnS@graphene architecture, employing 2D nanosheets of SnS and graphene as complementary building blocks via their controllable assembly, was fabricated by a hydrothermal and annealing approach. The well-developed 2D nanosheets of SnS and graphene, as well as the precise hierarchical control of various sublayers of the materials in the design are believed to function synergistically, so as to significantly stabilize the mechanical, electrical, and electrochemical properties of the anode material, despite its large volume changes with sodiation/desodiation during cycling. From the perspective of structural ability during cycling, the less structural changes of SnS after the conversion, expected a good structural stability and excellent cycling stability for the performance on the sodium ion battery. The resultant architecture can provide high reversible capacity and excellent high-rate capability. The superior cycling and rate performance, combined with the simplicity

of the optimized process, represents a promising strategy for the development of inexpensive and versatile synthesis techniques for energy storage and conversion applications.

4.5 References

[1] Bruce, P. G.; Scrosati, B.; Tarascon, J. M. Angew. Chem. Int. Edit. 2008, 47, 2930-2946.

[2] Yang, Z. G.; Zhang, J. L.; Kintner-Meyer, M. C. W.; Lu, X. C.; Choi, D. W.; Lemmon, J. P.; Liu, J. Chem. Rev. 2011, 111, 3577-3613.

[3] Liu, J.; Zhang, J. G.; Yang, Z. G.; Lemmon, J. P.; Imhoff, C.; Graff, G. L.; Li, L. Y.; Hu, J. Z.; Wang, C. M.; Xiao, J.et al. Adv. Funct. Mater. 2013, 23, 929-946.

[4] Kim, S. W.; Seo, D. H.; Ma, X. H.; Ceder, G.; Kang, K. Adv. Energy Mater. 2012, 2, 710-721.

[5] Ellis, B. L.; Makahnouk, W. R. M.; Makimura, Y.; Toghill, K.; Nazar, L. F. Nat. Mater. 2007, 6, 749-753.

[6] Lu, Y. H.; Wang, L.; Cheng, J. G.; Goodenough, J. B. Chem. Commun. 2012, 48, 6544-6546.

[7] Ong, S. P.; Chevrier, V. L.; Hautier, G.; Jain, A.; Moore, C.; Kim, S.; Ma, X. H.; Ceder, G. Voltage, Energy Environ. Sci. 2011, 4, 3680-3688.

[8] Wang, J. W.; Liu, X. H.; Mao, S. X.; Huang, J. Y. Nano Lett. 2012, 12, 5897-5902.

[9] Xu, Y. H.; Zhu, Y. J.; Liu, Y. H.; Wang, C. S. Adv. Energy Mater. 2013, 3, 128-133.

[10] Liu, Y. H.; Xu, Y. H.; Zhu, Y. J.; Culver, J. N.; Lundgren, C. A.; Xu, K.; Wang, C. S. ACS Nano 2013, 7, 3627-3634.

[11] Xiao, L. F.; Cao, Y. L.; Xiao, J.; Wang, W.; Kovarik, L.; Nie, Z. M.; Liu, J. Chem. Commun. 2012, 48, 3321-3323.

[12] Park, J.; Kim, J. S.; Park, J.-W.; Nam, T. H.; Kim, K. W.; Ahn, J. H.; Wang, G.; Ahn, H. J. Electrochim. Acta 2013, 92, 427-432.

[13] Lu, J.; Nan, C. Y.; Li, L. H.; Peng, Q.; Li, Y. D. Nano Res. 2013, 6, 55-64.

[14] Seo, J. W.; Jang, J. T.; Park, S. W.; Kim, C. J.; Park, B. W.; Cheon, J. W. Adv. Mater. 2008, 20, 4269-4273.

[15] Mahmood, N.; Zhang, C. Z.; Hou, Y. L. Small 2013, 9, 1321-1328.

[16] Huang, G.; Chen, T.; Chen, W.; Wang, Z.; Chang, K.; Ma, L.; Huang, F.; Chen, D.; Lee, J. Y. Small 2013, 9, 3693-3703.

[17] Zhang, Y. W.; Tian, J. Q.; Li, H. Y.; Wang, L.; Qin, X. Y.; Asiri, A. M.; Al-Youbi, A. O.; Sun, X. P. Langmuir 2012, 28, 12893-12900.

[18] Qu, B.; Ma, C.; Ji, G.; Xu, C.; Xu, J.; Meng, Y. S.; Wang, T.; Lee, J. Y. Adv. Mater. 2014, 26, 3854-3859.

[19] Xie, X.; Su, D.; Chen, S.; Zhang, J.; Dou, S.; Wang, G. Chem.-Asian J. 2014, 9, 1611-1617.

[20] David, L.; Bhandavat, R.; Singh, G. ACS Nano 2014, 8, 1759-1770.

[21] Sathish, M.; Mitani, S.; Tomai, T.; Honma, I. J. Phys. Chem. C 2012, 116, 12475-12481.

[22] Kong, D.; He, H.; Song, Q.; Wang, B.; Yang, Q.-H.; Zhi, L. RSC Adv. 2014, 4, 23372-23376.

[23] Su, D.; Dou, S.; Wang, G. Chem. Commun. 2014, 50, 4192-4195.

[24] Deng, Z. T.; Cao, D.; He, J.; Lin, S.; Lindsay, S. M.; Liu, Y. Solution ACS Nano 2012, 6, 6197-6207.

[25] Zhang, Y. J.; Lu, J.; Shen, S. L.; Xu, H. R.; Wang, Q. B. Chem. Commun. 2011, 47, 5226-5228.

[26] Cao, T.; Wang, G.; Han, W.; Ye, H.; Zhu, C.; Shi, J.; Niu, Q.; Tan, P.; Wang, E.; Liu, B.; Feng, J. Nat. Commun. 2012, 3, 887.

[27] Zeng, H.; Dai, J.; Yao, W.; Xiao, D.; Cui, X. Nat. Nanotechnol. 2012, 7, 490-493.

[28] Mak, K. F.; He, K.; Shan, J.; Heinz, T. F. Nat. Nanotechnol. 2012, 7, 494-498.

[29] Wei, R.; Hu, J.; Zhou, T.; Zhou, X.; Liu, J.; Li, J. Acta Mater. 2014, 66, 163-171.

[30] Wei, R.; Zhou, T.; Hu, J.; Li, J. Mater. Res. Exp. 2014, 1, 025018.

[31] Biacchi, A. J.; Vaughn, D. D.; Schaak, R. E. J. Am. Chem. Soc. 2013, 135, 11634-11644.

[32] Meyer, J. C.; Geim, A. K.; Katsnelson, M. I.; Novoselov, K. S.; Booth, T. J.; Roth, S. Nature 2007, 446, 60-63.

[33] Bertolazzi, S.; Brivio, J.; Kis, A. ACS Nano 2011, 5, 9703-9709.

[34] Zhang, B.; Ye, X. C.; Dai, W.; Hou, W. Y.; Xie, Y. Chem.-Eur. J. 2006, 12, 2337-2342.

[35] Chang, K.; Chen, W. X. ACS Nano 2011, 5, 4720-4728.

[36] Chhowalla, M.; Shin, H. S.; Eda, G.; Li, L.-J.; Loh, K. P.; Zhang, H. Nat. Chem. 2013, 5, 263-275.

[37] Gong, Y.; Yang, S.; Liu, Z.; Ma, L.; Vajtai, R.; Ajayan, P. M. Adv. Mater. 2013, 25, 3979-84.

[38] Fasolino, A.; Los, J. H.; Katsnelson, M. I. Nat. Mater. 2007, 6, 858-861.

[39] Chen, Z.; Yuan, Y.; Zhou, H.; Wang, X.; Gan, Z.; Wang, F.; Lu, Y. Adv. Mater. 2014, 26, 339-345.

[40] Arico, A. S.; Bruce, P.; Scrosati, B.; Tarascon, J. M.; Van Schalkwijk, W. Nat. Mater. 2005, 4, 366-377.

[41] Xiang, J. H.; Cao, H. Q.; Wu, Q. Z.; Zhang, S. C.; Zhang, X. R.; Watt, A. A. R. J. Phys. Chem. C 2008, 112, 3580-3584.

[42] Liu, Y.; Ma, W. S.; Liu, W. W.; Li, C.; Liu, Y. L.; Jiang, X. Y.; Tang, Z. Y. J. Mater. Chem. 2011, 21, 19214-19218.

[43] Xu, Y.; Zhao, W. W.; Xu, R.; Shi, Y. M.; Zhang, B. Chem. Commun. 2013, 49, 9803-9805.

[44] Aso, K.; Kitaura, H.; Hayashi, A.; Tatsumisago, M. J. Mater. Chem. 2011, 21, 2987-2990.

[45] Fernandes, P. A.; Sousa, M. G.; Salome, P. M. P.; Leitao, J. P.; da Cunha, A. F. CrystEngComm 2013, 15, 10278-10286.

[46] Wiedemeier, H.; Pultz, G. Zeit. Anorgan. Allgeme. Chem. 1983, 499, 130-144.

[47] Zhou, X. L.; Zhou, T. F.; Hu, J. C.; Li, J. L. CrystEngComm 2012, 14, 5627-5633.

[48] Luo, B.; Fang, Y.; Wang, B.; Zhou, J. S.; Song, H. H.; Zhi, L. J. Energy Environ. Sci. 2012, 5, 5226-5230.

[49] Chevrier, V. L.; Ceder, G. J. Electrochem. Soc. 2011, 158, A1011-A1014.

[50] Im, H. S.; Cho, Y. J.; Lim, Y. R.; Jung, C. S.; Jang, D. M.; Park, J.; Shojaei, F.; Kang, H. S. ACS Nano 2013.

[51] Cho, Y. J.; Im, H. S.; Kim, H. S.; Myung, Y.; Back, S. H.; Lim, Y. R.; Jung, C. S.; Jang, D. M.; Park, J.; Cha, E. H.; Cho, W. I.; Shojaei, F.; Kang, H. S. ACS Nano 2013, 7, 9075-9084.

[52] Yu, D. Y. W.; Prikhodchenko, P. V.; Mason, C. W.; Batabyal, S. K.; Gun, J.; Sladkevich, S.; Medvedev, A. G.; Lev, O. Nat. Commun. 2013, 4.

[53] Wang, L.; Wang, D.; Dong, Z.; Zhang, F.; Jin, J. Small 2014, 10, 998-1007.

[54] Sun, Y.; Zhao, L.; Pan, H. L.; Lu, X.; Gu, L.; Hu, Y. S.; Li, H.; Armand, M.; Ikuhara, Y.; Chen, L. Q.; Huang, X. J. Nat. Commun. 2013, 4.

[55] Koo, B.; Kim, H.; Cho, Y.; Lee, K. T.; Choi, N. S.; Cho, J. Angew. Chem. Int. Edit. 2012, 51, 8762-8767.

[56] Oh, S. M.; Myung, S. T.; Jang, M. W.; Scrosati, B.; Hassoun, J.; Sun, Y. K. Phys. Chem. Chem. Phys. 2013, 15, 3827-3833.

[57] Cao, Y.; Xiao, L.; Sushko, M. L.; Wang, W.; Schwenzer, B.; Xiao, J.; Nie, Z.; Saraf, L. V.; Yang, Z.; Liu, J. Nano Lett. 2012, 12, 3783-3787.

[58] Luo, W.; Schardt, J.; Bommier, C.; Wang, B.; Razink, J.; Simonsen, J.; Ji, X. J. Mater. Chem. A 2013, 1, 10662-10666.

[59] Wang, Y. X.; Chou, S. L.; Liu, H. K.; Dou, S. X. Carbon 2013, 57, 202-208.

[60] Palomares, V.; Casas-Cabanas, M.; Castillo-Martinez, E.; Han, M. H.; Rojo, T. Sci. 2013, 6, 2312-2337.

[61] Liu, Y. H.; Xu, Y. H.; Zhu, Y. J.; Culver, J. N.; Lundgren, C. A.; Xu, K.; Wang, C. S. ACS Nano 2013, 7, 3627-3634.

[62] Zhu, H.; Jia, Z.; Chen, Y.; Weadock, N.; Wan, J.; Vaaland, O.; Han, X.; Li, T.; Hu, L. Nano Lett. 2013, 13, 3093-3100.

[63] Datta, M. K.; Epur, R.; Saha, P.; Kadakia, K.; Park, S. K.; Kumta, P. N. J. Power Sources 2013, 225, 316-322.

[64] Wu, L.; Hu, X. H.; Qian, J. F.; Pei, F.; Wu, F. Y.; Mao, R. J.; Ai, X. P.; Yang, H. X.; Cao, Y. L. J. Mater. Chem. A 2013, 1, 7181-7184.

[65] Wang, Y.; Su, D.; Wang, C.; Wang, G. Electrochem. Commun. 2013, 29, 8-11.

[66] Wang, Y. X.; Lim, Y. G.; Park, M. S.; Chou, S. L.; Kim, J. H.; Liu, H. K.; Dou, S. X.; Kim, Y. J. J. Mater. Chem. A 2014, 2, 529-534.

[67] Su, D.; Ahn, H.-J.; Wang, G. Chem. Commun. 2013, 49, 3131-3133.

[68] Qian, J.; Xiong, Y.; Cao, Y.; Ai, X.; Yang, H. Nano Lett. 2014, 14, 1865-1869.

[69] Li, W.; Chou, S. L.; Wang, J. Z.; Kim, J. H.; Liu, H. K.; Dou, S. X. Adv. Mater. 2014, DOI: 10.1002/adma.201400794.

[70] Kim, Y.; Kim, Y.; Choi, A.; Woo, S.; Mok, D.; Choi, N.-S.; Jung, Y. S.; Ryu, J. H.; Oh, S. M.; Lee, K. T. Adv. Mater. 2014, 26, 4139-4144.

[71] Xie, X.; Su, D.; Chen, S.; Zhang, J.; Dou, S.; Wang, G. Chem. –Asian J. 2014, 9, 1611-1617.

[72] Qu, B.; Ma, C.; Ji, G.; Xu, C.; Xu, J.; Meng, Y. S.; Wang, T.; Lee, J. Y. Adv. Mater. 2014, 26, 3854-3859.

[73] Park, J.; Kim, J. S.; Park, J. W.; Nam, T. H.; Kim, K.-W.; Ahn, J. H.; Wang, G.; Ahn, H. J. Electrochim. Acta 2013, 92, 427-432.

[74] David, L.; Bhandavat, R.; Singh, G. ACS Nano 2014, 8, 1759-1770.

[75] Bang, G. S.; Nam, K. W.; Kim, J. Y.; Shin, J.; Choi, J. W.; Choi, S. Y. ACS App. Mater. Inter. 2014, 6, 7084-7089.

CHAPTER 5 BOOSTED CHARGE TRANSFER IN SNS/SNO2 HETEROSTRUCTURES: TOWARD HIGH RATE CAPABILITY FOR SODIUM-ION BATTERIES

Constructing hetero-nanostructure can endow nanomaterials fascinating performance in terms of high-speed electronics, optoelectronics and other aspects because of the built-in charge transfer driving force which is of benefit to the specific charge-transfer kinetics. Rational design and controllable synthesis of nano-heterostructure anode materials with high-rate performance, however, still remains a great challenge. Here, ultrafine SnS/SnO_2 heterostructures were successfully achieved and thus lead to boosted charge transfer within the nanocrystals. The mobility enhancement are attributed to reduction of the charge center scattering and interface effect of heterostructures, which induce an electric field within the nanocrystals, making them with much lower ion diffusion resistance, facilitates interfacial electron transport at the SnS/SnO_2 heterointerfaces. The electrical integrity of the electrode via the interfacial amorphous carbon layer anchoring the SnS/SnO_2 heterostructures directly to the graphene can be effectively retained. Enhancement in the electrochemical performance can be reflected by the excellent cycling stability (~73% retention after 500 cycles at 810 mA g^{-1}) and high rate capability (473 mA h g^{-1} at 2430 mA g^{-1}) of the C@SnS/SnO_2@graphene heterostructures.

5.1 Introduction

Rechargeable sodium-ion batteries have attracted a great deal of research interest as a promising alternative to lithium-ion batteries, owing to the low cost and abundant resources of sodium.[1-3] Inspired by the existing lithium ion battery technology, various attempts have been made to adapt anode materials for Li-ion chemistry to Na-based system. Unfortunately, most of the investigated anode materials suffer from lower specific capacity, poor rate capability and shorter cycling life, because Na^+ ions feature a larger ionic radius and molar mass than Li^+ ions.[4,5]

Currently, searching for a suitable anode material with excellent performance to meet the increasing demands for large-scale energy storage applications is still the major challenge. Although considerable research has been devoted to exploring new anode materials with high specific capacity or good cycling stability for application in Na-ion batteries,[6,7] rather less attention has been paid to the high-rate capacity which is a quite important aspect of performance for practical applications. Therefore, the rational design and controllable synthesis of anode materials with high-rate performance and superior cycle life are highly desirable. To obtain viable anode materials with high-rate capacity, it is particularly important to choose appropriate host materials with high theoretical sodium storage capacity as the building blocks. Among the limited number of Na-storage anode materials, SnO_2 has been extensively investigated due to its high theoretical capacity (~667 mA h g^{-1}) and abundance.[8,9] Practical applications of SnO_2 materials are seriously limited, however, by its poor intrinsic conductivity, low initial coulombic efficiency and inferior cycling stability.[10-12] Besides SnO_2, the unique layered structure with large

interlayer spacing and high reversible capacity of SnS make it another highly promising candidate,[13,14] Compared to metal oxide anodes, the corresponding metal sulfide possesses smaller band-gap energy and higher electrical conductivity, since the metal-sulfur bond is more covalent than the metal-oxygen bond.[15,16] Furthermore, SnS compound has higher reversibility than its equivalent oxide,[17,18] thus ensuring higher initial coulombic efficiency and reversible capacity.

Heterostructures have great potential applications ranging from high-speed electronics to optoelectronics devices because of their interface effects, giving unprecedented properties at interfaces.[19-21] It has been demonstrated that creating heterostructures by coupling nanocrystals with different band gaps will enhance the surface reaction kinetics and facilitate charge transport due to the internal electric field at heterointerfaces.[22] Wang et al. reported the ultrafast charge transfer in atomically thin MoS_2/WS_2 heterostructures.[23] Walukiewicz et al. investigated the charge transfer effects at the interfaces of CdO/SnTe heterostructures and found a large 4-fold enhancement of the electron mobility, which can be attributed to reduction of the charge center scattering.[24] Shao et al. designed a TiO_2(B)/anatase mixed-phase system with high Li storage capacity and excellent high-rate cycling capability, benefiting from the synergistic effects of the TiO_2(B)/anatase, which can enhance the Li^+ diffusion kinetics and electronic conductivity.[25]

Thus, from the perspective of enhancing the electronic conductivity and sodium-ion diffusion capability of anode materials, the skillful design and fabrication of a complex architecture by employing the SnS/SnO_2 heterostructure, might be a feasible strategy for a built-in charge transfer driving force, which will facilitate ion/electron diffusion during the cycling process. Nevertheless, to the best of our knowledge,

there is no report regarding the synthesis of SnS/SnO_2 hetero-nanostructures as anode material for Na-ion batteries. Herein, we proposed a unique architecture for amorphous carbon covered SnS/SnO_2 heterostructures anchored to graphene, which exhibited a remarkable high rate capability and ultra-long cycle life as anode for sodium-ion batteries.

5.2 Experimental methods

5.2.1 Materials Synthesis

5.2.1.1 Synthesis of C@SnO_2@Gr

The graphite oxide was prepared by a modified Hummers' method. SnO_2 nanoparticles were grown onto the GO nanosheets by a hydrothermal method. In a typical process, 0.25g $SnCl_2 \cdot 2H_2O$ was firstly dissolved in 20 mL ethanol to yield a clear solution. Then, 20 mL ethanol solution containing 40 mg GO was added into the clear solution under magnetic stirring for 20 minutes. The resultant solution was then transferred to an autoclave, which was kept in an oven at 160 ℃ for 10 h. The resultant product was separated and washed several times by centrifugation with de-ionized water after the autoclave was cooled down naturally. Subsequently, the products were dispersed in 20 mL de-ionized water via ultrasonication for 15 min. After the ultrasonication, 0.3 g glucose was added into the solution with a following vigorous stirring for 20 min. Then, the solution was transferred to an autoclave and kept in an oven at 160 ℃ for 10h. The product was obtained by centrifugation, with several washings in de-ionized water after the autoclave was cooled down. The resultant composite was dried at 70 ℃ under vacuum conditions for 12 h, followed by heating in a tube furnace under argon atmosphere at 500 ℃ for 5 h, yielding carbon-coated graphene tin oxide (C@SnO_2@Gr).

5.2.1.2 Synthesis of C@SnS/SnO_2@Gr

A simple sulfidation method was utilized to transform the surface SnO_2 to SnS. For the sulfidation process, a small quartz crucible containing the obtained C@SnO_2@Gr was loaded into a larger quartz boat. An excessive amount of thiourea was loaded onto the boat on the outside of the small quartz crucible for sulfidation of the SnO_2. The loaded boat was put into a tube furnace and heated at 350 °C for 6 h under argon. When the temperature was increased to 350 °C, the thiourea powder was melted, which produced hydrogen sulfide gas. The flow rate of argon, which was used as the carrier gas, was 200 mL min^{-1}. The final product was carbon-coated SnS/SnO_2@Gr composite (C@SnS/SnO_2@Gr).

5.2.1.3 Synthesis of C@SnS@Gr

The SnS@Gr composite was firstly synthesized through a hydrothermal treatment. 40 mg GO was dispersed in 40 mL ethylene glycol solution by ultrasonication for 2 h. Then 0.25 g tin chloride dihydrate and 0.084 g thiourea were dissolved in the above ethanol solution under magnetic stirring for 1 h. After that, the mixed solution was transferred to an autoclave and kept in an oven at 180 °C for 12 h. The product was obtained by centrifugation, with several washings in de-ionized water after the autoclave was cooled down. The C@SnS@Gr sample was prepared under the same procedure by coating a carbon layer on the SnS@Gr nanosheets.

5.2.1.4 Synthesis of C@SnS+SnO_2@Gr

The C@SnS+SnO_2@Gr mixture was synthesized by mixing the as-prepared C@SnO_2@Gr and C@SnS@Gr samples in a weight ratio of 1:1.

5.2.2 Materials Characterization

The crystalline structure of the as-prepared material was characterized by X-ray diffraction (XRD; GBC MMA diffractometer) with Cu Kα radiation at a scanning rate of 1° min^{-1}. (Rigaku Mini Flex 600). The morphologies and particle sizes of the samples were observed by field emission scanning electron microscopy (FE-SEM; FEI-NOVA NanoSEM 450 and Magellan, FEI, USA). The details of the crystal structure were further characterized by transmission electron microscopy (TEM), which was conducted on a Philips Tecnai 20 TEM operating at 200 kV. The TEM was linked to an energy dispersive spectral analysis (EDS) system. X-ray photoelectron spectroscopy (XPS) was conducted on a VG Multilab 2000 (VG Inc.) photoelectron spectrometer using monochromatic Al Kα radiation under vacuum at 2 × 10^{-6} Pa. All of the binding energies were referenced to the C 1s peak at 284.8 eV of the surface adventitious carbon. Raman analysis was performed with a JobinYvon HR800 Raman spectrometer. The thermal properties of the as-prepared samples were characterized by thermogravimetric analysis (TGA; TA Instruments 2000) under air over a temperature range of 50–800 ℃ with a ramp rate of 10 °C min^{-1}.

5.2.3 Electrochemical measurements

The electrochemical tests were carried out via CR2032 coin-type cells. The working electrodes were prepared by mixing the as-prepared materials, Super P, and sodium carboxymethyl cellulose/poly(acrylic acid) (1:1) in a weight ratio of 80:10:10. The resultant slurry was pasted on Cu foil and dried in a vacuum oven at 80 °C for 12 h, followed by pressing at 300 kg/cm^2. The mass loading of the materials on individual electrodes was about 1.0 ± 0.2 mg cm^{-2}. Electrochemical measurements were carried out using two-electrode coin cells with Na metal as counter and

reference electrode and glass microfiber (Whatman) film as the separator. The electrolyte consisted of a solution of 1 M $NaClO_4$ in ethylene carbonate/ diethyl carbonate (1/1; v/v) with 5 wt % fluoroethylene carbonate. Electrochemical impedance spectroscopy and cyclic voltammetry were conducted on a VMP-3 electrochemical workstation at a scan rate of 0.1 mV s^{-1}. The cells were galvanostatically charged and discharged over a voltage range of 0.01–2 V versus Na/Na^+ at different constant current densities, based on the weight of the samples, on a Land CT2001A battery tester. At least five parallel cells were tested for each electrochemical measurement, in order to make sure that the results were reliable and represented the typical behaviour of the samples.

5.3 Results and Discussion

The formation procedure for the C@SnS/SnO_2@Gr architecture (Gr=graphene) is shown in **Figure 5.1**. First, graphene oxide was synthesized by a modified Hummers' method. Second, tin oxide was grown onto the graphene by a hydrothermal method.[26] Subsequently, amorphous carbon was anchored to the SnO_2@Gr surface. Finally, C@SnS/SnO_2@Gr was obtained by a sulfidation process of as-prepared C@SnO_2@Gr with thiourea at 350 °C under argon condition.

The purity and crystalline phase of the samples were analyzed by powder X-ray diffraction (XRD). **Figure 5.2 a** presents XRD patterns of the C@SnO_2@Gr and C@SnS/SnO_2@Gr powders. All of the diffraction peaks in pattern A of **Figure 5.2 a** can be indexed to tetragonal rutile SnO_2,[26] indicating that pure and single-phase SnO_2 was prepared. After sulfidation, apart from the SnO_2 diffraction peaks, some entirely new peaks are observed (pattern B in **Figure 5.2 a**), which can be assigned

to the orthorhombic-SnS,[13] and no peaks for other impurities are found, revealing the coexistence of SnS and SnO_2. Moreover, the broadened diffraction peaks in pattern B indicate that the ultra-small particle size was not increased after sulfidation.

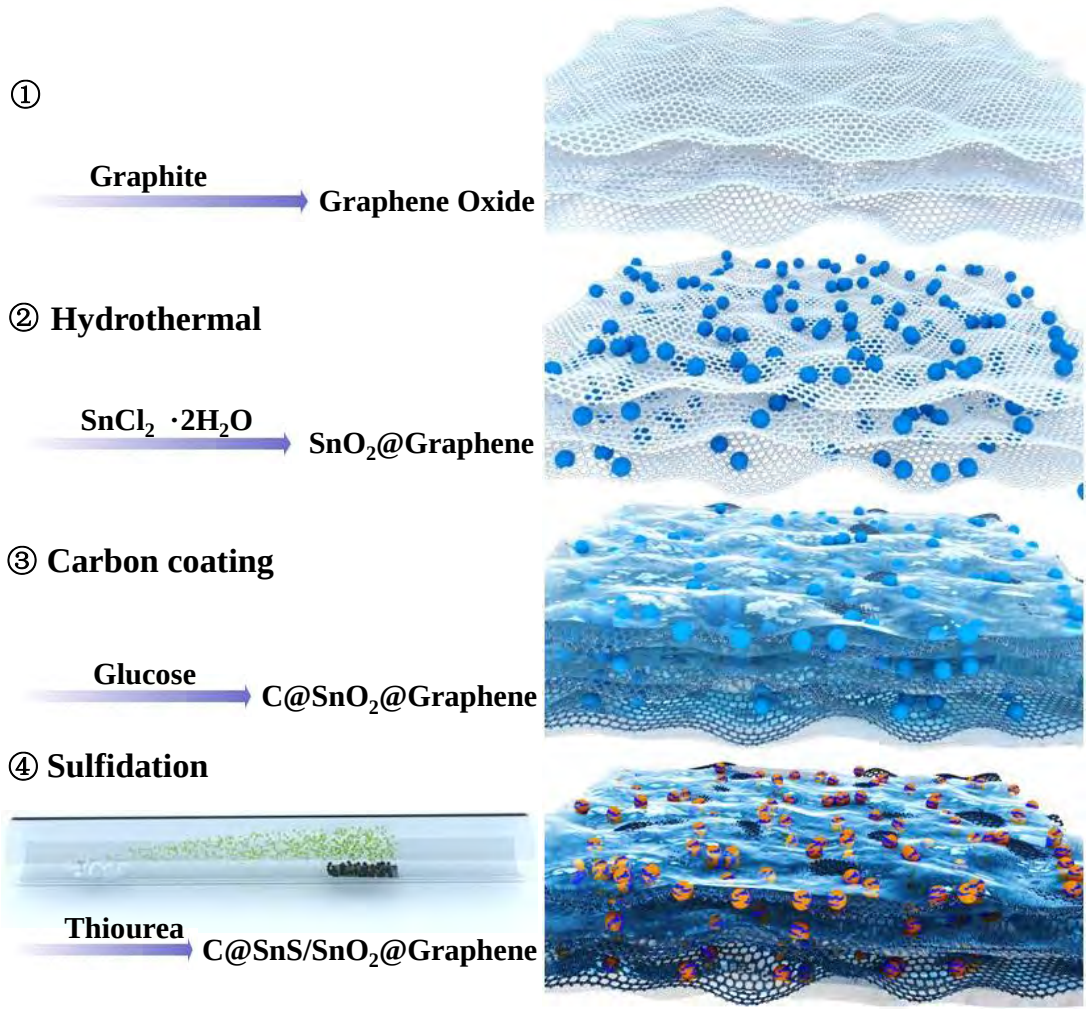

Figure 5.1 Schematic illustration of the formation procedure of the C@SnS/SnO2@Gr architecture.

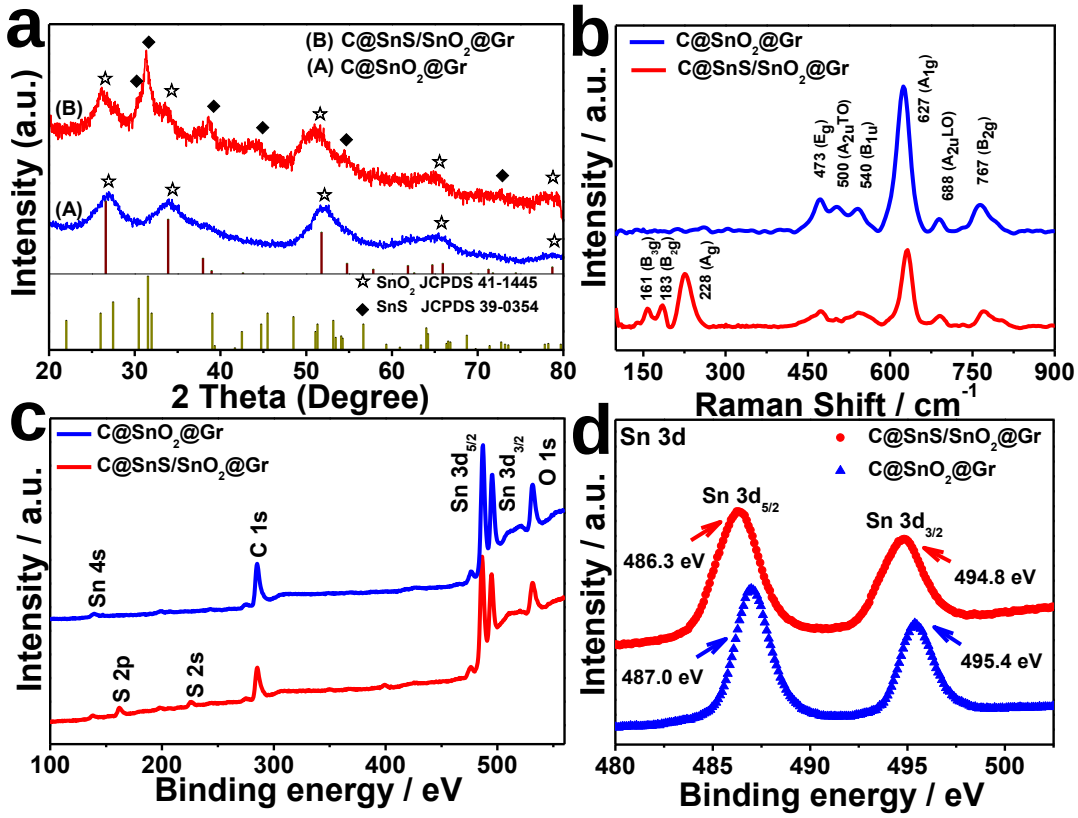

Figure 5.2 a) X-ray diffraction patterns of (A) C@SnO_2@Gr and (B) C@SnS/SnO_2@Gr. b) Room temperature Raman spectra of C@SnO_2@Gr and C@SnS/SnO_2@Gr samples. c) Typical XPS survey spectra and d) the corresponding Sn 3d XPS spectra of C@SnO_2@Gr and C@SnS/SnO_2@Gr.

Figure 5.2 b, and **Figure 5.3** shows the Raman spectra of the as-prepared samples. As shown in **Figure 5.2 b**, three fundamental peaks can be observed at 472 cm^{-1}, 631 cm^{-1}, and 774 cm^{-1} 473, 627, 767 in **Figure 5.2 b** in both the C@SnO2@Gr and the C@SnS/SnO_2@Gr materials, corresponding to the Eg, A1g, and B2g vibrations of SnO_2.[27, 28] Moreover, three typical Raman scattering peaks at 161, 183, and 228 cm^{-1} are identified for the C@SnS/SnO_2@Gr sample, which can be attributed to the B3g, B2g, and Ag vibrational modes of SnS, respectively.[29, 30] These peaks further confirm the successful formation of SnS in the C@SnO_2@Gr composite after the

sulfidation process. Note that the intensities of peaks from the SnO_2 in the C@SnS/SnO_2@Gr sample are reduced, owing to the interaction between SnO_2 and the in-situ generated SnS, which may diminish both the excitation laser and the emitted Raman signals.[28]

X-ray photoelectron spectroscopy (XPS) was conducted to investigate the surface electronic states and chemical compositions of the synthesized samples (**Figure 5.2 d**, **Figure 5.4**). It can be seen that the C@SnO_2@Gr sample (the top curve in **Figure 5.2 c**) only contains the elements Sn, O, and C, with photoelectron peaks appearing at binding energies of 487 (Sn 3d5/2), 495 (Sn 3d3/2), 531 (O1s), and 285 eV (C1s), respectively.[30] Compared with the spectrum of C@SnO_2@Gr, two additional peaks at 163 eV (S 2p) and 228 eV (S 2s) can be found in the survey spectrum of the C@SnS/SnO_2@Gr sample, suggesting the successful incorporation of S into the C@SnO_2@Gr hybrid.[13] As shown in **Figure 5.2 d**, the two peaks of Sn 3d for C@SnS/SnO_2@Gr both shifted to lower binding energies, as a result of the coupling effect of SnO_2 (Sn^{4+}) and SnS (Sn^{2+}) in the SnS/SnO_2 heterostructures. The peaks of 495.3 eV and 486.9 eV are ascribed to Sn $3d_{3/2}$ and $3d_{5/2}$ of Sn^{4+}, respectively, while the peaks 494.3 eV and 485.9 eV should be assigned to Sn $3d_{3/2}$ and $3d_{5/2}$ of Sn^{2+}, confirming the formation of the SnS/SnO_2 heterostructures. Moreover, the Sn^{2+}/Sn^{4+} ratio measured with XPS analysis is estimated to be around 1.1, which is consistent with the result of EDS spectrum (**Figure 5.5**). After the sulfidation reaction, the in-situ formation of SnS with the lower chemical valence and lower electronegativity of S occurred in close contact with SnO_2 at the boundaries, where the interaction between different orbitals of SnS and SnO_2 will alter the electronic states and band structure because of the conduction band and valence band potentials.[22, 31] This

would be beneficial for the enhancement of charge-transfer kinetics in electrochemical reactions.[22, 24]

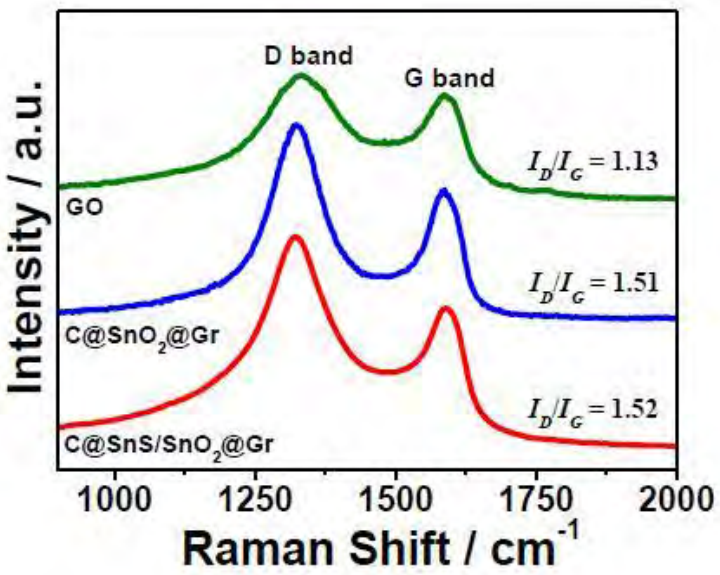

Figure 5.3 Raman spectra of graphene oxide, C@SnO_2@Gr and C@SnS/SnO_2@Gr. Two obvious carbon bands, the D band and G band peaks, can be observed for all samples. The peak at about 1592 cm^{-1} (G band) is related to the vibration of sp2-bonded carbon atoms in a 2-dimensional hexagonal lattice, while the 1334 cm^{-1} peak (D band) could be related to the defects and disorder in the hexagonal graphitic layers. The intensity ratio of the D to the G band (ID/IG) of GO is calculated as 1.13. For the C@SnO_2@Gr and C@SnS/SnO_2@Gr, however, the intensity ratios increased to about 1.51 and 1.52, respectively, demonstrating the GO reduction during the solvothermal process.

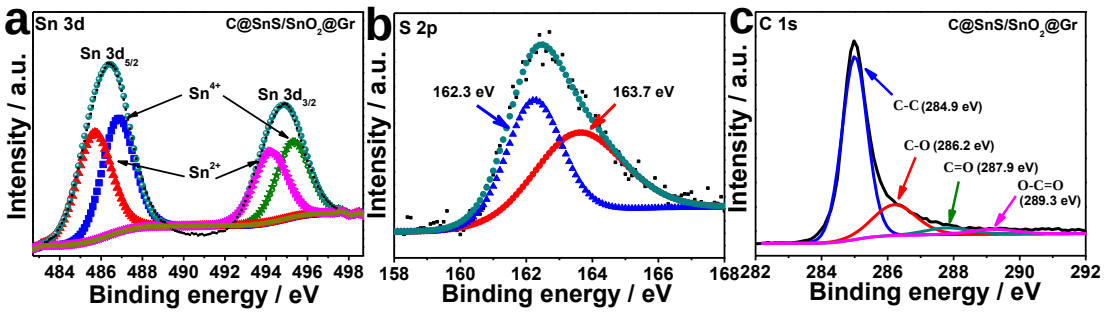

Figure 5.4 a) Sn 3d, b) S 2p and c) C1s region XPS spectrums of C@SnS/SnO_2@Gr. The peaks of Sn $3d_{3/2}$ (495.3 eV) and $3d_{5/2}$ (486.9 eV) should be derived from SnO_2, while the peaks 494.3 eV and 485.9 eV can be assigned to Sn $3d_{3/2}$ and $3d_{5/2}$ of SnS. The S 2p spectrum can be deconvolved into two peaks at 162.3 and 163.7 eV, which is attributed to the binding energies of S $2p_{3/2}$ and S $2p_{1/2}$, indicating the presence of SnS in the composite. The XPS spectrum of C 1s displays four fitted peaks at 284.9, 286.2, 287.9, and 289.3 eV, respectively.

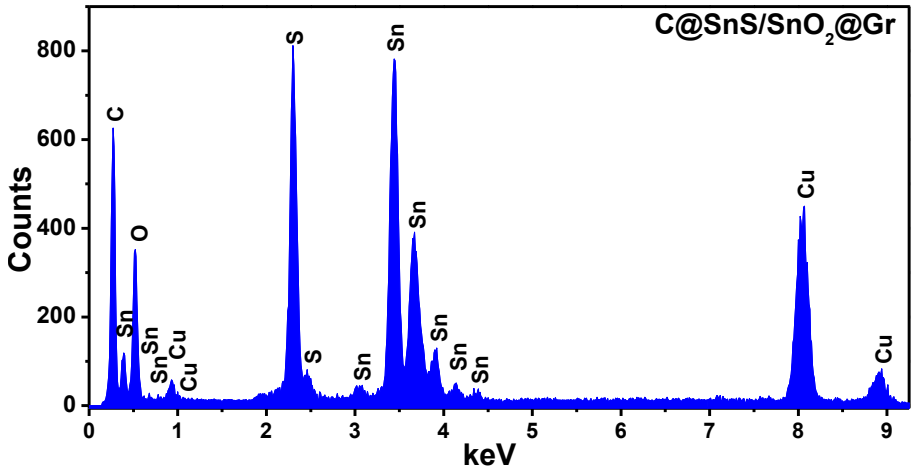

Figure 5.5 EDS spectrum of C@SnS/SnO_2@Gr. Wide area EDS analysis indicated about 9.34 wt% O, 10.33 wt% S, and 70.21 wt% Sn. The Sn^{4+}/Sn^{2+} ratio is about 1.1, indicating the generation of SnS/SnO_2 heterostructures.

From the TGA analysis (**Figure 5.6**), the amounts of graphene and carbon in the C@SnS/SnO_2@Gr composite are about 8 wt % and 23 wt %, respectively.

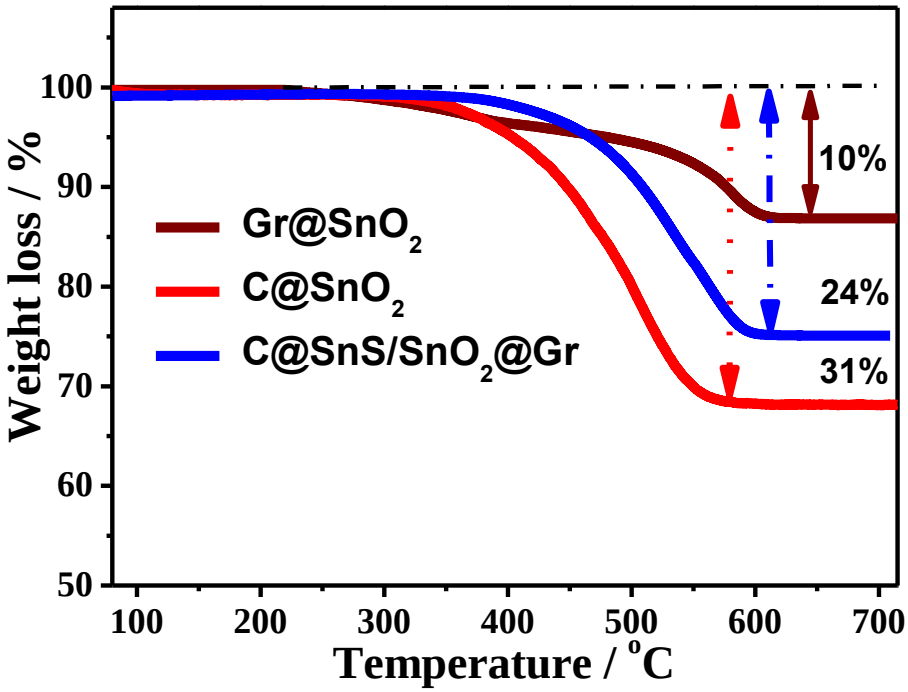

Figure 5.6 TGA curves of the Gr@SnO_2, C@SnO_2, and C@SnS/SnO_2@Gr. Considering that the C@SnO_2@Gr was prepared by coating carbon on Gr@SnO_2 nanosheets and that the weight of SnO_2 is 9 times that of the graphene, the amounts of amorphous carbon and graphene in C@SnS/SnO_2@Gr are around 23 wt% and 8 wt%, respectively.

The microstructure and morphology of the composites obtained were observed by scanning electron microscopy (SEM) and transmission electron microscopy (TEM). As shown in **Figure 5.7**, both C@SnO2@Gr (**Figure 5.7 a**) and C@SnS/SnO_2@Gr (**Figure 5.7 d**) have a uniform morphology over the whole surface. A large number of tiny nanoparticles (ca. 5 nm in size) are evenly distributed on graphene nanosheets (insets in **Figure 5.7 a,d**), manifesting the stable structure of the C@SnO_2@Gr

composite before and after the sulfidiation treatment, which is of great importance for the electrode materials in electrochemical testing. **Figure 5.7 b,e**, and **Figure 5.8** present representative TEM images of the C@SnO_2@Gr and C@SnS/SnO_2@Gr samples. It can be clearly observed that the few-layer graphene nanosheets have a great many ultrathin nanoparticles homogeneously anchored on them, which is consistent with the SEM images (**Figure 5.7 a,d**). Furthermore, the TEM images reveal that the C@SnS/SnO_2@Gr and C@SnO_2@Gr almost have the same morphology, which can further demonstrate the stability of the complex structure during the sulfidation reaction. The high-resolution TEM (HRTEM) image of the C@SnS/SnO_2@Gr hybrid (**Figure 5.7 f**) demonstrates the formation of SnS/SnO_2 nano-heterostructures. The lattice fringes of about 0.335 nm and 0.265 nm, respectively correspond to the (110) and (101) planes of SnO_2,[26] while the interatomic spacings of 0.293 nm and 0.322 nm correspond to the (101) and (021) planes of SnS.[29, 32] Both the SnS and the SnO_2 nanoparticles are in tight contact with each other and form heterojunctions in the interfacial area, which can enhance electronic conductivity and rapid ion/electron transfer.[25] Moreover, it is also interesting to see that the few-layer graphene nanosheets support the SnS and SnO_2 nanoparticles, while the carbon layer forms a coating at the outer edge, which can not only provide an effective buffer matrix for the SnS/SnO_2 nanoparticles to relieve the volume changes and maintain the structural integrity, but also improves the conductivity. The elemental mapping (**Figure 5.7 h--k**) unambiguously confirms the presence of C, O, S, and Sn elements in the C@SnS/SnO_2@Gr. The S and O elements are homogeneously distributed, which illustrates the in-situ formation of SnS in the SnO_2 matrix, resulting in the intimate contact of the two components and the formation of heterostructures.

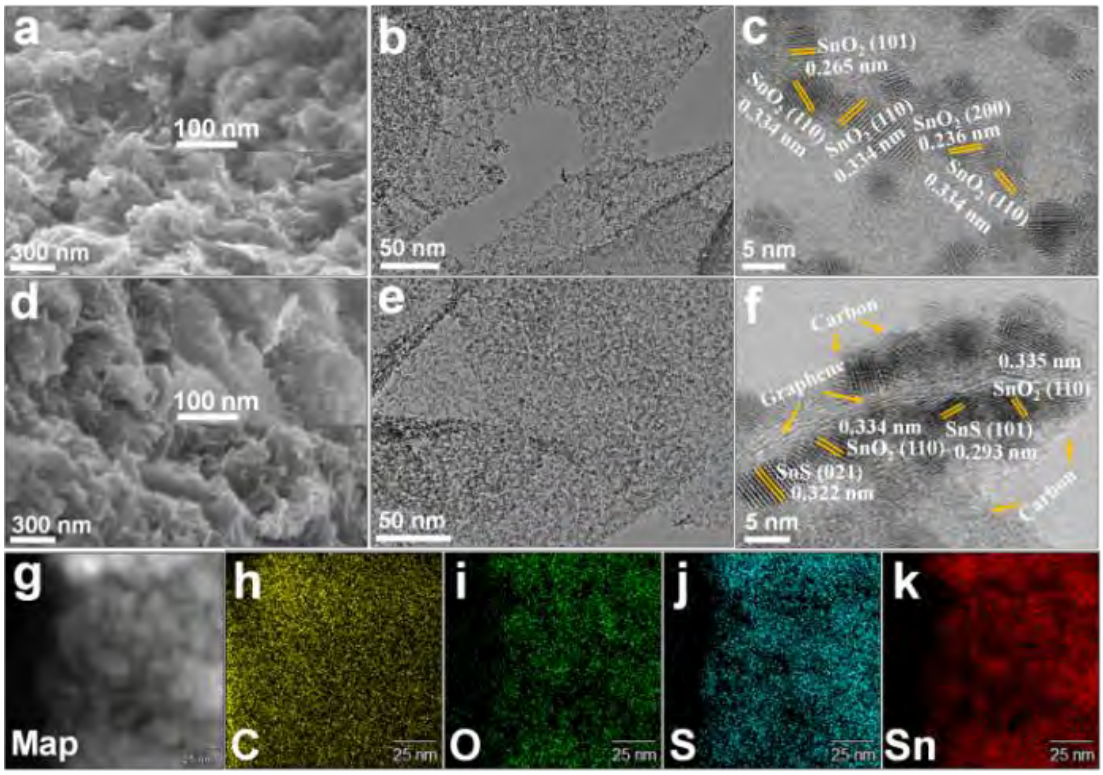

Figure 5.7 a) SEM image and b,c) TEM images of the C@SnO_2@Gr. d) SEM image and e,f) TEM images of the C@SnS/SnO_2@Gr architectures. g-k) TEM image and element mapping images of the C@SnS/SnO_2@Gr.

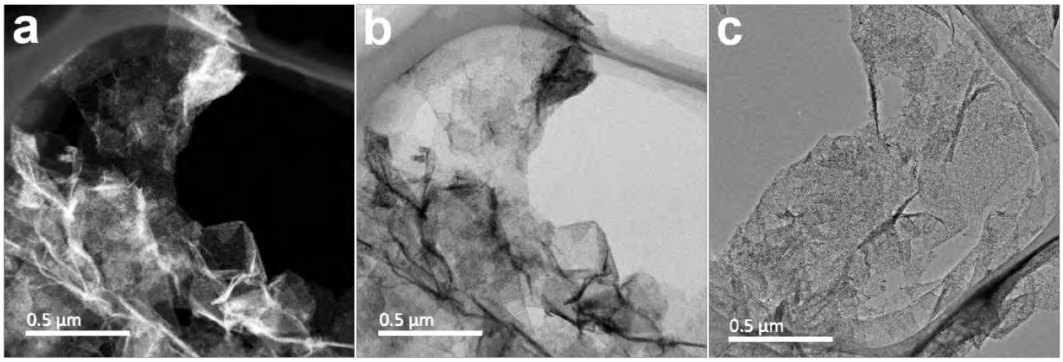

Figure 5.8 Scanning TEM (STEM) characterization of the C@SnS/SnO_2@Gr and C@SnO_2@Gr samples: (a) STEM – high angle annular dark-field (STEM-HAADF) image and (b) bright field TEM image of C@SnS/SnO_2@Gr. (c) TEM image of the C@SnO_2@Gr.

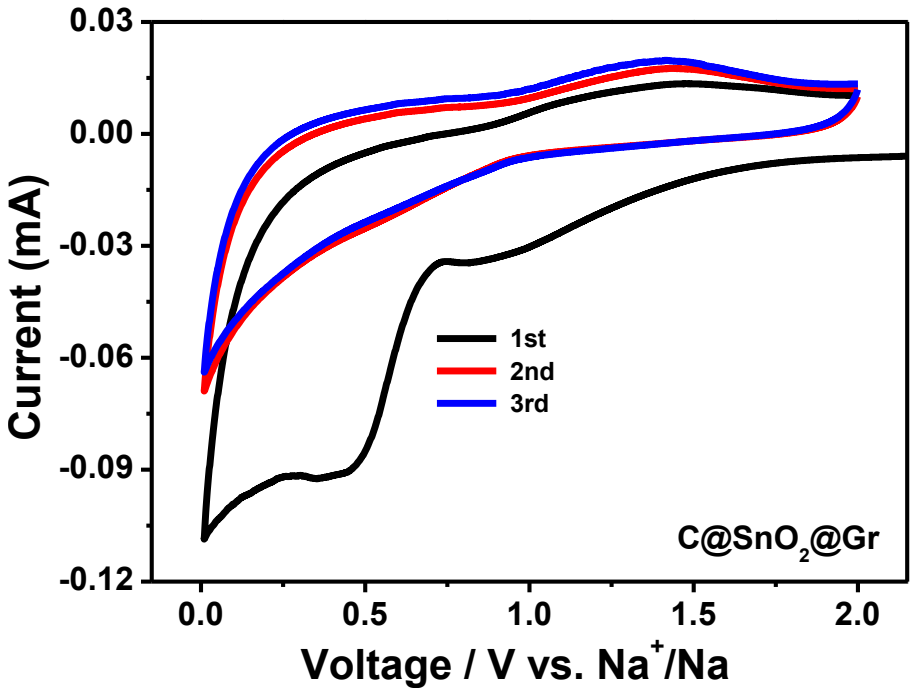

Figure 5.9 Cyclic voltammograms for the first 3 cycles of C@SnO_2@Gr electrode at a scanning rate of 0.1 mV s^{-1}.

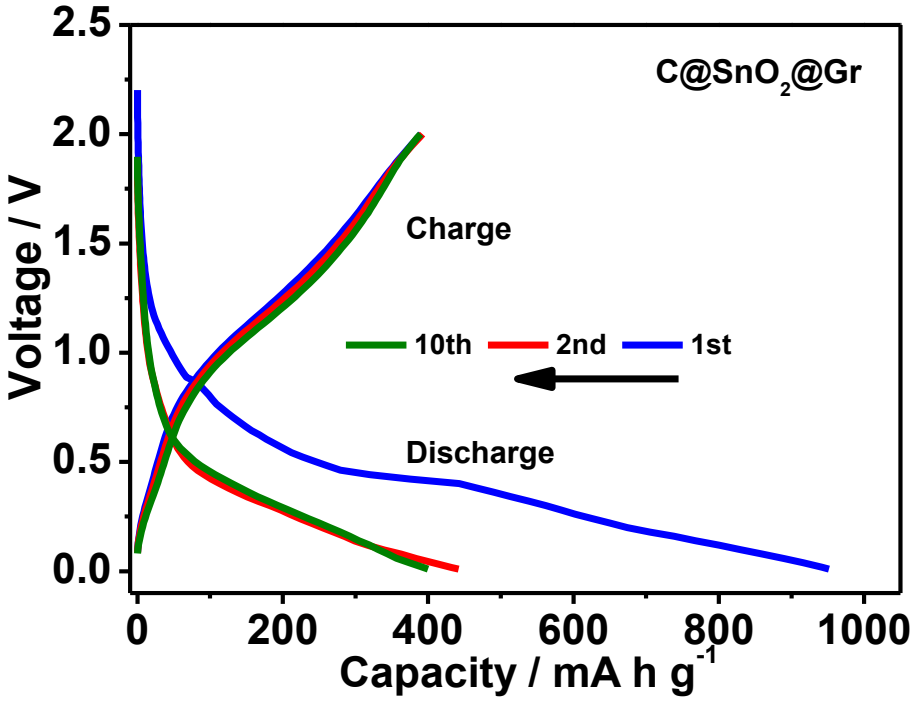

Figure 5.10 Galvanostatic discharge–charge profiles for selected cycles of C@SnO_2@Gr electrode at a current density of 30 mA g^{-1}.

The sodium ion storage behaviour of the materials was first investigated using cyclic voltammetry (CV). (**Figure 5.11 a, Figure 5.10**). During the first reduction process, a clear reduction peak appeared at approximately 0.75 V, which disappeared in the following negative scan, a result of the formation the solid electrolyte interface film.[13] From the 2nd cycle, three pairs of oxidation/reduction peaks, localized at 0.08 V/0 V, 0.23 V/0.15 V, and 0.73 V/0.68 V, appeared and remained stable, corresponding to the alloying/dealloying reactions.[13] The reduction peak at approximately 1.06 V in the CV curves can be ascribed to the conversion reaction of SnS, while the oxidation peak localized at about 1.15 V corresponds to the back-

conversion of Sn and Na_2S into the SnS phase. It is noteworthy that the CV curves almost overlap from the 2nd to the 5th cycles, reflecting the highly reversible nature of the electrochemical reactions in the C@SnS/SnO_2@Gr anode and ensuring prolonged cycling stability.

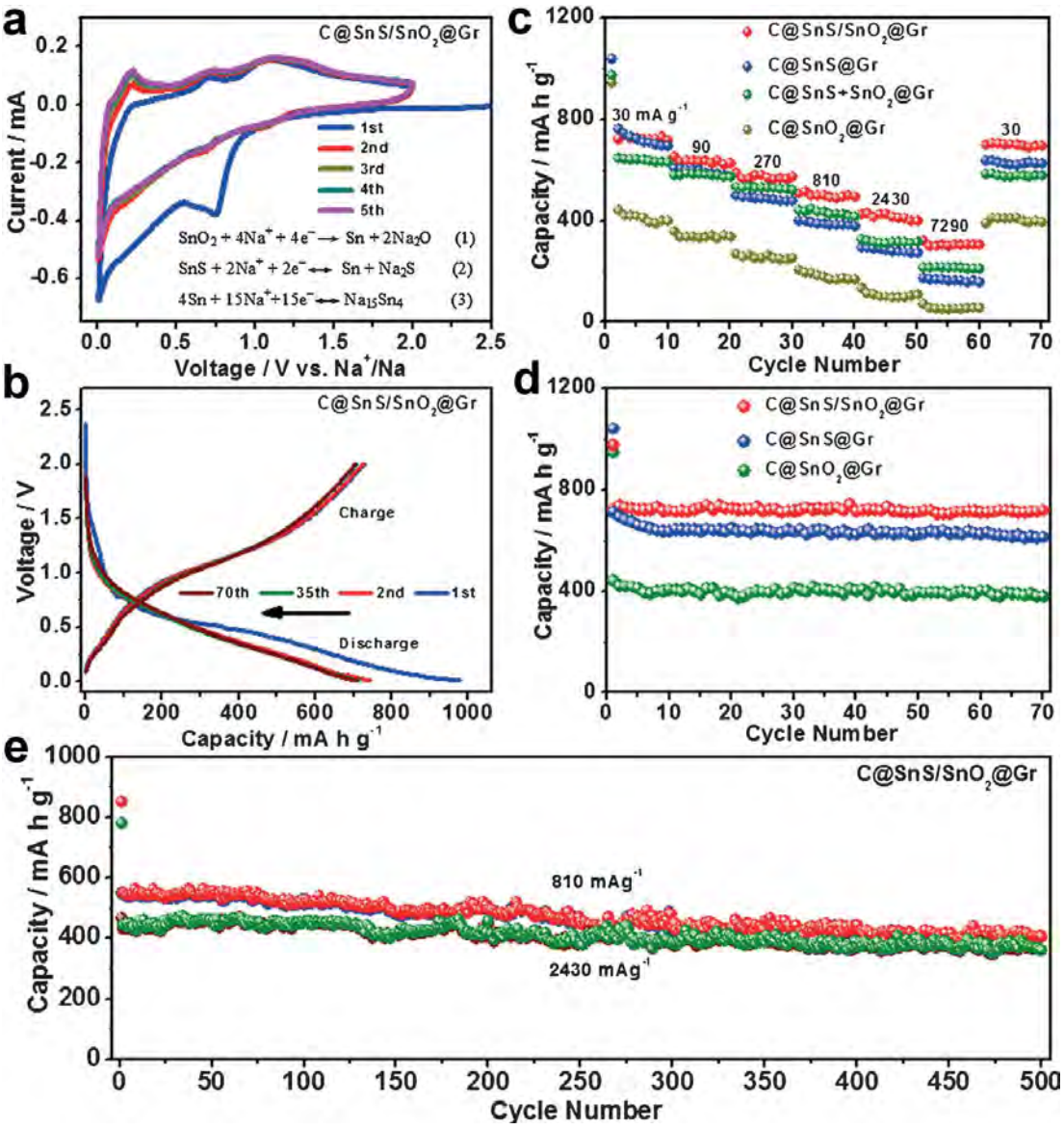

Figure 5.11 Electrochemical performance of C@SnS/SnO_2@Gr sample for sodium storage. a) Cyclic voltammograms for the first five cycles of the C@SnS/SnO2@Gr electrode at a scanning rate of 0.1 mVs-1. b) Galvanostatic discharge-charge profiles for selected cycles of the C@SnS/SnO_2@Gr electrode at 30 mAg^{-1}. c) Rate

capabilities of C@SnS/SnO_2@Gr, C@SnS@Gr, C@SnO_2@Gr, and C@SnS+SnO_2@Gr electrodes. d) Cycling performance of C@SnS/SnO_2@Gr, C@SnS@Gr, and C@SnO_2@Gr at 30 mAg^{-1}, and e) long-term cycling performance of the C@SnS/SnO_2@Gr electrode at different current densities.

The electrochemical performance of the electrodes was evaluated by galvanostatic discharge--charge measurements (**Figure 5.12**). The C@SnS/SnO_2@Gr composite shows a first discharge capacity of 976 $mAhg^{-1}$ and a charge capacity of 729 mA h g^{-1} at 30 mA g^{-1} (**Figure 5.11 b,c**), corresponding to an initial coulombic efficiency of 74.6 %. In contrast, the first cycle efficiency of the C@SnO_2@Gr is only 41.3 %, and the C@SnS@Gr exhibited a stable capacity of 637 mA h g^{-1} after 10 cycles (**Figure 5.11 c,d**). The C@SnS/SnO_2@Gr anode displays a higher reversible capacity than the C@SnO_2@Gr or C@SnS@Gr materials, which can be attributed to the synergistic effects of SnS/SnO_2.[25] After 70 cycles, the C@SnS/SnO_2@Gr electrode achieves a reversible capacity of 713 mA h g^{-1} with approximately 98 % capacity retention. **Figure 5.11 c** shows the rate capability of all the prepared electrodes from 30 mA g^{-1} to 7290 mA g^{-1}. As can be seen clearly, the C@SnS/SnO_2@Gr electrode features superior high-rate performance. On increasing the current density to 810 and 2430 mA g^{-1}, the specific capacity at these current densities is still 520 and 430 mA h g^{-1}, respectively, which is much higher than for the C@SnO_2@Gr or C@SnS@Gr or a mechanical mixture of them (C@SnS+SnO_2@Gr). **Figure 5.11 e** presents the long-term cycling performance of the C@SnS/SnO_2@Gr electrode when discharged/charged at high current densities. It can still deliver a discharge capacity of 409 mA h g^{-1} after 500 cycles at 810 mA g^{-1} (ca. 73 % retention), implying excellent cycling stability (**Figure 5.13**). More importantly, even after 500 cycles at

2430 mA g^{-1}, a reversible capacity close to 360 mA h g^{-1}(ca. 76 % retention) is still obtainable, indicating the superior high-rate cycling stability of C@SnS/SnO_2@Gr (**Figure 5.14**). The significantly improved Na^+ storage performance might be related to the synergetic enhancement of electron- and sodium-ion transport kinetics, benefiting from the internal electric field within the nanoparticles.[22, 25] Furthermore, the in-situ generation of SnS nanoparticles in the SnO_2 matrix can effectively immobilize the SnO_2, thus reducing the self-agglomeration of SnO_2 nanocrystals and maintaining good structural stability.[24] We also compare the rate performance of the C@SnS/SnO_2@Gr electrode in this work with the state-of-the-art results in previously published papers on SnO_2-, SnS-, SnS_2- and Sn-based systems (**Table 5.1**). The capacity and high-rate performance of the C@SnS/SnO_2@Gr composite is greatly superior to those of most reported anodes for Na-ion batteries. Such excellent performance shows that the as-prepared C@SnS/SnO_2@Gr composite has great potential as the anode in applications for Na-ion batteries.

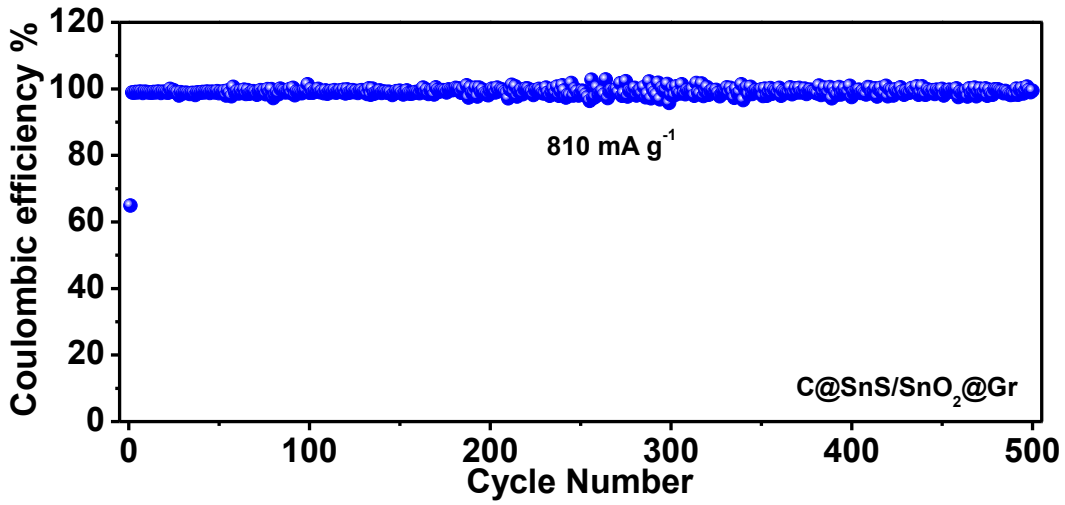

Figure 5.12 Coulombic efficiency of the C@SnS/SnO_2@Gr electrode at 810 mA g^{-1} for 500 cycles.

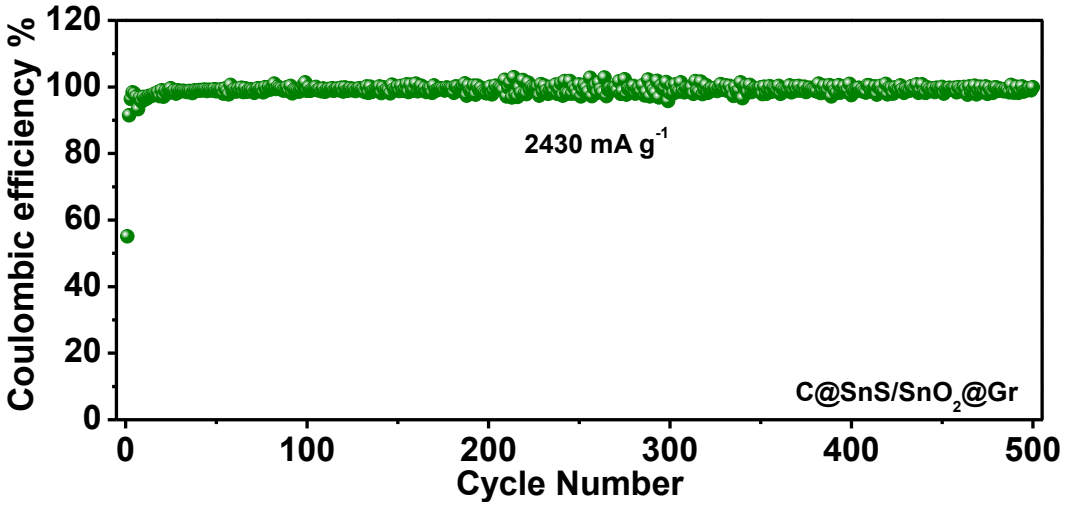

Figure 5.13 Coulombic efficiency of the C@SnS/SnO_2@Gr electrode at 2430 mA g^{-1} for 500 cycles.

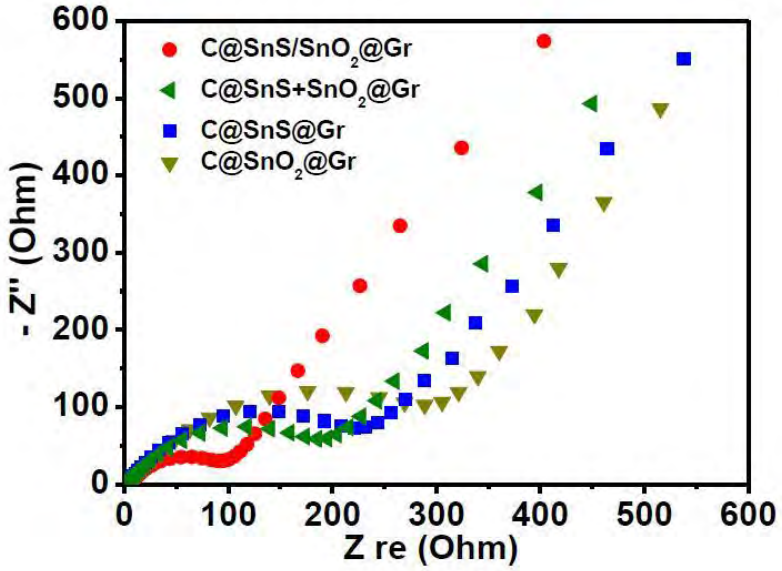

Figure 5.14 Nyquist plots of electrodes containing hybrid C@SnS/SnO_2@Gr, C@SnS+SnO_2@Gr, C@SnS@Gr, and C@SnO_2@Gr, obtained by applying a sine wave with an amplitude of 5.0 mV over the frequency range of 100 kHz–0.01 Hz.

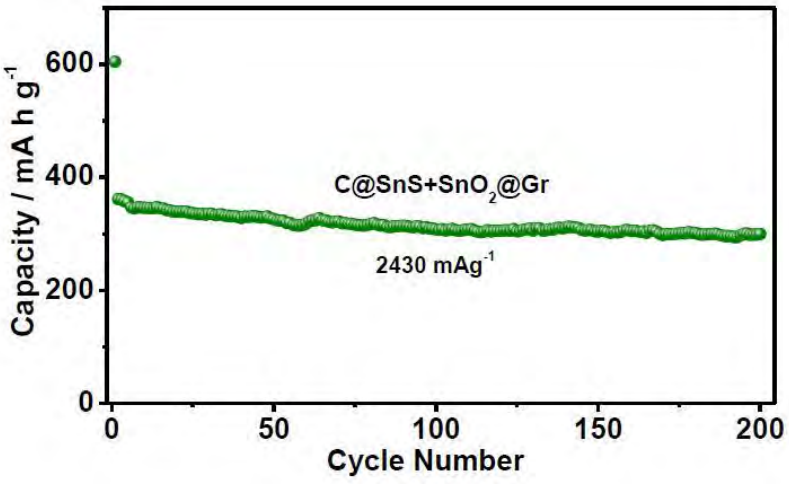

Figure 5.15 Long-term cycling performance of the C@SnS+SnO_2@Gr electrode at a current density of 2430 mA g^{-1}.

Electrochemical impedance spectroscopy (EIS) measurements were performed to research the kinetic differences between various electrodes. Both of the Nyquist plots shown in **Figure 5.9** present depressed semicircles in the high-medium frequency region and an inclined line in the low frequency region.[26] Of note is that the semicircle diameter for C@SnS/SnO_2@Gr is much smaller than that for C@SnO_2@Gr, C@SnS@Gr, and C@SnS+SnO_2@Gr, indicating enhanced electron- and sodium-ion transport after the formation of the SnS/SnO_2 heterostructures. The reduced charge-transfer impedance will increase the electrode kinetics and consequently improve the high-rate performance of the C@SnS/SnO_2@Gr electrode.Based on the above results, a possible mechanism for the enhancement of the Na^+ storage performance was proposed, as shown in **Figure 5.16**. In our system, SnO_2 is an n-type semiconductor with a wide band gap of 3.8 eV, while SnS works as a narrow-band-gap (1.3 eV) p-type semiconductor. Therefore, the SnS/SnO_2 p--n heterojunctions that are formed will induce a built-in electric field on the heterointerfaces, which will greatly accelerate the charge-transfer kinetics and result in high-rate capability. This is confirmed by the much lower charge-transport/diffusion resistance in the C@SnS/SnO_2@Gr electrode (**Figure 5.9**). During the discharging process, the direction of the electric field induced by the p--n heterojunction will point to SnS from the SnO_2 surface. Under this electric field, the charge accumulation layer at the interface is subjected to breakdown, and Na^+ diffusion in the bulk will become much easier, thus helping the Na^+ insertion.[34] After full sodiation, SnO_2 is changed into Na_xSn and Na_2O, whereas SnS is converted into Na_xSn and Na_2S. During the charge process, SnS micro-domain can release much more Na^+ owing to its higher reversibility than SnO_2 micro-domain.[31,

[32] In this case, a Na^+-rich region will form in the SnS phase and a Na^+-poor area in the SnO_2 phase. Because of the potential difference, it will induce a new electric field at the interface with a direction from SnS to SnO_2, which will facilitate Na^+ migration, promoting Na^+ extraction in the charge process. Furthermore, the structural and electrical integrity of the electrode via the interfacial amorphous carbon layer anchoring the SnS/SnO_2 nanoparticles to the graphene also play important roles in improving the electrochemical performance. Therefore, the outstanding performance can be ascribed to the following reasons: 1) the charge-transfer driving force originating from the SnS/SnO_2 nano-heterostructures; 2) the higher initial coulombic efficiency and reversible capacity provided by the SnS nanoparticles; 3) the short ion-diffusion paths due to the ultra-small nanoparticles; 4) the good structural stability and excellent electrical conductivity ensured by the carbon layer and the graphene network.

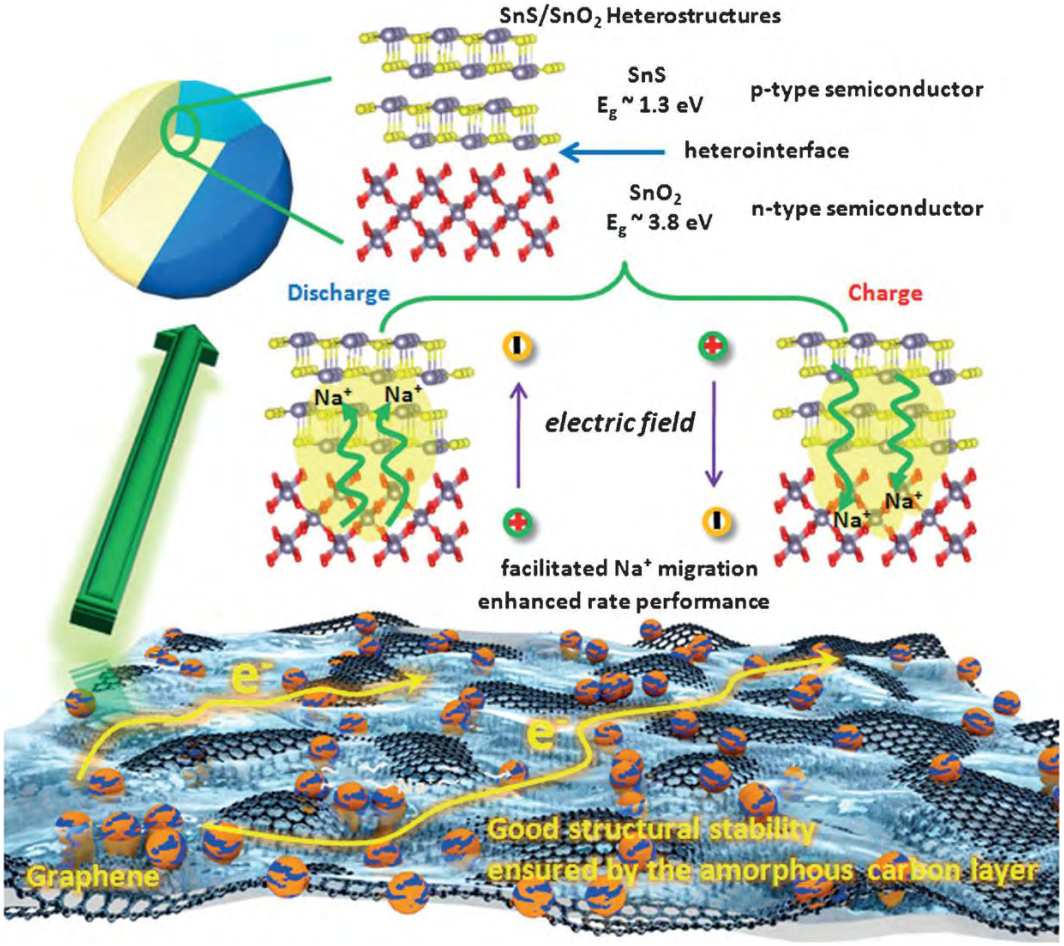

Figure 5.16 Summary of the enhanced high-rate capacity mechanism of the C@SnS/SnO_2@Gr in the Na-ion battery system.

Table 5.1 Comparison of electrochemical performance of C@SnS/SnO_2@Gr in this work with previously published reports on SnO_2, SnS, SnS_2, and Sn-based sodium ion battery anodes. The capacity and high-rate performance of our obtained C@SnS/SnO_2@Gr architecture was found to be much better than those of most reported anode materials for Na-ion batteries.

Sample	**Cycling Capacity (mA h g^{-1}) Current Density (mAg^{-1})**			**Rate Capacity (mA h g^{-1})**	
	1st	**50th**	**300th**		
C@SnS/SnO_2@Gr (This work)	**730** 30	**715** 30	**618** 30	**409** (**500 cycles**) **810**	**360** (**500cycles**) **2430**
SnO_2/N-doped Gr[35]	339 20	305 20	283 (100 cycles) 20	170 640	n/a
SnO_2–rGO[36]	406.9 100	~380 100	330 (150 cycles) 100	~170 500	125 1000
SnO_2/graphene aerogel[37]	451 20	~330 20	322 (100 cycles) 20	172 640	168 1000
SnO_2/graphene[38]	741 20	660 20	638 (100 cycles)	143 640	n/a

			20		
SnO_2@MWCNT[39]	~500 50	~380 50	n/a	260 250	n/a
SnO_2-C[40]	412 50	~250 50	n/a	192 500	n/a
SnO_2@PANI composite[41]	~667.8 300	~190 300	213	~130 800	110 1000
MWNTs@SnO_2@C[42]	452 50	300 50	200 150	213 500	110 1000
SnO_2–Fe_2O_3 composite[43]	227.6 50	223 50	n/a	154.6 200	n/a
SnS[44]	~500 125	370 (30 cycles) 125	n/a	390 500	300 1000
SnS@rGO[45]	~350 100	410 100	386 (100 cycles) 100	240 400	n/a
SnS-C[46]	~466 500	433 500	n/a	455 (10 cycles) 1000	415 (10 cycles) 3000
SnS–C[47]	568 100	540 100	n/a	452 800	n/a
SnS/C[48]	340 1000	~310 1000	266 1000	334 500	310 1000
Sn–SnS–C[49]	416 100	~450 100	407 (150 cycles) 100	348 800	n/a

SnS_2/C Nanospheres[50]	660 50	~600 50	570 (100 cycles) 50	~380 800	360 1000
SnS_2-rGO[51]	630 200	~630 200	628 (100 cycles) 200	~570 (10 cycles) 1000	~530 (10 cycles) 2000
SnS_2-graphene[52]	725 20	670 20	n/a	463 640	n/a
SnS_2/rGO[53]	~430 200	~570 200	509 200	400 (500 cycles) 800	n/a
Tin-Coated Viral Nanoforests[54]	~770 50	~580 50	~405 (150 cycles) 50	n/a	n/a
carbonized paper Sn@C[55]	231 10	150 (20 cycles) 10	n/a	n/a	n/a
Sn Nanofibers[56]	816 84.7	~780 84.7	776 (100 cycles) 84.7	784.53 (10 cycles) 847	650 (10 cycles) 1694
Sn@C[57]	447 500	~440 500	440 (200 cycles) 500	~415 (500 cycles) 1000	n/a

5.4 Conclusions

In conclusion, an effective approach, involving an interfacial amorphous carbon layer anchoring SnS/SnO_2 heterostructures directly to graphene nanosheets, has been developed. The formation of the SnS/SnO_2 heterostructures has been verified by HRTEM, Raman, and XPS analysis. When evaluated as an anode material for sodium-ion batteries, the C@SnS/SnO2@Gr features excellent performance and outstanding cycling stability at high rates, which is much superior to the performance of C@SnO_2@Gr, C@SnS@Gr, or a mechanical mixture of them. The boosted charge transfer in the heterostructures is demonstrated by the EIS measurements. The resulting improvement of Na-ion diffusion capability and electronic conductivity is mainly responsible for the extraordinary performance of the C@SnS/SnO_2@Gr electrode. The superior high-rate capability and ultra-long cycle life, accompanied by the simplicity of the synthetic process, make this approach a promising strategy for the development of simple and universal synthesis methods in applications for energy storage and conversion.

5.5 References

[1] X. Fan, J. Mao, Y. Zhu, C. Luo, L. Suo, T. Gao, F. Han, S. Liou, C. Wang, Adv. Energy Mater. 2015, 5, 1500174.

[2] H. Yu, Y. Ren,D. Xiao, S. Guo, Y. Zhu, Y. Qian, L. Gu, H. Zhou, Angew. Chem. Int. Ed. 2014, 53, 8963 – 8969; Angew. Chem. 2014, 126, 9109 – 9115.

[3] J. Liu, P. Kopold, C. Wu, P. Aken, J. Maier, Y. Yu, Energy Environ. Sci. 2015, 8, 3531 – 3538.

[4] S. Ong, V. Chevrier, G. Hautier, A. Jain, C. Moore, S. Kim, X. Ma, G. Ceder, Energy Environ. Sci. 2011, 4, 3680 – 3688.

[5] X. Zhou, Y. Zhong, M. Yang, M. Hu, J. Wei, Z. Zhou, Chem. Commun. 2014, 50, 12888 – 12891.

[6] W. Li, S. Chou, J.Wang, J. Kim, H. Liu, S. Dou, Adv. Mater. 2014, 26, 4037 – 4042.

[7] L. Wu, X. Hu, J. Qian, F. Pei, F. Wu, R. Mao, X. Ai, H. Yang, Y. Cao, Energy Environ. Sci. 2014, 7, 323 – 328.

[8] L. Pei,Q. Jin, Z. Zhu,Q. Zhao, J. Liang, J. Chen, Nano Res. 2015, 8, 184 – 192.

[9] Y. Zhao, C. Wei, S. Sun, L. Wang, Z. Xu, Adv. Sci. 2015, 2, 1500097.

[10] Y. Zhang, J. Xie, S. Zhang, P. Zhu, G. Cao, X. Zhao, Electrochim. Acta 2015, 151, 8 – 15.

[11] Z. Li, J. Ding, H. Wang, K. Cui, T. Stephenson, D. Karpuzov, D. Mitlin, Nano Energy 2015, 15, 369 – 378.

[12] Y. Wang, Y. Lim, M. Park, S. Chou, J. Kim, H. Liu, S. Dou, Y. Kim, J. Mater. Chem. A 2014, 2, 529 – 534.

[13] T. Zhou, W. Pang, C. Zhang, J. Yang, Z. Chen, H. Liu, Z. Guo, ACS Nano 2014, 8, 8323 – 8333.

[14] C. Zhu, P. Kopold,W. Li, P. Aken, J. Maier, Y. Yu, Adv. Sci. 2015, 2, 1500200.

[15] J. Huheey, E. Keiter, R. Keiter in Inorganic Chemistry: Principles of Structure and Reactivity, Harpercollins College Publishers, New York, 1993, pp. 138 – 251.

[16] L. Wu, H. Lu, L. Xiao, J. Qian, X. Ai, H. Yang, Y. Cao, J. Mater. Chem. A 2014, 2, 16424 – 16428.

[17] Y. Denis, P. Prikhodchenko, C. Mason, S. Batabyal, J. Gun, S. Sladkevich, A. Medvedev, O. Lev, Nat. Commun. 2013, 4, 2922.

[18] C. Bommier, X. Ji, Isr. J. Chem. 2015, 55, 486 – 507.

[19] X. Zhu, N. Monahan, Z. Gong, H. Zhu, K.Williams, C. Nelson, J. Am. Chem. Soc. 2015, 137, 8313 – 8320.

[20] P. Zubko, S. Gariglio, M. Gabay, P. Ghosez, J. Triscone, Annu. Rev. Condens. Matter Phys. 2011, 2, 141 – 165.

[21] C. Huang, S. Wu, A. Sanchez, J. Peters, R. Beanland, J. Ross, P. Rivera, W. Yao, D. Cobden, X. Xu, Nat. Mater. 2014, 13, 1096 – 1101.

[22] X. Chang, T. Wang, P. Zhang, J. Zhang, A. Li, J. Gong, J. Am. Chem. Soc. 2015, 137, 8356 – 8359.

[23] X. Hong, J. Kim, S. Shi, Y. Zhang, C. Jin, Y. Sun, S. Tongay, J.Wu, Y. Zhang, F. Wang, Nat. Nanotechnol. 2014, 9, 682 – 686.

[24] J. Nishitani, K. Yu, W. Walukiewicz, Appl. Phys. Lett. 2014, 105, 132103.

[25] J.Wang, Y. Zhou, Z. Shao, Electrochim. Acta 2013, 97, 386 – 392.

[26] C. Zhang, X. Peng, Z. Guo, C. Cai, Z. Chen, D.Wexler, S. Li, H. Liu, Carbon 2012, 50, 1897 – 1903.

[27] J. Cheng, H. Xin, H. Zheng, B.Wang, J. Power Sources 2013, 232, 152 – 158.

[28] M. Liu, J. Yang, Q. Qu, P. Zhu,W. Li, J. Power Sources 2015, 273, 848 – 856.

[29] S. Sohila, M. Rajalakshmi, C. Ghosh, A. Arora, C. Muthamizhchelvan, J. Alloys Compd. 2011, 509, 5843 – 5847.

[30] M. Fondell, M. Gorgoi, M. Boman, A. Lindblad, J. Electron Spectrosc. Relat. Phenom. 2014, 195, 195 – 199.

[31] D. Jiang, L. Chen, J. Zhu, M. Chen, W. Shi, J. Xie, Dalton Trans. 2013, 42, 15726 – 15734.

[32] J. Ning, K. Men, G. Xiao, L. Wang, Q. Dai, B. Zou, B. Liu, G. Zou, Nanoscale 2010, 2, 1699 – 1703.

[33] I. Kim, J. Seo, S. Oh, S. Patil, S. Hwang, Adv. Funct. Mater. 2015, 25, 4948 – 4955.

[34] T. Zhou, Y. Zheng, H. Gao, S. Min, S. Li, H. Liu, Z. Guo, Adv. Sci. 2015, 2, 1500027.

[35] X. Xie, D. Su, J. Zhang, S. Chen, A. Mondal, G. Wang, Nanoscale 2015, 7, 3164–3172.

[36] Y. Wang, Y. Lim, M. Park, S. Chou, J. Kim, H. Liu, S. Dou, Y. Kim, J. Mater. Chem. A 2014, 2, 529–534.

[37] X. Xie, S. Chen, B. Sun, C. Wang, G. Wang, ChemSusChem 2015, 8,2948–2955.

[38] D. Su, H. Ahn, G. Wang, Chem. Commun. 2013, 49, 3131–3133.

[39] Y. Wang, D. Su, C. Wang, G. Wang, Electrochem.Commun. 2013, 29, 8–11.

[40] Y. Lu, C. Ma, J. Alvarado, T. Kidera, N. Dimov, Y. Meng, S. Okada, J. Power Sources 2015, 284, 287–295.

[41] X. Zhao, Z. Zhang, F. Yang, Y. Fu, Y. Lai, J. Li, RSC Adv. 2015, 5, 31465–31471.

[42] Y. Zhao, C. Wei, S. Sun, L. Wang, Z. Xu, Adv. Sci. 2015, 2, 1500097.

[43] X. Wu, W. Wu, Y. Zhou, X. Huang, W. Chen, Q. Wang, Powder Technol. 2015, 280, 119–123.

[44] P. Dutta, U. Sen, S. Mitra, RSC Adv. 2014, 4, 43155–43159.

[45] L. Wu, H. Lu, L. Xiao, X. Ai, H. Yang, Y. Cao, J. Power Sources 2015, 293, 784–789.

[46] S. Choi, Y. Kang, Nano Res. 2015, 8, 1595–1603.

[47] L. Wu, H. Lu, L. Xiao, J. Qian, X. Ai, H. Yang, Y. Cao, J. Mater. Chem. A 2014, 2, 16424–16428.

[48] C. Zhu, P. Kopold, W. Li, P. Aken, J. Maier, Y. Yu, Adv. Sci. 2015, 1500200.

[49] L. Wu, X. Hu, J. Qian, F. Pei, F. Wu, R. Mao, X. Ai, H. Yang, Y. Cao, J. Mater. Chem. A 2013, 1, 7181–7184.

[50] J. Wang, C. Luo, J. Mao, Y. Zhu, X. Fan, T. Gao, A. Mignerey, C. Wang, ACS Appl. Mater. Interfaces 2015, 7, 11476−11481.

[51] B. Qu, C. Ma, G. Ji, C. Xu, J. Xu, Y. Meng, T. Wang, J. Lee, Adv. Mater. 2014, 26, 3854–3859.

[52] X. Xie, D. Su, S. Chen, J. Zhang, S. Dou, G. Wang, Chem. Asian J. 2014, 9, 1611–1617.

[53] Y. Zhang, P. Zhu, L. Huang, J. Xie, S. Zhang, G. Cao, X. Zhao, Adv. Funct. Mater. 2015, 25, 481–489.

[54] Y. Liu, Y. Xu, Y. Zhu, J. Culver, C. Lundgren, K. Xu, C. Wang, ACS Nano 2013, 7, 3627–3634.

[55] W. Chen, D. Deng, Carbon 2015, 87, 70–77.

[56] D. Nam, T. Kim, K. Hong, H. Kwon, ACS Nano 2014, 8, 11824–11835.

[57] Y. Liu, N. Zhang, L. Jiao, Z. Tao, J. Chen, Adv. Funct. Mater. 2015, 25, 214–220.

CHAPTER 6 SURFACE ENGINEERING AND DESIGN STRATEGY FOR SURFACE-AMORPHIZED TIO2@GRAPHENE HYBRIDS TOWARDS HIGH POWER LI-ION BATTERY ELECTRODES

Surface-amorphization provides unprecedented opportunities for altering and tuning material properties, including through its effect on the surface atomic arrangement or surface electric-field distribution, so that surfaces and structures can be engineered with increased populations of active sites, which is a cross-cutting issue for energy conversion and storage. The rational design and controllable synthesis of surface-amorphized inorganic materials, however, still represent a long-standing challenge. Here, surface-amorphized TiO_2@graphene has been designed and synthesized using a low temperature-phase transformation technique. The as-prepared surface-amorphized (SA) microstructure was confirmed by high resolution transmission electron microscopy, as well as electron paramagnetic resonance and diffuse reflectance spectroscopy. The SA-TiO_2@graphene composite exhibits significantly improved cycling stability and rate capability compared to well-crystallized TiO_2@graphene and bare TiO_2 electrodes. These improvements can be ascribed to the electrically conductive framework constructed from graphene sheets and the surface-amorphization, which induces an electric field within the nanocrystals, endowing them with much lower lithium-ion diffusion resistance, facilitates lithium-ion transport in both insertion and extraction processes, and enhances electrolyte absorption capability. The concept of surface-amorphization thus offers an innovative and general approach toward designing battery materials with enhanced performance.

6.1 Introduction

Electrode materials with battery-like high capacity and capacitor-like rate performance are highly desirable, since they would significantly advance next-generation energy storage technology.[1] TiO_2 has received increasing attention as an anode material for lithium-ion batteries (LIBs) due to its good reversible capacity and low volume expansion upon lithiation, as well as its low cost and safe lithiation potential.[2] The low lithium-ion mobility within the crystalline phase TiO_2, however, together with its poor electrical conductivity, means that only a thin surface layer of the host material is available for Li intercalation at high rates.[3] These issues are still challenges that hinder the electrochemical performance of this material.

Several strategies have been proposed to address each of the issues mentioned above individually. The low lithium-ion mobility has been addressed by (i) decreasing the length of the lithium-ion diffusion pathways, for example, by using mesoporous,[3] nanostructured, or nanosized materials; or by (ii) facilitating the lithium-ion mobility, for example, by using less dense structural phases.[4] On the other hand, the conductivity has been improved by (i) coating TiO_2 with carbon[5] or Al_2O_3,[6] or (ii) linking TiO_2 with carbon nanotubes (CNTs) or graphene or other conductive networks,[7] or (iii) doping the TiO_2. Traditionally, electrode materials have been sought that have well-crystallized phases, so that nearly all high energy-density cathodes for rechargeable lithium batteries are well-crystallized materials in which lithium and other cations occupy distinct sites.[8] This ~~–or~~dering paradigm" may have led the community to overlook a large class of materials in which there are atomic arrangements with only short-range order that appear to exist in a random (disordered) fashion; some of these materials may offer higher capacity and better

stability relative to the well-crystallized phases.[9] Interestingly, very recent work has demonstrated that amorphous/disordered materials may form percolation pathways via the opening of active diffusion channels, which could not only potentially facilitate ionic and electronic diffusion, but also enhance mass transport within these phases.[10] The Li-ion diffusion in amorphous materials proceeds more rapidly than in crystalline materials with similar particle size and morphology.[9,11] For instance, Siegel et al. have shown that the ionic conductivity of amorphous Li_2O_2 is 2×10^{-7} S/cm, which is 12 orders of magnitude larger than that in the crystalline phase.[12] In addition, defects induced by amorphous phases, such as dangling bonds and oxygen vacancies, typically lead to unexpected electronic states in the band gap that result in improved electrical conductivity.[13] Once a certain limit is reached, however, a change in the opposite direction is inevitable. Samuelis et al. found that amorphous-rich material exceeding certain levels of oxygen vacancies is detrimental to the lithium ion diffusivity because they represent defects that hinder the mobility of lithium ions.[14] Therefore, the approach of introducing amorphous phases requires well-designed surface microstructures and combination with other strategies to further improve the electrochemical performance.

Fortunately, surface-amorphization (SA) provides unprecedented opportunities for altering and tuning material properties. SA could facilitate lithium diffusion into the bulk materials and alter the electrochemical reactivity to Li, thus increasing the accessible volume to near-full capacity. Based on these considerations, we propose a robust hierarchical network architecture with anti-aggregation properties through the assembly of graphene and SA-TiO_2, which provides (i) large surface area and electrolyte absorption capability compared with other nanostructures, leading to adequate electrode-electrolyte contact; (ii) lower Li^+ interfacial transfer resistance

due to close packing of the TiO_2 and graphene, and (iii) improved electronic conductivity and rapid ion/electron transport pathways induced by the SA, which are of benefit to the high power performance. Inspired by these unique properties of SA-TiO_2, we can imagine that the lithium-ion storage properties of TiO_2 electrodes could be further optimized by combining a hierarchical network architecture and with the surface amorphization of TiO_2.

In this work, we report a unique SA-TiO_2@graphene architecture with a remarkable high rate capability, achieved by coupling the advantages of the highly conductive network offered by graphene with the surface amorphization. The surface amorphization was achieved by a low temperature (65 ℃) phase transition using titanium glycolate as precursor. The low temperature drives the titanium glycolate to transform into anatase phase and allows a surface-amorphized layer to be generated under mild conditions during the phase transition. After that, a simple ultraviolet (UV)-assisted reduction technique was used to construct hybrid architectures combining SA-TiO_2 with graphene as complementary building blocks. The resulting SA-TiO_2@graphene architecture offers the unique characteristics needed for high-power anode materials. As a consequence, the optimal SA-TiO_2@graphene hybrid architecture exhibits substantial improvements in both cycling stability and rate capability. The composite electrode exhibits a high specific capacity of 103 mA h g^{-1} at a rate of 50 C, 9.3 times higher than that of the reference TiO_2. It also shows superior cycling capacity (~ 108 mA h g^{-1}) over 1500 cycles at the high rate of 20 C, together with ~ 100% coulombic efficiency, proving its excellent tolerance of ultra-fast insertion and extraction of lithium ions for long-life LIBs.

6.2 Experimental methods

6.2.1 Materials Synthesis and Assembly

6.2.1.1 Experimental materials and method for GO sheets

Natural graphite powder was oxidized to graphite oxide by the modified Hummers method. Specifically, graphite powder (0.04 g) was dispersed in 50 ml concentrated H_2SO_4 in an ice bath. 3.0 g $KMnO_4$ was then added gradually. The mixture was stirred for 2 h and then diluted with deionized water. 10 ml of 30% H_2O_2 was then added to the solution until the color of the mixture changed to bright yellow. The graphite oxide (GO) prepared in this way was re-dispersed in deionized water and then exfoliated to GO sheets by ultrasonication. A brown homogeneous supernatant was obtained by repeated centrifuging and washing. Deionized (DI) ultrapure water (18 MΩ. cm^{-1}) was used for solution preparation.

6.2.1.2 Synthesis of Surface-Amorphized TiO_2 Spheres

2 mL of $Ti(OBu)_4$ was added to 10 mL of ethylene glycol (EG). This mixture was kept under vigorous stirring at room temperature for 12 h. This solution was then quickly poured into 100 mL of acetone. This mixture was kept under vigorous stirring at room temperature for another 2 h, yielding a white precipitate that was harvested by centrifugation. This solid, comprising titanium glycolate spheres, was washed several times with ethanol by successive rounds of centrifugation and removal of the supernatant. In the next step, the titanium glycolate product was added to 20 mL isopropanol and 10 mL H_2O, and this mixture was stirred for 10 h at 65 °C to produce the surface-amorphized-TiO_2 spheres, which were isolated by centrifugation, washed with ethanol several times, and dried in an oven at 60 °C for 24 h.

TiO_2@graphene hybrid particles were prepared via simultaneous photoreduction of GO and TiO_2 precursors. A typical GO reduction was carried out in a 80 mL vial containing an aqueous suspension of surface-amorphized TiO_2 spheres (0.2 g) in the presence of 50 mL ethanol containing 1.0 mL of 4 mg mL-1 GO. The slurry was irradiated in ultraviolet (UV) light ($\lambda \leq 350$ nm) using a 18 W light emitting diode (LED) lamp for 2 h. After irradiation, the particles were centrifuged and washed with DI water three times. The final products were dried in an oven at 60 °C before use. The reduced GO concentration was calculated to be ~2.0 wt %.

6.2.2 Characterization

The crystalline structure of the as-prepared material was characterized by X-ray diffraction (Rigaku Mini Flex 600). The morphologies and particle sizes of the samples were observed by field emission scanning electron microscopy (FEI-NOVA NanoSEM 450 and Magellan, FEI, USA). The details of the crystal structure were further characterized by transmission electron microscopy (TEM), which was conducted on a JEOL JEM-ARM200F transmission electron microscope operating at 200 kV. Selected area electron diffraction (SAED) patterns were recorded using a Gatan charge coupled device (CCD) camera in a digital format. The TEM was linked to an energy dispersive spectrum analysis (EDS) system. The Brunauer–Emmett–Teller (BET) specific surface areas of the samples were evaluated on the basis of nitrogen adsorption isotherms using a Micromeritics ASAP 2020MC gas adsorption apparatus (USA). X-ray photoelectron spectroscopy (XPS) was conducted on a VG Multilab 2000 (VG Inc.) photoelectron spectrometer using monochromatic Al Kα radiation under vacuum at 2×10^{-6} Pa. All of the binding energies were referenced to the C 1s peak at 284.8 eV of the surface adventitious carbon. The ultraviolet–visible

diffuse reflectance spectra (DRS) were measured using the diffuse reflectance method with a Shimadzu UV-2600 spectrophotometer using an integrating sphere accessory. $BaSO_4$ was used as a reflectance standard in ultraviolet–visible diffuse reflectance experiments. Continuous-wave electron paramagnetic resonance (EPR) experiments were carried out using a Bruker ELEXSYS E580 spectrometer operating in the X-band (9.4 GHz) mode and equipped with an Oxford CF935 helium flow cryostat with an ITC-5025 temperature controller. The g tensors were calibrated for homogeneity and accuracy by comparison to a coal standard, $g = 2.00285 \pm 0.00005$. The receiver gain and number of scans were adjusted to every spectrum of a particular sample to enable comparisons at a reasonable signal-to-noise ratio.

6.2.3 Electrochemical measurements

The electrochemical tests were carried out via CR2032 coin type cells. The working electrodes were prepared by mixing the as-prepared materials, Super P, multi-walled carbon nanotube (MWCNT), and sodium carboxymethyl cellulose / polyacrylic acid (1:1) at a weight ratio of 70:10:10:10. The resultant slurry was pasted on Cu foil and dried in a vacuum oven at 150 °C for 3 h, followed by pressing at 300 kg cm^{-2}. The loading of the materials on individual electrodes was 1.0 ± 0.2 mg cm^{-2}. Electrochemical measurements were carried out using two-electrode coin cells with Li metal as counter and reference electrode. Celgard (product 2400) was used as the separator for the lithium-ion battery. The cell electrolyte for the lithium-ion battery was $LiPF_6$ (1 M) in ethylene carbonate (EC) / diethylene carbonate (DEC) / ethyl-methyl carbonate (EMC) [1:1:1 (v/v/v) with 5 wt% fluoroethylene carbonate (FEC)]. Electrochemical impedance spectroscopy (EIS) and cyclic voltammetry (CV) were conducted on a VMP-3 electrochemical workstation at a scan rate of 0.2 mV s^{-1}.

The cells were galvanostatically charged and discharged at different constant current densities, based on the weight of the samples, on a Land CT2001A battery tester. At least five parallel cells were tested for each electrochemical measurement, in order to make sure that the results were reliable and represented the typical behavior of the samples.

6.3 Results and Discusion

In order to prepare surface-amorphized TiO_2, a low temperature phase transformation method was used in our work, because it offers the possibility of better controlling the reaction pathways on the molecular level.[15] It has been reported that the synthesis of TiO_2 by conventional sol−gel methods is difficult to achieve, as the hydrolysis rates of the precursors are too fast, which, in turn, does not allow separation between the nucleation and growth stages. In order to overcome this problem, ethylene glycol (EG) was selected as a solvent as well as a reactant. Glycols are attractive, as when mixed with alkoxide, they are reactive enough to form glycolate precursors or mixed alkoxide/glycolate derivatives displaying much lower hydrolysis rates. They not only act as an oxygen-supplying agent for the metal oxide, but also strongly influence surface, particle size, morphology, and assembly properties. The slow hydrolysis rates, mainly a consequence of the moderate reactivity of the C–O bond, in combination with the stabilizing effect of the organic species, lead to the formation of low-crystallinity products that are often characterized by uniform particle morphologies and tunable crystallite sizes in the range of just a few nanometers.[15] Inspired by these advantages, uniform titanium glycolate spheres were prepared and chosen as precursor, because materials with a spherical morphology have high packing density and good particle mobility to form a

compact electrode layer, and actually exhibit the optimal material morphology in conventional electrode fabrication.[16] Our investigation of the synthetic processes indicated that the reaction temperature was the most important factor, because it critically influences the crystallization and the surface microstructure of the product. If the temperature was too low (room temperature), no anatase phase or crystalline product could be obtained. If the reaction temperature was too high (above 120 ℃), however, the rate of reaction and the crystallinity of the product were high, and there was no surface-amorphized layer generated under these conditions. During the phase transformation, the density difference between titanium glycolate and TiO_2 results in cracks on the sphere‘s surface. Since the titanium glycolate spheres have low density, and the spheres are quite loose, H_2O can penetrate through the cracks on the surface and enter the inner part of the titanium glycolate sphere (**Figure 6.1** a). Thus, hydrolysis also occurs within the precursor spheres and leads to the formation of small TiO_2 particles in the surface layer. These small TiO_2 particles could act as nuclei for further growth. As the phase transformation proceeds, the TiO_2 particles grow gradually into interconnected nanoparticles.[17] We found that at relatively low temperatures (65 ℃), the surfaces of the interconnected nanoparticles was constructed from even smaller primary TiO_2 particles with only short-range order and unbonded atoms. The hierarchical nanoporous structure of TiO_2 with a surface-amorphized layer is thus formed under mild conditions during the phase transformation.

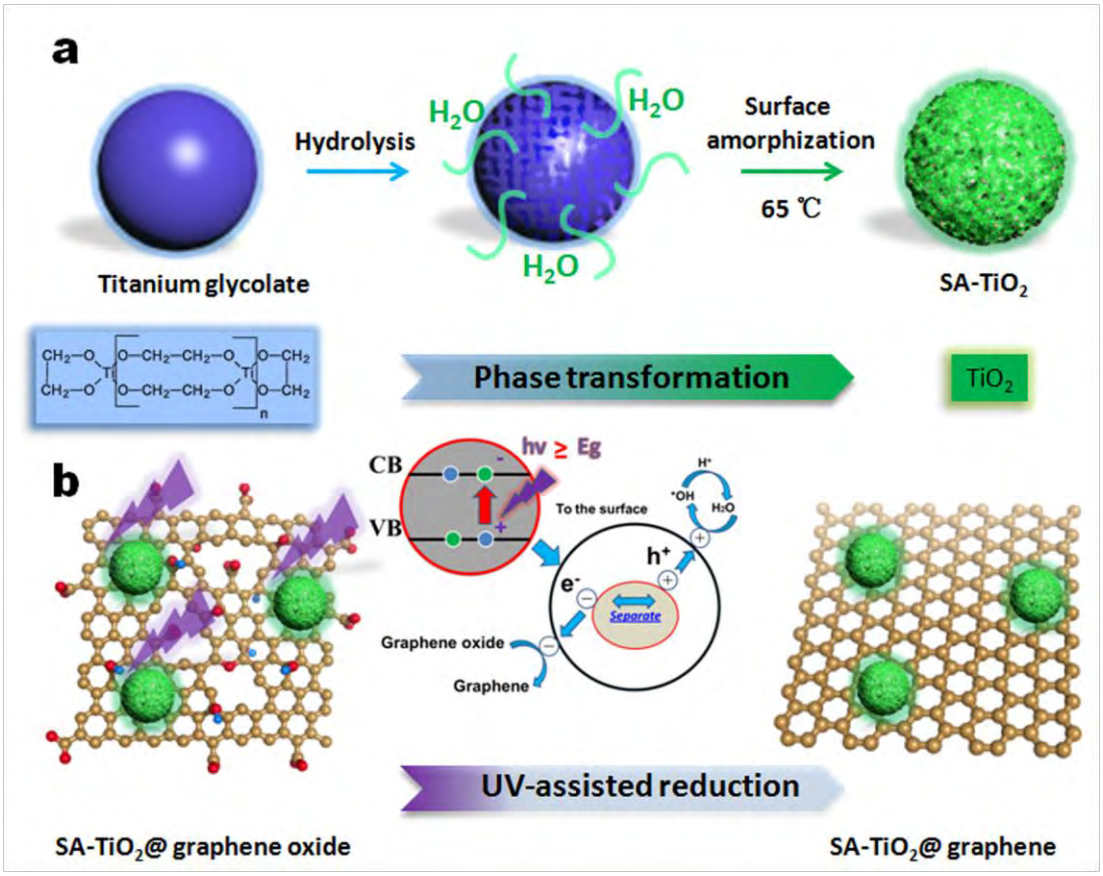

Figure 6.1 Schematic illustration of the preparation of SA-TiO_2@graphene in two steps. a) Phase transformation between titanium glycolate and TiO_2 results in nanoporous structure on the sphere‘s surface; the hierarchical nanoporous structure of TiO_2 with a surface-amorphized layer is thus formed under low temperature during the phase transformation at a low hydrolysis rate. b) The UV-assisted reduction technique was used to construct hybrid architectures combining SA-TiO_2 with graphene as complementary building blocks.

Figure 6.2 Change in color of SA-TiO_2 nanoparticles with GO before and after UV irradiation for 2 h. A suspension of SA-TiO_2 nanoparticles is also shown for comparison.

After successful preparation of the SA-TiO_2, we mixed it with graphene oxide (GO) in ethanol and subjected it to steady state UV irradiation. The total amount of GO used for assembly with TiO_2 was 2.0 wt %. A change in color from light brown to dark brown to black can be observed as the reduction of GO proceeds (**Figure 6.2** in the Supporting Information). This color change has previously been suggested as reflecting partial restoration of the network within the carbon structure and has been witnessed through chemical reduction of the GO sheets. Since TiO_2 particles carry surface charge in suspensions, they can be readily suspended in polar solvents. Thus, the SA-TiO_2-GO composite becomes readily soluble in polar solvents. Upon UV irradiation of a de-aerated suspension of SA-TiO_2, one observes charge separation. In the presence of ethanol, the holes are scavenged to produce ethoxy radicals, thus leaving the electrons to accumulate within the TiO_2 particles, as described in **Reaction** (1).[18] The accumulated electrons then interact with the graphene oxide sheets and reduce the amounts of certain functional groups [**Reaction** (2)]. In the present experiments, graphene oxide, with its extended epoxy and carboxylate

groups, readily interacts with TiO_2 particles and undergoes reduction under UV irradiation. The surface hydroxyl groups of TiO_2 undergo charge transfer interaction with carboxylic acid functional groups on GO, and thus, the direct interaction between SA-TiO_2 and graphene provides the basis to obtain SA-TiO_2@graphene composite.

$$TiO_2 + C_2H_5OH \rightarrow TiO_2\,(e^- + h^+) \xrightarrow{h\nu} TiO_2\,(e^-) + {}^{\bullet}C_2H_4OH + H^+ \quad (1)$$

$$TiO_2\,(e^-) + \text{graphene oxide (GO)} \xrightarrow{h\nu} TiO_2 + \text{graphene} \quad (2)$$

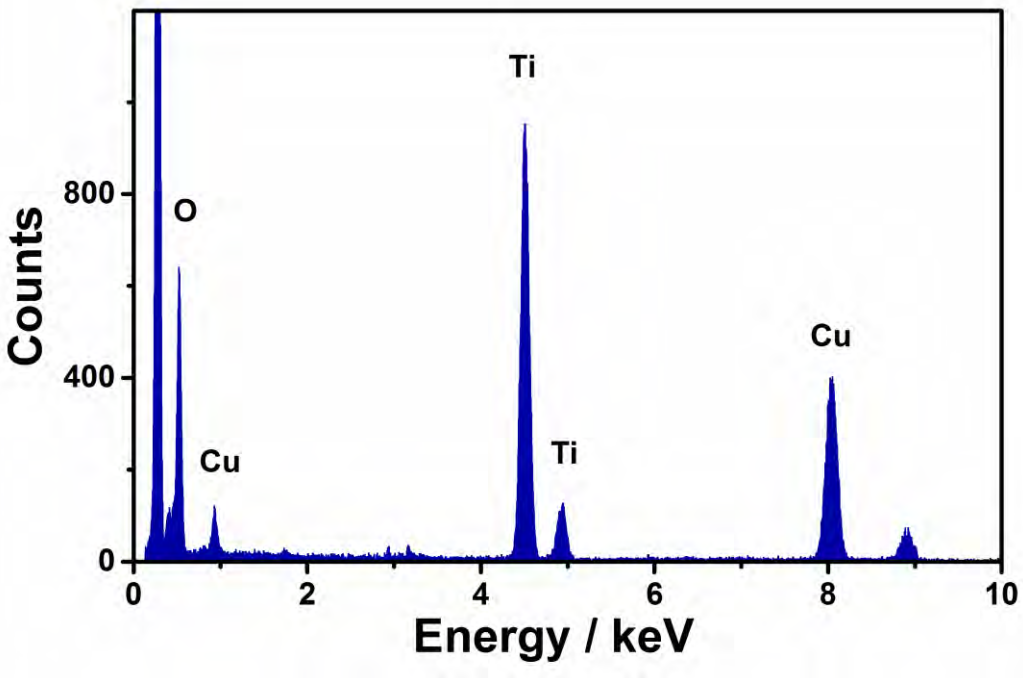

Figure 6.3 EDS spectrum of SA-TiO_2 nanoparticles.

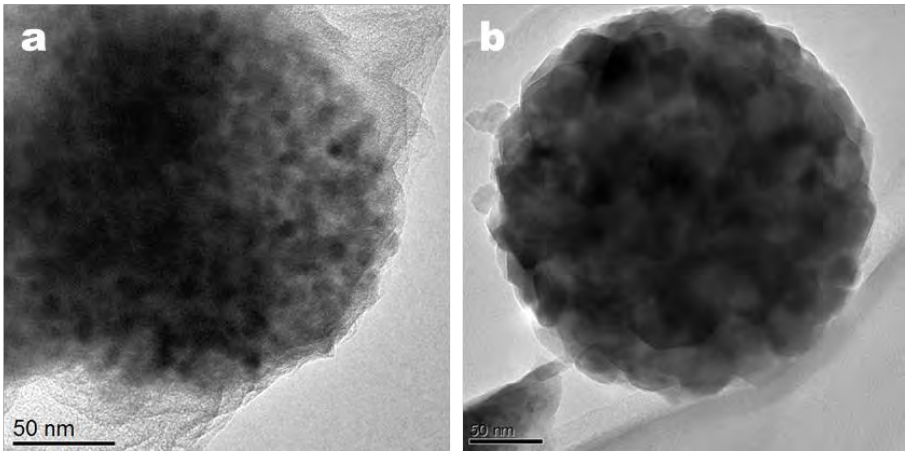

Figure 6.4 TEM images of SA-TiO_2@graphene (a) and C-TiO_2@graphene (b).

The morphology and microstructure of the SA-TiO_2 on graphene sheets were investigated by transmission electron microscopy (TEM) and scanning electron microscopy (SEM). It is interesting to see from the TEM images (**Figure 6.5** a, b) that the nanospheres consist of closely interconnected nanoparticles forming a mesoporous network of TiO_2, where the uniform TiO_2 nanospheres have a size of ~ 100 nm. This sort of porous structure could also offer excellent capability to accommodate strain and structural changes during battery cycling. The corresponding selected area electron diffraction (SAED) pattern (inset image in **Figure 6.5** b) shows clear diffraction rings, and it, along with the EDS spectrum (**Figure 6.3**) recorded from the corresponding area, suggests the polycrystalline nature of the whole nanosphere, and matches well with tetragonal anatase. A high resolution TEM (HRTEM) image confirms the crystalline features of the closely interconnected TiO_2 nanoparticles inside the nanospheres by clear lattice fringes

(**Figure 6.5 c**, **Figure 6.4**). The lattice fringes with a spacing of 3.5 Å can be assigned to the most stable and frequently observed anatase TiO_2 (101) planes, although it is interesting to find from the HRTEM image (**Figure 6.5** c) that the outer part of the nanoparticles consists of surface-amorphized structures forming an amorphous shell. The magnified TEM image shows that the thickness of the amorphous shell in **Figure 6.5** e, g is about 3.0 nm. The structure diagram from the simulation of the corresponding surface-amorphized TiO_2 shows that the amorphous shell could be constructed of TiO_2 particles with only short-range order and unbonded atoms, and these disordered structures not only provide more entrances for Li ions, but also offer plentiful surface oxygen vacancies, significantly increasing the specific surface area and assisting the adsorption capability of the electrolyte (**Figure 6.5** f). A thick and milky diffraction background can also be observed in the SAED pattern beside the TiO_2 diffraction rings, which suggests that the SA-TiO_2 contains amorphous or disordered phases, consistent with the HRTEM observations. It is well-known that graphene fabricated by the UV-assisted technique has restored sp^2 networks and multiple available oxygen-centered surface groups, which will allow unified connection between the GO and the exposed oxygen atoms at the surface of the TiO_2 nanoparticles. [18] The SEM images in **Figure 6.5** d also clearly show that the uniform TiO_2 nanospheres with a size of ~ 100 nm are well encapsulated by the graphene sheets.

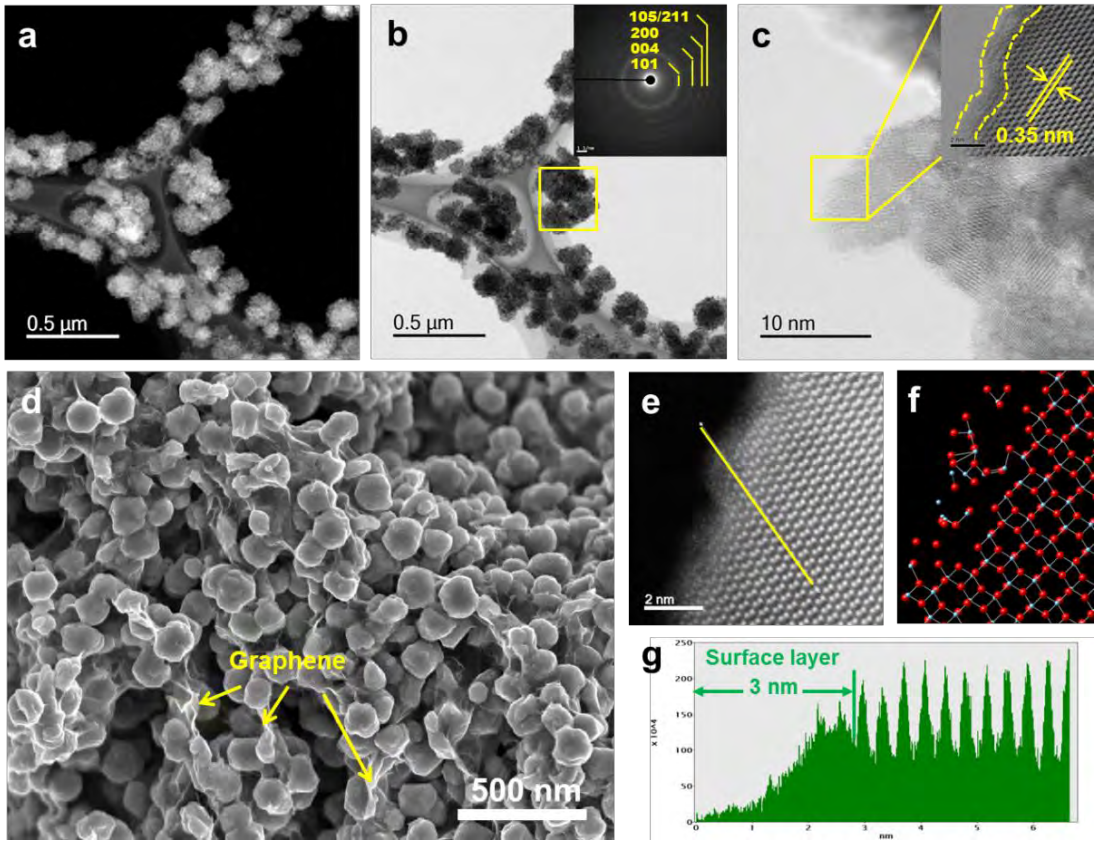

Figure 6.5 Electron microscope characterization of the SA-TiO_2 and SA-TiO_2@graphene samples: a) scanning transmission electron microscopy – high angle annular dark-field imaging (STEM-HAADF) and b) bright field TEM images of SA-TiO_2 with uniform sphere-like structure (with the inset in panel (b) the SAED pattern of the corresponding area). c) HRTEM image of the surface of a single SA-TiO_2 nanosphere, with the inset a magnified view of the region enclosed by the yellow box, which shows a clearly amorphous surface. d) SEM image of SA-TiO_2@graphene shows that the uniform TiO_2 nanospheres are well encapsulated by the graphene. e) Magnified STEM-HAADF image of the amorphous surface and f) Structure diagram from a simulation of the surface constructed from short-range-ordered TiO_2 particles and unbonded atoms. g) Measurement of surface layer depth corresponding to the line in panel (e).

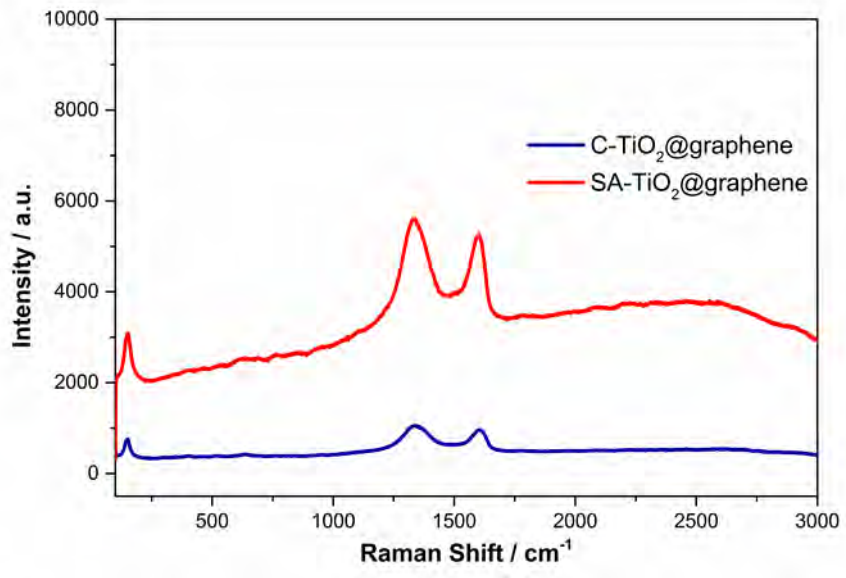

Figure 6.6 Raman spectra of SA-TiO_2@graphene and C-TiO_2@graphene.

The crystal structure and microstructure of the samples were further analyzed by X-ray diffraction (XRD). **Figure 6.7** a compares the XRD patterns of SA-TiO_2 and SA-TiO_2@graphene. All samples show diffraction peaks at 2θ = 25.36°, 37.90°, 48.15°, 54.05°, and 62.86°, which can be indexed to the (004), (200), (105), (211), and (204) planes of anatase TiO_2 (space group: I4 1 /amd, JCPDS No. 21-1272), respectively, confirming that the synthesized TiO_2 is anatase. Besides the distinctive diffraction peaks of anatase TiO_2, no obvious diffraction peak of graphene is observed for the SA-TiO_2@graphene sample, suggesting that the stacking of the graphene sheets remains disordered. We further conducted Raman measurements (**Figure 6.6**). Two obvious carbon bands, the D band and G band peaks, could be observed for both samples. Compared to the crystallized-TiO_2@graphene (C-TiO_2@graphene) samples, a peak at around 148.7 cm^{-1}, corresponding to the characteristic vibrational modes of anatase with a large featureless background, was observed for the SA-TiO_2@graphene samples, with the large background in the

Raman spectra suggesting that a thin amorphous phase/layer possibly exists on the surface of the SA-TiO_2@graphene [20b]. Nitrogen isotherm adsorption-desorption curves together, with the pore size distribution for the SA-TiO_2@graphene, are presented in **Figure 6.7** b. For SA-TiO_2@graphene, a type IV isotherm is observed, which is characteristic of mesoporous materials. Based on the Barrett–Joyner–Halenda (BJH) equation, the main pore size (inset in **Figure 6.7** b) in SA-TiO_2@graphene is 8 nm. The specific surface area of SA-TiO_2@graphene is 326 $m^2 g^{-1}$.

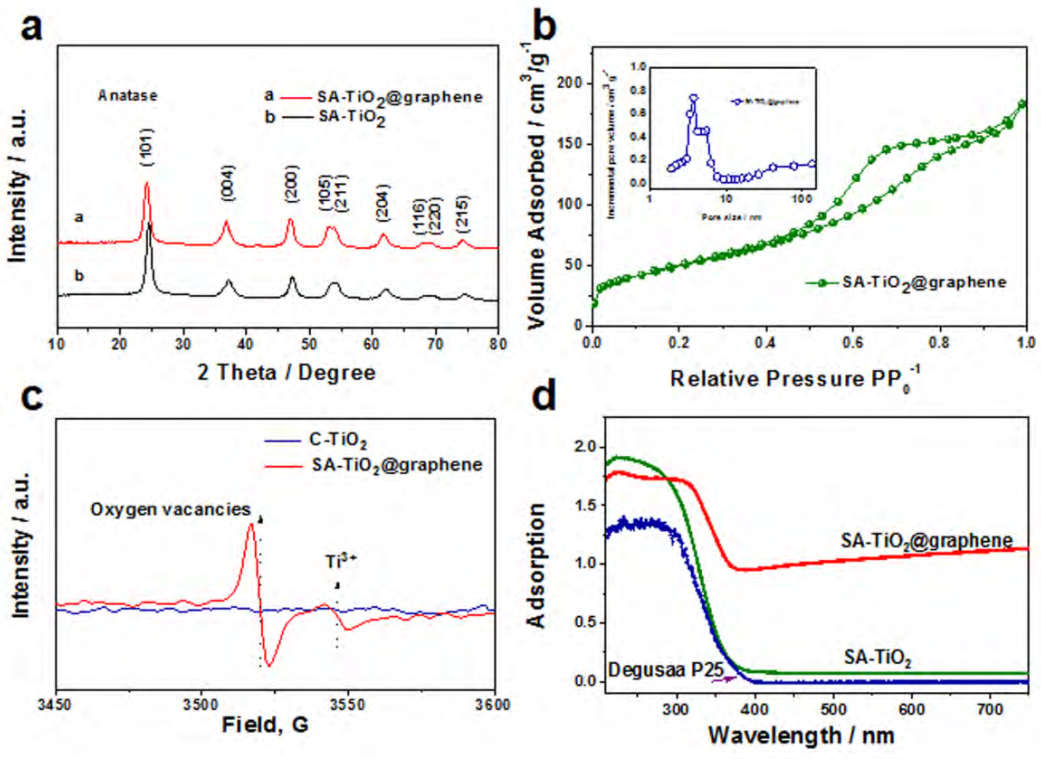

Figure 6.7 a) XRD patterns of SA-TiO_2@graphene (a) and SA-TiO_2 (b). b) Nitrogen adsorption and desorption isotherms (inset: pore size distribution) of SA-TiO_2@graphene. c) EPR spectra for SA-TiO_2@graphene and C-TiO_2 (C-TiO_2 heated in air, details in Supporting Information). d) Ultraviolet–visible diffuse reflectance

spectra of SA-TiO_2@graphene, SA-TiO_2, and commercial Degussa P25 TiO_2 as reference.

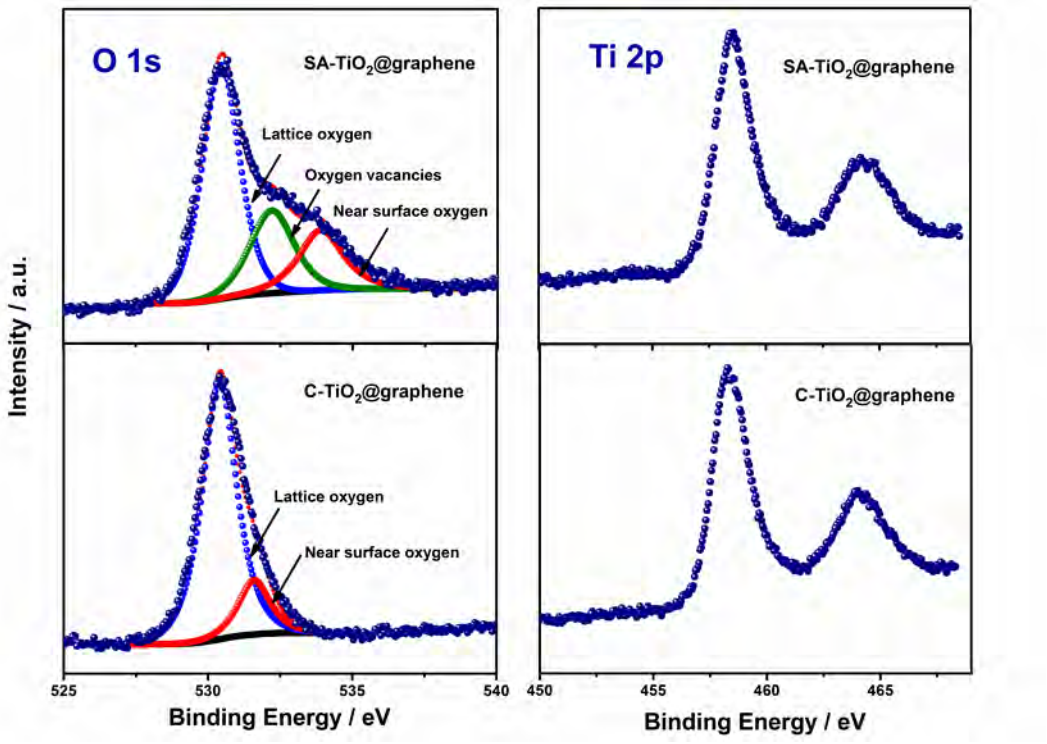

Figure 6.8 XPS spectra of SA-TiO_2@graphene and C-TiO_2@graphene.

In order to further confirm the existence of the amorphous surface layer of TiO_2 in the samples, electron paramagnetic resonance (EPR) measurements and X-ray photoelectron spectroscopy (XPS) were conducted to investigate the surface and physical properties of TiO_2. Compared to the heat-treated (600 ℃ in argon) C-TiO_2 samples, the appearance of an intense signal for the SA-TiO_2@graphene can be ascribed to oxygen vacancies, which may due to the single electron trapped on the oxygen vacancy states in the EPR spectra (**Figure 6.7** c). Notably, the creation of surface-amorphized TiO_2 not only results in oxygen vacancy formation, but also creates Ti^{3+} interstitials in the TiO_2 matrix. In both cases, Ti is in excess with respect

to O, and they both decrease the optical band gap of TiO_2. Moreover, oxygen vacancies are not only the most important defects in TiO_2, but also the most prevalent defects in many oxides, which greatly affect their chemical and physical properties. We have also studied the surface chemical bonding and valence bands of the samples with XPS. The binding energies from the samples were calibrated with respect to the C 1s peak from the carbon tape at 284.8 eV. Ti 2p and O 1s XPS peaks confirmed the formation of TiO_2 (**Figure 6.8**). The oxygen vacancies close to the surface lead to shifting of the core level of O 1s and the valence band to higher binding energies. The broad and asymmetric nature of the peak is ascribed to the various coordinations of oxygen in the SA-TiO_2. The O 1s XPS peak could be fitted into three peaks. The lowest binding energy peak located at 530.4 eV can be assigned to the lattice oxygen species. The highest binding energy peak at 533.9 eV is attributed to the near-surface oxygen, such as from surface hydroxylation, adsorbed H_2O. In addition, a new peak located at 532.2 eV is observed in the SA-TiO_2 sample, which can be assigned to oxygen vacancies.[19] There is no clear evidence, however, for Ti^{3+}. This is because Ti^{3+} is susceptible to oxidation by O_2 in air and cannot survive long.[20] The oxygen vacancies are more likely to be located in the disordered outer layer, considering that the crystalline phases are almost identical and large structural alteration was observed in this layer. The UV/visible (UV/Vis) spectroscopy of SA-TiO_2 and SA-TiO_2@graphene demonstrated higher absorbance over the full region (200 - 800 nm) than for the Degussa P25, and a steep increase in light absorbance is observed in both these two samples at wavelengths below 400 nm, which indicates that the photon trapping capacity of SA-TiO_2 was significantly enhanced, so that it maintains a high level of absorbance throughout the entire region. UV/Vis spectroscopy was used to confirm the presence of oxygen vacancies. It was

reported that the SA-TiO_2 spectrum features an increase in absorption between 400–800 nm due to free electrons, local Ti^{3+} centers (a band at 620 nm), and oxygen vacancies (bands at 1060, 441, and 486 nm).[4a] From the UV/Vis reflectance spectra of SA-TiO_2 (**Figure 6.7 d**), a significant increase in the absorbance compared to Degussa P25 in the visible light region for SA-TiO_2 can be observed, which confirms the presence of oxygen vacancies.

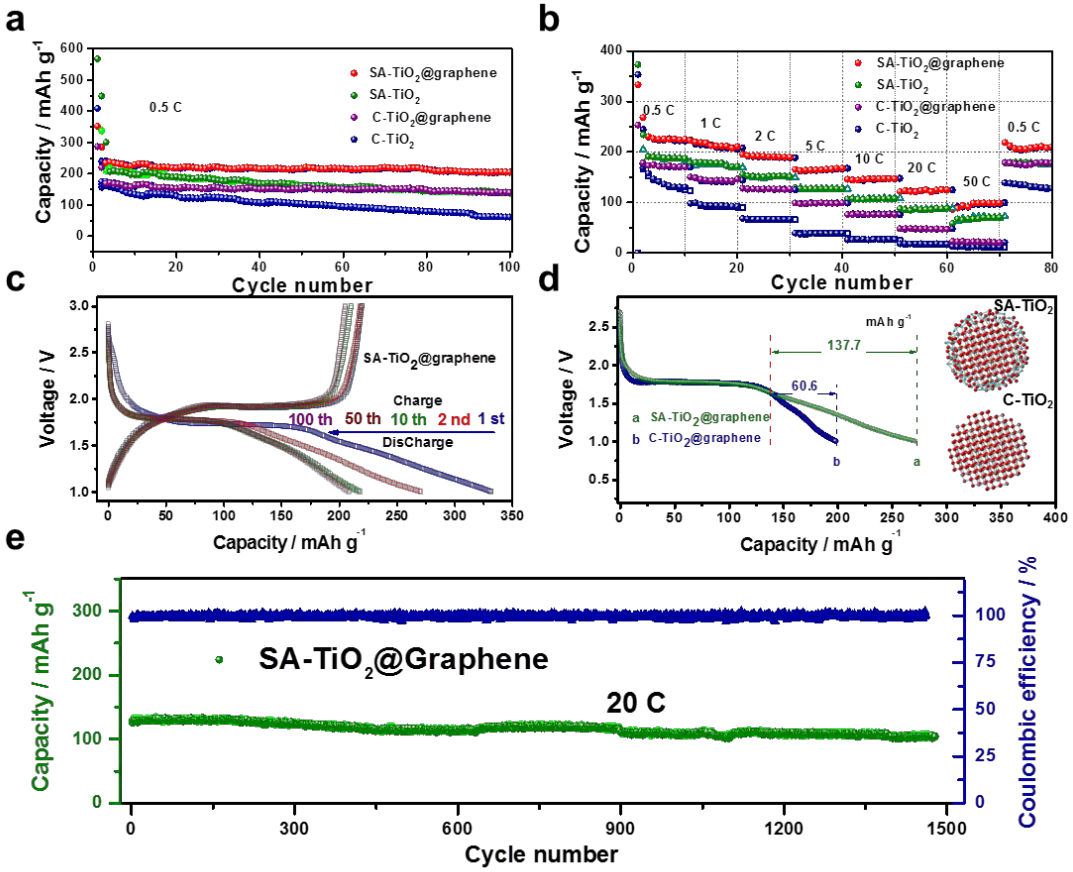

Figure 6.9 Electrochemical performance of SA-TiO_2@graphene electrodes. a) Capacity retention through 100 cycles at 0.5 C for the samples. b) Cycling performance of as-prepared samples at various current rates. c) Galvanostatic charge/discharge profiles at various cycles. d) Potential profiles of the SA-TiO_2@graphene and C-TiO_2@graphene for the cathodic cycle at the current density of 0.5C, with the inset showing the structures of the TiO_2 particles; e) Long-term

cycling performance of SA-TiO_2@graphene at the high current density of 20 C, showing the reversible capacity value of 108 mAh g^{-1} after 1500 cycles with coulombic efficiency of ~ 100%.

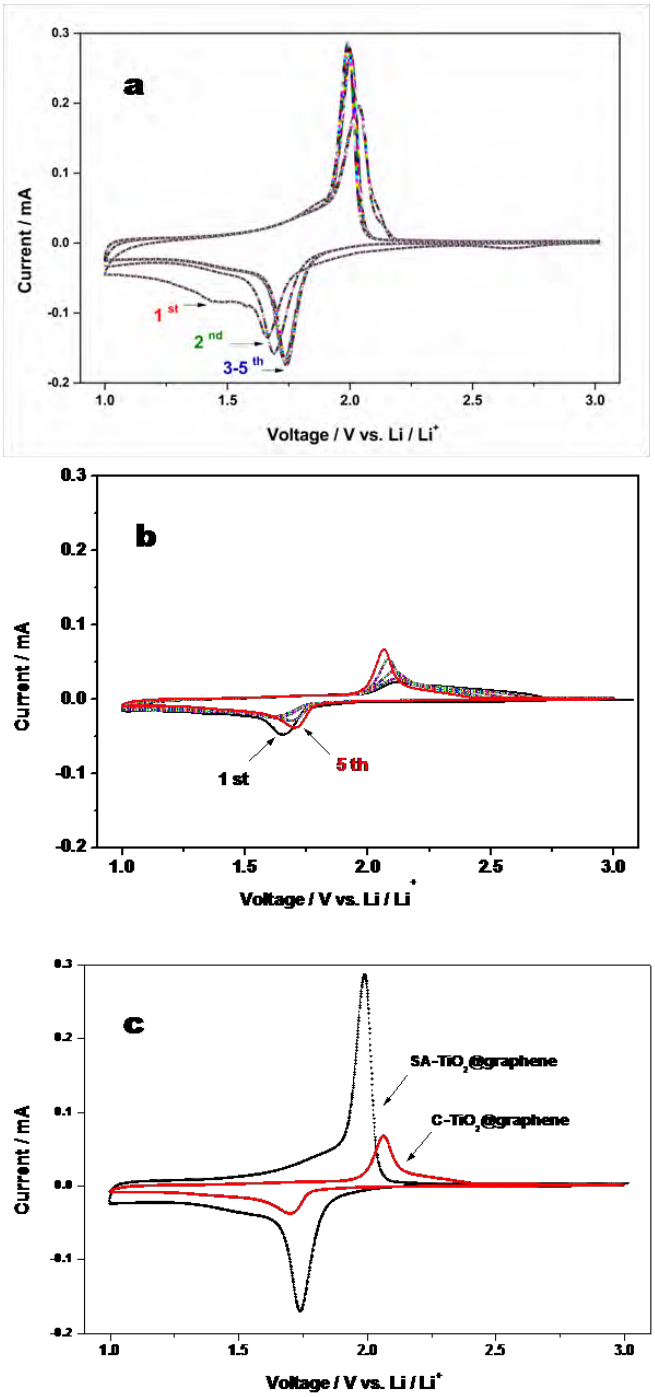

Figure 6.10 Cyclic voltammograms for the first 5 cycles of (a) SA-TiO_2@graphene, (b) C-TiO_2@graphene; and (c) 5th cycle CVs of both samples for comparison at the scan rate of 0.2 mV/s.

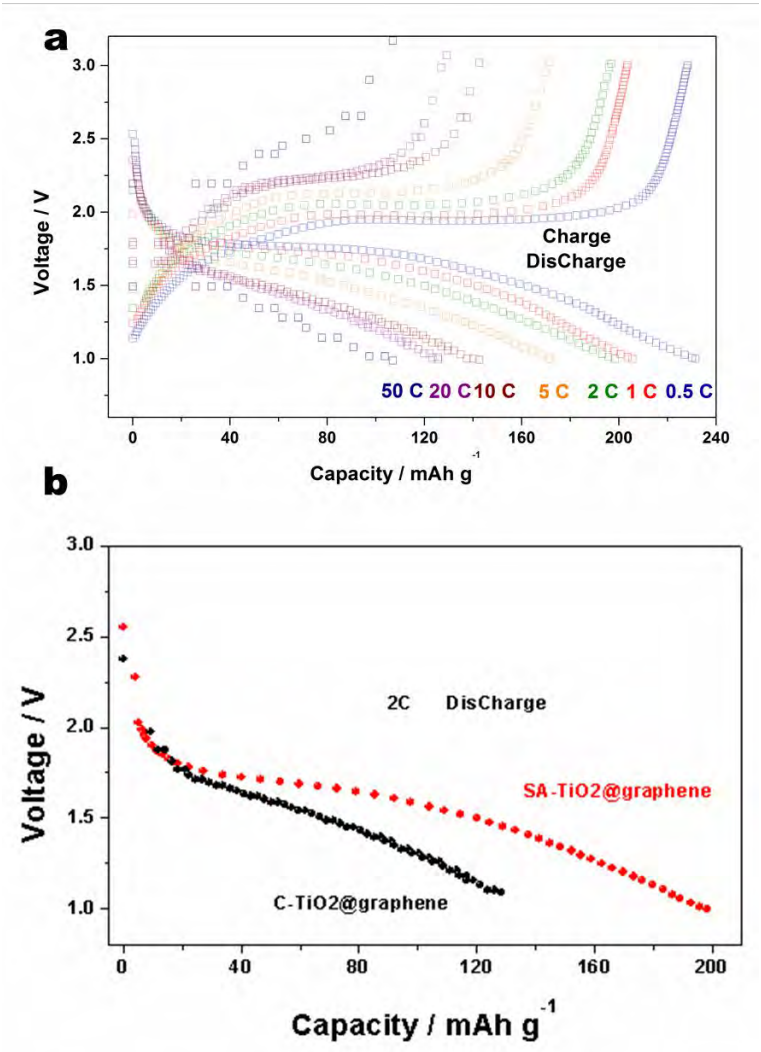

Figure 6.11 (a) Charge and discharge curves of SA-TiO_2@graphene at different current rates from 0.5 C - 50 C. (b) Potential profiles of the SA-TiO_2@graphene and C-TiO_2@graphene for the cathodic cycle at the current density of 2 C.

To demonstrate the effectiveness of the surface-amorphized structure of SA-TiO_2@graphene in improving rate-capacity, the lithium-insertion/extraction properties of SA-TiO_2@graphene as anode were investigated by galvanostatic

charge-discharge measurements. **Figure 6.9** a shows the discharge (Li^+ insertion) and charge (Li^+ extraction) curves of a SA-TiO_2@graphene electrode at the rate of 0.5 C (84 mA g^{-1}). In a voltage window of 1−3 V, the discharge and charge capacities of the 1st cycle are 332 and 273.4 mAh g^{-1}, respectively. Clearly, this electrode shows superior cyclic retention to 100 cycles. Both the SA-TiO_2@graphene and the SA-TiO_2 are found to be effective in improving Li-storage, showing a greatly enhanced discharge capacity after 100 cycles (205.1 mAh·g^{-1} for SA-TiO_2@graphene, and 141.7 mAh·g^{-1} for SA-TiO_2), while only 61.8 mAh·g^{-1} was achieved with C-TiO_2. In **Figure 6.9** c and **Figure 6.10**, the SA-TiO_2@graphene showed the typical electrochemical characteristics of anatase TiO_2, exhibiting cathodic insertion of lithium at 1.75 V and anodic extraction of lithium at 1.95 V vs. Li/Li^+. The better Li^+ storage performance of the SA-TiO_2@graphene in comparison with that of C-TiO_2@graphene can be observed from the cyclic voltammograms (CVs) (Figure S6). The voltage difference between the anodic and cathodic peaks (ΔE_p) reflects the degree of polarization of the electrode. SA-TiO_2@graphene has a much lower ΔE_p value than C-TiO_2@graphene. Therefore, the SA-TiO_2@graphene is less polarized and has faster electrochemical reaction kinetics. This result agrees well with the electrochemical performance results shown in **Figure 6.9 b**. The CV curves of both samples remained almost unchanged after three cycles, demonstrating that the electrochemical reaction was stable and reversible. More strikingly, with respect to the reference TiO_2, the specific capacity of SA-TiO_2@graphene is substantially increased at all investigated charge-discharge rates, as demonstrated in **Figure 6.9** b and **6.9** d. **Figure 6.9** b and **Figure 6.11** illustrate the specific charge obtained at different C-rates (0.5 C, 1 C, 2 C, 5 C, 10 C, 20 C and 50 C, equal to 0.084, 0.168, 0.336, 0.840, 1.680, 3.360 and 8.400 A g^{-1}, respectively) as a function of the number

of cycles. For example, the specific capacity of SA-TiO_2@graphene at the rate of 50 C is as high as 103 mA h g^{-1}, 9.3 times higher than that of the reference C-TiO_2. Importantly, after the high rate measurements, the specific capacity of SA-TiO_2@graphene at 0.5 C can recover to the initial value, indicating its high reversibility. It also shows superior cycling capacity (~ 108 mA h g^{-1}) over 1500 cycles at the high rate of 20 C, along with ~ 100% coulombic efficiency, proving its excellent tolerance of ultra-fast insertion and extraction of lithium ions for long-life LIBs.

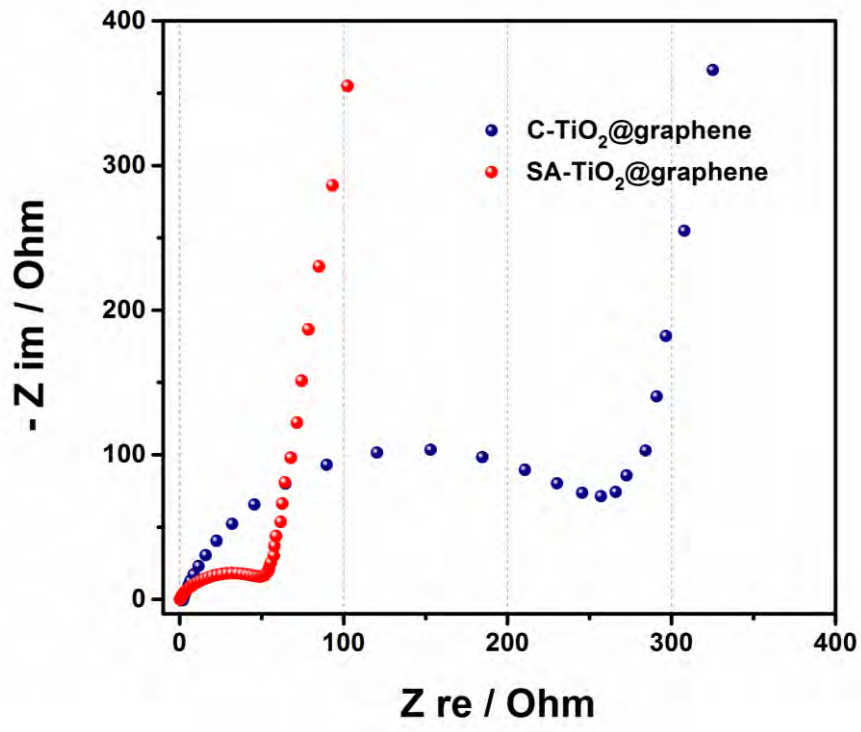

Figure 6.12 Nyquist plots of electrodes containing hybrid SA-TiO_2@graphene and C-TiO_2@graphene, obtained by applying a sine wave with an amplitude of 5.0 mV over the frequency range from 100 kHz to 0.01 Hz.

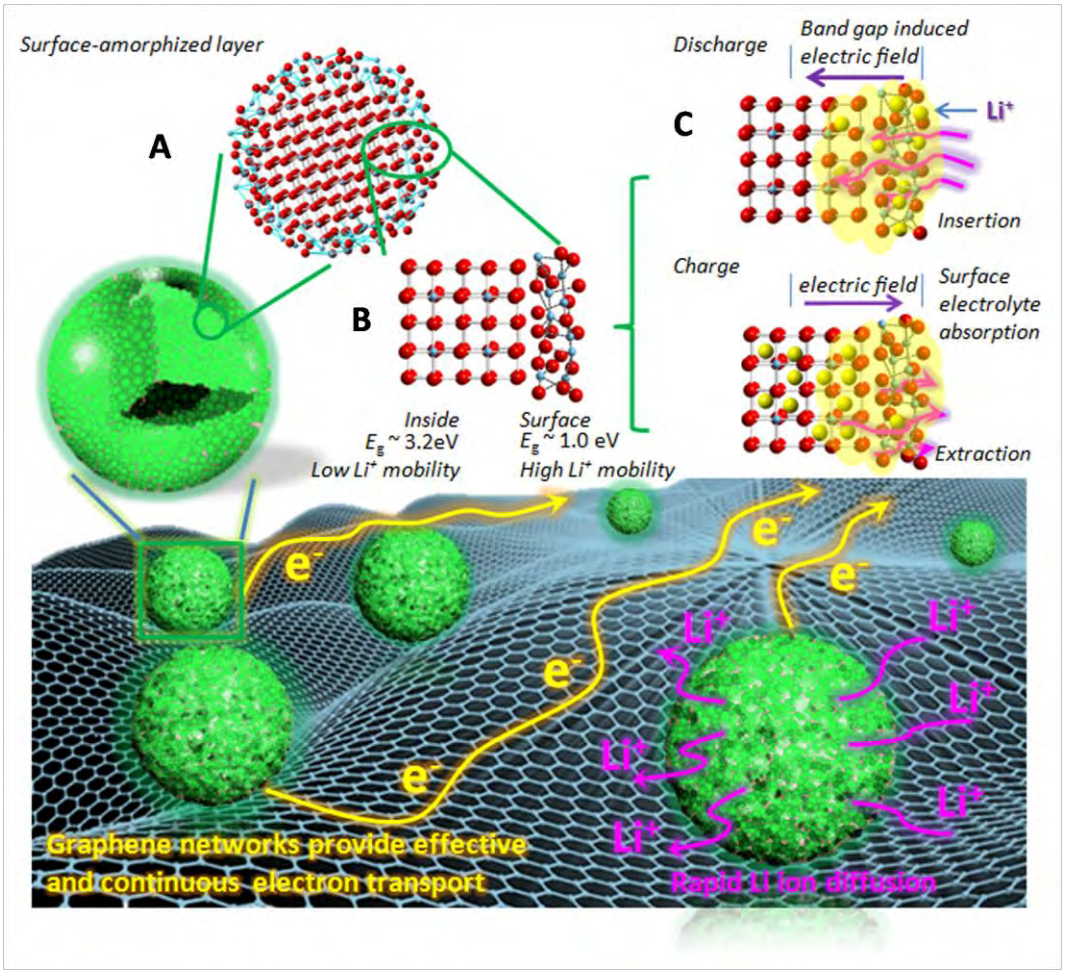

Figure 6.13 Summary of the enhanced high rate performance mechanism of the SA-TiO_2@graphene in the Li battery system. The surface amorphous layer (Region A) with its narrow band gap (~1.0 eV) has plenty of oxygen vacancies and Ti^{3+} ions, which together with the crystalline structure inside (band gap, E_g = 3.2 eV) (Region B) induces an electric field during the charge/discharge process to facilitate deeper charge diffusion within the materials (Region C). In the meanwhile, the graphene matrix provides an effective and continuous electrically conducting network. The highly porous surface amorphous layer also helps in electrolyte absorption.

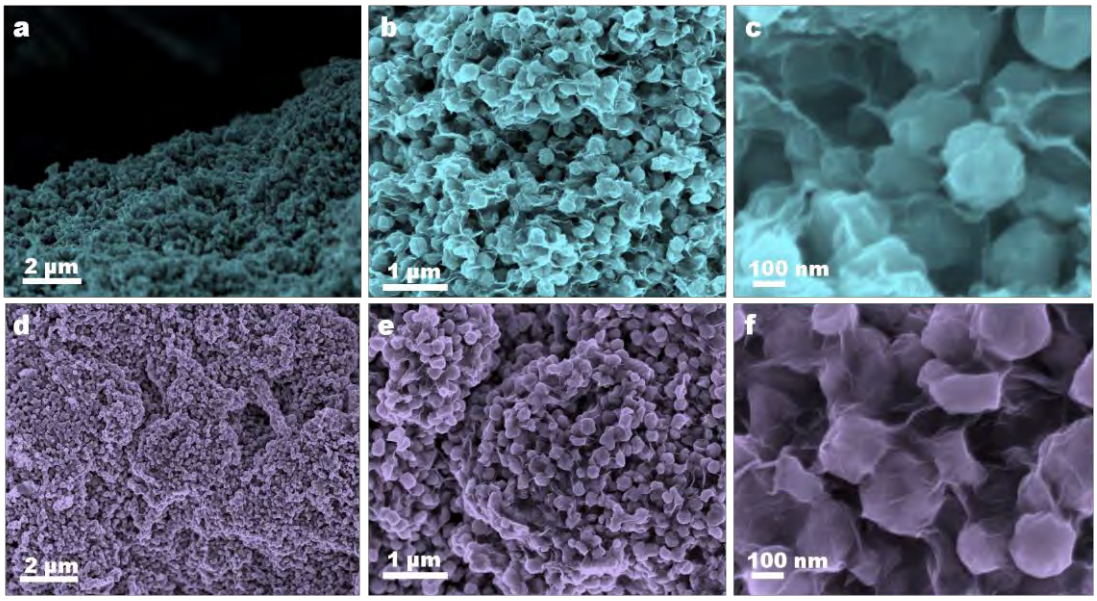

Figure 6.14 Cross-sectional (a, b, c) and top-view (d,e, f) SEM images of SA-TiO_2@graphene show that the uniform TiO_2 nanospheres are well encapsulated by the graphene.

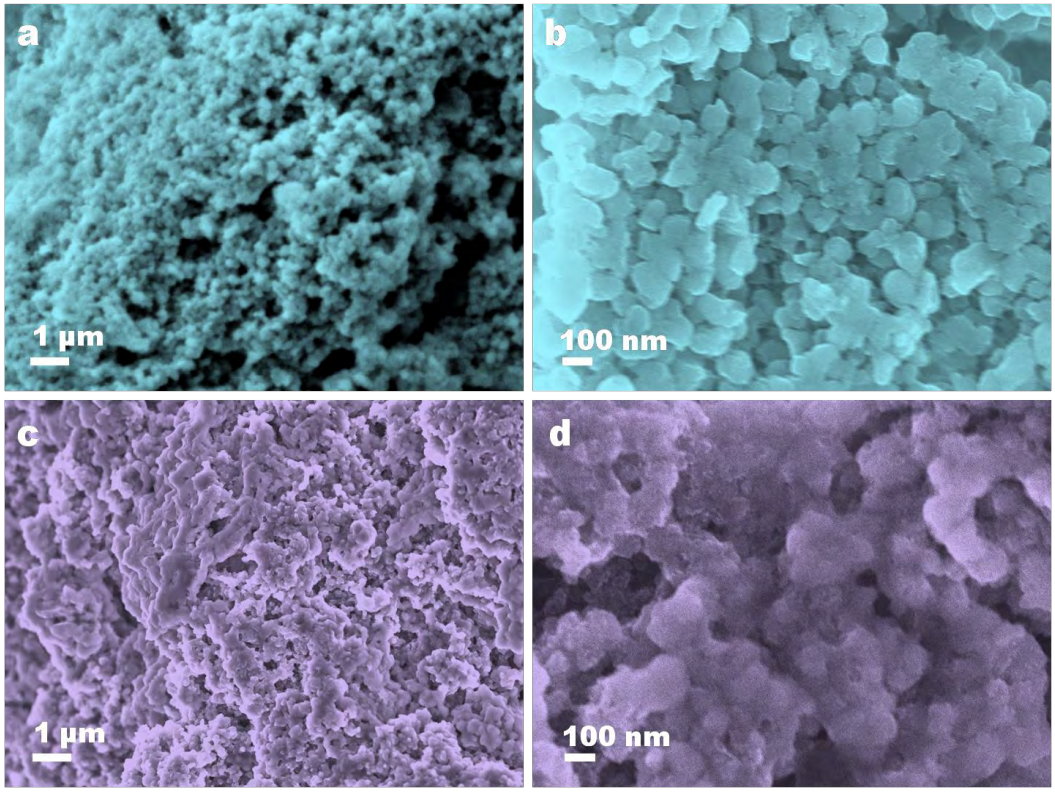

Figure 6.15 Typical SEM images of SA-TiO_2@graphene electrode before (a,b) and after (c, d) 10 cycles at the current density of 336 mA g^{-1}.

In a control experiment, C-TiO_2@graphene was synthesized following the same procedures as for the synthesis of the SA-TiO_2@graphene and then heat-treated in air at 600 ℃ to eliminate the surface-amorphized layer. The capacity for C-TiO_2@graphene is 139.7 $mAh \cdot g^{-1}$ (**Figure 6.9**a), which is lower than that of the SA-TiO_2@graphene (205.1 $mAh \cdot g^{-1}$) and higher than that of C-TiO_2 (61.8 $mAh \cdot g^{-1}$). That is because the particle size and the surface-amorphized layer of TiO_2 are of great importance for its electrochemical performance. The distance from the surface to the core drastically affects the ability to store charge at high C-rates. Because the surface atomic arrangement affects the specific charge at moderate C-rates, for example, from 0.5 to 50 C, the effective diffusion length for lithium ions is 24 nm under the charge/discharge rate of 0.5 C, and 3.2 nm under 50 C.[21] The lithium-ion mobility also becomes extremely low for lithium-ion content higher than that of $Li_{0.5}TiO_2$. [4a] Consequently, storing lithium ions beyond $Li_{0.5}TiO_2$ can only be achieved near the surface, and thus, higher specific charge capacities are obtained with increasing specific surface area. It has been demonstrated that ordinary crystalline anatase TiO_2 gives only the orthorhombic $Li_{0.5}TiO_2$, while Li_xTiO_2 ($x >$ 0.5) with higher lithium storage capacity can indeed be formed in ultra-small TiO_2 as a result of the quantum-size confinement effect.[22] In our work, the thickness of the surface layer is ~ 3 nm. The amorphous-layer-induced defects such as dangling bonds and oxygen vacancies typically lead to unexpected electronic states in the band gap that result in improved electrical conductivity (**Figure 6.12**). The calculated band gaps for crystalline TiO_2 and amorphous TiO_2 are 3.2 and 1.0 eV, respectively.[13] The surface amorphous layer in our work is different from an amorphous structure with only poor crystallinity.[23] The surface amorphous layer

with its narrow band gap (~1.0 eV) has plenty of oxygen vacancies and Ti^{3+} ions, which together with the crystalline structure inside (band gap, E_g = 3.2 eV) induces an electric field during the charge/discharge process to facilitate deeper charge diffusion within the materials (**Figure 6.13**). We believe that the TiO_2 with different band gaps creates an electric field effect for lithium storage that may occur in the deep region of TiO_2 and thus increases the capacity to some extent. Below the plateau of phase transformation from tetragonal to orthorhombic (~ 1.75 V), a sloping curve appears, in which the capacity comes from the lithium-ion intercalation beyond $Li_{0.5}TiO_2$ (**Figure 6.9** d). The capacity beyond $Li_{0.5}TiO_2$ for SA-TiO_2@graphene is about 137.7 $mAh \cdot g^{-1}$, which is nearly double that of C-TiO_2@graphene (60.6 $mAh \cdot g^{-1}$). The narrow band gap of the surface amorphous layer also improves the electronic conductivity and rapid ion/electron transport pathways, and it also has benefits for high power performance. Moreover, the amorphous layer with high surface area possesses better adsorption capability for ions and molecules to facilitate Li^+ transfer across the electrolyte/TiO_2 interface, due to the higher local concentration. In addition, the weak connections between the SA-TiO_2 nanospheres are responsible for the poor cycling and rate performance during lithium insertion/extraction processes. When the SA-TiO_2 nanospheres are well encapsulated by the graphene, however, using a simple UV-assisted reduction technique, the graphene provides an interconnected conductive network which significantly improves the cycling and rate performances. The excellent high-rate performance is attributed to the substantial decrease in charge-transfer resistance due to the unique structure of the SA-TiO_2@graphene.[24] The stable cycling of an electrode has strict requirements in terms of structural stability at the particle level, because small changes in particle morphology could cause electrode-level cracking

and failure. After 10 deep cycles at the current density of 336 mA g^{-1}, the morphology of the SA-TiO_2@graphene was examined with SEM and there is no obvious structural change after cycling. As the SEM micrographs in Figure S10d demonstrate, we can see a thin solid electrolyte interphase (SEI) film on the sample surface after 10 cycles. The partially reversible SEI formation might also contribute to the enhanced capacity.

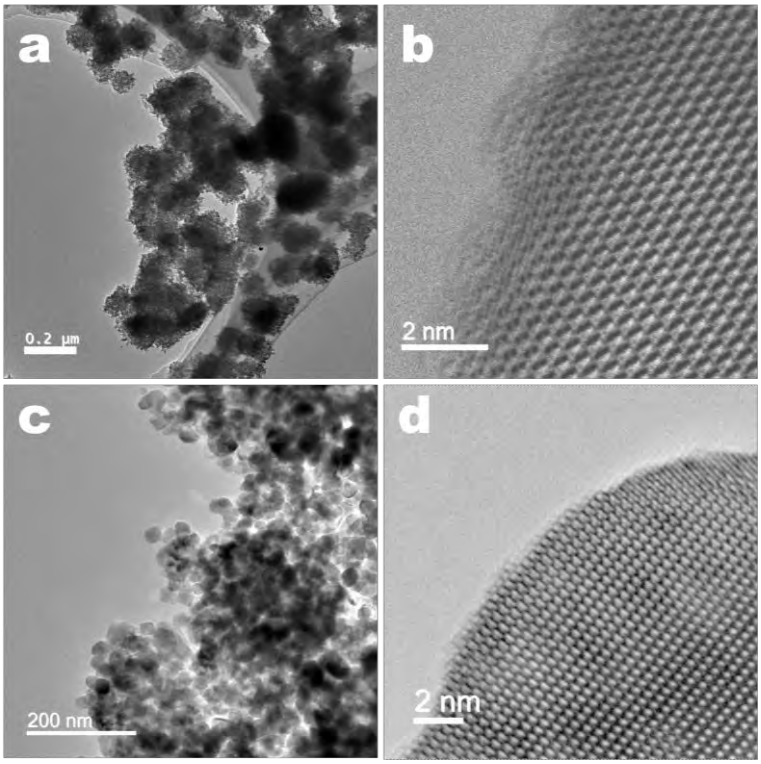

Figure 6.16 TEM and HRTEM images of SA-TiO_2 (a, b) and C-TiO_2 (c, d), respectively.

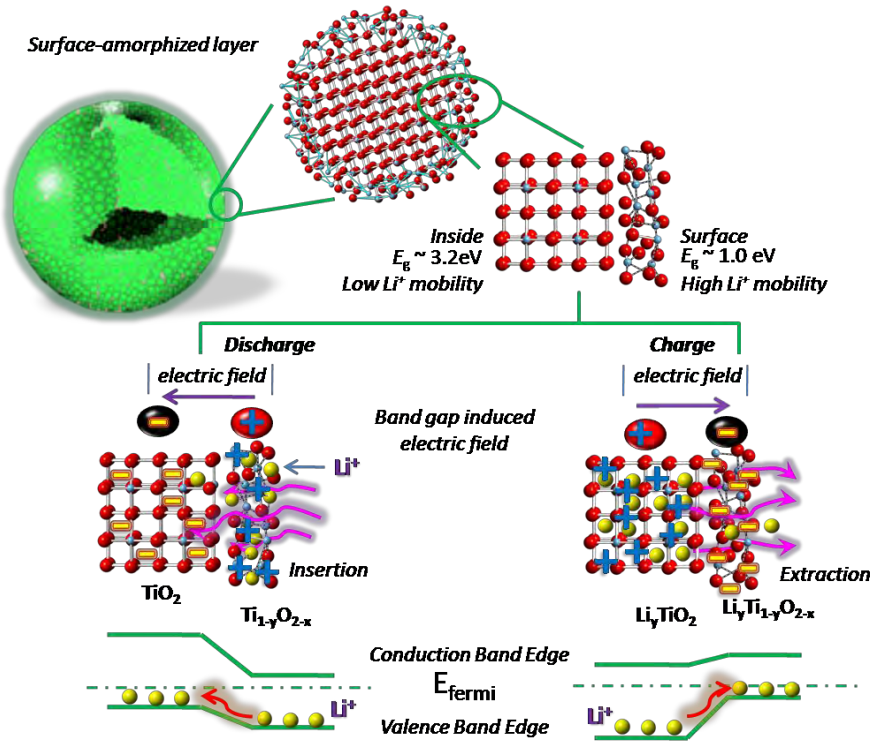

Figure 6.17 Summary of the enhanced high rate performance mechanism of the SA-TiO_2@graphene in the Li battery system.

6.4 Conclusions

We have designed and successfully fabricated surface amorphized (SA)-TiO_2@graphene composites. A thin amorphous TiO_2 layer was created on crystalline TiO_2 nanospheres under mild conditions and assembled with graphene via a UV-assisted reduction technique. We evaluated the SA-TiO_2@graphene as an electrode material for lithium ion batteries and found that it exhibited greatly improved lithium insertion/extraction performance compared with crystalline TiO_2. The optimal SA-TiO_2@graphene hybrid architecture exhibits a substantial improvement in lithium specific capacity from 0.5 C to 50 C. More strikingly, the specific capacity of the composite at the rate of 50 C is as high as 103 mA h g^{-1}, 9.3 times higher than that of the reference TiO_2. We attributed the greatly enhanced lithium storage properties of the SA-TiO_2@graphene nanocrystals to the lower lithium ion diffusion and electronic conduction resistance, and better surface adsorption in the amorphous layer. These improvements benefit from the electric field introduced by the surface-amorphization within the nanocrystals, which leads to much lower lithium-ion diffusion resistance, facilitates its transport in both insertion and extraction processes, and also enhances the electrolyte absorption capability. This concept thus offers an innovative and general approach toward designing battery materials with better performance.

6.5 References

[1] M. Kapilashrami, Y. Zhang, Y.-S. Liu, A. Hagfeldt, J. Guo, Chem. Rev. **2014**, 114, 9662.

[2] M. Dahl, Y. Liu, Y. Yin, Chem. Rev. **2014**, 114, 9853.

[3] H. Liu, Z. Bi, X.-G. Sun, R. R. Unocic, M. P. Paranthaman, S. Dai, G. M. Brown, Adv. Mater. **2011**, 23, 3450.

[4] a) E. Ventosa, A. Tymoczko, K. Xie, W. Xia, M. Muhler, W. Schuhmann, ChemSusChem **2014**, 7, 2584; b) Z. Wang, X. Li, H. Xu, Y. Yang, Y. Cui, H. Pan, Z. Wang, B. Chen, G. Qian, J. Mater. Chem. A **2014,** 2, 12571.

[5] T. Xia, W. Zhang, Z. Wang, Y. Zhang, X. Song, J. Murowchick, V. Battaglia, G. Liu, X. Chen, Nano Energy **2014,** 6, 109.

[6] S. C. Jung, H.-J. Kim, J. W. Choi, Y.-K. Han, Nano Lett. **2014,** 14, 6559.

[7] G. Zhang, H. B. Wu, T. Song, U. Paik, X. W. Lou, Angew. Chem. Int. Ed. **2014,** 53, 12590.

[8] X. Zhang, F. Meng, S. Mao, Q. Ding, M. J. Shearer, M. S. Faber, J. Chen, R. J. Hamers, S. Jin, Energy Environ. Sci. **2015**, 8, 862-868.

[9] J. Lee, A. Urban, X. Li, D. Su, G. Hautier, G. Ceder, Science **2014,** 343, 519.

[10] O. B. Chae, J. Kim, I. Park, H. Jeong, J. H. Ku, J. H. Ryu, K. Kang, S. M. Oh, Chem. Mat. **2014,** 26, 5874.

[11] E. Uchaker, Y. Z. Zheng, S. Li, S. L. Candelaria, S. Hu, G. Z. Cao, J. Mater. Chem. A **2014,** 2, 18208.

[12] F. Tian, M. D. Radin, D. J. Siegel, Chem. Mat. **2014,** 26, 2952.

[13] G. Kulbir Kaur, S. Chandra Veer, J. Phys.: Condens. Mat. **2013,** 25, 475501.

[14] J.-Y. Shin, J. H. Joo, D. Samuelis, J. Maier, Chem. Mat. **2011,** 24, 543.

[15] M. Niederberger, Acc. Chem. Res. **2007,** 40, 793.

[16] B. Liu, L.-M. Liu, X.-F. Lang, H.-Y. Wang, X. W. Lou, E. S. Aydil, Energy Environ. Sci. **2014,** 7, 2592.

[17] L.-S. Zhong, J.-S. Hu, L.-J. Wan, W.-G. Song, Chem. Commun. **2008,** 1184.

[18] G. Williams, B. Seger, P. V. Kamat, ACS Nano **2008,** 2, 1487.

[19] W. Bi, C. Ye, C. Xiao, W. Tong, X. Zhang, W. Shao, Y. Xie, Small **2014,** 10, 2820.

[20] C. Mao, F. Zuo, Y. Hou, X. Bu, P. Feng, Angew. Chem. **2014,** 126, 10653.

[21] a) P. G. Bruce, B. Scrosati, J.-M. Tarascon, Angew. Chem. Int. Ed. **2008,** 47, 2930; b) T. Xia, W. Zhang, W. Li, N. A. Oyler, G. Liu, X. Chen, Nano Energy **2013,** 2, 826.

[22] W. J. H. Borghols, D. Lutzenkirchen-Hecht, U. Haake, E. R. H. van Eck, F. M. Mulder, M. Wagemaker, Phys. Chem. Chem. Phys. **2009,** 11, 5742.

[23] T. Xia, W. Zhang, J. Murowchick, G. Liu, X. Chen, Nano Lett. **2013,** 13, 5289.

[24] T. Zhou, W. K. Pang, C. Zhang, J. Yang, Z. Chen, H. K. Liu, Z. Guo, ACS Nano **2014,** 8, 8323.

CHAPTER 7 HIGHLY ORDERED DUAL POROSITY MESOPOROUS COBALT OXIDE FOR SODIUM ION BATTERIES

Highly ordered mesoporous cobalt oxide (Co_3O_4) has been synthesized and applied as an electroactive material in sodium ion battery anodes. Mesoporous silica was used as the template for the generation of dual porosity cobalt oxide with spherical mesopores and porous nanochannels. The most notable feature of our dual porosity mesoporous Co_3O_4 is that the highly ordered structure can provide much better transport pathways than the reference bulk Co_3O_4 derived nanostructure, because it can facilitate the mass transport of electrolyte in the larger pores and sodium ion diffusion in the smaller pores, and also provide a large electrode-electrolyte interface for electrolyte adsorption due to the surface disorder of the Co_3O_4. The outstanding dual porosity mesopores in the cobalt oxide allow better transport pathways and thus lead to an initial capacity of 707 $mAhg^{-1}$ at the current density of 90 mA g^{-1}, with capacity of 416 mAh g^{-1} still retained after 100 cycles. The sodium uptake/extraction is confirmed to take place through a reversible conversion reaction, based on ex-situ characterization techniques, which identify dual porosity mesoporous Co_3O_4 as a high performance sodium ion battery anode material.

7.1 Introduction

In recent years, highly ordered mesoporous materials have received significant attention in the materials research community because of their special framework topologies, high surface areas, and controllable particle size, pore size, and pore volume, allowing them to play a key role in various fields such as adsorption, gas storage, catalysis, biochemistry, and electronics.[1] Recently, ordered mesoporous materials have gained much attention as promising candidate energy storage materials, since ordered mesoporous frameworks with uniform sizes on the nanoscale can offer opportunities to improve electrochemical performance.[2] The greatest advantage of ordered mesoporous materials in the electrode field is the presence of well-defined mesopores, which are believed to act as a kind of physical buffer for volume changes and as mass transport pathways during charge and discharge.[3]

Sodium-ion batteries (SIBs) have recently again attracted increasing attention for large-scale energy storage in renewable energy and smart grid applications, because of both the low costs associated with the high natural abundance of sodium and the decent energy densities bestowed by its similar chemical nature to Li [4]. Many mature electrode materials for the Li-ion chemistry have been investigated as drop-in replacements for Na-ion batteries. Among them, Co_3O_4 is regarded as a promising active electrode material on the basis of its low cost, high specific capacitance, and environmental benignity[5]. For instance, Co_3O_4 is considered as a potential Li-ion battery anode material due to its theoretical capacity of ~ 890 mA h g^{-1}, over twice that of graphite[5b]. Despite its great promise, however, there still are major challenges that need to be addressed for the practical application of Co_3O_4 in SIBs,

which include low electronic conductivity, as well as a slow charge-discharge rate and large volume changes during the Na^+ insertion and extraction processes, resulting in poor cycling stability, for which the larger size of the Na-ion relative to the Li-ion is generally believed to be responsible.[5b, 5c, 6].

To circumvent these challenges, a variety of approaches have been attempted to improve the electrochemical properties of Co_3O_4, such as the fabrication of nanostructures with different morphologies[5b, 5d, 6-7], the fabrication of composites incorporated with conducting matrices [8], and porous-structure designs with high surface area[5b, 9] . One highly desirable and promising approach to address the aforementioned drawbacks is the rational design of mesoporous Co_3O_4 with well-defined microstructures[9-10]. The obvious advantages of mesoporous microstructures are seen in the properties of their elegant architectures: (1) the interlaced networks of interconnecting mesopores can provide superior channels for high electrode-electrolyte contact area and electrolyte penetration/adsorption; (2) the mesoporous architectures can supply an elastic space to buffer the large volume expansion during the Na^+ insertion-extraction process, thus enhancing the cycling performance; (3) in addition, the secondary microstructures with high surface area can facilitate extra active sites for Na^+ storage and a short Na^+ diffusion distance among the primary nanoblocks[10a, 11]. These benefits are also critical and significant for optimizing the cycling and rate performance of sodium ion batteries[12].

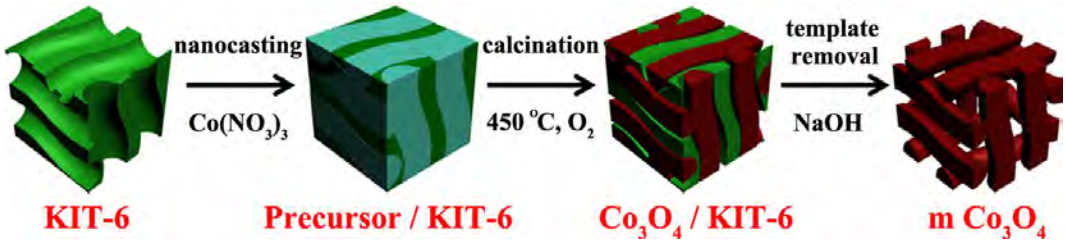

Figure 7.1 Schematic diagram of synthesis of mesoporous Co_3O_4 *via* the nanocasting route by using calcined 3D cubic *Ia3d* KIT-6 silica as a sacrificial template.

Herein, we demonstrate an efficient method for direct fabrication of highly ordered mesoporous Co_3O_4 (m-Co_3O_4) microspheres by utilizing cubic mesostructured silica (KIT-6) as a sacrificial template (**Figure 7.1**). The ordered mesoporous structure was used to accommodate the large volume changes during sodiation/desodiation. The large voids in the mesoporous structure appear to buffer the volume expansion/contraction during battery cycling, without active particle isolation. Dual porosity mesoporous Co_3O_4 (m-Co_3O_4) can provide much better transport pathways than the reference bulk Co_3O_4 (b-Co_3O_4) derived nanostructures, which can facilitate the mass transport of electrolyte in the larger pores and sodium ion diffusion in the smaller pores of m-Co_3O_4. Also, the surface disorder of the Co_3O_4 also provides a large electrode-electrolyte interface for electrolyte adsorption, which is beneficial for achieving a high power density. The ordered m-Co_3O_4 sodium storage material can deliver a reversible capacity of 416 mAh g^{-1}, with excellent cycling stability. m-Co_3O_4 stores the Na ions through reversible Na de/intercalation reactions, as also confirmed by ex-situ X-ray diffraction (XRD) technique.

7.2 Experimental sections

7.2.1 Synthesis of KIT-6 silica

Three-dimensional (3D) cubic Ia3d KIT-6 mesoporous silica materials were prepared according to the procedure described by Ryoo and co-workers.[14a] For a typical preparation procedure, 10 g of Pluronic P123 ($EO_{20}PO_{70}EO_{20}$, Mw = 5800, Sigma-Aldrich) was dissolved in 350 g of 0.6 M HCl (Sigma-Aldrich, 36.5 - 38.0 %) solution under vigorous stirring in a closed Schott-Duran blue cap reagent bottle (500 mL). Then, 10 g of 1-Butanol (Sigma-Aldrich, ≥ 99.4 %) was added into the mixture and stirred at 35 ℃ overnight. Subsequently, 20.8 g of tetraethoxysilane (TEOS, Sigma-Aldrich, ≥ 99.0 %) was gently dropped into the homogeneous solution. This mixture was maintained at 35 ℃ for 24 h under vigorous stirring and aged at 105 ℃ for 24 h under static conditions in a Teflon-lined autoclave. The precipitate was filtered without washing and dried at 100 ℃ for 24 h. The KIT-6 silica was obtained after calcination at 550 ℃ for 5 h under air atmosphere with a heating rate of 5 ℃ /min.

7.2.2 Synthesis of mesoporous Co_3O_4

Mesoporous Co_3O_4 was prepared via the nanocasting route by using calcined 3D cubic Ia3d KIT-6 silica as a sacrificial template. Typically, 0.5 g of KIT-6 silica was dispersed in 20 mL ethanol. Afterward, 2.0 g of $Co(NO_3)_2 \cdot 6H_2O$ (Sigma-Aldrich, ≥ 98 %) was added into the glass container. This mixture was ultrasonicated for 1 h and stirred at 40 ℃ in an uncapped condition to evaporate the ethanol. Then, the dried powder was calcined at 350 ℃ for 3 h under air atmosphere with a heating rate of 1 ℃ /min. The obtained product (1.0 g) was added into the solution containing 10 g of ethanol and 1.0 g of $Co(NO_3)_2 \cdot 6H_2O$, and stirred at room temperature to remove

the ethanol. Afterward, the resulting powder was calcined at 450 ℃ for 6 h under air atmosphere with a heating rate of 1 ℃ /min to form KIT-6/Co_3O_4 composite. The KIT-6 silica template was removed by treatment with 3 M NaOH (Sigma-Aldrich, ⩾ 98 %) solution at 70 ℃ for 12 h. This removal process was repeated twice. After a centrifugation and washing treatment, the mesoporous Co_3O_4 was obtained and dried at 60 ℃ overnight for further use.

The reference bulk Co_3O_4 was prepared through sintering $Co(NO_3)_2 \cdot 6H_2O$ at 450 ℃ for 6 h under air atmosphere.

7.2.3 Structural and physical characterizations

The ordering of materials was characterized by small-angle X-ray scattering (SAXS) with a Nanostar U small-angle X-ray scattering system (Bruker, Germany) using Cu Kα radiation (λ = 1.54056 Å). The unit-cell parameter a_0 was calculated by the following formulas: $d_{211} = 2\pi/q_{211}$; and $a_0 = \sqrt{6} * d_{211}$. The wall thickness, $w = a_0/3.0919 - D/2$ (where D represents the pore size distribution). The crystal structure and phase of products were characterized using wide-angle X-ray diffraction (XRD, Bruker D8, Germany) with Ni-filtered Cu Kα radiation (40 kV, 40 mA). The morphologies of samples were observed by field-emission scanning electron microscopy (FESEM, JEOL-7500). The microstructure details and chemical composition were further investigated by transmission electron microscopy (TEM, JEOL-2010), operated at an acceleration voltage of 200 kV. Nitrogen sorption isotherms were measured at 77 K with a Micromeritcs Tristar 3020 analyzer (USA). Before measurements, the samples were degassed under vacuum at 180 ℃ for 6 h. The Brunauer-Emmett-Teller (BET) method was utilized to calculate the specific surface areas (S_{BET}), using adsorption data in a relative pressure range from 0.04 to

0.2. The pore volumes and pore size distributions were derived from the adsorption branches of isotherms using the Barrett-Joyner-Halenda (BJH) model. The total pore volume, V_t, was estimated from the amount adsorbed at a relative pressure P/P_0 of 0.995.

7.2.4 Electrochemical characterizations

The electrochemical tests were carried out via CR2032 coin type cells. The working electrodes were prepared by mixing the as-prepared materials, Super P, sodium carboxymethyl cellulose / polyacrylic acid (1:1) at a weight ratio of 70:20:10. The resultant slurry was pasted on Cu foil and dried in a vacuum oven at 150 °C for 3 h, followed by pressing at 300 kg cm^{-2}. The loading of the materials on individual electrodes was 1.0 ± 0.2 mg cm^{-2}. Electrochemical measurements were carried out using two-electrode coin cells with Na metal as counter and reference electrode and glass microfiber (Whatman) as the separator. The electrolyte consisted of a solution of 1 M $NaClO_4$ in ethylene carbonate (EC) / propylene carbonate (PC) (1:1, v/v) with 5 wt% fluoroethylene carbonate (FEC). Electrochemical impedance spectroscopy (EIS) and cyclic voltammetry (CV) were conducted on a VMP-3 electrochemical workstation at a scan rate of 0.1 mV s^{-1}. The cells were galvanostatically charged and discharged over a voltage range of 0.01-2.5 V versus Na/Na^+ at different constant current densities, based on the weight of the samples, on a Land CT2001A battery tester. At least five parallel cells were tested for each electrochemical measurement, in order to make sure that the results were reliable and represented the typical behavior of the samples.

7.3 Results and discussion

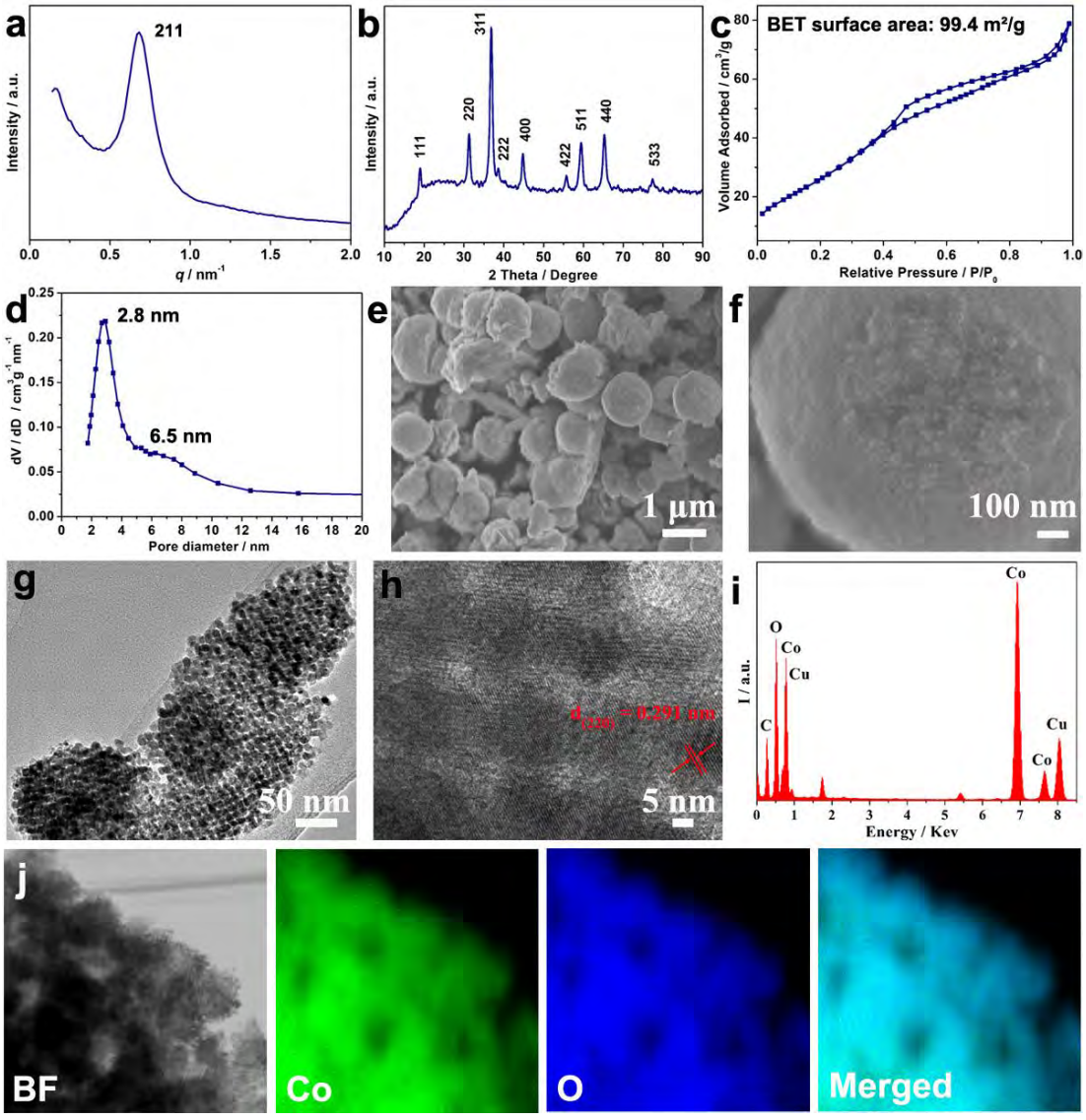

Figure 7.2 Characterization of physicochemical properties and morphology of m-Co_3O_4. (a) SAXS and (b) XRD patterns of m-Co_3O_4 microspheres. (c) N_2 sorption isotherms, and (d) corresponding pore size distribution curve of m-Co_3O_4 microspheres. (e) FE-SEM images of three-dimensional cubic mesoporous silica KIT-6 templates. (f) FE-SEM, (g) TEM, and (h) HRTEM images of m-Co_3O_4 microspheres. (i) EDS spectrum of m-Co_3O_4 microspheres. (j) Element mapping images of the m-Co_3O_4 with corresponding TEM image.

Due to the uncontrollable nature of the hydrolysis and assembly of cobalt precursor and surfactant, it is still difficult to prepare mesoporous Co_3O_4 with high structural ordering and well-defined morphology. It is clear that the nanocasting strategy provides a universal pathway to the synthesis of mesoporous metal oxides with highly defined pore systems and crystallization.[13] It is particularly worth noting that KIT-6 features an interpenetrating bicontinuous network of mesopore channels. Such highly branched and accessible features make it an excellent template for the nanocasting approach.[14] Therefore, herein, the mesoporous silica KIT-6 was selected as the hard template for the fabrication of m-Co_3O_4.

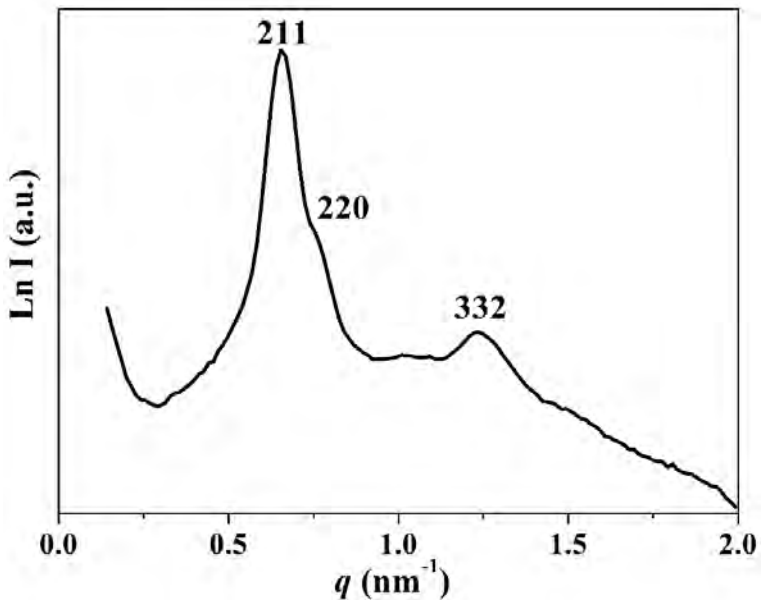

Figure 7.3 Small-angle X-ray scattering (SAXS) pattern of three-dimensional cubic mesoporous silica KIT-6 template.

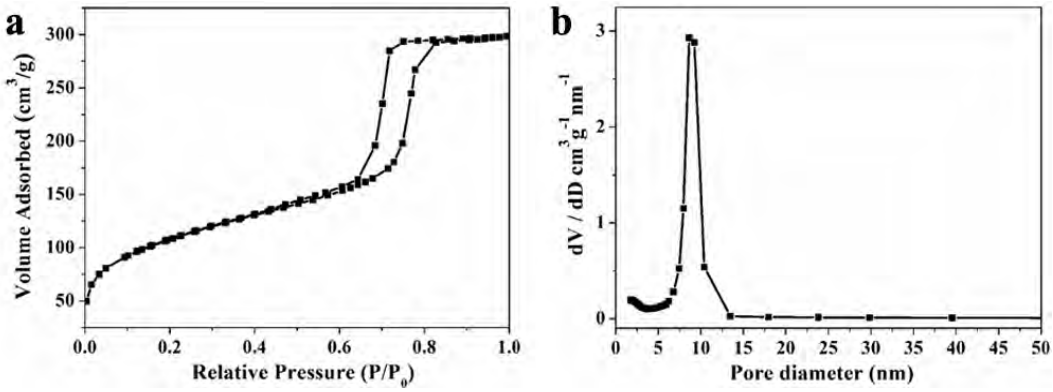

Figure 7.4 (a) N_2 sorption isotherm and (b) corresponding pore size distribution curve of three-dimensional cubic mesoporous silica KIT-6 template.

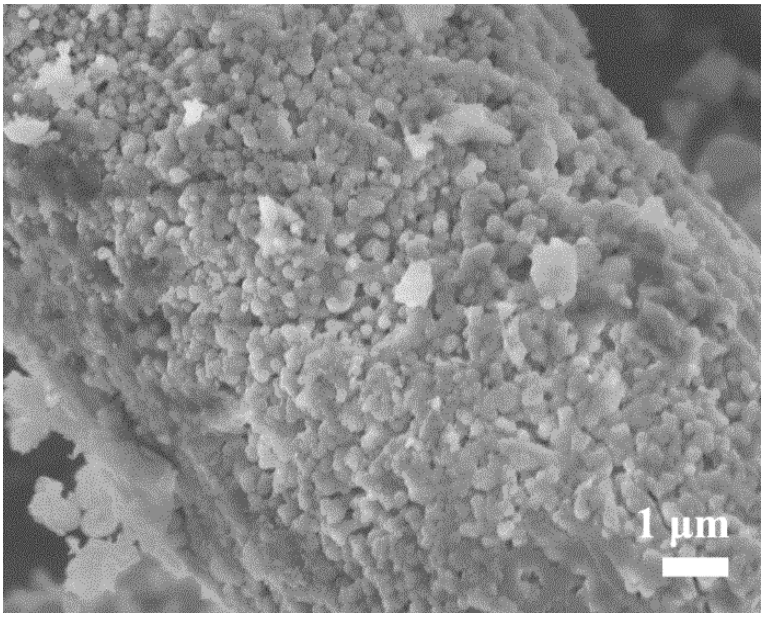

Figure 7.5 FE-SEM image of three-dimensional cubic mesoporous silica KIT-6 template.

Three-dimensional cubic mesoporous silica (KIT-6) was prepared according to previous reports, using triblock copolymer Pluronic P123 and 1-butanol as the structure-directing agents, and tetraethoxysilane as the silica source in a diluted HCl solution. The structural ordering of the prepared KIT-6 was characterized by small-

angle X-ray scattering (SAXS), and three obvious peaks corresponding to (211), (220), and (332) reflections were observed, indicating the highly ordered *Ia3d* cubic structure (**Figure 7.3**). Moreover, the nitrogen sorption isotherms of KIT-6 show a representative type IV curve with a sharp capillary condensation step at high relative pressure and an H2-type hysteresis loop, suggesting uniformity of the mesopores (**Figure 7.4**). In addition, the prepared KIT-6 has a Brunauer-Emmett-Teller (BET) surface area of 387.3 m^2g^{-1}, a total pore volume of 0.46 cm^3g^{-1}, and a narrow pore size distribution centered at 8.9 nm.

In this approach, $Co(NO_3)_2 \cdot 6H_2O$ was employed as the cobalt source to be impregnated within the KIT-6 mesopore channels through the nanocasting method. To ensure well filled pores and complete nanocasting, this impregnation process was repeated, then followed by calcination in air. Finally, the mesoporous Co_3O_4 was obtained after removal of the KIT-6 hard template by leaching with 3 M NaOH aqueous solution. Significantly, this as-prepared mesoporous Co_3O_4 preserves the cubic *Ia3d* mesoporous structure, as revealed by the SAXS pattern. A sharp scattering peak at q = 0.68 nm^{-1} that corresponds to the (211) reflection can be observed (**Figure 7.2 a**). It is noteworthy that the scattering peak for the (211) reflection shifts to higher q-value in comparison with the original KIT-6 template (q = 0.66 nm^{-1}). That is, the unit-cell parameter a_0 decreases from 23.4 (KIT-6) to 22.6 nm (mesoporous Co_3O_4), indicating a certain shrinkage of the mesostructure.

The crystal and phase purity of mesoporous Co_3O_4 was characterized by wide-angle X-ray diffraction (XRD). As revealed in **Figure 7.2 b**, all positions of the diffraction peaks can be assigned to the pure face-centered cubic (fcc) phase of Co_3O_4 (space group: Fd3m (227), JCPDS card no. 42-1467). The high intensity of the diffraction peaks implies a well-crystallized structure. In addition, the average

crystallite size is approximately 8.7 nm, as calculated by the Debye-Scherrer formula from the half-width of the diffraction peak in the XRD pattern corresponding to the (311) reflection. Moreover, the porosity and textural properties were measured using N_2 sorption isotherms, which present a typical type IV curve with an H1 hysteresis loop, indicating a mesostructure with *Ia3d* channels (**Figure 7.2 c**). Accordingly, the BET surface area is 99.4 m^2g^{-1}, and the total pore volume is 0.12 cm^3g^{-1}. Simultaneously, this mesoporous Co_3O_4 exhibits a narrow pore size distribution centered at ~ 2.8 nm, based on the adsorption branch of the isotherm, as calculated by the Barrett-Joyner-Halenda (BJH) model (**Figure 7.2 d**). This result agrees very well with the wall thickness of the KIT-6 template (~ 3.1 nm), demonstrating the successful nanocasting process. Additionally, a broad peak centered at ~ 6.5 nm also can be observed, confirming the dual porosity.

The morphology and microstructure of the obtained mesoporous Co_3O_4 were further observed by field-emission scanning electron microscopy (FE-SEM) and transmission electron microscopy (TEM). It was found that the KIT-6 template has an irregular morphology and is agglomerated, with a large number of spherical particles ~ 200 nm in diameter (**Figure 7.5**). Microspheres with ~ 1 μm in diameter appear for the mesoporous Co_3O_4 after this nanocasting process (**Figure 7.2 e**), however. Interestingly, these mesoporous Co_3O_4 microspheres are composed of neatly aligned tiny spherical nanoparticles with uniform size of about 8 nm (**Figure 7.2 f**). This could be ascribed to the different interconnectivity between the two channel systems of the KIT-6 template, resulting in self-assembly to form large clusters with a dense coupled framework. Indeed, this well-ordered, interconnected, mesostructured network of mesoporous Co_3O_4 microspheres is clearly observed from the TEM and high-resolution TEM (HRTEM) images (**Figure 7.2 g and 7.2 h**). The

mean crystallite size is estimated to be ~ 8.5 nm, which is in good accordance with the FE-SEM image and the XRD results. Furthermore, the lattice interplanar spacing of 0.291 nm is clearly distinguishable and corresponds to the (220) planes of the mesoporous Co_3O_4 microspheres, demonstrating their high crystallinity (Figure 2h). Additionally, the energy dispersive spectroscopy (EDS) results and the elemental mapping images of the mesoporous Co_3O_4 microspheres show the presence of the elements Co and O, and the absence of Si element, suggesting the complete removal of the KIT-6 template from the mesoporous Co_3O_4 microspheres (**Figure 7.2 i and 7.2 j**). Notably, the architecture of these unique microspheres with uniform mesopore channels, high surface area, and interconnected tiny nanoparticles is beneficial because it offers sufficient interface area between the electrolyte and the electrode material.

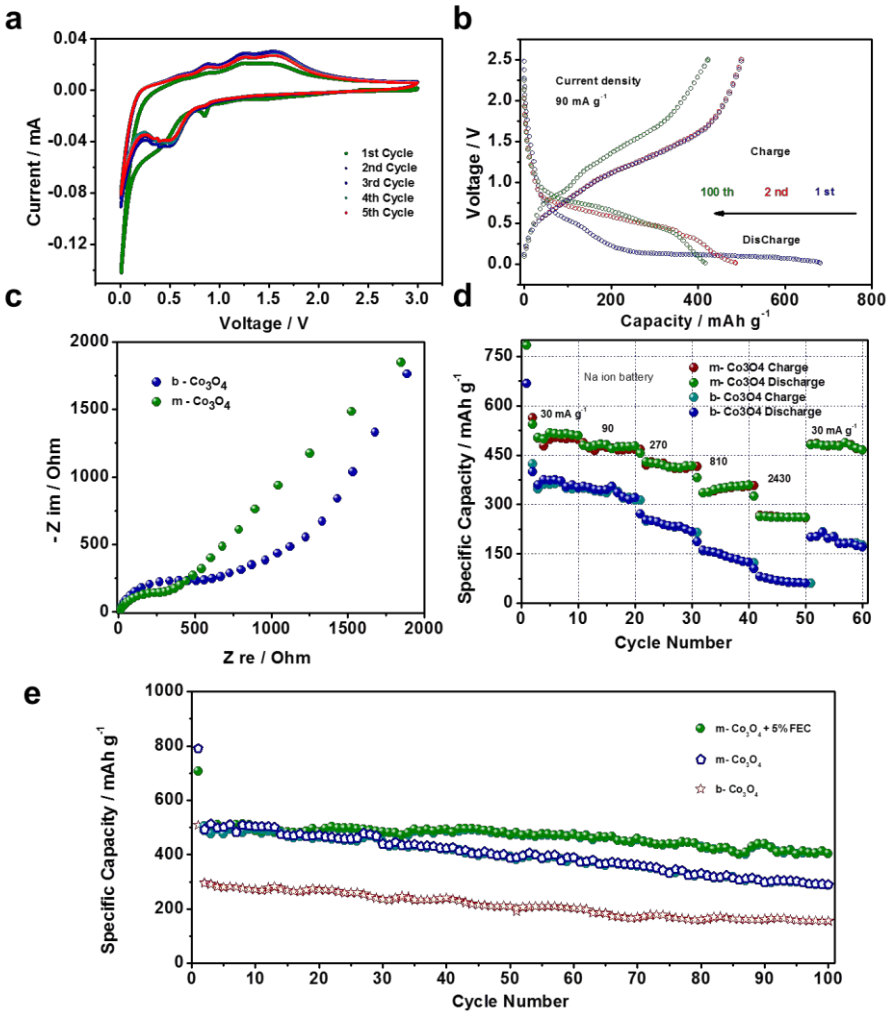

Figure 7.6 Electrochemical properties of m-Co_3O_4 in Na ion battery. (a) Cyclic voltammograms for the first five cycles of the m-Co_3O_4 electrode at a scanning rate of 0.1 mV s^{-1}, (b) Galvanostatic discharge-charge profiles for selected cycles of the m-Co_3O_4 electrode at a current density of 90 mA g^{-1}, (c) Nyquist plots of electrodes containing hybrid m-Co_3O_4 and b-Co_3O_4, obtained by applying a sine wave with an amplitude of 5.0 mV over the frequency rang ofe 100 kHz 0.01 Hz, (d) comparisons of rate capabilities of m-Co_3O_4 and b-Co_3O_4 electrode at different current densities, and (e) representative cycling performances of electrodes with m-Co_3O_4 and b-Co_3O_4 with or without FEC in the electrolyte.

A series of comparative electrochemical measurements were performed to investigate the anode performance of m-Co_3O_4 and b-Co_3O_4 electrodes. Cyclic voltammetry (CV) curves are shown in **Figure 7.6 a**, in which one redox couple in the initial cycle is present at around 0 and 0.41 V in the cathodic and anodic processes, respectively. These peaks should correspond to the reversible reaction between Na^+ ions and Co_3O_4, which is related to the reduction of Co_3O_4 to Co and the formation of Na_2O. The other broad peak in the discharge voltage range (~ 0.86 V) should be ascribed to the formation of an irreversible solid electrolyte interphase (SEI) layer. The organic SEI layer can be dissolved reversibly, which could contribute to the reversible capacity during the charge and discharge processes. In the subsequent cycles, only one broad cathodic peak can be observed at ~ 0.47 V for the m-Co_3O_4 and b-Co_3O_4 electrodes (**Figure 7.9**). The overlapping CV curves in the 2^{nd} to 5^{th} cycles indicate the stability of m-Co_3O_4 compared to the b-Co_3O_4. The CV measurements clearly illustrate the reversible Na storage capability of the m-Co_3O_4, and all the redox peaks of the m-Co_3O_4 are well matched to the charge-discharge plateaus (**Figure 7.6 b**). The reduced charge-transfer resistance compared to that of the b-Co_3O_4 electrodes is another factor proving the high reactivity of the m-Co_3O_4 electrode (**Figure 7.6 c**). The electrochemical performance of the m-Co_3O_4 was systematically evaluated by galvanostatic discharge-charge measurements. Remarkably, a relatively high capacity of 782 mAh g^{-1} is achieved in the initial cycle at a current density of 30 mA g^{-1} in the case of the m-Co_3O_4 (**Figure 7.6 d**). More importantly, the as-prepared m-Co_3O_4 exhibits good high-rate performance. On increasing the current density to 810 and 2430 mA g^{-1}, the specific capacities at these current densities are still 357 and 267 mAh g^{-1}, respectively (**Figure 7.6 d and**

Figure 7.10). The irreversible capacity value obtained from the above-mentioned reactions is comparatively smaller than the observed irreversible capacity in the first discharge, indicating that the first cycle irreversible capacity mainly resulted from the reductive electrolyte decomposition and the formation of a SEI. Additives such as fluoroethylene carbonate (FEC), which is known for stabilizing the SEI layer in Na-ion batteries, were also introduced into the electrolyte (**Figure 3e**) in order to further improve its electrochemical performance. The outstanding dual porosity m-Co_3O_4 allows better transport pathways and thus leads to an initial capacity of 707 mAh g^{-1} at the current density of 90 mA g^{-1}, and after 100 cycles, capacity of 416 mAh g^{-1} is still retained. These results are in stark contrast to the b-Co_3O_4 and the m-Co_3O_4 without FEC in the electrolyte, which show continuous and progressive capacity decay as the cycling progresses.

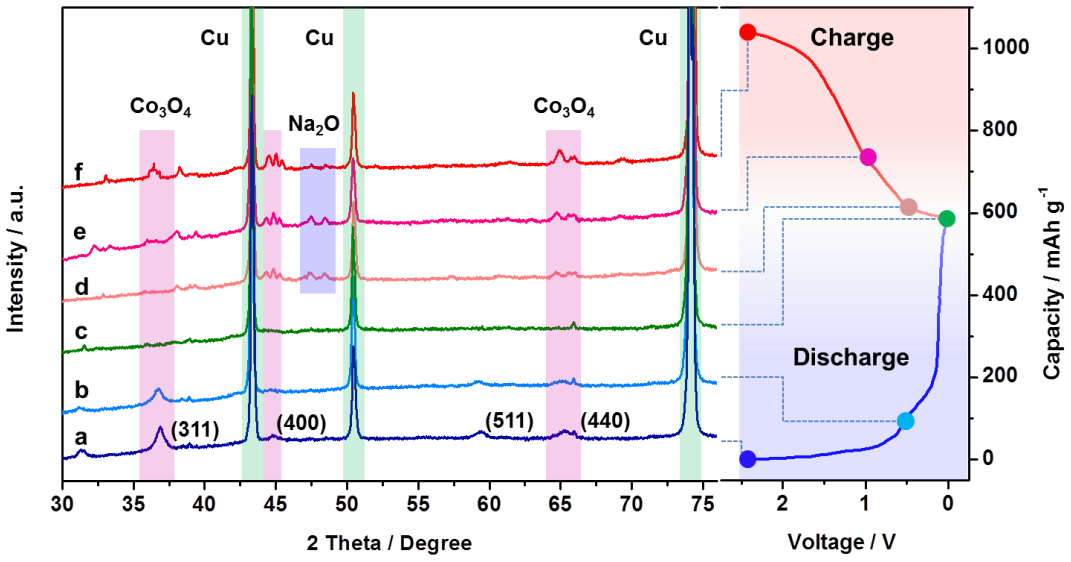

Figure 7.7 Ex-situ XRD patterns of the m-Co_3O_4 electrode collected at various points as indicated in the corresponding voltage profile: (a) fresh electrode, (b) after first discharge to 0.5 V, (c) after first discharge to 0.01 V, (d) after first charge to 0.5 V, (e) after first charge to 1.0 V, and (f) after first charge to 2.5 V.

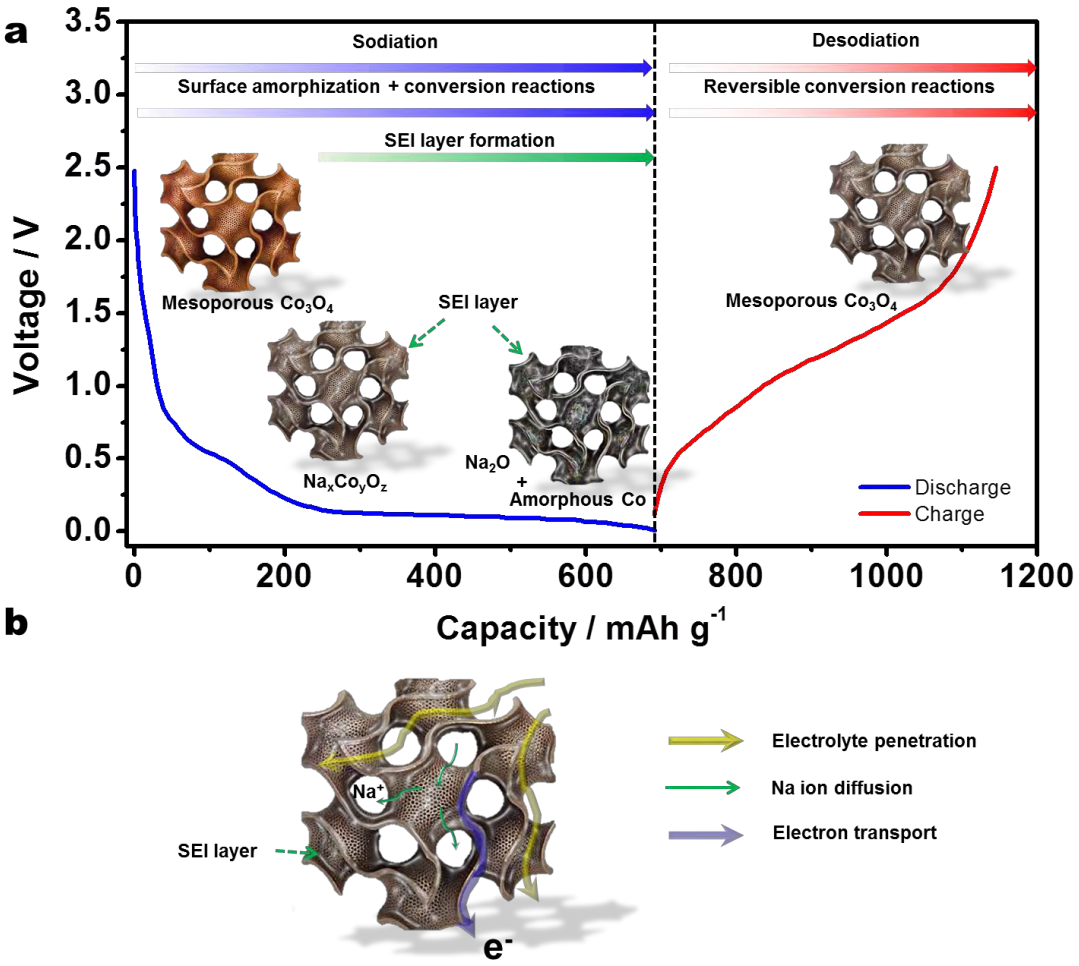

Figure 7.8 Schematic illustration of the Na storage behavior in m-Co_3O_4 electrode: (a) summary of sodiation/desodiation cycle, (b) electron and ion transport in a microsphere during discharge.

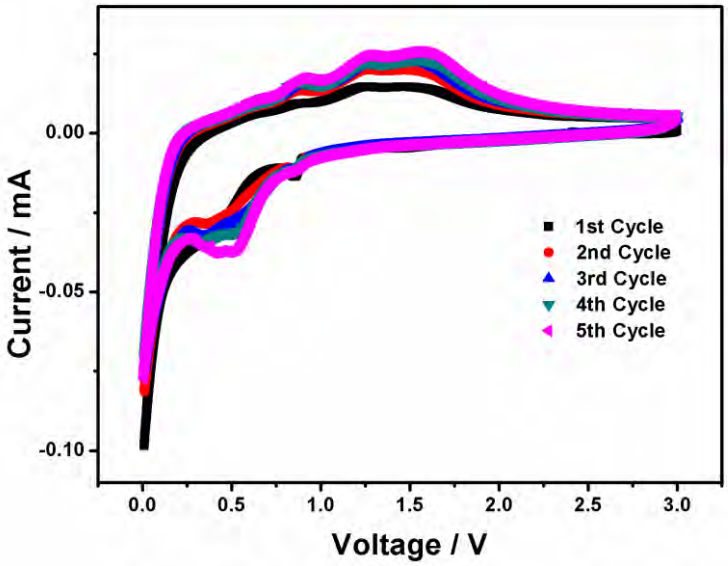

Figure 7.9 Cyclic voltammograms for the first five cycles of the b-Co_3O_4 electrode at a scanning rate of 0.1 mV s^{-1}.

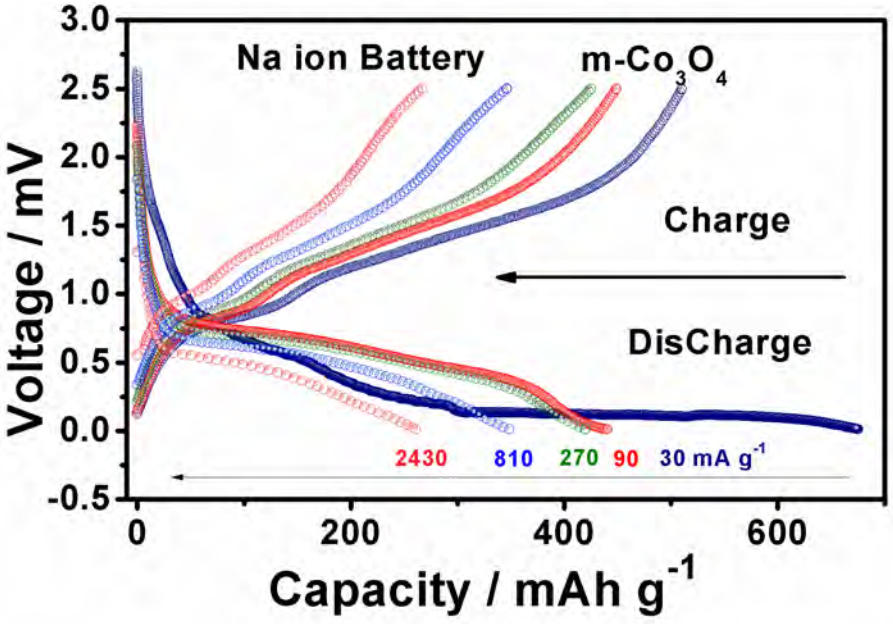

Figure 7.10 Galvanostatic discharge charge profiles for selected cycles of the m-Co_3O_4 electrode at different current densities.

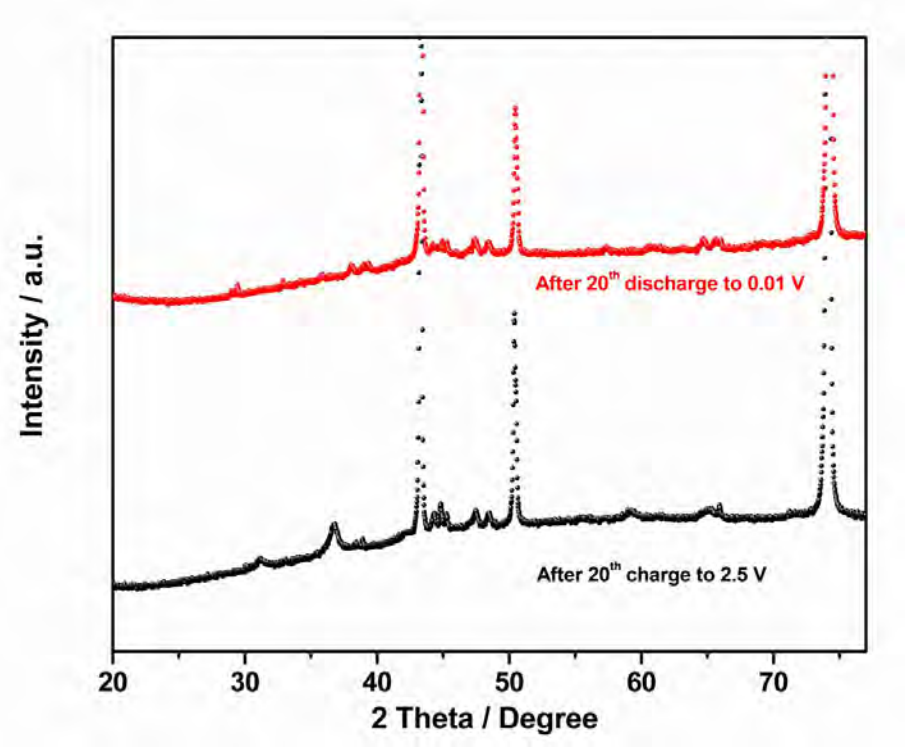

Figure 7.11 ex-situ XRD patterns of the m-Co_3O_4 electrode collected at fully discharge and charge state.

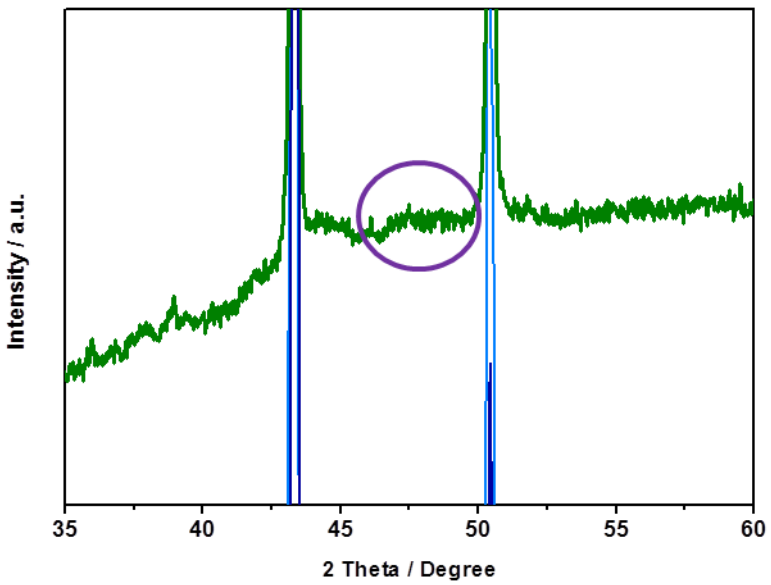

Figure 7.12 Enlarged ex-situ XRD patterns of the m-Co_3O_4 electrode collected after first discharge to 0.01 V.

In order to further clarify the structural changes upon sodiation/desodiation, ex situ XRD analysis of the m-Co_3O_4 was performed on the electrodes after cycling. **Figure 7.7** presents the ex-situ XRD patterns of the fully discharged-charged electrodes for the first cycle. In the fresh electrode, the XRD pattern demonstrates that all the diffraction peaks are well indexed to the cubic Co_3O_4 phase (JCPDS no. 00-043-1003), with a small unknown peak at around 32.7°. In the first cycle charge back to 2.5 V, the ex-situ XRD pattern confirms the existence of the Co_3O_4 phase. Surprisingly, all the diffraction peaks for the Co_3O_4 phase tend to disappear, and a new phase of Na_2O (JCPDS no. 00-003-1074) appears when the electrode is discharged to 0.01 V. At the same time there should also be evidence of Co phase formation. Unfortunately, there is a significant overlap of this peak with the copper current collector peak in the measured XRD patterns. On the other hand, when the electrode was charged back to 2.5 V, all diffraction peaks for the Co_3O_4 phase reappeared. These findings suggest that the conversion reaction is not completed in the first discharge to 0.01 V, so that the Co_3O_4 phase still exists in the first discharge and becomes visible again when the electrode is charged back to 2.5 V. It is anticipated that the discharge capacity will keep on increasing until all the materials become involved in the conversion reaction, and then the capacity will remain constant or may decline. **Figure 7.8** a summarizes the sodiation/desodiation mechanism in the m-Co_3O_4 electrode. In the first discharge, Na ions are inserted into m-Co_3O_4 via surface reconstruction reactions. $Na_xCo_yO_z$ is then partially transformed into Co_xO and Na_2O through conversion reactions, accompanied by surface amorphization through further sodiation. In this process, Na ions are stored in the $Na_xCo_yO_z$ and Na_2O phases, accompanied by capacitive reactions. The subsequent charge process involves Na de-intercalation reactions to form $Na_xCo_yO_z$. The dual

porosity mesoporous structure can provide much better transport pathways than the bulk Co_3O_4 derived nanostructures, which can facilitate the mass transport of electrolyte in the larger pores and sodium ion diffusion in the smaller pores of the dual porosity material (**Figure 7.8 b**), and also provides a large electrode-electrolyte interface for electrolyte adsorption due to the surface disorder of Co_3O_4.

7.4 Conclusions

The present work proposes a dual porosity mesoporous sodium insertion material, m-Co_3O_4, for NIBs. Mesoporous Co_3O_4 was prepared via the nanocasting route by using calcined 3D cubic *Ia3d* KIT-6 silica as a sacrificial template. The outstanding dual porosity of m-Co_3O_4 allows better transport pathways and thus leads to an initial capacity of 707 mAh g^{-1}, which is reached at the current density of 90 mA g^{-1}, with capacity of 416 mAh g^{-1} still retained after 100 cycles. Importantly, the as-prepared m-Co_3O_4 exhibits good high-rate performance. On increasing the current density to 810 and 2430 mA g^{-1}, the specific capacities at these current densities are still 357 and 267 mAh g^{-1}, respectively. The excellent Na-storage properties are due to the unique, highly ordered, dual porosity, mesoporous nanostructure in m-Co_3O_4, which provides much better transport pathways than the bulk Co_3O_4 derived nanostructures and can facilitate the mass transport of electrolyte in larger pores and sodium ion diffusion in smaller pores. It also provides a large electrode-electrolyte interface for electrolyte adsorption due to the higher surface disorder of the m-Co_3O_4. We further discovered through ex-situ techniques that the sodium uptake/extraction takes place through reversible conversion reactions.

7.5 References

[1] [a] D. Gu, F. Schuth, Chem. Soc. Rev. 2014, 43, 313-344; [b] W. Li, Q. Yue, Y. Deng, D. Zhao, Adv. Mater. 2013, 25, 5129-5152.

[2] D. Gu, W. Li, F. Wang, H. Bongard, B. Spliethoff, W. Schmidt, C. Weidenthaler, Y. Xia, D. Zhao, F. Schüth, Angew. Chem., Int. Ed. 2015, 54, 7060-7064.

[3] G. Wang, H. Liu, J. Horvat, B. Wang, S. Qiao, J. Park, H. Ahn, Chem. - A Eur. J. 2010, 16, 11020-11027.

[4] [a] A. S. Arico, P. Bruce, B. Scrosati, J. M. Tarascon, W. Van Schalkwijk, Nat. Mater. 2005, 4, 366-377; [b] P. G. Bruce, B. Scrosati, J.-M. Tarascon, Angew. Chem., Int. Ed. 2008, 47, 2930-2946; [c] J. B. Goodenough, Y. Kim, Chem. Mater. 2010, 22, 587-603; [d] H. K. Liu, Mater. Res. Bull. 2013, 48, 4968-4973; [e] X. W. Lou, L. A. Archer, Z. C. Yang, Adv. Mater. 2008, 20, 3987-4019; [f] S. P. Ong, V. L. Chevrier, G. Hautier, A. Jain, C. Moore, S. Kim, X. Ma, G. Ceder, Energy & Enviro. Sci. 2011, 4, 3680-3688. [e] L. Wu, X. Hu, J. Qian, F. Pei, F. Wu, R. Mao, X. Ai, H. Yang, Y. Cao, Energy Environ. Sci., 2014, 7, 323-328. [f] L. Wu, H. Lu, L. Xiao, X. Ai, H. Yang, Y. Cao, J. Mater. Chem. A, 2015,3, 5708-5713. [g] L. Wu, H. Lu, L. Xiao, X. Ai, H. Yang, Y. Cao, J. Power Sources 2015, 293, 784–789.

[5] [a] F. Cheng, Z. Tao, J. Liang, J. Chen, Chem. Mater. 2008, 20, 667-681; [b] Y. Li, B. Tan, Y. Wu, Nano Lett. 2008, 8, 265-270; [c] M. V. Reddy, G. V. S.

Rao, B. V. R. Chowdari, Chem. Rev. 2013, 113, 5364-5457; [d] F. Ding, W. Xu, G. L. Graff, J. Zhang, M. L. Sushko, X. Chen, Y. Shao, M. H. Engelhard, Z. Nie, J. Xiao, X. Liu, P. V. Sushko, J. Liu, J.-G. Zhang, J. Am. Chem. Soc. 2013, 135, 4450-4456; [e] H.-W. Shim, A.-H. Lim, J.-C. Kim, E. Jang, S.-D. Seo, G.-H. Lee, T. D. Kim, D.-W. Kim, Sci. Rep. 2013, 3.

[6] H. Sun, H. M. Ang, M. O. Tade, S. Wang, J. Mater. Chem. A 2013, 1, 14427-14442.

[7] [a] X. Wang, X. L. Wu, Y. G. Guo, Y. T. Zhong, X. Q. Cao, Y. Ma, J. N. Yao, Adv. Funct. Mater. 2010, 20, 1680-1686; [b] J. S. Chen, T. Zhu, Q. H. Hu, J. J. Gao, F. B. Su, S. Z. Qiao, X. W. Lou, ACS Appl. Mater. Interf. 2010, 2, 3628-3635; [c] H. Y. Sun, M. Ahmad, J. Zhu, Electrochimica Acta 2013, 89, 199-205; [d] G. L. Xu, J. T. Li, L. Huang, W. F. Lin, S. G. Sun, Nano Energy 2013, 2, 394-402.

[8] [a] S. L. Xiong, J. S. Chen, X. W. Lou, H. C. Zeng, Adv. Funct. Mater. 2012, 22, 861-871; [b] B. J. Li, H. Q. Cao, J. Shao, G. Q. Li, M. Z. Qu, G. Yin, Inorg. Chem. 2011, 50, 1628-1632; [c] N. Jayaprakash, W. D. Jones, S. S. Moganty, L. A. Archer, J. Power Sources 2012, 200, 53-58.

[9] [a] L. Li, G. M. Zhou, X. Y. Shan, S. F. Pei, F. Li, H. M. Cheng, J. Power Sources 2014, 255, 52-58; [b] H. T. Sun, X. Sun, T. Hu, M. P. Yu, F. Y. Lu, J. Lian, J. Phys. Chem. C 2014, 118, 2263-2272.

[10] [a] G. Y. Huang, S. M. Xu, S. S. Lu, L. Y. Li, H. Y. Sun, ACS Appl. Mater. Interf. 2014, 6, 7236-7243; [b] Y. Xiao, C. W. Hu, M. H. Cao, J. Power Sources 2014, 247, 49-56; [c] X. Yin, Z. X. Wang, J. X. Wang, G. C. Yan, X.

H. Xiong, X. H. Li, H. J. Guo, Mater. Lett. 2014, 120, 73-75; [d] H. Sun, X. Sun, T. Hu, M. Yu, F. Lu, J. Lian, J. Phys. Chem. C 2014, 118, 2263-2272.

[11] [a] H. Huang, W. Zhu, X. Tao, Y. Xia, Z. Yu, J. Fang, Y. Gan, W. Zhang, ACS Appl. Mater. Interf. 2012, 4, 5974-5980; [b] L. Hu, N. Yan, Q. W. Chen, P. Zhang, H. Zhong, X. R. Zheng, Y. Li, X. Y. Hu, Chem.-Eur. J. 2012, 18, 8971-8977; [c] L. Tian, H. L. Zou, J. X. Fu, X. F. Yang, Y. Wang, H. L. Guo, X. H. Fu, C. L. Liang, M. M. Wu, P. K. Shen, Q. M. Gao, Adv. Funct. Mater. 2010, 20, 617-623; [d] S. L. Xiong, C. Z. Yuan, M. F. Zhang, B. J. Xi, Y. T. Qian, Chem.-Eur. J. 2009, 15, 5320-5326; [e] C. Yuan, L. Yang, L. Hou, L. Shen, X. Zhang, X. W. Lou, Energy & Environ. Sci. 2012, 5, 7883-7887.

[12] T. F. Zhou, W. K. Pang, C. F. Zhang, J. P. Yang, Z. X. Chen, H. K. Liu, Z. P. Guo, ACS Nano 2014, 8, 8323-8333.

[13] [a] A. H. Lu, F. Schüth, Adv. Mater. 2006, 18, 1793-1805; [b] A. Rumplecker, F. Kleitz, E.-L. Salabas, F. Schüth, Chem. Mater. 2007, 19, 485-496.

[14] [a] R. Ryoo, S. H. Joo, S. Jun, J. Phy. Chem. B 1999, 103, 7743-7746; [b] W. Yue, A. H. Hill, A. Harrison, W. Zhou, Chem. Commun. 2007, 2518-2520.

CHAPTER 8 CONCLUSIONS AND OUTLOOK

8.1 General conclusions

Undoubtedly, the most difficult issue facing the demonstration of Na/Li-ion batteries is how to achieve high energy density and long cycle life. With the ability to prepare various 2D nanosized materials, combined with advanced nanofabrication techniques, current research on the preparation of SIB anode materials depends on not only the choice of functional active material components, crystal phase, and structure, but also on the spatial organization/assembly, surface exposure, interaction between the individual components, and geometric properties of the composites. By using 2D nanomaterials with unique properties, planar hybrids, porous hierarchical architectures, and vertically stacked heterostructures have been prepared, which have shown impressive properties, enhanced functions, and improved performance. Even so, there are still many tough challenges to overcome before high energy storage systems based on SIBs can be achieved in the future.

For the first part, a hybrid SnS@graphene architecture, employing 2D nanosheets of SnS and graphene as complementary building blocks via their controllable assembly, was fabricated by a hydrothermal and annealing approach. The well-developed 2D nanosheets of SnS and graphene, as well as the precise hierarchical control of various sublayers of the materials in the design are believed to function synergistically, so as to significantly stabilize the mechanical, electrical, and electrochemical properties of the anode material, despite its large volume changes with sodiation/desodiation during cycling. From the perspective of structural ability

during cycling, the less structural changes of SnS after the conversion, expected a good structural stability and excellent cycling stability for the performance on the sodium ion battery. The resultant architecture can provide high reversible capacity and excellent high-rate capability. The superior cycling and rate performance, combined with the simplicity of the optimized process, represents a promising strategy for the development of inexpensive and versatile synthesis techniques for energy storage and conversion applications.

Second, an effective approach, involving an interfacial amorphous carbon layer anchoring SnS/SnO_2 heterostructures directly to graphene nanosheets, has been developed. The formation of the SnS/SnO_2 heterostructures has been verified by HRTEM, Raman, and XPS analysis. When evaluated as an anode material for sodium-ion batteries, the C@SnS/SnO_2@Gr features excellent performance and outstanding cycling stability at high rates, which is much superior to the performance of C@SnO_2@Gr, C@SnS@Gr, or a mechanical mixture of them. The boosted charge transfer in the heterostructures is demonstrated by the EIS measurements. The resulting improvement of Na-ion diffusion capability and electronic conductivity is mainly responsible for the extraordinary performance of the C@SnS/SnO_2@Gr electrode. The superior high-rate capability and ultra-long cycle life, accompanied by the simplicity of the synthetic process, make this approach a promising strategy for the development of simple and universal synthesis methods in applications for energy storage and conversion.

Followed by, we have designed and successfully fabricated surface amorphized (SA)-TiO_2@graphene composites. A thin amorphous TiO_2 layer was created on crystalline TiO_2 nanospheres under mild conditions and assembled with graphene via

a UV-assisted reduction technique. We evaluated the SA-TiO_2@graphene as an electrode material for lithium ion batteries and found that it exhibited greatly improved lithium insertion/extraction performance compared with crystalline TiO_2. The optimal SA-TiO_2@graphene hybrid architecture exhibits a substantial improvement in lithium specific capacity from 0.5 C to 50 C. More strikingly, the specific capacity of the composite at the rate of 50 C is as high as 103 mA h g^{-1}, 9.3 times higher than that of the reference TiO_2. We attributed the greatly enhanced lithium storage properties of the SA-TiO_2@graphene nanocrystals to the lower lithium ion diffusion and electronic conduction resistance, and better surface adsorption in the amorphous layer. These improvements benefit from the electric field introduced by the surface-amorphization within the nanocrystals, which leads to much lower lithium-ion diffusion resistance, facilitates its transport in both insertion and extraction processes, and also enhances the electrolyte absorption capability. This concept thus offers an innovative and general approach toward designing battery materials with better performance.

The last work proposes a dual porosity mesoporous sodium insertion material, m-Co_3O_4, for NIBs. Mesoporous Co_3O_4 was prepared via the nanocasting route by using calcined 3D cubic *Ia3d* KIT-6 silica as a sacrificial template. The outstanding dual porosity of m-Co_3O_4 allows better transport pathways and thus leads to an initial capacity of 707 mAh g^{-1}, which is reached at the current density of 90 mA g^{-1}, with capacity of 416 mAh g^{-1} still retained after 100 cycles. Importantly, the as-prepared m-Co_3O_4 exhibits good high-rate performance. On increasing the current density to 810 and 2430 mA g^{-1}, the specific capacities at these current densities are still 357 and 267 mAh g^{-1}, respectively. The excellent Na-storage properties are due to the

unique, highly ordered, dual porosity, mesoporous nanostructure in m-Co_3O_4, which provides much better transport pathways than the bulk Co_3O_4 derived nanostructures and can facilitate the mass transport of electrolyte in larger pores and sodium ion diffusion in smaller pores. It also provides a large electrode-electrolyte interface for electrolyte adsorption due to the higher surface disorder of the m-Co_3O_4. We further discovered through ex-situ techniques that the sodium uptake/extraction takes place through reversible conversion reactions.

8.2 Outlook

Firstly, it should be admitted that the study of 2D-based functional composite anodes for the energy storage is still in its infant stage. The underlying mechanisms of Na/Li storage in 2D materials are still unclear, so more and deep understanding with respect to the surface functionalities/defects, the hierarchical structures, and kinetic transport at the electrode/electrolyte interface is needed to achieve better electrochemical performance. For example, the high surface area of graphene and its composites may lead to large irreversible capacity loss in the first cycle, and porous graphene-based composites exhibit small tap densities and consequently, an unfavorably low volumetric capacity.

Secondly, the compatibility of each of the components in the 2D materials needs to be further improved, and heterostructure interface problems still exist due to the weak interaction forces in the hybrid structure, although not in heterostructures with crystalline bonding. Meanwhile, comparisons between amorphous and crystalline materials might prove to be an interesting area. The charge storage mechanism of such amorphous materials is still vague, and explanations are leaning more towards pseudocapacitive behavior instead.

Thirdly, some special conditions are often needed to obtain novel 2D structures, which often lead to a high-cost synthesis. Thus, controllable low-cost and large-scale synthesis techniques for novel 2D nanostructures need to be developed by integrating various advanced technologies, since the high cost of electrode materials significantly restricts scalable production and application.

Fourthly, design and large scale synthesis of novel orexisting high theoretical capacity electrode materials (e.g. alloy materials) in 2D form is likely to be the next performance growth point for SIB anode materials. Since the discovery of graphene, many other 2D materials have been coming into the spotlight. They form a very large family that includes hexagonal boron nitride, transition metal dichalcogenides, metal oxides, common clays, and the recently discovered transition metal carbides, as well as silicene, germanene, phosphorene, and stanene. All of them have great promise and will inevitably cause a new peak in SIB research. On the other hand, most of the materials used for hybridization with 2D anode materials are inorganic nanomaterials, such as alloy metals, metal oxides, and carbonaceous nanomaterials. One of the future directions lies in the combination of 2D anode materials with polymers to create 2D-based polymer composites for a wide range of applications.

Finally, in addition to the materials, investigation of isolated active materials is no longer sufficient to solve all the different kinds of challenges for the development of large-scale energy storage. We have to optimize the electrode by using high tensile-strength binders, conductive network etc. Further studies are also needed on electrolytes, additives, and binders, which can greatly influence the electrode performance. With continuous endeavors by all parties concerned, it is expected that

the high performance 2D materials and composites can be applied in commercialized high-performance energy storage system in the near future.

APPENDIX A: LIST OF PUBLICATIONS

From 2013-2016

1. **Tengfei Zhou**, Wei Kong Pang, Chaofeng Zhang, Jianping Yang, Zhixin Chen, Hua Kun Liu, Zaiping Guo*, Enhanced Sodium-ion Battery Performance by Structural Phase Transition from Two-dimensional Hexagonal-SnS_2 to Orthorhombic-SnS, ***ACS Nano*** **2014**, 8 (8), 8323-8333 (**IF = 13.334, Cited: 117**)
2. **Tengfei Zhou**, Yang Zheng, Hong Gao, Shudi Min, Sean Li, Hua Kun Liu, Zaiping Guo*, Surface Engineering and Design Strategy for Surface‐Amorphized TiO_2@ Graphene Hybrids for High Power Li‐Ion Battery Electrodes, ***Advanced Science***, **2015**, 2, 1500027 (**New, Cited: 9**)
3. Yang Zheng[+], **Tengfei Zhou**[+](**Co-first author**), Chaofeng Zhang, Jianfeng Mao, Huakun Liu, Zaiping Guo*, Boosted Charge Transfer in SnS/SnO_2 Heterostructures: Toward High Rate Capability for Sodium‐Ion Batteries, ***Angewandte Chemie International Edition*** **2016**, 55 (10), 3408-3413 (**IF = 11.71, Cited: 26**)
4. Jianping Yang[+], **Tengfei Zhou**[+](**Co-first author**), Rui Zhu, Xinqi Chen, Zaiping Guo*, Jianwei Fan, Hua Kun Liu, Wei-Xian Zhang, Highly Ordered Dual Porosity Mesoporous Cobalt Oxide for Sodium‐Ion Batteries, ***Advanced Materials Interfaces***, **2016**, 3, 1500464 (**New, Cited: 3**)
5. Chaoji Chen, Henghui Xu, **Tengfei Zhou**, Zaiping Guo, Lineng Chen,

Mengyu Yan, Liqiang Mai, Pei Hu, Shijie Cheng, Yunhui Huang, Jia Xie, Integrated Intercalation‐Based and Interfacial Sodium Storage in Graphene‐Wrapped Porous $Li_4Ti_5O_{12}$ Nanofibers Composite Aerogel, ***Advanced Energy Materials,*** **2016**, 6, 1600322 (**IF = 15.23, Cited: 6**)

6. Youwen Liu, Xuemin Hua, Chong Xiao, **Tengfei Zhou**, Pengcheng Huang, Zaiping Guo, Bicai Pan, Yi Xie, Heterogeneous Spin States in Ultrathin Nanosheets Induce Subtle Lattice Distortion To Trigger Efficient Hydrogen Evolution, ***Journal of the American Chemical Society,*** **2016**, 138 (15), 5087-5092 (**IF = 13.04, Cited: 11**)
7. Hong Gao, **Tengfei Zhou**, Yang Zheng, Yuqing Liu, Jun Chen, Huakun Liu, Zaiping Guo*, Integrated Carbon/Red Phosphorus/Graphene Aerogel 3D Architecture via Advanced Vapor-Redistribution for High-Energy Sodium-Ion Batteries, ***Advanced Energy Materials,*** **2016**, DOI: 10.1002/aenm.201601037 (**IF = 15.23, Cited: 1**)
8. Hongqiang Wang, **Tengfei Zhou**, Dan Li, Hong Gao, Guoping Gao, Aijun Du, Hua Kun Liu, Zaiping Guo*, Ultrathin Cobaltosic Oxide Nanosheets as an Effective Sulfur Encapsulation Matrix with Strong Affinity Towards Polysulfides, ***ACS Applied Materials & Interfaces,*** **2016,** DOI: 10.1021/acsami.6b07961. (**IF = 7.145, Cited: 0**)
9. Yuanzhen Chen, Wei Kong Pang, Haihua Bai, **Tengfei Zhou**, Yong-Ning Liu, Sai Li, Zaiping Guo, Enhanced Structural Stability of Nickel-cobalt Hydroxide via Intrinsic Pillar Effect of Metaborate for High-power and Long-life Supercapacitor Electrodes, ***Nano Letter,*** **2016,** DOI: 10.1021/acs.nanolett.6b04427 (**IF = 13.779, Cited: 0**)
10. Kangzhe Cao, Lifang Jiao, Wei Kong Pang, Huiqiao Liu, **Tengfei Zhou**,

Zaiping Guo, Yijing Wang, Huatang Yuan, $Na_2Ti_6O_{13}$ Nanorods with Dominant Large Interlayer Spacing Exposed Facet for High‐Performance Na‐Ion Batteries, ***Small,* 2016**, 12 (22), 2991-2997 (**IF = 8.32, Cited: 1**)

11. Shudi Min, Chongjun Zhao, Peiwen Ju, **Tengfei Zhou**, Hong Gao, Yang Zheng, Hongqiang Wang, Guorong Chen, Xiuzhen Qian, Zaiping Guo, Facile Synthesis of Nickel-foam-based Nano-architectural Composites as Binder-free Anodes for High Capacity Li-ion Batteries, ***Journal of Power Sources***, **2016**, 304, 311-318 (**IF = 6.217, Cited: 1**)

12. Liyong Ding, Huan Chen, Qingqian Wang, **Tengfei Zhou**, Qingqing Jiang, Yuhong Yuan, Jinlin Li, Juncheng Hu, Synthesis and Photocatalytic Activity of Porous Bismuth Oxychloride Hexagonal Prisms, ***Chemical Communications***, **2016**, 52 (5), 994-997 (**IF = 6.834, Cited: 6**)

13. Chaofeng Zhang, Ruixiang Yu, **Tengfei Zhou**, Zhixin Chen, Huakun Liu, Zaiping Guo, Mass Production of Three-dimensional Hierarchical Microfibers Constructed from Silicon–carbon Core–shell Architectures with High-Performance Lithium Storage, ***Carbon* 2014**, 72, 169-175 (**IF = 6.20, Cited: 14**)

14. Renjie Wei, **Tengfei Zhou**, Juncheng Hu, Jinlin Li, Glutatione Modified Ultrathin SnS_2 Nanosheets with Highly Photocatalytic Activity for Wastewater Treatment, ***Materials Research Express***, **2014** 1 (2), 025018 (**Cited: 3**)

15. Renjie Wei, Juncheng Hu, **Tengfei Zhou**, Xianlong Zhou, Jinxiong Liu, Jinlin Li, Ultrathin SnS_2 Nanosheets with Exposed {001} Facets and Enhanced Photocatalytic Properties, ***Acta Materialia,* 2014,** 66, 163-171 (**IF = 5.058, Cited: 42**)

16. Hang Liu, Man Luo, Juncheng Hu, **Tengfei Zhou**, Rong Chen, Jinlin Li, β-

Bi_2O_3 and Er^{3+} Doped β-Bi_2O_3 Single Crystalline Nanosheets with Exposed Reactive {001} Facets and Enhanced Photocatalytic Performance, ***Applied Catalysis B: Environmental*****, 2013** 140, 141-150 (**IF= 8.328, Cited: 33**)

APPENDIX B: AWARDS RECEIVED

1 ISEM Postgraduate Student Merit Award, University of Wollongong, 2015.

2 International Postgraduate Research Scholarships, Department of Education and Training, Australian Government, 02/2013-09/2016.